

https://dspace.org/

# Geophysical methods for tunnel detection and characterization of a coal mine in Ermelo

**Moleleki, Nkimo Stephen**

**2019**

https://hdl.handle.net/10539/29620

Moleleki, Nkimo Stephen. (2019). Geophysical methods for tunnel detection and characterization of a coal mine in Ermelo. University of the Witwatersrand, https://hdl.handle.net/10539/29620

Downloaded from a DSpace repository. https://dspace.org/

# GEOPHYSICAL METHODS FOR TUNNEL DETECTION AND CHARACTERIZATION OF A COAL MINE IN ERMELO

**Nkimo Stephen Moleleki**




A dissertation submitted to the Faculty of Science, University of the Witwatersrand, in fulfilment of the requirements for the degree of Master of Science

1 November 2019, Johannesburg.

## DECLARATION

I declare that this dissertation is my own, unaided work. It is being submitted for the Degree of Master of Science at the University of the Witwatersrand, Johannesburg. It has not been submitted before for any degree or examination at any other University.



_____

Nkimo Moleleki

1st day of November 2019 at Johannesburg

## ABSTRACT

Void detection with gravity, DC resistivity and Ground Penetrating Radar (GPR) have been ubiquitously documented. Two techniques, namely magnetic and time-domain electromagnetic (TDEM), have received less attention. This research was aimed at evaluating the capability of four geophysical methods, namely gravity (specifically microgravity) as benchmark well known for tunnel and subsurface cavity detection, magnetics and time-domain electromagnetic (TDEM) methods, as well as a low frequency broad band ground penetrating radar (GPR) to delineate shallow mine adits (tunnels), characterize their physical properties (dimensions, strike, whether air-filled or water-filled) and depth. However, an old colliery on the farm called Driehoek in the Ermelo district discussed in this document was only accessible for a very limited time period as open cast mining was to commence and the low frequency GPR had to be abandoned but was used to delineate mine workings at a depth of 40 m at another site (Vlakhoogte Coal Mine near Delmas in Mpumalanga) and is briefly reported on. Thus, the main geophysical methods being evaluated were reduced to three. A suitable study area available with shallow tunnel development was this old colliery underlain mostly by electrically resistive sandstones of ~180 ohm.m, with more conductive minor shales and siltstones as country rock and coal seams exploited by checkerboard and bord and pillar mining method at shallow depth of ~5 m from surface.

Both magnetic and microgravity data were collected on the same grid pattern overlaying each other, but the TDEM consisted of a single line cross-cutting the microgravity grid pattern at an angle of about 35 degrees from the north. Evidence of underground openings was seen from a reconnaissance resistivity survey and a TDEM apparent resistivity pseudo section (resistivity values from the TDEM were orders of magnitude higher (~750 ohm.m) than the surrounding rock (~180 ohm.m)). 2D modelling of the microgravity and magnetic datasets was undertaken by using the free-ware Grav2dc and Mag2dc programs respectively. 3D density modelling however revealed that the openings are not tunnels but rather openings that will be referred to as bords/cavities. The results of 2D modelling of microgravity and magnetic datasets revealed that the bords are buried ~5 m from surface, have a width of ~3 m and have a stope width of 2 m. Forward modelling software, GmodIntrp.for and MagModIntrp.for, were used to produce 3D density and susceptibility models of the subsurface from the microgravity and magnetic data respectively and displayed in Geosoft Oasis Montaj. From the 3D density voxel model, a

density contrast of these voids/bords of -2.47 g/cm$^3$ with regards to the surrounding sandstone gave modelling results close to the theoretical value of -2.50 g/cm$^3$ for air-filled cavities leading to the conclusion that the bords do not contain water. The 3D models did not reveal the strike of these bords although some were inferred to be interconnected from the visualization of the 3D density model.

The success of the study could be bolstered beyond doubt through producing a conclusive 3D geological model that is a representation of the subsurface incorporating 3D models of all the datasets and not just microgravity and magnetics. The final conclusion is that the three methods under study can be successfully used to delineate openings (bords, drives, galleries, shafts and portals) at coal mines and to contribute towards reducing the cost of drilling by pinpointing where these openings can be intercepted. Knowing the lithology and its respective physical properties in the area thoroughly will contribute to deciding which geophysical methods are most applicable to address the problem.

This dissertation is dedicated to my guardian and mother, Mots'elisi Tau who encouraged me to do and finish a master's degree and never stopped believing in me even when I felt overwhelmed and doubtful thoughts crept into my mind.

## ACKNOWLEDGEMENTS

I would like to extend my most sincere gratitude to the following people and organisations for their help in making this research a success. This work could not have been possible without them:

- National Research Foundation (NRF) for funding this research.
- Mr. Simon Netshiozwi of Kimopax Ltd for giving me an opportunity to work at his mine and funding my field trip.
- My supervisors Prof. Edgar Stettler and Dr. Michael Jones for their supervision of this research. Special thanks to Prof. Stettler for taking time out of his ever-busy schedule to agree to meet me whenever I asked, for giving me full access to his personal software and overseeing the research to completion. Dr. Michael Jones for not enjoying the first weeks of his retirement to ensure that this work was completed with success. I thank him very much.
- David Ngobeni of the Council for Geosciences (CGS) for the TEMFAST-48 system he lent me as well as the dongle for processing the data. His insights are highly appreciated in processing the data.
- Dr. Leonie Maré of CGS for helping with the physical property measurements on the samples picked in-situ.
- Prof. Susan Webb for the information she provided prior to the field trip on how to collect good quality gravity data and the guidance she provided on data processing and forward modelling.
- My colleagues that helped me with the field data acquisition; Seeiso Moshoeshoe, Sikelela Gomo and Pontsho Makhateng.
- Dr. Stephanie Enslin-Scheiber for always being willing to discuss my project with me and bounce off ideas to improve it.
- My family and friends for their relentless support throughout the research.

# TABLE OF CONTENTS

DECLARATION ..... ii

ABSTRACT ..... iii

ACKNOWLEDGEMENTS ..... vi

TABLE OF CONTENTS ..... vii

LIST OF FIGURES ..... x

CHAPTER 1 - INTRODUCTION ..... 1

1.1 General Introduction ..... 1

1.1.1 Locality ..... 11

1.1.2 Background Geology ..... 12

1.2 Aims and Objectives ..... 14

1.3 Hypotheses ..... 14

1.4 Prospectus (Summary of upcoming chapters) ..... 15

CHAPTER 2 - METHODS AND PROCEDURES ..... 16

2.1 SURVEY DESIGN ..... 16

2.1.1 Preamble ..... 16

2.1.2 Microgravity ..... 16

2.1.3 Time Domain Electromagnetic Method ..... 21

2.1.4 Magnetic Method ..... 26

2.2 FORWARD MODELLING ..... 34

2.2.1 Preamble ..... 34

2.2.2 Microgravity ..... 38

2.2.3 Magnetic Method ..... 41

2.3 DATA COLLECTION ..... 42

2.3.1 Microgravity ..... 42

2.3.2 Time domain electromagnetic method ..... 45
2.3.3 Magnetic Method ..... 47
2.4 Chapter 2 Summary ..... 49
CHAPTER 3 - GEOPHYSICAL DATA FILTERS ..... 51
3.1 Preamble ..... 51
3.1.1 Fourier Transform ..... 51
3.1.2 Butterworth Filter ..... 53
3.1.3 Nth-order polynomial (for removing the regional field) ..... 54
CHAPTER 4 - DATA REDUCTION AND PROCESSING ..... 57
4.1 Preamble ..... 57
4.2 Microgravity ..... 57
4.2.1 Data Reduction ..... 57
4.2.2 Data processing and gridding ..... 67
4.3 Magnetic Method ..... 72
4.3.1 Data reduction ..... 72
4.3.2 Data processing and gridding ..... 73
4.4 Time domain electromagnetic method ..... 77
4.4.1 Data reduction and processing ..... 77
4.5 Chapter Summary ..... 80
CHAPTER 5 - DATA MODELLING AND RESULTS ..... 81
5.1 Preamble ..... 81
5.1.1 Lithological physical properties ..... 86
5.2 Microgravity ..... 87
5.2.1 3D Modelling and visualization ..... 93
5.3 Magnetic Method ..... 96

5.3.1 3D Magnetic Modelling and visualization ..... 101
5.4 TDEM Method ..... 104
5.4.1 TDEM modelling and results ..... 104
5.5 Chapter 5 Summary ..... 115
CHAPTER 6 - DATA INTERPRETATION, INTEGRATION AND DISCUSSION ..... 116
6.1 Preamble ..... 116
6.2 Data Interpretation ..... 116
6.2.1 Microgravity ..... 116
6.2.2 Magnetic Method ..... 123
6.2.3 Time Domain Electromagnetic Method ..... 126
6.3 Data Integration and Discussion ..... 130
CHAPTER 7 - CONCLUSIONS AND FUTURE RECOMMENDATIONS ..... 138
Appendix A ..... 141
Appendix B ..... 142
Appendix C ..... 143
REFERENCES ..... 144

# LIST OF FIGURES

**Figure 1.1.** Satellite image of Vlakhoogte colliery at surface where underground mining took place in the 1960s and open cast working took place recently as seen in the right upper corner. The open cast workings are an eye sore. .....3

**Figure 1.2.** Mine plan showing bord and pillar design (taken from Golturenko, 2018) overlain on the satellite image of Vlakhoogte colliery. The workings are approximately 40 m deep. .....4

**Figure 1.3.** Enlargement of the mine plan in Figure 1.2 to show the pillars which are represented by the small squares (white on the left and pink on the right), and the sometimes-uneven pattern against the dyke, a brown feature trending north-north east to south-south west in the centre of the map. The pillars are ~7 x 7 m in diameter and 3m high and the bord part is about ~ 6 x 6 m in diameter. .....4

**Figure 1.4. Top image:** Line traverses of radar over mined-out area as shown by mine plans. **Bottom three images:** The resulting radargrams of lines C2, C3 and C4 with the top axis showing the distance (in metres), the left vertical scale showing the depth (in metres) and the right vertical scale showing time (in nanoseconds). From Golturenko (2018). Areas of intense change of properties are indicated in red and coincide approximately with the depth of tunnelling. But the images are not clear cut and large variations exist between the three traverses. However, the penetration of the GPR is remarkable.....7

**Figure 1.5.** High resolution (100 m line separation and 50 m flight height) airborne magnetic survey over a section of an old colliery (from E. Stettler, personal communication). The undermined area is distinctly visible by the disturbed pattern in the upper central part of the map that is labelled as undermined area. The high frequency peaks have a clear WNW-SSE strike pattern indicating the possible orientation of the bord and pillar mining. .....8

**Figure 1.6.** Six theoretical magnetic forward models testing the effect of orientation, background contrast and dimensions of the stopes. All the models have a magnetic susceptibility of 0.01 SI units for the country rock except (e) and (f) which have 0.001 SI units. They all have a magnetic declination of -23.06° and inclination of -60°. They all are at a depth of 6 m from surface, all have a stope width of 3 m but different separation between the stopes. Figures 1.6a and 1.6b have stopes that are 40 m wide

and 50 m apart. Figures 1.6c to 1.6f have stopes that are 20 m wide and 100 m apart. .....11

**Figure 1.7.** Map of South Africa showing the Ermelo Coalfields (a red star surrounded by the Highveld and Witbank Coalfields also denoted by red stars) in Mpumalanga Province (blue) where the study area is located. Map created using QGIS and locations of the coalfields obtained from CGS (2012). .....12

**Figure 1.8.** Geological cross section of the Karoo Supergroup showing the coal deposits of the Ecca group. The Witbank and the Highveld coalfields bound the study area of Ermelo coalfields from the north east and west respectively (Hancox and Götz, 2014). Define dg and sg .....13

**Figure 2.1.** Google Earth image showing proposed location of the microgravity grid (in red) plotted on Google Earth (using Global Mapper13). On the right of the grid is the access to the tunnels and the insert image depicts an enlargement of the grid location. .....20

**Figure 2.2.** Current flow into the ground from a central loop transient EM system. This is an example of a receiver loop within a transmitter loop. Modified from Fantaye (2010). .....23

**Figure 2.3.** Representation of the earth's geomagnetic field as a giant bar magnet (left). GNP is geomagnetic north pole, GSP is geomagnetic south pole, NP is geographic north pole, SP is geographic south pole, ME is magnetic equator. On the right, components of the geomagnetic field (F) showing the declination (Dec) and inclination (Inc). The vertical component of the geomagnetic field is denoted as VMI (Vertical magnetic Intensity). Adapted from Dentith and Mudge, (2014). .....27

**Figure 2.4.** Time variations of the external geomagnetic field. The top two diagrams are the diurnal plots and the bottom plot shows the largely erratic plot of the field disturbed by a magnetic storm with an amplitude of about 50 nT. Taken from Dentith and Mudge, (2014). .....30

**Figure 2.5.** Underground tunnel opening showing a weathered coal seam and traces of pyrite and precipitated sulphur.....31

**Figure 2.6.** A picture showing the proposed location of magnetic grid (in yellow) plotted on Google Earth (using Global Mapper13). On the right-hand side of the grid is the cliff and access to the tunnels and the insert image represents a zoomed-in version of the survey grid pattern. .....32

**Figure 2.7.** A picture showing a planned microgravity (red) and magnetic (yellow) grid patterns (using Global Mapper13) based on the position of the resistivity line (blue). .....33

**Figure 2.8.** The mining permit area showing the underlying geology. This low-resolution map is used with permission from Kimopax Ltd and is not edited in any way. The geology key is in the bottom left corner. .....35

**Figure 2.9.** 2D Wenner-Schlumberger electrical resistivity vertical section for the reconnaissance section to guide the choice of the location for the survey. The vertical section is situated on the flat area above and parallel to the cliff including the coal seam in which the tunnels striking SE to NW occur and aligned to veer away from the cliff. That is, access to the underground was made through the coal seam as shown where adits occur. The photo was taken looking to the west and the resistivity section is adjacent to the cliff area but further west and about 60 m away from the edge at its nearest point. The photo of the vertical section shown below the resistivity section does not cover the complete extent of the resistivity section, but only about 72 m (shown by black dotted lines) of a 300 m long line.....36

**Figure 2.10.** A postulated vertical geological section based on observations used to guide 2D forward modelling of microgravity and magnetic methods. The model shows a postulated unrealistic horizontal overburden that was eventually superfluous in the final microgravity models as with gravity, horizontally layered strata only contribute to the background or regional gravity field and bodies must be at least slightly dipping or change in the vertical dimension to produce an anomalous effect, for instance uneven weathering. The tunnels in the model are designated by the blue squares with a strike length of 50 m in both directions and with a density of 0.0 g/cm$^3$ which was taken as the practical density of air. The host rock is the sandstone. The black coal seam is included in the section to show the position of the seam along the tunnels. It must be noted that this is an ideal case, but the pillars are not entirely coal.....37

**Figure 2.11.** A grav2dc microgravity model showing three tunnels (in blue), the bedrock (white background) and the overburden (in red). The model shows 3 scenarios, a neutral, a worst case and best-case scenario. Microgravity can delineate the tunnels even in the presence of a varying overburden because the overburden produces a longer wavelength variation and in spite of that the amplitude of the anomaly is about -0.158 mgal, which is much larger than the sensitivity of the gravimeter of about +/- 0.04 mgal

and above the expected geological noise level. However, the accuracy of the gravity measurements and the terrain must be very high. ..... 41

**Figure 2.12.** Magnetic model produced from Mag2dc, 2.75D modelling software. The background rock is the sandstone with an average susceptibility of 0.00023 SI. The blue rectangles are the tunnels with an assumed susceptibility of 0 SI. The magnetic intensity of the anomaly with the smallest amplitude is about -0.07 nT which is quite small. The tunnels are 5 m wide, 2 m high and are 5 m apart. ..... 42

**Figure 2.13.** (A) Field photo and (B) location diagram of the grid pattern layout of the microgravity data collection plotted in Geosoft Oasis Montaj (Educational kit 2018). L1 is the first traverse away from the cliff edge (as seen in Figure 2.9) accessing entrance to the tunnels up to the fourth line (L4) and the circles show measurement points spaced at 2 m apart. The picture on the left shows how the tape was laid out on the ground and where the stations were separated with brown tags adhered to the ground by green duct tape. This picture also shows that the terrain was relatively level and not rugged (see Appendix B for a topographic sheet of the study area). ..... 44

**Figure 2.14.** Google Earth map of the field station, repeat and base station measurements locations showing the pattern followed to acquire the microgravity data. There are a total of 14 repeat measurements from the 4 lines making 3 loops. The red dots represent the internal repeat measurements, while the yellow dots represent the external repeat measurements. The blue dot represents the base station which is about 50 m EES of the survey grid location. ..... 45

**Figure 2.15.** GPS data plot of the microgravity grid (black), magnetic grid (red) and TDEM line (blue) where the data were collected. ..... 46

**Figure 2.16.** Grid layout of how the magnetic data were collected showing all the 14 lines plotted in Geosoft Oasis Montaj (Education kit 2018). The lines are labelled L0E which is the first line from the right to the last line L13E. The lines were collected from the south to north (bottom-up direction). ..... 48

**Figure 3.1.** Shape of the Butterworth filter function for different filter degrees (n), as used in Geosoft Educational Kit (2018). Modified from Pashtoon (1987). ..... 54

**Figure 4.1.** A plot of gravimeter readings in mgal before (blue solid line) and after (orange solid line) the removal of drift. The drift in this loop is about 0.085 mgal over a period of 1 hour 40 minutes. ..... 60

**Figure 4.2.** A plot of gravimeter readings in mgal before (solid blue line) and after (solid orange line) the removal of drift. This is loop 2 which is made of two lines. The drift in

this loop over a longer period of 3 hours 20 minutes is about 0.205 mgal. This drift is removed, and this is seen from the fact that the gravity reading at the base station is zero for the drift corrected plot. The meter drifted much, and it is not surprising because of the 3-hour plus loop period. ..... 61

**Figure 4.3.** A plot of gravimeter readings in mgal before (solid blue line) and after (solid orange line) the removal of drift. This is loop 3 which is made-up of one line. The drift in this loop is 0.03 mgal over a period of 2 hours. This is quite interesting compared to the drift of the first loop which is 0.085 mgal over a shorter time of 1 hour 40 minutes as it hints that a loop period of around 2 hours is probably optimum for this gravity meter. ..... 62

**Figure 4.4.** A plot of line 1 which is the first loop showing plots of elevation (m) and Bouguer anomaly (mgal) against northing. From the figure, the variation of the amplitude in mgal of the anomalies is ±0.03 mgal and no regional trend is removed yet. This loop has 1 internal and 2 external (on loop 2) repeat measurements. Although there is a positive correlation between the elevation data and the BA values, this is considered fortuitous as the variation in BA values is much more than the variation in elevation differences (these have a 0.2 m maximal value). ..... 65

**Figure 4.5.** Plots of lines 2 and 3 of elevation (m) and Bouguer anomaly (mgal) against northing making loop 2. The amplitude variation of the anomaly size is ±0.02 mgal. Again, no regional field is removed yet. This loop has a total of 4 internal and 4 external repeat measurements. ..... 66

**Figure 4.6.** A plot of line 4 which is the third loop showing elevation (m) and Bouguer anomaly (mgal) against northing. The amplitude of the anomaly is ±0.03 mgal. ..... 67

**Figure 4.7.** A workflow of processing and gridding microgravity data in Geosoft Oasis Montaj where the result is three profiles that are modelled in Grav2dc. ..... 68

**Figure 4.8.** An artificially sun shaded map of the relative Bouguer anomaly data which includes the regional field to be removed. The colour bar is histogram equalized and the black circles on the map indicate the locations of the data points. ..... 69

**Figure 4.9.** A grid of the estimated first order regional field within and outside the Bouguer map. The regional field must extend outside the BA map to control the behaviour of the 3D polynomial surface on the boundary of the BA map. The black dots show points where the estimated gravity values were located to which the polynomial surface was fitted, which represented the regional field. The regional field is a third order 3D

polynomial surface. The image on the right shows the insert of the artificially sun shaded Bouguer anomaly map overlain onto the larger regional field map. .....70

**Figure 4.10.** An artificially sun shaded map of the residual gravity data after the removal of the first order regional gravity field. However, a slight increase in gravity values is still visible going from north to south that will be removed in a second step of regional removal. .....71

**Figure 4.11.** Base station readings (top figure) showed a diurnal variation of 18.6 nT (28420.0 nT – 28401.6 nT) over a period of about 3 hours and 13 minutes. The diurnal variation of the base station after smoothing became 17.8 nT (28419.915 nT – 28402.121 nT) over the same period as before smoothing. This is a small change in the amplitude of the magnetic field intensity which shows that the base station data were not noisy and this would not have an effect on the field station readings. .....73

**Figure 4.12.** Sun shaded total magnetic intensity map which has line levelling errors. The noise emphasized by the sun shading is apparent as streaky lines which should not be interpreted as geological information. .....74

**Figure 4.13.** Levelled sun shaded total magnetic intensity map. The map still has the regional field trend which is removed using Mag2dc especially on the part that is overlain with the microgravity map because that region is the subject of interpretation and target area for correlation of the two datasets. .....76

**Figure 4.14.** A flow chart model followed to process the TEM data.....78

**Figure 4.15.** Data editing windows (ZONDTEM1D) that are used to remove bad data points probably due to superparamagnetic effects. Care must be taken not to erroneously remove points with information, only those believed, to represent noise. The frame on the right-hand side represents apparent resistivity (red axis) against time and transient response (blue axis) against time.....79

**Figure 4.16.** Windows used for forward modelling of the data. Top left is the pseudo section of the model, top right image is the **interactive** model that can be edited by clipping and moving the blocky red line that shows the layers thickness. Bottom left is the model section which is a response of the layered model as controlled by the top right corner. Bottom right shows the model parameters table whose values can be manually input for the initial model. These values are the number of layers **N**, depth to the layers **h,** the thickness of layers **z,** and 3 parameters not specified here namely the polarizability **η** of a layer**,** decay constant **τ** and conductivity **ς**.....79

**Figure 5.1.** The sun shaded residual gravity map overlain on the total magnetic intensity map. The total magnetic intensity map's colour bar is on the right and the residual gravity map colour bar is on the left. Black lines L1, L2 and L3 are the lines trending north to south that were extracted from the gridded data and will be modelled with both Grav2dc and Mag2dc. ..... 83

**Figure 5.2.** A workflow used to produce 3-D models of both gravity and magnetic data. The Fortran programs "Conreg", "GmodIntrp" and "MagModIntrp" are code written by Prof. Stettler and are used with permission from the developer. ..... 84

**Figure 5.3.** Borehole locations on the study area plotted on Google Earth marked with red squares. Borehole BH001 is closest to the survey area (red lines) and its log was used to make a vertical borehole section of thickness against lithological layering. The depth from surface of borehole BH001 is 55.47 m and only three lithologies were intercepted. ..... 85

**Figure 5.4.** A stope completely depleted of coal and only the sandstone layer left behind. The poles are used to support the roof. This shows why there was no need to include the coal seam in the models. ..... 87

**Figure 5.5.** Gravity models showing a good fit to the data extracted from the grid for a postulated realistic geological scenario and known densities consisting of tunnels (in blue), sandstone (beige) and overburden (brown). (A) Is a model of line1 trending showing a single tunnel/void which gives an anomaly amplitude of about -0.045 mgal. (B) A model of line2 depicting three tunnels/voids giving a good fit to the measured gravity data and with the largest anomaly with an amplitude of about -0.065 mgal. (C) A best attained fit to the measured data with three tunnels/voids and the maximum response from one of the tunnels being about -0.063 mgal. The discrepancy between the observed and modelled gravity data in C is not as small as with both A and B and is ascribed to density variations in the sandstone not considered in the general geological scenario..... 90

**Figure 5.6.** A) The artificial sun shaded BA map with 1$^{st}$ order regional field removed. B**)** The 2$^{nd}$ order regional field removed during modelling in Grav2dc, reconstructed with Conreg (as explained earlier) is subtracted from the BA map with 1$^{st}$ order regional field removed. The resulting surface of the 2$^{nd}$ order regional field **(B)** is not sun shaded. The resulting residual map is shown in Figure 5.7. ..... 91

**Figure 5.7.** The sun shaded residual microgravity map devoid of any N-S trends on which interpretations will be made. ..... 92

**Figure 5.8.** An inverse distance weighted GModIntrp voxel model imaged in Geosoft. It is a 3D representation of the half-space from the microgravity data models and above it, the residual microgravity map as a digital terrain data is overlain. The colour bar on the left is for the residual microgravity data while the one on the right represents the density contrasts within the model with respect to sandstone. The hot colours represent high density and cold colours represent low density values. .....94

**Figure 5.9.** A 3D model showing the isolated iso-surfaces (blue bodies) that represent volumes of low densities preserved in the inverse distance weighted gridded model as seen in Figure 5.8. .....95

**Figure 5.10.** A 3D rotated model looking underneath shown from below looking upwards and the back showing the iso-surfaces. It is rotated to display the bottom alignment of the map with respect to the iso-surfaces. .....95

**Figure 5.11.** Model lines L1, L2 and L3 produced from Mag2dc. The tunnels (blue) have a zero magnetic susceptibility and the host rock was assigned a susceptibility that is a compromise between the coal susceptibility and the host rock's own susceptibility which provides a good fit to the measured data. The brown layer is the overburden included in the models with a very small susceptibility and average thickness of about 2 m. A) shows the model with two tunnels fitted and the total amplitude of the anomaly is about 0.66 nT. B) Three tunnels are fitted into the model with the biggest anomaly size of about -0.29 nT. C) Two tunnels are fitted into the model with the anomaly size of about -1.0 nT.....98

**Figure 5.12.** Forward model with a "hole" in the model aimed at validating the magnetic models based on the observed data. The model has a background rock in red, with a susceptibility of 0.002 SI, a tunnel of 0 susceptibility and an anomaly amplitude of about -1.25 nT. .....99

**Figure 5.13.** The regional magnetic field reconstructed from the Mag2dc modelled lines which were each 50 m long. It must be noted that this map covers the same area as the BA gravity map for consistency of interpretation and not the entire total magnetic field map.....100

**Figure 5.14.** (A) Diurnally corrected artificially sun shaded total magnetic intensity map that has directional noise along the survey lines that is clearly seen as streaky lines in the data. (B) A levelled total magnetic intensity map exhibiting less or no streaks than seen on the unlevelled map. This micro-levelled map will be used in the interpretation of the data. .....101

**Figure 5.15.** 3D models of susceptibility of the half-space interpolated between 2D magnetic data models. Both models are similar but rotated. The low susceptibility regions are clipped out of the model to visualize such regions within high susceptibility regions. ..... 102

**Figure 5.16.** 3D magnetic susceptibility models spatially clipped at about the top -5 m to show the low susceptibility regions that are inside of the model. ..... 103

**Figure 5.17.** Models that are not filled but edge plotted and the low susceptibility iso-surfaces (blue bodies) preserved in the models. The iso-surface of ~7.0 x $10^{-5}$ SI starts at a depth of 5 m below the surface. ..... 103

**Figure 5.18.** An example taken and modified from Cooper and Munday (2012) showing the relationship between the voltage decay with time. The decay is rapid/sharp on resistive ground (red curve) and slow/smooth on conductive ground (black curve). 105

**Figure 5.19.** A representation of "conductivity" equated with the rate of decaying voltage (emf) against "depth" equated with increasing time channels (Modified from EM Geosci, 2018). "Conductivity" (vertical axis) gives an average "conductivity" of the half-space, subsurface and its variation with depth (increasing time channels) of different successive layers and can give a conductivity depth image, or CDI as it is known. ..... 106

**Figure 5.20. Left**: Data editor window used to clean the observed transient build-up (blue axis) and apparent resistivity curves (red axis). **Right**: Model editor window used to calculate the resistivity and transient behaviour from the observed curves. The bottom axis shows model depth in metres. The blocky red solid line indicates the layered earth model where the vertical sections indicate changes in layer resistivity and the horizontal sections layer thickness (Taken from ZondTEM1D manual, 2017). ..... 107

**Figure 5.21.** ZondTEM1D screen dump window used for modelling of the data before carrying out the inversion. The top panel is the model apparent resistivity against time, the middle panel is the starting model layered section which is a response from the individual soundings that are modelled using the model editor windows (bottom panel, left) and the model table window (bottom right). The solid dotted line shows the observed apparent resistivity curve while the open dotted line curve shows the modelled apparent resistivity curve. The misfit between the two curves gives the root mean square error (RMS). ..... 109

**Figure 5.22.** Inverted models from sounding curves. Lines with solid dots represent measured curves and lines with open circles represent curves fitted by the inversion

algorithm to the measured data and produce the best model at the station that best represents the subsurface at that point. The resultant model is given by the solid blocky line which for sounding 3 (on the left) represents: Layer 1 = 1m thick, 12 Ω.m; Layer 2 = 40 m thick,750 Ω.m; Layer 3 = 15 Ω.m and infinitely thick. Sounding 8 (on the right) represents: Layer 1 = 30 m thick, 170 Ω.m; Layer 2 = 30 m thick, 90 Ω.m and Layer 3 = 30 Ω.m.....111

**Figure 5.23.** Inversion models for sounding curve 9. Solid dots represent observed curves and lines with open circles represent curves fitted by the inversion. The image on the right is the model table that shows the layer parameters that were incorporated into the inversion to produce such model: highlighted in red is the resistivity and thickness of the layers. The model converged with an error of 2.0%.....112

**Figure 5.24.** Soundings 12 and 16 depicting four-layer inversion models. Lines connected by solid dots represent the measured curves and lines connected by open dots represent the curves of the best inversion estimate of the layered earth that fits the sounding data at that point. .....113

**Figure 5.25.** Four-layer inversion model of Sounding 18 at distance 135 m of a 150 m long line. Lines connected by solid dots represent the measured curves and lines connected by open dots represent the curves of the best inversion estimate of the layered earth that fits the sounding data. The image on the right is the model table that shows the parameters that were obtained from the inversion to produce the model on the left. The model converged with the error of 0.6%. .....113

**Figure 5.26.** Inversion results from the sounding data. The top section is the apparent resistivity with respect to time after switch-off and the bottom section is the colour coded first pass apparent resistivity section showing model depth vs distance. The cold colours show low conductivity and the warm colours show high conductivity. .....114

**Figure 6.1.** Bouguer anomaly map from which three lines, L1, L2 and L3 were extracted and modelled in Grav2dc. **A** to **A'** shows the direction of L2 that is modelled to produce a 2D model of the earth.....117

**Figure 6.2.** 2D model of the 50 m long Line2 running from North (**A**) to South (**A'**) showing three bords fitted to the observed data and with a misfit of 0.02 mgal between the observed and modelled data. The size of the biggest anomaly is -0.065 mgal and of the smallest anomaly is about -0.058 mgal. This figure is similar to Figure 5.5B but with the addition of the coal seam. .....119

**Figure 6.3.** A residual gravity map showing what are interpreted as bords. Special attention is paid to the bords intercepted by line, L2 shown by the white dotted line **A** to **A'**. Some bords are not clearly resolved on the map. .....120

**Figure 6.4.** Gravity data model compared with the final residual microgravity map. The model is made from line **A** to **A'** which is north to south. The residual microgravity map from Figure 6.3 is rotated 90 degrees clockwise so as to align it with the model in correct directions. Note the values of the gravitational acceleration produced by the bords; -0.065 mgal on the model and -0.063 mgal on the map. .....121

**Figure 6.5.** Iso-surfaces representing the modelled bords are shown in blue and have a density contrast of -2.467 g/cm$^3$ as depicted by the colour bar. The model is a wire-frame so that the bords can be easily shown. This model is a 9 m x 50 m x 20 m (9000 m$^3$) volume. The bords from this model have 3 m width and 3 m thickness (height). The thickness is not 2 m as on the 2D models. This may be due to non-precise clipping (lowest density values were preserved as iso-surfaces) of the low-density regions in the 3D visualization. .....122

**Figure 6.6.** A mined-out opening that was accessed and had dimensions of 2 m thickness (stope width) and 4 m wide as was measured with a laser rule when accessed. Of interest is the single line brick wall built to offer roof support and keep illegal miners out. .123

**Figure 6.7.** Levelled Total Magnetic Intensity (TMI) map from whose portion lines of magnetic data were modelled in Mag2dc. Interpreted model is from line, L2 trending North to South.....124

**Figure 6.8.** 2D Mag2dc model of line, L2 trending south to north. Notice how the wording has been changed from tunnels to bords/cavity since the interpretation. .....125

**Figure 6.9.** A 3-D voxel visualization of the earth model. **Left**: solid model with low susceptibility data values clipped. **Right**: wireframe model showing iso-surfaces that represent low susceptibility values as represented by the colour bar on the left. .....126

**Figure 6.10.** Apparent resistivity pseudo section (top) and the colour coded model section (middle) from which the pseudo section is calculated through the least squares inversion process. The bottom image (C) is a plot of apparent resistivity against depth and distance of the interpreted data from ZondTEM1D (results of the middle image). This highlights better the first 35 m and depicts an offset on the sandstone layer on the top image. The dots indicate where the sounding measurements are known and were used for the interpolation.....129

**Figure 6.11.** A comparison of 2.75D models from line 2 of microgravity data from Grav2dc (top) and magnetic data from Mag2dc (bottom). The overburden is thicker on the magnetic model. ..... 131

**Figure 6.12. Top**: TDEM pseudosection plotted in relation to the residual microgravity map on Google Earth. North is to the right. **Bottom**: Interpreted residual microgravity map (left) compared with the interpreted TDEM section (right). Both images show offset cavities at the point where they intersect. This is better shown by the image on the bottom right corner. This image shows an offset on the highly resistive layer shown in pink. ..... 134

**Figure 6.13.** Interpreted geology cross section derived from 3D density models (visualized as Geosoft's voxel model), microgravity residual grid, TDEM cross section and borehole geophysical data ..... 135

# CHAPTER 1 - INTRODUCTION

## 1.1 General Introduction

South Africa being endowed with unparalleled mineral wealth has many abandoned mines and undermined areas being encroached upon by a rapidly growing population searching both for leftover minerals and living space. Where old mine records have been lost or are not as accurate as today's demands dictate, locating underground stopes, drives, galleries, shafts, and portals, remotely, is not a routine process yet.

Using geophysics to detect underground openings is a daunting task. Several factors need to be taken into consideration when delineating a target. Is the opening a cave system, a cavity, a mine, a void (dry cavity) or even a tunnel/adit (Daniels, 1988)? Is the contact sharp (as in a mine), or gradational (as in a dissolving dolomite)? What also contributes to the challenges associated with this study is the fact that these openings may be as shallow as 5 m, about 100 m deep, man-made, natural and occurring under different geological environments which may be dolomitic or clayey (Daniels, 1988). For instance, if the opening is natural (due to subsidence), this might be caused by the dissolution of the host carbonates rocks. For man-made openings, it is helpful to know whether the opening extends for large distances and whether fracturing is associated with it due to stress relief resulting from removing the host rock.

What makes this task even more difficult from a geophysical perspective is the depth-to-diameter ratio of the tunnels for all geophysical methods. A tunnel 1 m in diameter should be easier to detect from surface at a depth of 5 m than at 50 m (Sloan, 2015). Empirically, what this means is that for the geophysical method to delineate a tunnel, its width must be equal or greater than about 20% of the burial depth. This is possible in coal mines, especially abandoned ones due to the collapsing stopes which widen the opening, thus enhancing the depth-to-diameter ratio. Knowing what the target cavity is, is not enough, there also is a need to know if it is filled with water or debris, what the host rock is and the expected orientations and the dimensions. Each of these parameters is very important in influencing the choice of

geophysical method to be used to investigate the target bearing in mind that there should be a physical property contrast for the geophysical method to work.

The issue of void and tunnel detection also has a definitive economic, social and safety concern that impacts property evaluations, citizen safety, construction and mining. The importance of being able to approximately pinpoint where the underground adits occur in 3D space is of much importance. Many papers have been published on void/tunnel detection using Ground Penetrating Radar (GPR) and electrical resistivity tomography (ERT) (e.g. Hatherly, 2013; Martinez-Pagán et al., 2013; Munk and Sheets, 1997; Peters et al., 1994). The research aims here are thus to consider and illustrate detection with 3 geophysical methods commonly used, namely magnetics, electromagnetics and gravity. Many tunnels have been made a long time ago and old mine plans are simply not available anymore. A void detection capability is therefore of fundamental importance to avoid the subsidence of erected structures because failure to do so may incur great financial loss or loss of life. Also, coal and other mining companies upon re-exploiting previously mined areas need to identify adits and pillars, where pillars are earmarked for mining if the confidence exists that the locality has potential for mineral extraction. Van Schoor and Fourie (2015) state that there may be an opportunity in re-mining old coal workings, especially bord-and-pillar mines as recent developments made in open cast mining make them again economical.

To highlight the daunting task of mapping such tunnels, an example to motivate the study is given from the Vlakhoogte Coal Mine near Delmas, east of Johannesburg, Mpumalanga South Africa (Golturenko, 2018), mined underground in the 1960s and where presently new value is being sought by open cast mining of the remaining pillars. Figure 1.1 is a satellite image that depicts the present surface conditions, which is cultivated land. However, in the top right-hand corner of the image is an abandoned open cast operation, which is a visual and environmental problem. In Figure 1.2, an original mine plan which was available from the 1960s is overlain on the Google image. It shows one of the oldest mining methods namely, the bord and pillar mining method used in those days. The little squares which are shown more clearly in the enlarged diagram (Figure 1.3), represent the pillars left behind. They are approximately 7 x 7 m in size and the surrounding coal (bord or ‘rooms’) removed in blocks are ~6 x 6 m. It is clear that a vast amount of coal is left in place. The seam at Vlakhoogte is about 40 m below surface

and the individual voids and pillars would be very difficult to detect with any geophysical technique except with ~~a~~ ground penetrating radar provided the host rock is not conductive.




**Figure 1.1.** Satellite image of Vlakhoogte colliery at surface where underground mining took place in the 1960s and open cast working took place recently as seen in the right upper corner. The open cast workings are an eye sore.

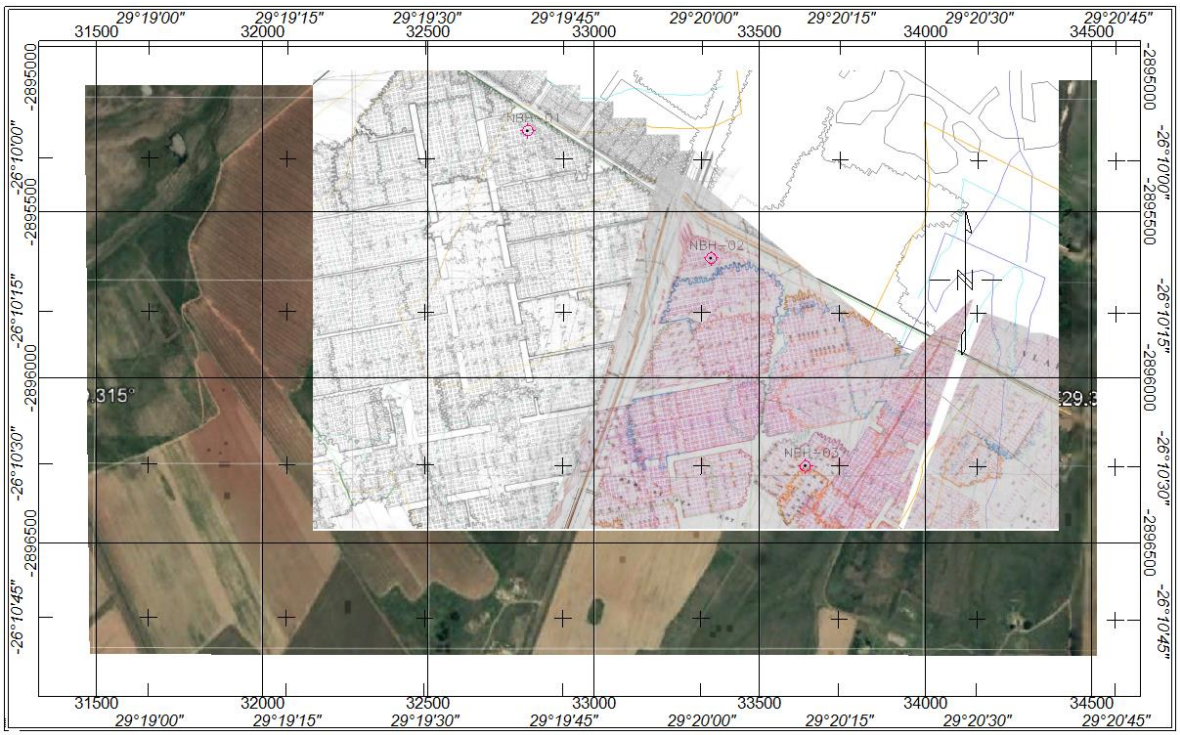


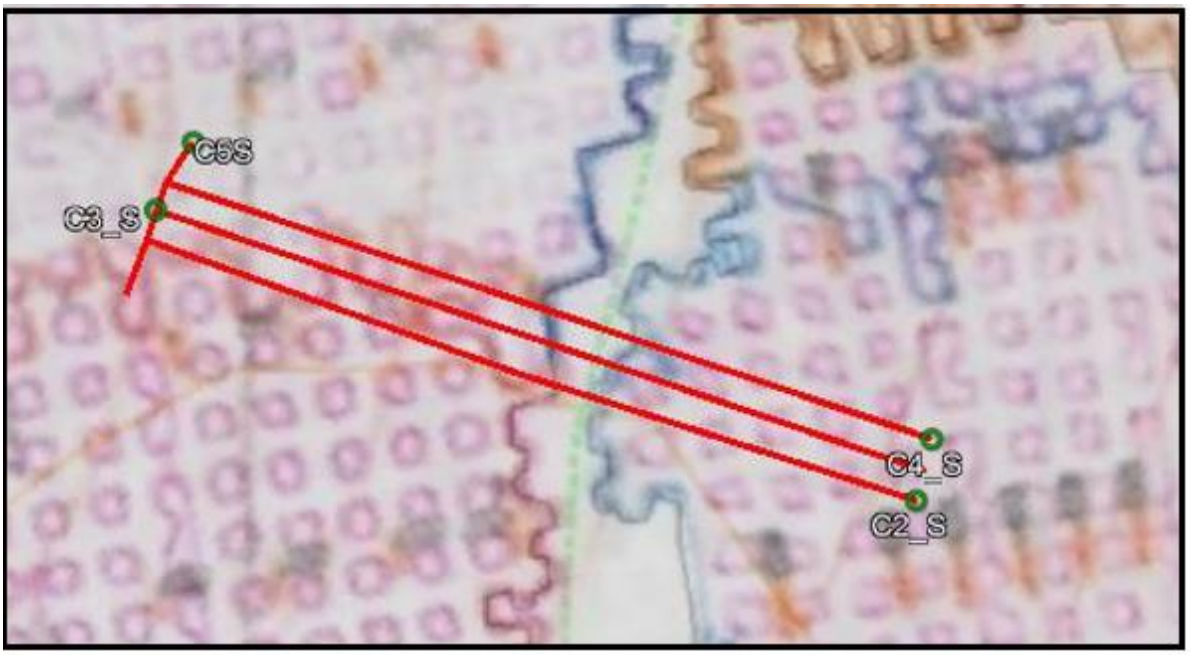

**Figure 1.2.** Mine plan showing bord and pillar design (taken from Golturenko, 2018) overlain on the satellite image of Vlakhoogte colliery. The workings are approximately 40 m deep.

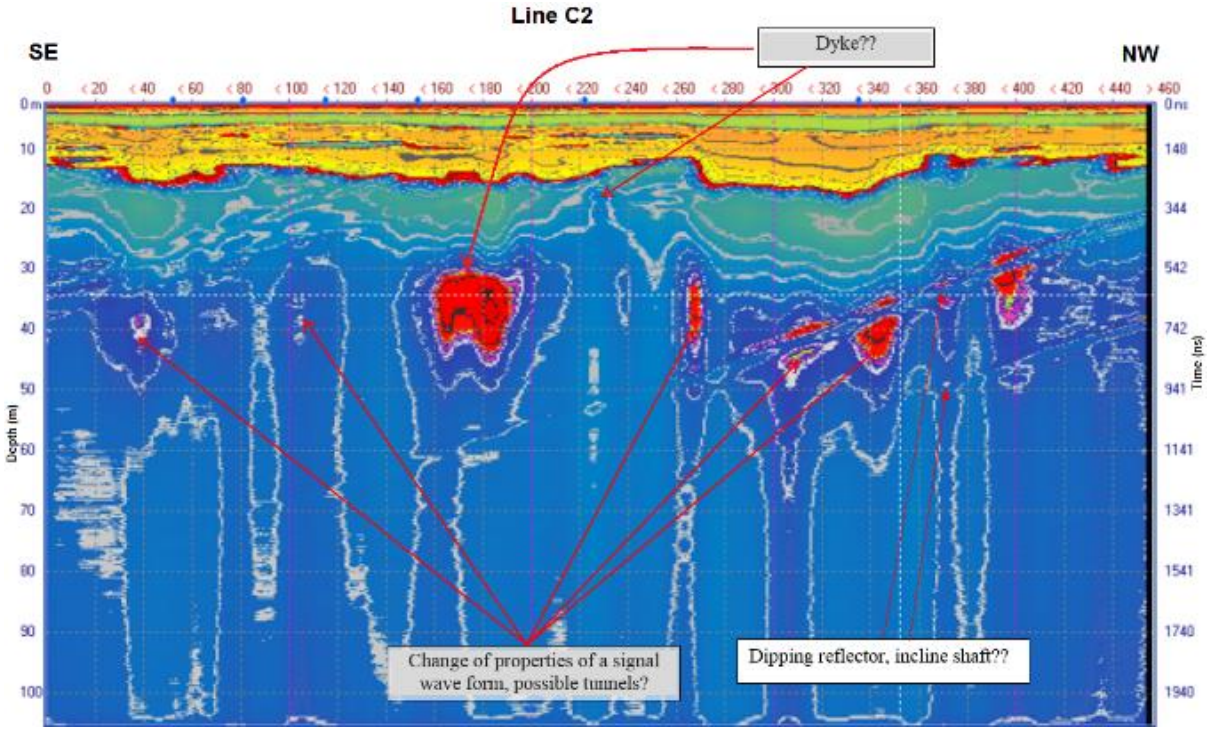



**Figure 1.3.** Enlargement of the mine plan in Figure 1.2 to show the pillars which are represented by the small squares (white on the left and pink on the right), and the sometimes-uneven pattern against the dyke, a brown feature trending north-north east to south-south west in the centre of the map. The pillars are ~7 x 7 m in diameter and 3m high and the bord part is about ~ 6 x 6 m in diameter.

The bord and pillar design is a checkerboard pattern and varies between mines depending on the age and the strength of the supporting strata and the optimum size of the pillars is critical. If the pillars are too thin and far apart, the mine will collapse and if they are too large, say 8 m, significant quantities of valuable material are left behind (Nayak and Dalai, 2010).

Figure 1.4 present the results of a lightweight and portable monopulse, LOZA ground penetrating radar (GPR) survey at Vlakhoogte (Golturenko, 2018). These data are presented here to provide an example of how GPR does delineate stopes even though it could not be used in the study area. Unfortunately, this equipment is not commercially available, and this survey was conducted for the mine owners. The Russian owners of the LOZA GPR system state that the radar had a frequency band of 1-25 MHz. The transmitter produces a powerful 21kV pulse, and antennas are 6 meters long for the 25 MHz and longer than 6 m for lower frequencies. The receiver sensitivity is 100 μV, using a time scan of 2048 ns with a sampling time of 1 ns. The unverified Vlakhoogte radar images possibly indicate the tunnels at the expected depth of approximately 40 m. These radar results are added to address and strengthen the fact that radar can work for delineating workings at coal mines if the strata is not conductive. This method was not incorporated at the study area because time was a constraint since mining in the area was ready to commence. Another area could have been chosen to try out radar, but it was not an easy expedition to acquire a test site as colliery owners are hesitant to allow anyone on their property because of perceived risks associated with allowing students on site and what happens to the data they collect. There is also the problem of illegal miners that posed a security threat to both the student and the mine owners.


C3_S
C4_S
C2_S


Line C2
SE
NW
Dyke??
Change of properties of a signal wave form, possible tunnels?
Dipping reflector, incline shaft??
Depth (m)
Time (ns)

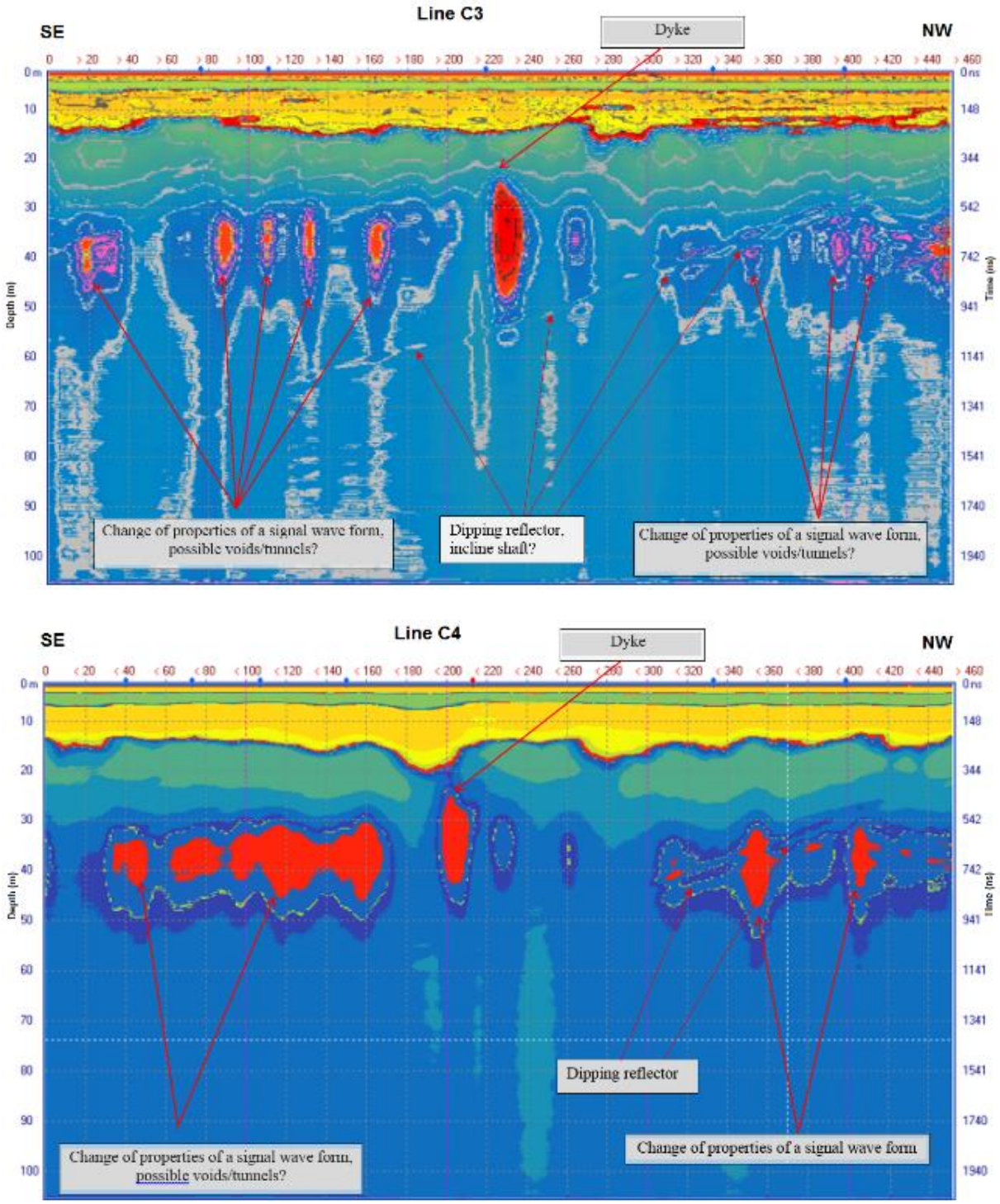



**Figure 1.4. Top image:** Line traverses of radar over mined-out area as shown by mine plans. **Bottom three images:** The resulting radargrams of lines C2, C3 and C4 with the top axis showing the distance (in metres), the left vertical scale showing the depth (in metres) and the right vertical scale showing time (in nanoseconds). From Golturenko (2018). Areas of intense change of properties are indicated in red and coincide approximately with the depth of tunnelling. But the images are not clear cut and large variations exist between the three traverses. However, the penetration of the GPR is remarkable.

A high-resolution (100 m line separation and 50 m flight height) aeromagnetic survey performed over old colliery also near Delmas in Mpumalanga (not at the exact location of the GPR survey) is depicted in Figure 1.5. In this classified image we can see the effect of the mining in the NW corner in the Delmas vicinity where the variation is apparent in the upper central part of the map bounded by the solid black line. The high frequency peaks have a clear NW-SE strike pattern indicating the possible orientation of the bord and pillar mining and magnetic surveys could be a more general and easy way of identifying undermined areas in coal fields. This motivated the choice of magnetic method in this study. The cause of the high frequency disturbances is unclear but could be due to absence of material or decomposition minerals that originated from the breakdown of pyrite in coal and forming new magnetic minerals as discussed further in the next section. It is not known how extensive this behavior has been witnessed but this example has partially led to the magnetic technique being incorporated into being used at the test site near Ermelo, the site used in the study.

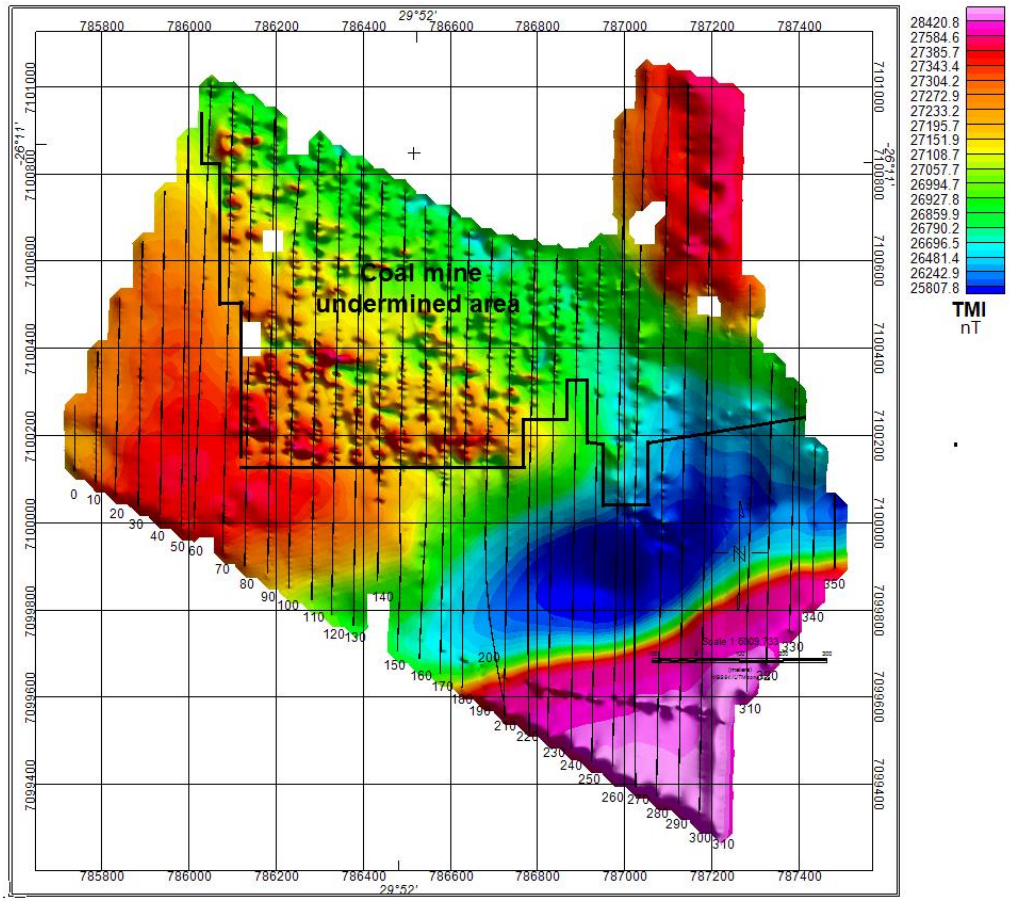



**Figure 1.5.** High resolution (100 m line separation and 50 m flight height) airborne magnetic survey over a section of an old colliery (from E. Stettler, personal communication). The undermined area is distinctly visible by the disturbed pattern in the upper central part of the map that is labelled as undermined area. The high frequency peaks have a clear WNW-SSE strike pattern indicating the possible orientation of the bord and pillar mining.

Table 1.1 summarizes surface geophysical methods previously used to delineate tunnels at coal mines. The table gives the geophysical methods appropriate for delineating old mine workings and near surface cavities. Due to the varying geological environments (from soft rock to hard rock) as well as the void type or adits, past experiences have shown that a combination of geophysical techniques should be used to attempt to identify or delineate such voids. Since no single geophysical method can completely characterize the underground adits or voids, the applicability of three geophysical methods, two of which are less well represented in the literature namely time domain electromagnetic (TDEM) and magnetic methods will be tested together with the microgravity method. While magnetic method is well motivated for in the example studies above, the TDEM is known to work in delineating the tunnels if they host water (Van Schoor and Fourie, 2014).

**Table 1.1.** Geophysical methods that have previously been used to delineate air and water filled voids and tunnels showing exploited physical property contrast, depth range, resolution, and survey type. (Adapted from Van Schoor and Fourie, 2014)

| | **Physical property contrast** | **Typical required depth range** | **Typical required resolution** | **Appropriate geophysical methods** | **Suitable survey geometry** |
|---|---|---|---|---|---|
| Delineation of old workings (full mining extent) | Air-filled: density, conductivity Water-filled: conductivity | 0 – 50 m | Accuracy < 5 m | TDEM, Microgravity, Resistivity/IP | Grid surveys on surface |
| Near surface cavity detection | Voids: density, resistivity, conductivity, dielectric, thermal Water-filled: conductivity, resistivity, dielectric | 0 – 20 m | 1 – 2 m | Thermal imaging, GPR, resistivity/IP, FDEM, TDEM | Grid surveys – preferably low altitude airborne grid surveys |

TDEM: Time-domain electromagnetic method
IP: Induced polarization
FDEM: Frequency-domain electromagnetic method
GPR: Ground penetrating radar

A decision had to be made on the choice of the methods to use to delineate tunnels at a coal mine, and a rigorous review of the literature was made. It was found that the magnetic method is not the preferred method for tunnel detection at a coal mine except in cases of magnetic signatures of burnt coal (Van Schoor and Fourie, 2014). The data imaged in Figure 1.5 demonstrate that the magnetic method could well work if there is a susceptibility contrast associated with mineral alteration of the coal. This was the hypotheses at this point since no modeling was done to account for that, and so to strengthen the idea of electing to use the magnetic method, forward models were calculated (Figure 1.6). A total of six models were made, each having three tunnels referred to as stopes. The dimensions of these tunnels that are 100 m apart are labelled on the models. They all are at a depth of 6 m from surface, all have a stope width of 3 m but have different widths in each case (40 m and 20 m). The amplitude of the magnetic intensity in each case is shown to elucidate the size of an anomaly emanating from given physical properties and dimensions of a model specified.

These forward models in Figure 1.6 were made without the physical property measurements of the actual lithology from the study area known but mostly based on the information about the geometry of the rooms from the mine owner, Mr. Simon Netshiozwi (personal communication) . These models revealed that the magnetic susceptibility contrast of the country rock, sandstone and the tunnel (air) is the most influential parameter in the magnetic intensity variation for tunnel detection. A decision was thus made to use the magnetic method with the first choice methods of gravity (microgravity) and time domain electromagnetic method (TDEM).

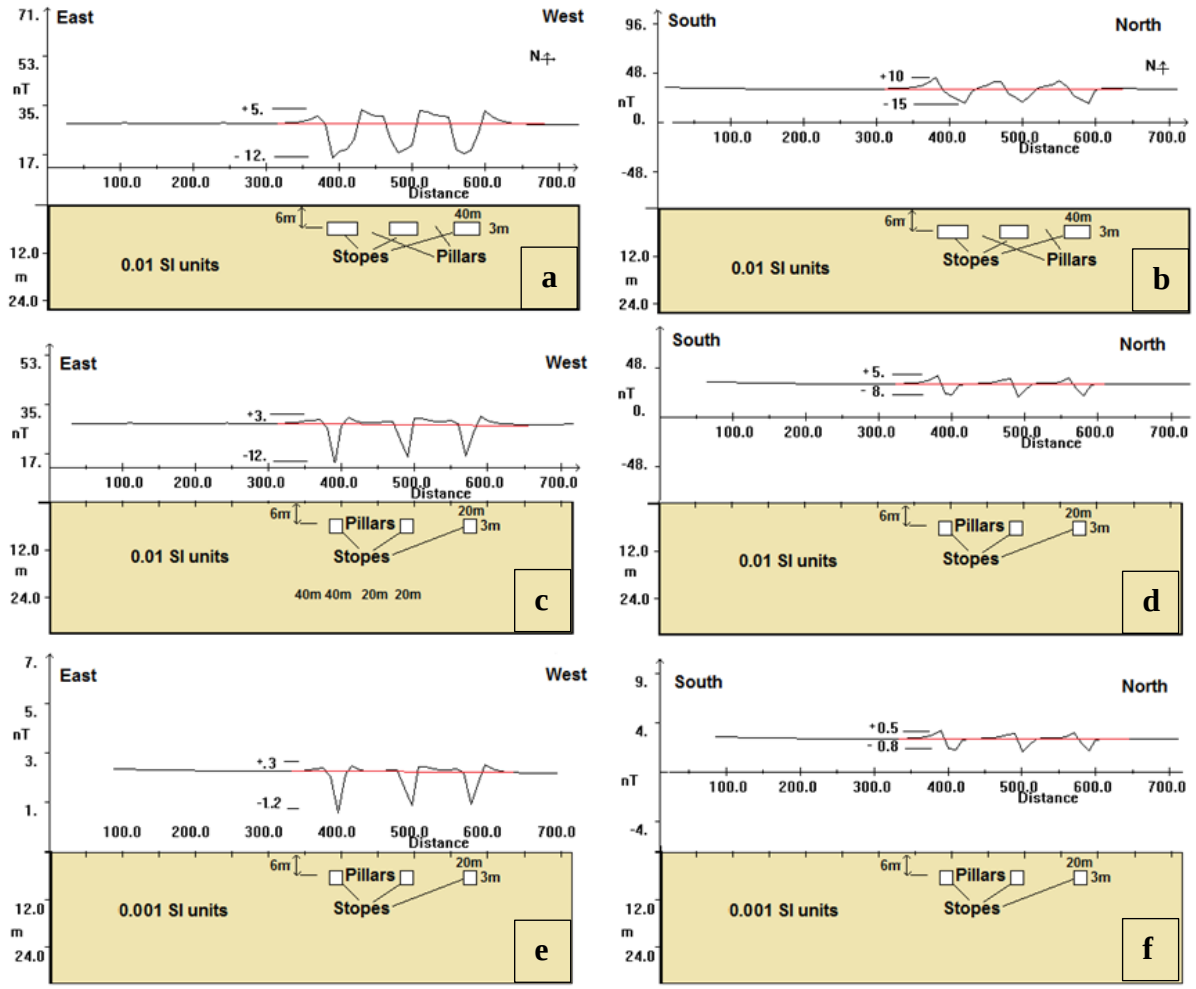



**Figure 1.6.** Six theoretical magnetic forward models testing the effect of orientation, background contrast and dimensions of the stopes. All the models have a magnetic susceptibility of 0.01 SI units for the country rock except (e) and (f) which have 0.001 SI units. They all have a magnetic declination of -23.06° and inclination of -60°. They all are at a depth of 6 m from surface, all have a stope width of 3 m but different separation between the stopes. Figures 1.6a and 1.6b have stopes that are 40 m wide and 50 m apart. Figures 1.6c to 1.6f have stopes that are 20 m wide and 100 m apart.

### 1.1.1 Locality

This section discusses the actual study area location and not the locations that were used in the examples to motivate for this study. The study area is in the province of Mpumalanga and falls within the municipal confines of the town of Ermelo (Figure 1.7). The Ermelo coalfields range in depths from 0 – 100 m and the coal seams dip gently to the southwest with minor folding

(Van Schoor and Fourie, 2015). These coalfields are bounded by the Witbank Coalfield in the north, Highveld Coalfields in the west and Utrecht Coalfield to the south as shown in Figure 1.7. The primary objective was to test the different techniques at an abandoned underground coal mine where tunneling and galleries occur within the first 100 m depth, they are even shallower at the study area occurring within the first 10 m. Such a site was found on the farm, Driehoek and had the added advantage that access to the site was easily established. Simon Netshiozwi of Kimopax was instrumental in arranging access to this defunct coal mine when it was not easy to get one.

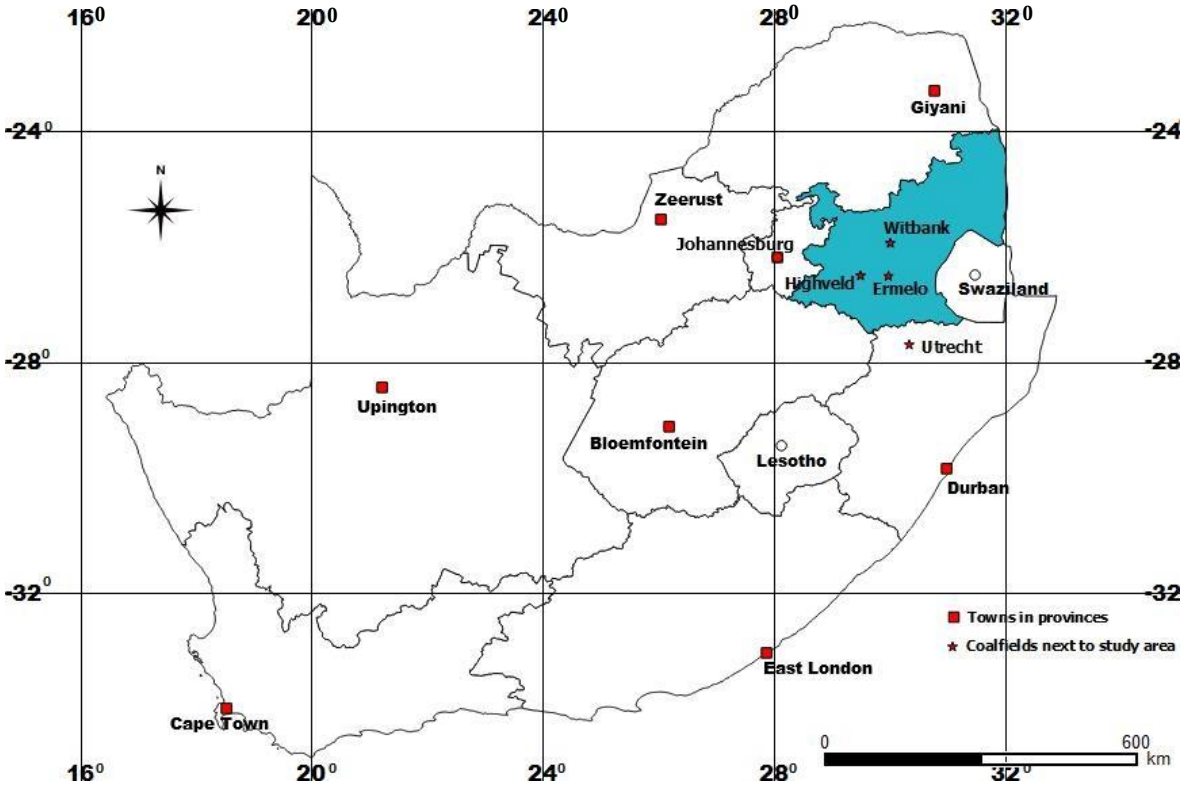



**Figure 1.7.** Map of South Africa showing the Ermelo Coalfields (a red star surrounded by the Highveld and Witbank Coalfields also denoted by red stars) in Mpumalanga Province (blue) where the study area is located. Map created using QGIS and locations of the coalfields obtained from CGS (2012).

## 1.1.2 Background Geology

The study area of the Ermelo coalfields is within the Vryheid Formation of the Ecca Group of the Karoo Supergroup. The Karoo basin is lithostratigraphically subdivided into the Dwyka, Ecca and Beaufort Groups succeeded by the Molteno, Elliot, Clarens and Drakensburg

formations (S.A.C.S, 1980)(see Figure 1.8). The Ermelo coalfields host up to eight coal seams within the middle Ecca Group sediments of the Karoo Supergroup, but not all are present in the various sectors (Van Schoor and Fourie, 2015). The rock types found within the Vryheid Formation are mainly shales, coal, sand- and siltstones and some conglomerates (Jonson et al., 1996).

Coal was first mined in South Africa in 1857 and currently South Africa is the sixth largest producer of coal throughout the world (Hancox and Götz, 2014). The coal deposits in the Karoo basin range in age from early Permian to late Triassic and their classification is based on their metamorphism, resulting in compactness of the coal (S.A.C.S, 1980). The majority of the economical coal deposits are within the Vryheid Formation which is about 70 m to 500 m thick (Hancox and Götz, 2014).

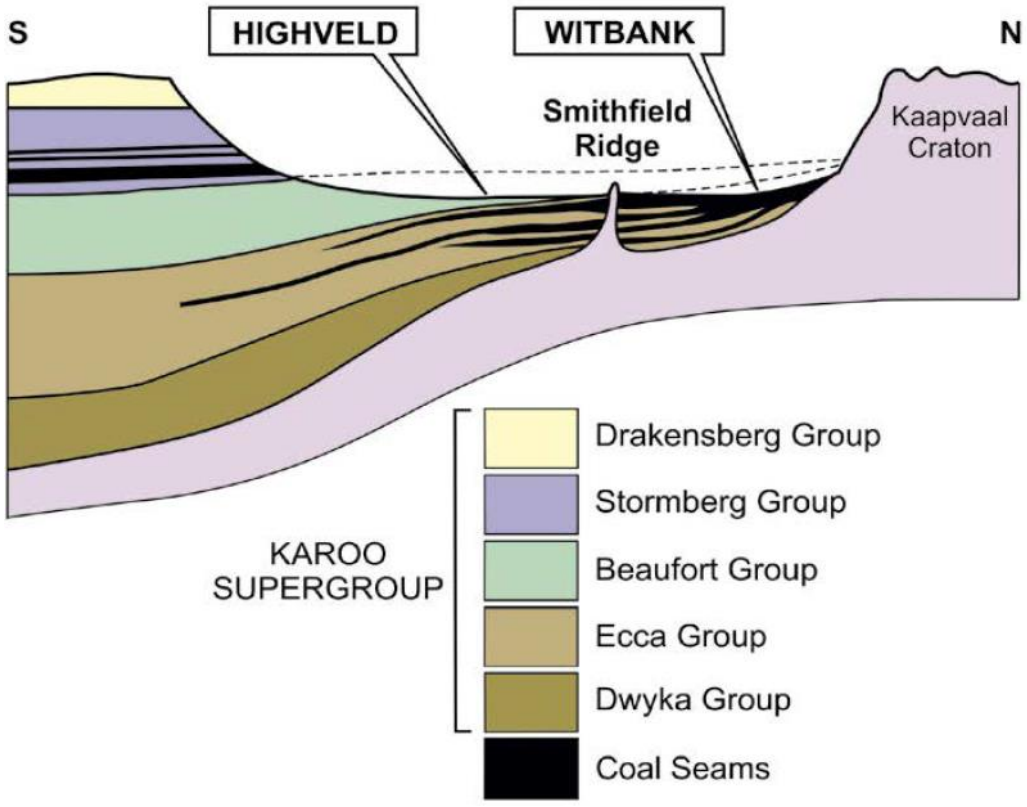



**Figure 1.8.** Geological cross section of the Karoo Supergroup showing the coal deposits of the Ecca group. The Witbank and the Highveld coalfields bound the study area of Ermelo coalfields from the north east and west respectively (Hancox and Götz, 2014).

## 1.2 Aims and Objectives

This research aims to detect isolated portals and tunnels which may be inclined towards the dip of the lithology and are only a few metres below surface at Driehoek Coal mine in the Ermelo district using microgravity (very high-resolution gravity mapping), the time domain electromagnetic (TDEM), magnetic and resistivity methods. Every geophysical method has its own strengths and its weaknesses, so it is important to have more than one method that should complement each other.

The experimental site was previously an underground mine and when mining was stopped due to low grade coal on the then mined seam C where the stopes would be, the farm was sold (personal communication with Simon Netshiozwi, mine owner). Mining was recently resumed as an open pit project and the new owner needed to know where to mine safely and to what extent in order to avoid collapses. This posed an opportunity to evaluate the usefulness of these methods for this particular project, with very specific physical properties and geometry. The time period for data acquisitioning was constrained because it had to be completed before the blasting would commence.

## 1.3 Hypotheses

Air-filled tunnels are more readily detectable with microgravity than water-filled tunnels due to larger density contrast. The air-filled tunnels have a larger density contrast with the surrounding rock than water-filled tunnels, hence this will increase the magnitude of the gravity anomaly. With TDEM however, water-filled tunnels are easier to detect than air-filled tunnels due to the increase in electrical conductivity contrast between water and the host rock. Water with a pH of about 6 is more conductive than a neutral pH and this also increases the conductivity contrast. This does not mean that dry tunnels are not detectable with the TDEM method, but it will be easier to detect if they are water-filled. With the magnetic method, the tunnels could be easily detectable if the coal is altered due to the presence of water because this would cause an increase in its susceptibility as it could be burnt due to spontaneous combustion (Bell et al., 2001) or it is hypothesized that the alteration in the coal resulting in pyrite could form a magnetic iron oxide to explain the magnetic signature (Bell et al., 2001) seen in Figure 2.5.

## 1.4 Prospectus (Summary of upcoming chapters)

The dissertation is divided into seven chapters and Chapter 1 introduces and motivates the research, gives a brief overview of the geology, the problems that can be solved with the findings of the research, the aims of the research and work done elsewhere with GPR and magnetics to address the same problem of tunnel/adit detection. Chapter 2 details the theoretical background of each method, motivates for the use of TDEM, gravity and magnetic methods with forward modeling, resulting in a design for each survey. This chapter also states why 2D electrical resistivity was used as a reconnaissance survey to guide the forward modelling of the three methods.

Chapter 3 discusses some of the geophysical filters used in enhancing the geophysical data, in particular, magnetic and gravity data. Chapter 4 gives an account of the steps followed in reducing and processing the acquired data. This chapter also elaborates on how the data were gridded incorporating the gridding procedures mentioned in Chapter 3. Chapter 5 shows how the data were modelled in 2D (magnetic, gravity and TDEM) and 3D (magnetic and gravity), and what results were produced as a result of having reduced, processed, gridded and lastly modelled the data. This is termed quantitative interpretation. Although qualitative interpretations usually guide quantitative interpretations, no qualitative interpretations on the data are made in Chapter 5, those are done in Chapter 6.

Some of the information produced in Chapter 5 may be once again mentioned in Chapter 6 for the purposes of qualitative interpretation on what the results produced in Chapter 5 mean. This chapter is very important because it integrates the datasets and infers a message that microgravity and TDEM methods strongly correlate. Chapter 7 reports that microgravity and TDEM methods have delineated the bords with confidence while the same cannot be said for magnetic method. The new mine owner who generously offered access to his property has no record of where previous mining occurred (through mine plans), and no geophysics was done on this mine in the past. Chapter 7 further recommends what measures could be followed to improve such studies in future or what could have been done to improve the study

# CHAPTER 2 - METHODS AND PROCEDURES

## 2.1 SURVEY DESIGN

### 2.1.1 Preamble

For this study, a reconnaissance survey line was undertaken using the 2-dimensional electrical resistivity method to better understand the lithological layering and the overburden thickness, and to estimate the depth of the tunnels below surface. Schlumberger array was used to acquire the resistivity data on a 300 m long line doing a single roll along. The electrode spacing was 1.5 m. The resistivity data were then used to guide the location of the microgravity, TDEM and magnetic grids.

It is important to understand at what depths the tunnels are expected to occur if a properly spaced grid is to be designed for microgravity method in particularly. The reason for this is that, in order to avoid aliasing, a good rule of thumb is to separate measurement stations by no more than half the expected target depth (LaFehr and Nabighian, 2012; Reid, 1980) for the microgravity survey in particular. Measurements made with a laser rule on site showed that the mine tunnels are ~5 m wide, buried about 4 – 5 m (information provided by the owner knowing that upper seam C was mined at that depth) with 5 - 6 m wide and 2 m high pillars.

### 2.1.2 Microgravity

#### 2.1.2.1 Theoretical background

Not much attention will be paid to describing the mathematical first principles of the gravity geophysical technique here as it is standard in any textbook on geophysical exploration (e.g. Dobrin, 1976; Dohr, 1975; Telford et al., 1978). This account rather presents a brief description of what gravity as a geophysical technique is, what microgravity represents and why it is important to address this aspect for this research. The gravity technique in essence uses a small mass at or above the surface of the Earth to determine the gravitational acceleration of the Earth

vertically at its surface to make inferences about the density distribution of geological units below the surface of the Earth.

The gravity technique as used in geophysical exploration and surveying is a passive method that makes use of the gravitational force (Hinze et al., 2013). This technique is influenced by the ruggedness of the terrain, the gravity meter drift itself and tidal variations in the gravity field. This is a disadvantage as one cannot obtain an immediate clear picture of subsurface conditions as with for instance the resistivity depth image (RDI) because the temporal and spatial changes in the gravity data first have to be corrected to obtain meaningful results. The easily calculated gravitational force, $\boldsymbol{F}$ in Newtons (**N**), is the acceleration of a mass (in kg) experienced over 1 m/sec$^2$, as a result of the attraction (denoted by a minus sign in the expression) of the mass in the presence of another body as expressed in equation 2.1

$$\boldsymbol{F} = -G\frac{m_1 m_2}{\boldsymbol{r}^2} \tag{2.1}$$

where:

- $m_1$ and $m_2$ are the masses of bodies 1 and 2 respectively in kilograms
- $\boldsymbol{r}$ is the separation distance between the two masses in metres
- $G$ is the universal gravitational constant.

In practice, this is the attraction of all mass towards the centre of the Earth since the Earth, due to its very large mass traps any smaller mass in its gravitational field (Hinze et al., 2013). It is important to note that the force of gravity between two objects on the Earth's surface is negligible because their mass, compared to that of the Earth, is extremely small. So, in geophysical surveying, the gravity force field depends only on the Earth's attraction on a small object (Hinze et al., 2013) and minute variations in the gravity force or attraction allow us to infer the density distribution of the subsurface of the Earth.

The gravitational attraction can be measured in an absolute way by historical pendulums and instrumentation that lets a standard mass fall freely in the Earth's gravitational field and

measuring its acceleration with lasers and accurate clocks. In fact, in 1993, absolute gravity measurements were made in the vicinity of Cape Town and Pretoria to provide a basis for the calibration of gravimeters belonging to the South African institutions involved (Kleywegt et al., 1996). These are called absolute instruments but are impractical outside a laboratory environment, except a few cases of some used in the field. In the field, in this study, a relative gravimeter is used that is quite delicate and measures only the difference in the vertical gravitational acceleration between a base station and the field station (Long and Kaufmann, 2013). One such instrument is the Scintrex CG-5 gravimeter that has resolution of 0.001 mgal (Scintrex Limited., 2017) and a standard deviation of < 0.005 mgal. (The gravitational acceleration of the Earth is approximately 9.78 m/s$^2$ which translates into 978 gal. Gravimeters measure in units of one thousandth of a gal or $10^{-5}$ m.s$^{-2}$ and the Scintrex CG-5 has a detection limit of almost one microgal).

Hinze et al. (2013) put into perspective what the relative gravimeters really do measure. They state that there is no other way to independently measure the gravitational force of the Earth without employing a mass, so, the acceleration, $\boldsymbol{g}$ of a mass of a free-falling body from Newton's second law of free fall is:

$$\boldsymbol{F} = m_1 \boldsymbol{g} \tag{2.2}$$

This gives the force acting on a mass $m_1$ due to the presence of another mass $m_2$. For the terrestrial situation, $m_2$ is the mass of the Earth and equation 2.1 can be modified using equation 2.2 in terms of $\boldsymbol{g}$ (measured in milligals) as:

$$\boldsymbol{g} = \frac{\boldsymbol{F}}{m_1} = G\frac{m_2}{\boldsymbol{r}^2}\,. \tag{2.3}$$

It is the change in gravitational acceleration $\Delta\boldsymbol{g}$ that is measured in geophysical surveying and density (mass per unit volume of a material) is the physical property that provides the contrast in $\boldsymbol{g}$. Equation 2.3 is given in a general form assuming a homogenous sphere, but it can be modified for different geometries.

The gravity method detects very small changes in gravitational acceleration caused by density variations in the Earth's crust (Van Schoor and Fourie, 2015). Microgravity is an extension of the gravity technique that uses a very close spaced measurement grid pattern to create a high resolution coverage to detect minute changes in the gravity field (Styles et al., 2005). This technique also needs careful field procedures to produce good quality data. These types of surveys are *inter alia* aimed at detecting subsurface cavities.

As much as this method has proven to give remarkable results in subsurface cavity and tunnel (buried up to about 12-15 m depth with diameters from as little as 2 m) detection (Van Schoor and Fourie, 2015; Orfanos and Apostolopoulos, 2012; Butler, 2008; Johnson and Snow, 2002), the method is slow, tedious and requires intensive data processing and highly accurate measurements of position and elevation differences (called levelling) as well as terrain corrections if useful results are to be obtained.

### 2.1.2.2 Gravity survey

For the study site, the adits whose portals were accessible, were air filled and had no water, but this does not necessarily mean that the tunnels that were inaccessible were dry. Air-filled tunnels offer the largest density contrast compared to water-filled tunnels due to the complete absence of material in the tunnel compared to water-filled tunnels that offer only a 60% anomaly amplitude of the same dry tunnel (Bishop et al., 1997). Man-made cavities especially tunnels may be disturbed by fracturing in the surrounding wall rock, lowering the density of the rock and this may help increase the perceived diameter of the tunnel (a phenomenon known as the halo effect) and hence its visible gravity effect (Daniels, 1988).

Using preliminary information mentioned at the start of this chapter to assist in avoiding aliasing and enable proper sampling, the measurement spacing between measurement points (commonly called the gravity stations) was calculated using forward modeling to be 2 m along line with a line separation of 3 m. The 3 m line separation was elected with the intention of obtaining a dense grid bearing in mind the time required to carry out the survey and to cover a wider area over say, 2 m line separation. The station grid would then consist of 6 lines, each

50 m long as is shown on Figure 2.1. The pattern was transferred onto Google Earth to show where the traverses would be made.




**Figure 2.1.** Google Earth image showing proposed location of the microgravity grid (in red) plotted on Google Earth (using Global Mapper13). On the right of the grid is the access to the tunnels and the insert image depicts an enlargement of the grid location.

Since a gravimeter experiences drift (instrumental and tidal) while doing a survey, one or more base stations must be chosen at which readings will be observed at the beginning and end of each loop of field station measurements to establish a drift correction. Returning to the base station on an hourly to 90-minute interval is good practice. It is important to note that the shorter the time taken between base readings, the greater the likelihood of accurately removing the drift (LaFehr and Nabighian, 2012). The elevation measurements were to be acquired coincidentally with the gravity stations using a real time kinematic mode (RTK), Trimble 4600 LS unit GPS.

### 2.1.3 Time Domain Electromagnetic Method

### 2.1.3.1 Theoretical background

TDEM/TEM (Time Domain Electromagnetic or Transient Electromagnetic Method) is a geophysical technique that excites the subsurface with a square wave driven, primary current flowing in the primary loop (Mc Neill, 1996). This action induces a current flow in the subsurface and the decay of the induced (or secondary) current is recorded. Electromagnetic field strengths are recorded with either the primary or receiver loops depending on the loop configuration. A current of known magnitude is induced in the ground via a transmitter loop on surface with a known square wave ac current and accompanying primary magnetic field (Mc Neill, 1996). When the current is abruptly switched off, the decaying primary magnetic field induces a current flow in the subsurface beneath the transmitter loop that is a mirror image of the primary current except with the current flowing in the opposite direction (Lenz's law). This current has a secondary magnetic field that changes direction ($\partial \vec{B}/\partial t$) and decays with time (Hallbauer and Nyabeze, 2013).

Maxwell's equations can be used to mathematically describe the propagation of electric and magnetic fields through a medium (Telford et al., 1990). Low frequency electromagnetic waves travel into the Earth by diffusion and are governed by Maxwell's equations below. One such equation, equation 2.4b is Faraday's law of electromagnetic induction whose differential form gives the expression for the primary electrical field of the current carrying loop (Telford et al., 1990). The equivalent of this electric field is the time varying magnetic field whose decay after the current is abruptly turned off gives information about the conductivity of the subsurface.

$$\nabla \times \vec{H} = \vec{J} + \frac{\partial \vec{D}}{\partial t} \quad \text{(Ampere's law)} \qquad (2.4a)$$

$$\nabla \times \vec{E} = -\frac{\partial \vec{B}}{\partial t} \quad \text{(Faraday's law)} \qquad (2.4b)$$

$$\nabla . \vec{B} = 0 \quad \text{(Gauss's law for magnetic field)} \qquad (2.4c)$$

$$\nabla . \vec{D} = \rho' \quad \text{(Gauss's law for electric field)} \qquad (2.4d)$$

where:

$\vec{\boldsymbol{J}}$ is current density (A/m$^2$).

$\rho'$ is charge density (Coulomb/m$^3$).

$\vec{\boldsymbol{E}}$ electric field intensity (V/m).

$\vec{\boldsymbol{B}}$ the magnetic induction or flux density (T).

$\vec{\boldsymbol{D}}$ is dielectric displacement in (C/m$^2$).

$\vec{\boldsymbol{H}}$ is the magnetic field intensity in Ampere-turn/m (A/m).

Also, depending on the medium under consideration (highly resistive targets in this study), additional equations are (Telford et al., 1990):

$\vec{\boldsymbol{J}} = \sigma\vec{\boldsymbol{E}}$, $\vec{\boldsymbol{D}} = \varepsilon\vec{\boldsymbol{E}}$ and $\vec{\boldsymbol{B}} = \mu\vec{\boldsymbol{H}}$ where $\sigma$ is conductivity (S/m), $\varepsilon$ is the dielectric constant (F/m) and $\mu$ is magnetic susceptibility (H/m).

From Maxwell's equations, the electric field $\vec{\boldsymbol{E}}$ related to the abrupt changes in the magnetic field will cause a current flow in the underlying conductive half space, $\boldsymbol{J} = \sigma\vec{\boldsymbol{E}}$. The resulting changes in the magnetic field induces secondary electric currents (eddy currents) in the Earth which act to oppose the decrease in the primary magnetic field. The receiver coil then records the voltage induced by the changes in the secondary magnetic field which will give information about the conductivity response of the subsurface (Mc Neill, 1996).

A receiver loop can be outside, inside or coincident with the transmitter loop depending on the coupling required (i.e. the orientation of the loops based on the target orientation and depth. A transmitter loop is a receiver loop in the case of this study). It is in this receiver loop where the voltage is recorded as a result of the change in current which induces the magnetic field that decays with time (Barrocu and Ranieri, 2000). This phenomenon is shown in Figure 2.2.

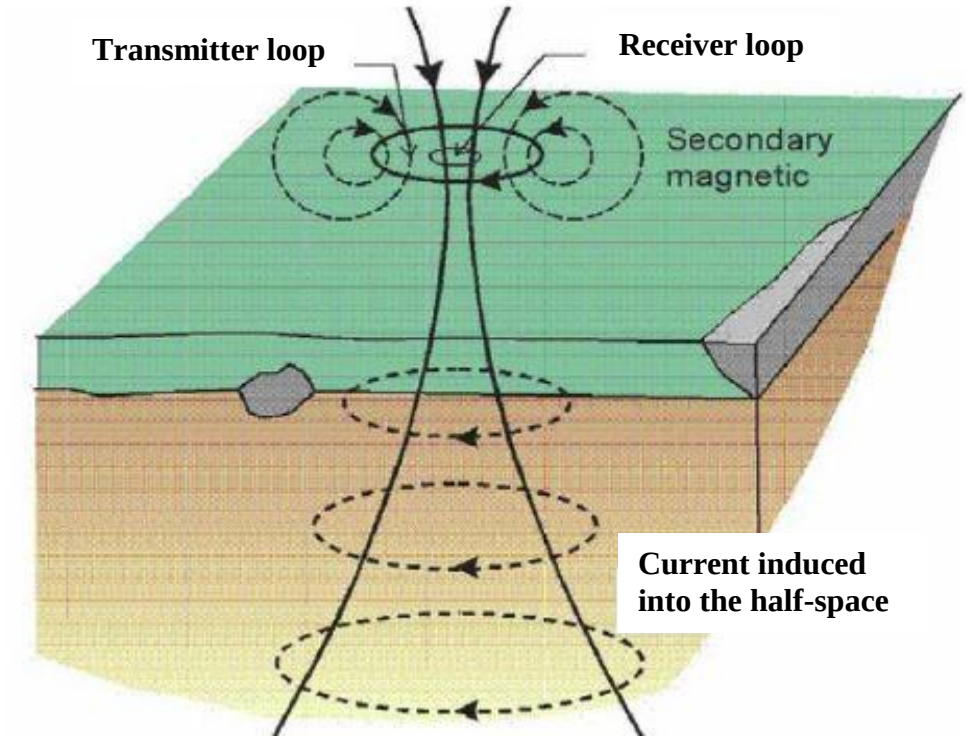



**Figure 2.2.** Current flow into the ground from a central loop transient EM system. This is an example of a receiver loop within a transmitter loop. Modified from Fantaye (2010).

The magnetic fields due to the induced secondary currents sample larger underground areas as they diffuse deeper also become weaker as they lose strength but still give information about deeper structures. However, TDEM being a bulk sampling technique of resistivity makes it less likely that a high resistivity small void adds enough resistivity to the bulk resistivity to make a meaningful difference as the secondary currents diffuse deeper and wider into the subsurface. According to Hai et al. (2015) the existence of abandoned mined-out areas affects the balance of stresses underground resulting in the collapse of the mined-out areas as the hanging wall of stopes/voids encounter more stress and therefore become less solid. This causes the stope/void to have a lower resistivity footprint than just due to the dimensions of the void alone and that is the effect that is more readily TEM detectable. TEM is therefore a good geophysical tool to detect mined-out areas and offers a solution to identifying collapsed phenomena using the resistivity contrast.

Some of the TEM method advantages/disadvantages are listed below:

- It has a higher vertical and lateral resolution compared to DC resistivity

- Since current flow is induced into the subsurface no electrodes have to be inserted into the subsurface.
- It is a non-intrusive method and can be readily employed in areas that are not easy to access.
- The ambient noise can be removed by stacking. However, no stacking was needed in this study.
- It has low sensitivity to geologic noise such as surface inhomogeneities and anisotropy (Kaufman, 2001). However, being insensitive to resistivity anisotropy is not an advantage here as voids/stopes etc. cause anisotropic effects that one would like to detect.

Apart from the advantages listed above, it must also be stated that electrical resistivity and electromagnetic geophysical methods are complimentary to each other. Resistivity is more sensitive in detecting a resistive body in a more or less resistive environment than electromagnetics. Electromagnetics is better at identifying a conductive body in a less or more conductive surrounding. Whereas resistivity could detect a 2000 Ωm body in a 1000 Ωm background, the electromagnetic technique would probably have difficulty in identifying the 2000 Ωm body from the background (McNeill, 1996).

### 2.1.3.2 Design layout

The original planned survey grid pattern for the gravity data acquisition consisted of 6 lines each 50 m long, 2 m station spacing along lines and a 3 m line separation. For TDEM however, the electromagnetic waves sample the subsurface in the vicinity below the transmitter loop and produce an average or bulk resistivity. With time the waves migrate downwards and outwards, losing energy and thus resolution capability by producing an average resistivity over a larger volume of Earth such that small voids and tunnels would be unlikely to contribute significantly to the transient sounding decay beyond a certain depth or lateral distance. It is important to analyze the individual soundings to observe the early time transients, which for a layered earth scenario will give information on the transition from one lithological medium to another (AEMR, 2002). So, if these recordings of transient decay are overlain on the microgravity data,

then a correlation between a steeper decay in the TDEM transient curve due to higher resistivity (air) and a low gravity value may indicate the presence of a tunnel/void. As the smallest loop size that could be used without being influenced by superparamagnetic effects (determined from a few test soundings on site) was 25 m x 25 m (see below), the very small station spacing chosen for the microgravity and magnetic measurements is not as applicable. This is because the current flow will bulk sample the resistivity over initially at least 625 $m^2$ and then expand in time and depth.

A few soundings made on site with a TEM-FAST 48 system also helped to test which loop size gives a good response. The information that the tests were expected to reveal included the preferred loop size, the recording time and the magnitude of the transmitted current. As much as it is important to use the optimum transmitter current depending on whether the targets are deep or shallow, it is also wise to use the maximum current at the same station having two measurements taken at each station (Corriols et al., 2009). The reason behind this is that a smaller current will give information about the shallow layers and the maximum current with more recording time will give information about deeper structures. Data is recorded as long as the secondary magnetic fields are not swamped by ambient noise which is easily recognized from the decay curve where it starts recording erratic behavior. At areas with lower noise, longer recording times can be applied (Corriols et al., 2009). However, there can also be cases where the conductivity of the shallow layers is high, and it takes longer for the secondary field to dissipate completely. So, the choice of the transmitter frequency should be made carefully so as to preserve information in the late times.

Contrary to other TEM systems, the TEM-FAST 48 is lightweight, compact and allows very small loop sizes. However, in South Africa a loop size of smaller than 25 m x 25 m causes the recording of superparamagnetic effects that cause distortion of the transient decay in the late time (Buselli, 1981). But besides this drawback, it is an ideal system to use in areas which are not easily accessible. The transmitter, receiver and battery are in a single case weighing about 5 kg. The system has a 12 V battery which can power up to 50 soundings, with approximately 12 soundings acquired in an hour (AEMR, 2002). So, the TDEM survey was to be a grid coincident with the microgravity grid with 6 lines, 50 m long, 3 m apart and the station spacing of 5 m over 2 m of microgravity. A 25 m x 25 m loop size would be tested on site before being used.

## 2.1.4 Magnetic Method

### 2.1.4.1 Theoretical Background

The Earth's magnetic field is caused by currents flowing between the solid inner and molten outer Fe, Ni-rich core of the Earth (Jacobs, 1967) and resembles the field of a large bar magnet positioned inside the Earth between the North and South Pole (Van Schoor and Fourie, 2015) (Figure 2.3). According to Telford et al. (1990), this geomagnetic field is composed of three parts as far as exploration geophysics is concerned and for prospecting purposes, the unit of measure used is the nanotesla (nT):

1. The internal field originating from the core known as the main field that varies at the surface of the Earth with the intensity of about 20000 nT to 70000 nT. This is responsible for the induced and remanent magnetism of rocks.

2. Small field perturbations that originate outside the Earth and vary rapidly. These are associated with electric currents in the ionized layers of the upper atmosphere and are caused mainly by the solar wind interacting with the Earth's magnetic field. These field variations include; solar diurnal variations with a 24-hour period and an amplitude range of 30 nT depending on the latitude, lunar variations with a 25-hour period and an amplitude of 2 nT and magnetic storms (Figure 2.4) which have amplitudes of up to 1000 nT. Magnetic storms which do occur occasionally are the only major concern for prospecting geophysics, while diurnal field disturbances have a less significant effect and can be corrected for by use of a magnetometer as a base station.

3. Spatial variations of the main field and are normally smaller than the main field and constant in time and place. They are caused by local magnetic anomalies in the near-surface crust of the Earth, largely due to variations in crustal (mostly) magnetite content and are the target of magnetic surveys. Reference will be made to these spatial variations in this text. This is the lithospheric field and has induced and remanent components.

The geomagnetic field which varies according to hemispheres is a vector and at a point is defined by its intensity (F) and its direction defined by its dip or inclination (Inc) and declination (Dec). The declination describes the field's direction on a horizontal plane and is defined as the difference between the true north and the magnetic north going around clockwise. (Figure 2.3) (Dentith and Mudge, 2014).

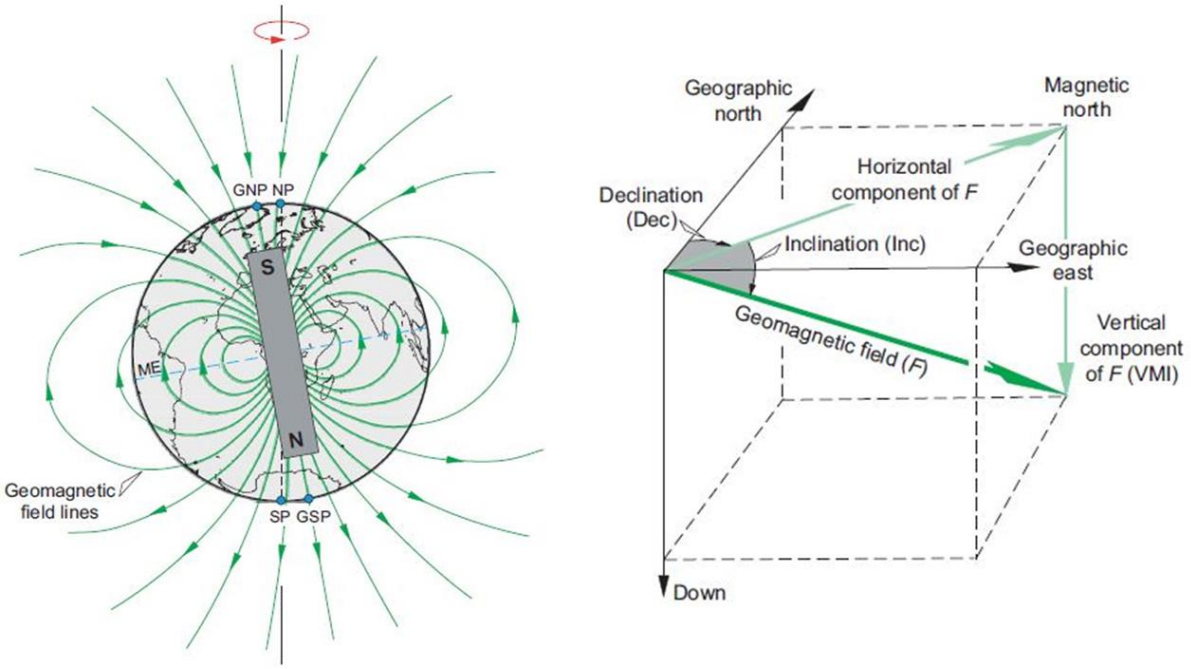



**Figure 2.3.** Representation of the earth's geomagnetic field as a giant bar magnet (left). GNP is geomagnetic north pole, GSP is geomagnetic south pole, NP is geographic north pole, SP is geographic south pole, ME is magnetic equator. On the right, components of the geomagnetic field (F) showing the declination (Dec) and inclination (Inc). The vertical component of the geomagnetic field is denoted as VMI (Vertical magnetic Intensity). Adapted from Dentith and Mudge, (2014).

The International Geomagnetic Reference Field (IGRF) is a worldwide background field valid for 5-year periods and gives the direction and strength of the field at any location and attempts to predict temporal changes of the field at that location into the future. The IGRF is vital in magnetic surveying because it provides the ability to enhance and interpret the data. It is mainly used for large scale combining of data sets from different ages. The IGRF should not be confused with the local regional field to be removed before modelling commences and which depends on the target(s) to be isolated.

The instrument used to measure the magnetic field is called a magnetometer and it measures absolute total magnetic field intensity values although only relative differences are required (Dentith and Mudge, 2014). The proton precession magnetometer makes measurements of total magnetic field strength over time and can make total magnetic intensity (TMI) measurements with a resolution to at least 0.1 nT (Dentith and Mudge, 2014). Proton magnetometers have been largely replaced in field measurements by optically pumped Cs, Rb or K-vapour total field magnetometers. A caesium vapour magnetometer, G859 used in this study, has a high sensitivity of 0.08 nT. For all magnetometers, the instrument should be kept away from any man-made magnetic objects for accurate measurements. These include electrical wires, metal fences and metal objects on the torso of the operator (watches, rings, cell phones, etc.) and boots with lots of metal.

**Magnetic Anomalies and Prospecting**

Local changes in the main field result from variations in the magnetic mineral content of near-surface rocks (Telford et al., 1990). Geological formations emulate buried magnets or assemblies of magnets because of their magnetic properties (Van Schoor and Fourie, 2015) which are superimposed on the Earth's magnetic field. If the measurements of the magnetic field are taken over such structures, the result will be variations (or anomalies) from the undisturbed magnetic field of the Earth (Van Schoor and Fourie, 2015). The size and shape of these anomalies is influenced by the degree of magnetization, direction of magnetization, and depth and geometry of these geological structures. The rocks on the Earth's crust are essentially either or both induced (always) and remanent magnetized and the distinction can be made on the basis of the present day geomagnetic field (Reeves, 2005). Sometimes these rocks can be used to tell how the field was in the past. Magnetic surveys aim at deriving the subsurface parameters from the observed magnetic anomalies (Van Schoor and Fourie, 2015).

Magnetic anomalies measured in the Earth's field are a result of two types of magnetization, namely induced and remanent (or permanent) magnetization. Remanent magnetization may be in any direction but is only really noticed if it is in roughly the opposite direction of the Earth's field. Induced magnetism is always in the same direction as the Earth's field. If the Earth's field were to be switched off, the induced field would disappear but the remanent magnetization

would remain (Van Schoor and Fourie, 2015). The magnitude of induced magnetization (**M**) is proportional to the Earth's field (**F**) and the proportionality constant is referred to as the magnetic susceptibility (**k**), which is a measure of the extent to which a material may be magnetized when subjected to an external magnetic field:

$$\boldsymbol{M = kF} \tag{2.5}$$

It is the spatial distribution of this susceptibility within the geological formations that magnetic surveys intend to infer as a function of position and depth (i.e. in 3D), as it is linearly related to the magnetic field strength. Measurements of susceptibility on their own must also be done on outcrops and in the laboratory and averaged to provide an estimate of the bulk susceptibility of the formations. These measurements are used in the modelling of magnetic data to obtain realistic geological answers and susceptibility images of the subsurface. Susceptibility is a dimensionless quantity (but differs by 4 pi depending on the system it is measured in (cgs or SI)), but the unit of measure of the magnetic field strength is the Tesla (T) and nanotesla (nT) for measurements used in exploration.

**Diurnal variations**

Short, rapid and external variations of the Earth's magnetic field arising from the electric currents flowing in the ionized layer of the upper atmosphere and the ionosphere emanate from the Sun's radiation (Dentith and Mudge, 2015). These variations produce magnetic fields which cause interference within the Earth's magnetic field. This causes the Earth's field to vary over minutes and hours especially during the day and is considerably quieter at night when the hemisphere is shielded from the Sun's radiation (Dentith and Mudge, 2015). These daily variations (or diurnal variations) have a range of about 30 nT (Figure 2.4).

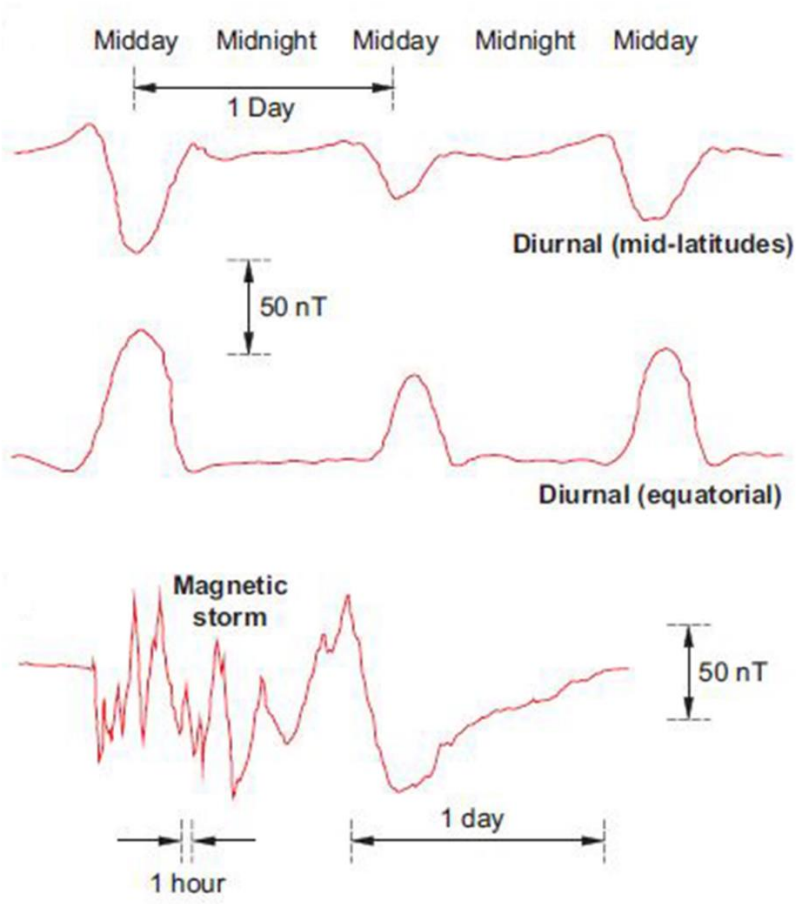



**Figure 2.4.** Time variations of the external geomagnetic field. The top two diagrams are the diurnal plots and the bottom plot shows the largely erratic plot of the field disturbed by a magnetic storm with an amplitude of about 50 nT. Modified from Dentith and Mudge, (2014).

### 2.1.4.2 Design Outline

The purpose of using the magnetic method was inspired by the first visit that was made to the site to do physical observations and to aid with proper field planning (see also Chapter 1). It was observed that there were what was thought to be pyrite or traces of sulphur on the in-situ coal seam at the mined-out region (Figure 2.5).

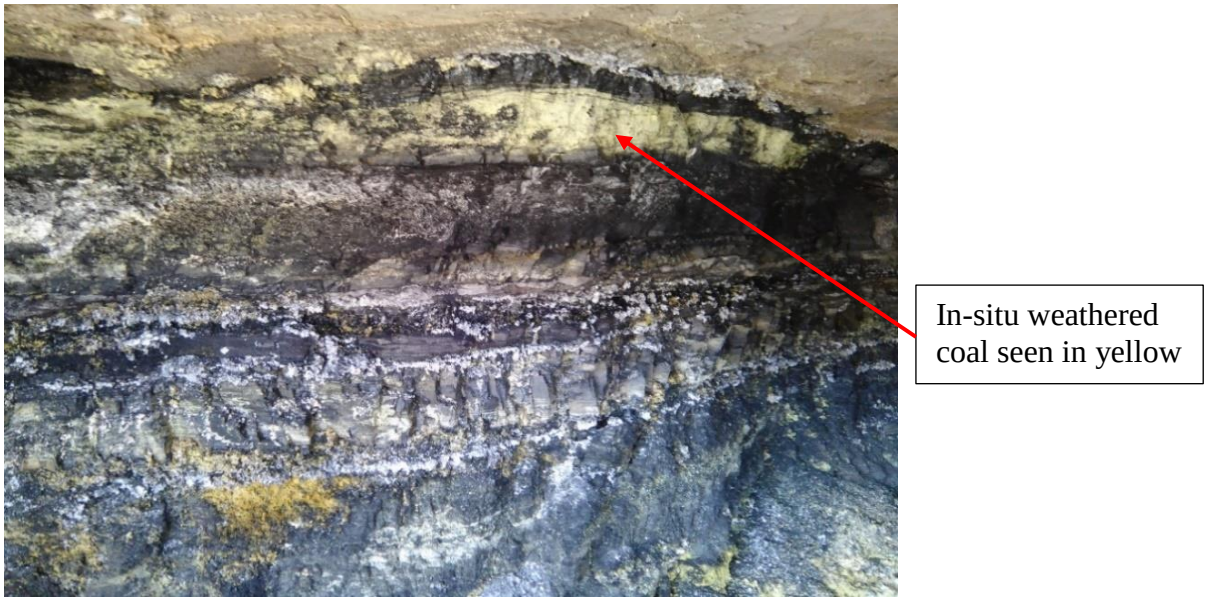



**Figure 2.5.** Underground tunnel opening showing a weathered coal seam and traces of pyrite and precipitated sulphur.

The reason for employing the magnetics method was to use it to constrain both the microgravity and the time-domain electromagnetic results. This is because pyrite and its decomposed minerals would give rise to a slight susceptibility increase (Bell et al., 2001; Mohalik, 2016; Yohe, 1958) which would give a contrast between the tunnels and the pillars. A decrease in coal grade results in a rise of seam moisture since oxidation is influenced by moisture content in coal (Yohe, 1958), oxygen content and other factors like a rise in susceptibility (Bell et al., 2001).

The magnetic data collection grid pattern was designed to overlap and extend the gravity grid pattern. using a total of 20 lines with a station spacing of 2 m and line separation of 3 m (Figure 2.6). Navigation for collecting the magnetic data was provided by uploading the grid to a Garmin Etrex handheld GPS which was used by an assistant walking at least 10 m in front of the magnetometer to avoid electronic interference from the handheld GPS with the magnetometer. A proton precession magnetometer (Geometrics 856) was used as a base station to record the diurnal variations of the Earth's magnetic field in the area, recording at 2 Hz and a Cesium vapour (Geometrics Cs vapor) used as a roving magnetometer.

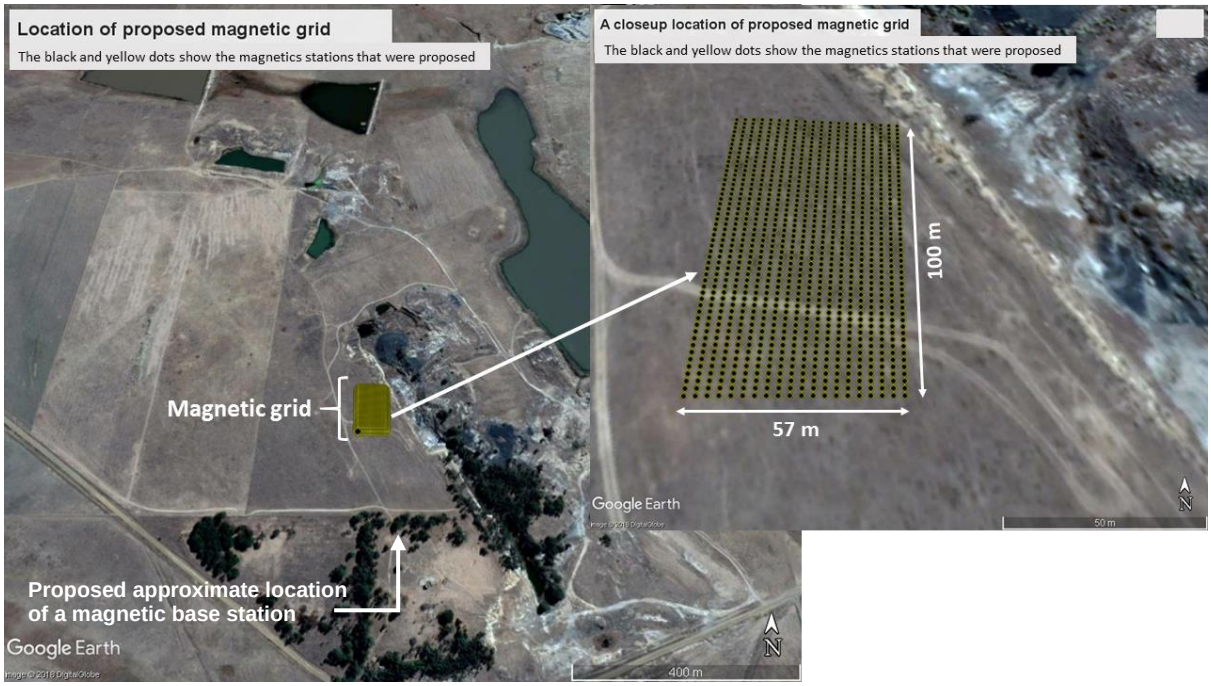



**Figure 2.6.** A picture showing the proposed location of magnetic grid (in yellow) plotted on Google Earth (using Global Mapper13). On the right-hand side of the grid is the cliff and access to the tunnels and the insert image represents a zoomed-in version of the survey grid pattern.

The locality and orientation of both the microgravity and magnetic grids were guided by the resistivity survey. These grids overlay the resistivity line (blue) as shown in Figure 2.7. The reason behind this was that the results of the resistivity line could be used to guide the forward modelling of the two methods especially how to properly incorporate the overburden thickness from the microgravity. This is because the overburden thickness if varied does offer gravitational acceleration change as will be seen in Figure 2.11.




**Figure 2.7.** A picture showing a planned microgravity (red) and magnetic (yellow) grid patterns (using Global Mapper13) based on the position of the resistivity line (blue).

## 2.2 FORWARD MODELLING

### 2.2.1 Preamble

There are two kinds of forward modelling; the first makes use of geological and geophysical information to determine if the method at hand will be feasible for such a survey, while the second one makes use of the geology and geophysical data measured in the field to match the measured anomaly response with a postulated geological model of the subsurface. Prior to the acquisition of both gravity and magnetic datasets, forward models of both methods were performed for planning, and this is an important planning phase of a geophysical survey that will aid in the success or failure of the study.

Before forward modelling, it helps to have a picture of the geological model that the forward model is meant to resemble. This was relatively easy as the geology of the area is indicated on the mining permit (Figure 2.8) and visiting the site allowed for physical observations and collection of samples on which physical property measurements were made. The map alone, does not suffice to produce a subsurface model and a geological cross section of the strata is necessary. If no cross section is available, a reconnaissance geophysical survey is necessary from which a tentative cross section can be produced to constrain the modelling of the data, hence the use of the reconnaissance resistivity survey.

Forward modelling was done with the approximated physical property values and dimensions of the target (depth extent, width, height) bearing in mind the sensitivities of the instruments being used (about +/- 0.04 mgal for the gravimeter and 0.08 nT for the magnetometer). According to Hinze et al. (2013), geophysical property information is needed from the rocks sampled to assist in modelling the subsurface volume of the earth being investigated. These rock properties are summarized in Chapter 5.

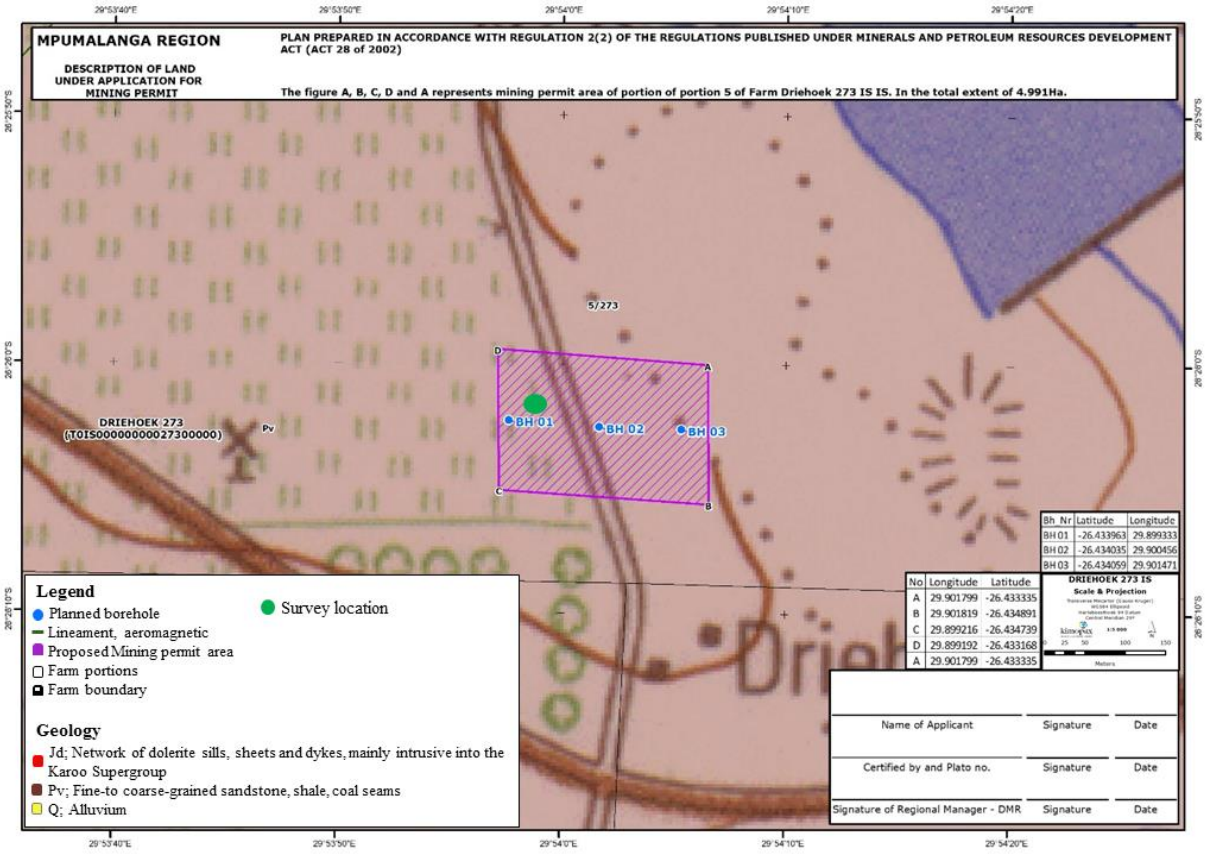



**Figure 2.8.** The mining permit area showing the underlying geology. This low-resolution map is used with permission from Kimopax Ltd and is not edited in any way. The geology key is in the bottom left corner.

As mentioned earlier, a 2-dimensional electrical resistivity survey was done to characterize the overburden thickness and the possible variations of the layering in the half space. The Wenner-Schlumberger array combination was chosen for this purpose as this array is a good compromise in determining both vertical and horizontal geological features (Loke, 1999).

The resistivity survey was also helpful in identifying the location in the permit area to do the magnetic, microgravity and TDEM surveys, because this method has been proven successful in delineating openings within coal seams (Johnson et al., 2002; McCann et al., 1987; Van Schoor, 2002). Such openings are characterized by a relatively high resistivity compared with the surrounding rock provided they are dry. However, regions with resistivities varying by orders of magnitude within coal seams are known such as encountered by Johnson et al. (2002) and caused by factors such as temperature, porosity and moisture content of the rocks. Thus, the resistivity values alone from the cross section (Figure 2.9) cannot be confidently used for

the identification of voids/stopes as being the localities with high resistivity within the coal seam. It is more effective to track the coal layer (usually with a resistivity of $10^2$ Ωm) and then infer the presence of mined-out regions from lateral resistivity anomalies within the layer.

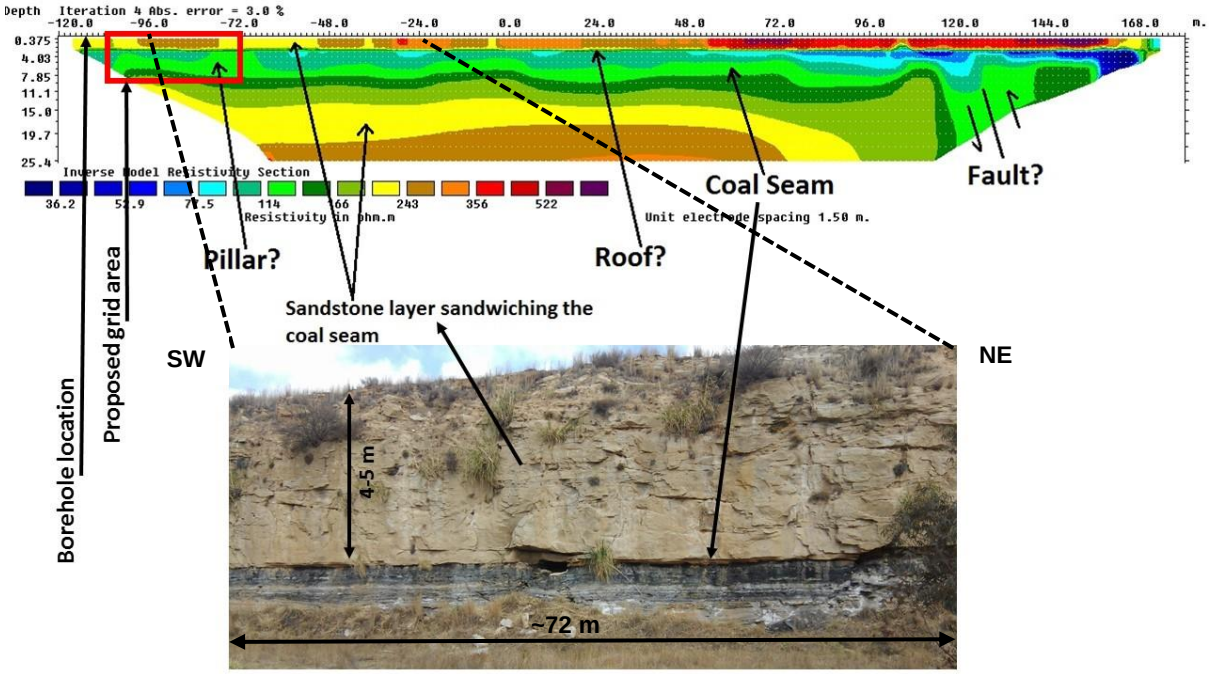



**Figure 2.9.** 2D Wenner-Schlumberger electrical resistivity vertical section for the reconnaissance section to guide the choice of the location for the survey. The vertical section is situated on the flat area above and parallel to the cliff including the coal seam in which the tunnels striking SE to NW occur and aligned to veer away from the cliff. That is, access to the underground was made through the coal seam as shown where adits occur. The photo was taken looking to the west and the resistivity section is adjacent to the cliff area but further west and about 60 m away from the edge at its nearest point. The photo of the vertical section shown below the resistivity section does not cover the complete extent of the resistivity section, but only about 72 m (shown by black dotted lines) of a 300 m long line.

As the visible stopes only gave a limited access, (they were bricked up going further west into the cliff for obvious reasons) the resistivity survey was used to determine if variations in the depth, width and the extent of the pillars possibly occurs from what was observed in the cliff. For microgravity and TEM, it is helpful to know the variation in overburden thickness as it is of consideration in the regional field determination (Figure 2.10). A geological model (Figure 2.10) developed from the interpretation of the DC resistivity survey was used to provide forward modeling parameters for gravity and magnetic forward modeling. The model in Figure 2.10 has density values but it must be noted that it is not only intended for gravity modelling

but is also a conceptual basis for magnetic models with suitable susceptibilities instead of density values. The unrealistically uniform overburden in Figure 2.10 has a density of 1.92 g/cm$^3$ (Telford et. al., 1990), sandstone bedrock density is 2.57 g/cm$^3$ and the density of air is 0 g/cm$^3$.

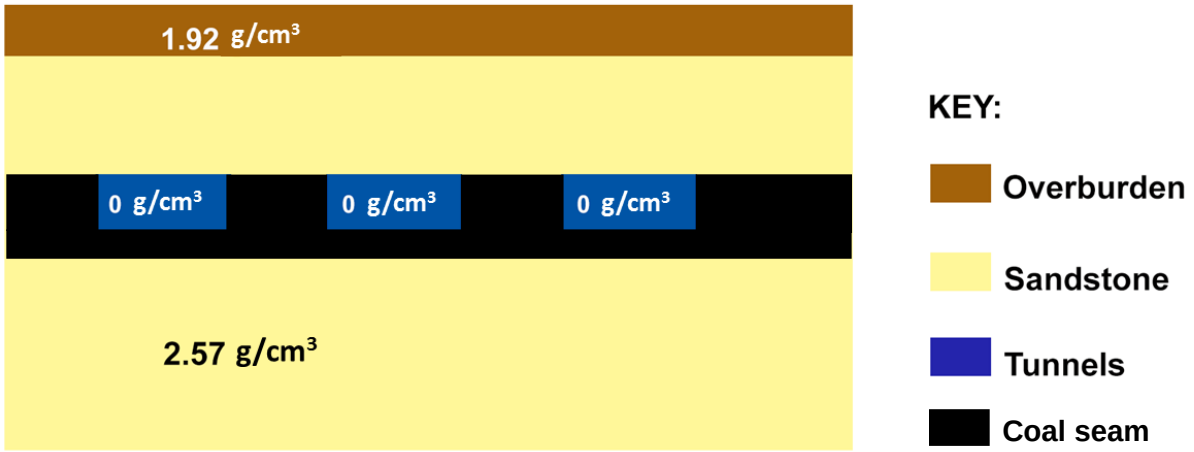



**Figure 2.10.** A postulated vertical geological section based on observations used to guide 2D forward modelling of microgravity and magnetic methods. The model shows a postulated unrealistic horizontal overburden that was eventually superfluous in the final microgravity models as with gravity, horizontally layered strata only contribute to the background or regional gravity field and bodies must be at least slightly dipping or change in the vertical dimension to produce an anomalous effect, for instance uneven weathering. The tunnels in the model are designated by the blue squares with a strike length of 50 m in both directions and with a density of 0.0 g/cm$^3$ which was taken as the practical density of air. The host rock is the sandstone. The black coal seam is included in the section to show the position of the seam along the tunnels. It must be noted that this is an ideal case, but the pillars are not entirely coal.

The physical properties and ranges for forward modeling of both gravity and magnetic methods are summarized in Table 2.1. The coal is a horizontal layer and so it would not have any effect on the modeling results of gravity and magnetic methods. It is however included in the geological cross section.

**Table 2.1**. Summary of the physical property values used in the forward model of the gravity and magnetic methods. The overburden susceptibility is not included in the models because it will not have any effect on the magnetic models.

| | Density (g/cm$^3$) | Susceptibility (SI) | Strike of a body (m) |
|---|---|---|---|
| Sandstone | 2.57 | 0.227x10$^{-3}$ | > 1000 |
| Tunnels | 0 | 0 | 50 |
| Overburden | 1.92 | None | > 1000 |

## 2.2.2 Microgravity

The application of the microgravity technique like any other geophysical technique demands a familiarization with the geology of the area of interest and a quantitative knowledge of the physical properties of the rocks, in this case the density. The density of the in-situ rock may vary from the density of the rock sample measured in the laboratory due to pressure changes (LaFehr and Nabighian, 2012). This is because pressure affects porosity which determines the bulk density. This should hardly be the case since this is a shallow investigation.

The bulk density of a rock $\rho_b$ is a function of the matrix density$\rho_m$, porosity ϕ and the density of the fluid $\rho_f$ occupying the rock's cavities (LaFehr and Nabighian, 2012):

$$\rho_b = \rho_m(1-\phi) + \rho_f\phi$$

The bulk density of any rock is equal to the sum of its constituent mineral densities, each multiplied by the percent volume, $\emptyset_n$ of the rock it occupies (LaFehr and Nabighian, 2012):

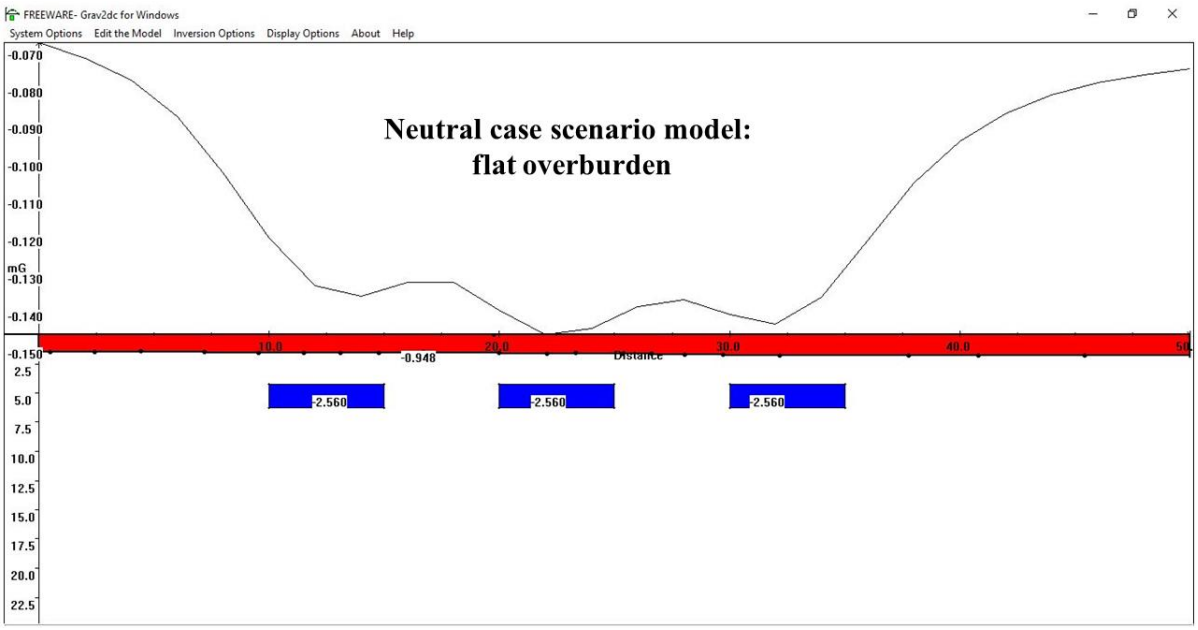
$$\rho_b = \rho_1\emptyset_1 + \rho_2\emptyset_2 + \rho_3\emptyset_3 + \cdots$$

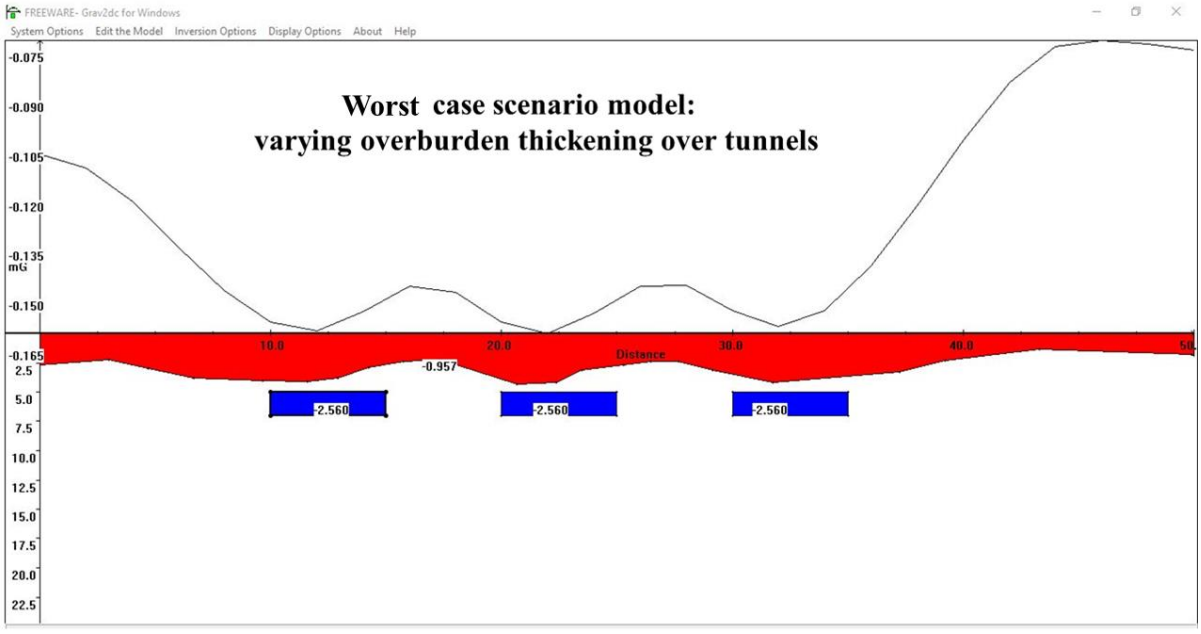
This knowledge will help in the interpretation of the microgravity data. From the microgravity data, the density contrast between the rocks of interest and those surrounding them shall be inferred. The resulting gravity measurement will be either a negative or positive anomaly on the background gravity response depending on the contrast and on the regional field being removed. On a data map, regions of either high or low gravity will be seen.

Grav2dc, a 2.75-dimensional modelling program written by Prof. Gordon Cooper of University of the Witwatersrand (Cooper, 1993) was used to calculate the microgravity forward model. With the calculation, it was considered that the standard sensitivity of the CG-5 gravimeter is about 0.005 mgal according to the manufacturer, Scintrex Ltd (2017), but usually found to be ~0.04 mgal under normal field conditions (Heath et al., 2017). In the forward model in Figure 2.11, an overburden of varying thickness was added on purpose to test its effect on the anomaly and this causes gravity variations which have longer wavelengths than those due to the tunnels. The infinitely long (strike) overburden thickness of about 2 m incorporated into the forward models was taken from the geoelectrical section in Figure 2.9. Density of the overburden used in the three models in Figure 2.11 is taken from a publication by Telford et al. (1990) as 1920 $kg/m^3$.

Figure 2.11 shows three different cases of gravity forward models where each model incorporates three tunnels (blue) within the sandstone background (white) and the overburden (red) of varying thickness. These models are similar and the only difference among them is the variation in overburden thickness. They all have tunnels that are 5 m wide, 2 m stope width and a strike of 50 m. The top figure is a model of an unrealistically flat overburden (a neutral case), while the second figure provides the worst case scenario (a thickening of the overburden may mistakenly be taken to be a tunnel and so this is taken to be a worst case scenario. This may be due to post mining subsidence infill) of the overburden's signal varying coherently with that of the tunnels. The third figure has the overburden added such that it opposes the effect of the tunnels and provides a best-case scenario. From the forward models in Figure 2.11, it is clear that the effect of both the overburden and the voids of 0 $kg/m^3$ contribute towards the gravity variations but the voids have a substantially larger contribution because of the much larger density contrast of -2560 $kg/m^3$ between tunnel and host rock that resulted in an amplitude of approximately -0.143 mgal, -0.141 mgal and -0.158 mgal for the neutral case, best case and worst case scenarios respectively. This implies that the tunnels could be fairly

resolved taking into consideration other geological noise such as that caused by terrain or variation in host rock density other than that associated with voids. The density contrast between the overburden and the sandstone as seen in the models is -948 kg/m$^3$ for the first and third models and -957 kg/m$^3$ for the second model.



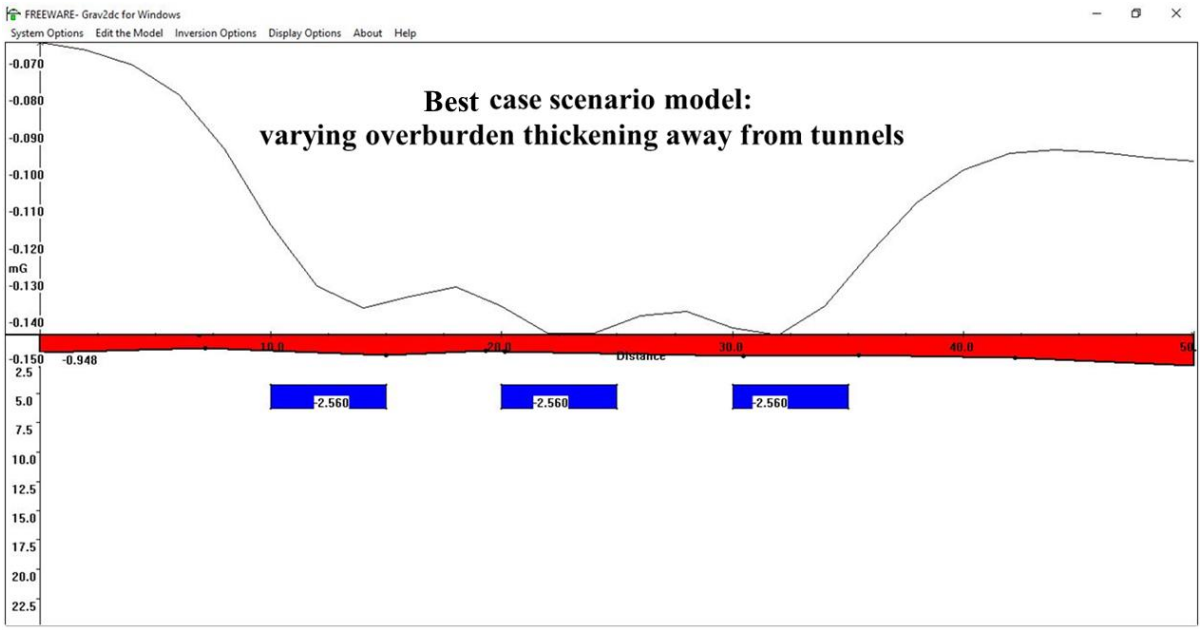



**Figure 2.11.** A grav2dc microgravity model showing three tunnels (in blue), the bedrock (white background) and the overburden (in red). The model shows 3 scenarios, a neutral, a worst case and best-case scenario. Microgravity can delineate the tunnels even in the presence of a varying overburden because the overburden produces a longer wavelength variation and in spite of that the amplitude of the anomaly is about -0.158 mgal, which is much larger than the sensitivity of the gravimeter of about +/- 0.04 mgal and above the expected geological noise level. However, the accuracy of the gravity measurements and the terrain must be very high.

## 2.2.3 Magnetic Method

The forward modelling was guided by the geological model in Figure 2.10. The susceptibility values were taken from the Council for Geosciences (CGS) database (Maré et al., 1997) and measurements on the sandstone samples collected from the study area. Their average susceptibility is $0.227 \times 10^{-3}$ SI. The susceptibility of the tunnels is that of air which is approximately zero and it was taken as such.

The magnetic model produced from Mag2dc (Cooper, 2013), 2.75D modelling software written by Prof. Gordon Cooper of the University of the Witwatersrand in Figure 2.12 shows three tunnels (in blue) that are 5 m wide with a stope height of 2 m and 5 m apart.

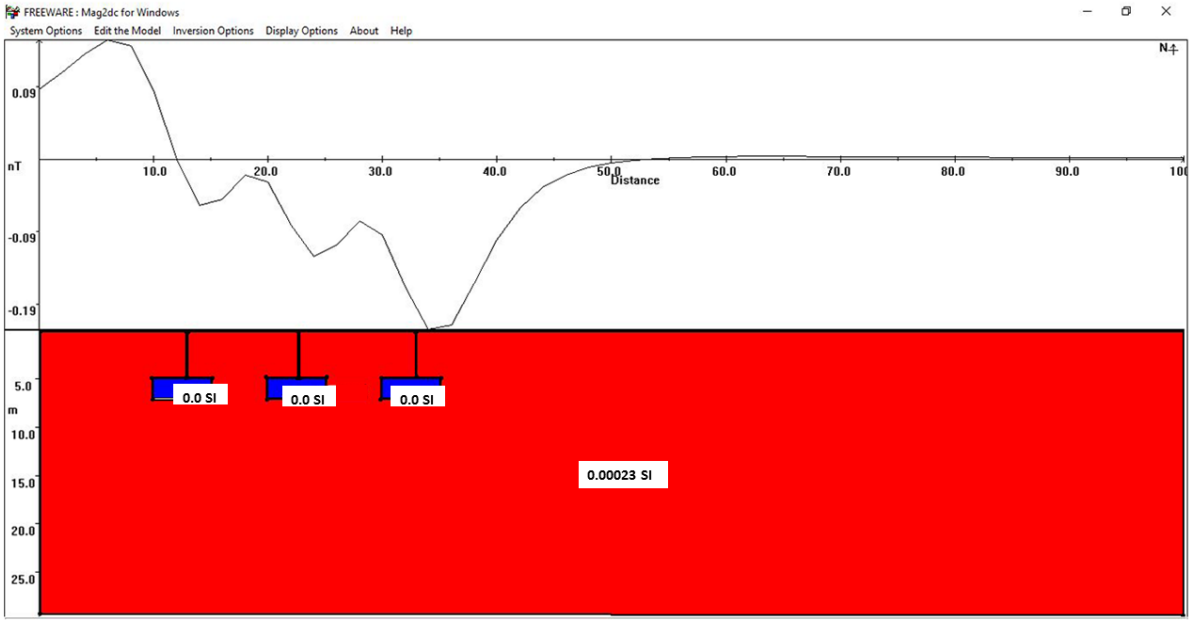



**Figure 2.12.** Magnetic model produced from Mag2dc, 2.75D modelling software. The background rock is the sandstone with an average susceptibility of 0.00023 SI. The blue rectangles are the tunnels with an assumed susceptibility of 0 SI. The magnetic intensity of the anomaly with the smallest amplitude is about -0.07 nT which is quite small. The tunnels are 5 m wide, 2 m high and are 5 m apart.

## 2.3 DATA COLLECTION

### 2.3.1 Microgravity

The microgravity survey was carried out using a Scintrex CG-5 gravimeter and a real time kinematic mode (RTK), Trimble 4600 LS unit differential GPS. Elevation measurements were taken with an accuracy of ±1 cm (determined from the average of the repeat measurement differences) and horizontal position data with a precision of at least 5 cm. Each gravity station was recorded with a delay time of 60 seconds using a remote to avoid tilting the gravimeter although the instrument does tilt correction. The measurement at a station was repeated if the following occurred: the GPS signal of the non-differential antenna equipped with the instrument used to calculate the earth tide, was noisy (spikey and not clear) and the standard deviation of the CG-5 measurement was above 0.05 mgals.

The gravity measurement grid pattern (Figure 2.13) was covered using a line separation of 3 m and 2 m station spacing with a total of 4 lines. The 2m station spacing is excessive given the time limitation to complete the survey but was done to have some redundancy in the data hence the technique microgravity (dense sampling and quality of gravity data), as there was no chance of repeating measurements once the premises had been vacated. Each line was 50 m long thus constituting a total of 104 station measurements plus 14 repeat measurements (Figure 2.14). All data were acquired in two days. Therefore ~13.5% of the total measurements were repeat measurements for the purpose of good quality control on the data. Good field practice dictates at least 10% repeat measurements in each loop (Murray and Tracey, 2001).

A hand-held GPS was used for direction in the layout of the measurement grid pattern. The lines were laid out with a tape measure and the stations marked with small tags on the grassy ground attached with duct tape (Figure 2.13). In order to provide a stable area where the tripod was laid, the grass was cleared. A lot of rain fell on the first day of a two-day window before the area was to be cleared for blasting and mining to commence but no measurements were made in the rain due to the delicacy of the gravimeter. These conditions forced the survey to be 4 lines and not the initially planned 6 lines, however the design parameters were still maintained at 2 m station spacing, 3 m line separation and 50 m long each line as mentioned earlier and the measurements are summarized in Table 2.2.

**Table 2.2.** A summary of the acquired loops and repeat measurements.

| Loops | Lines | Internal repeats | External repeats |
|---|---|---|---|
| Loop 1 | Line 1 | 1 | 2 |
| Loop 2 | Line 2 and Line 3 | 4 | 4 |
| Loop 3 | Line 4 | 2 | 1 |

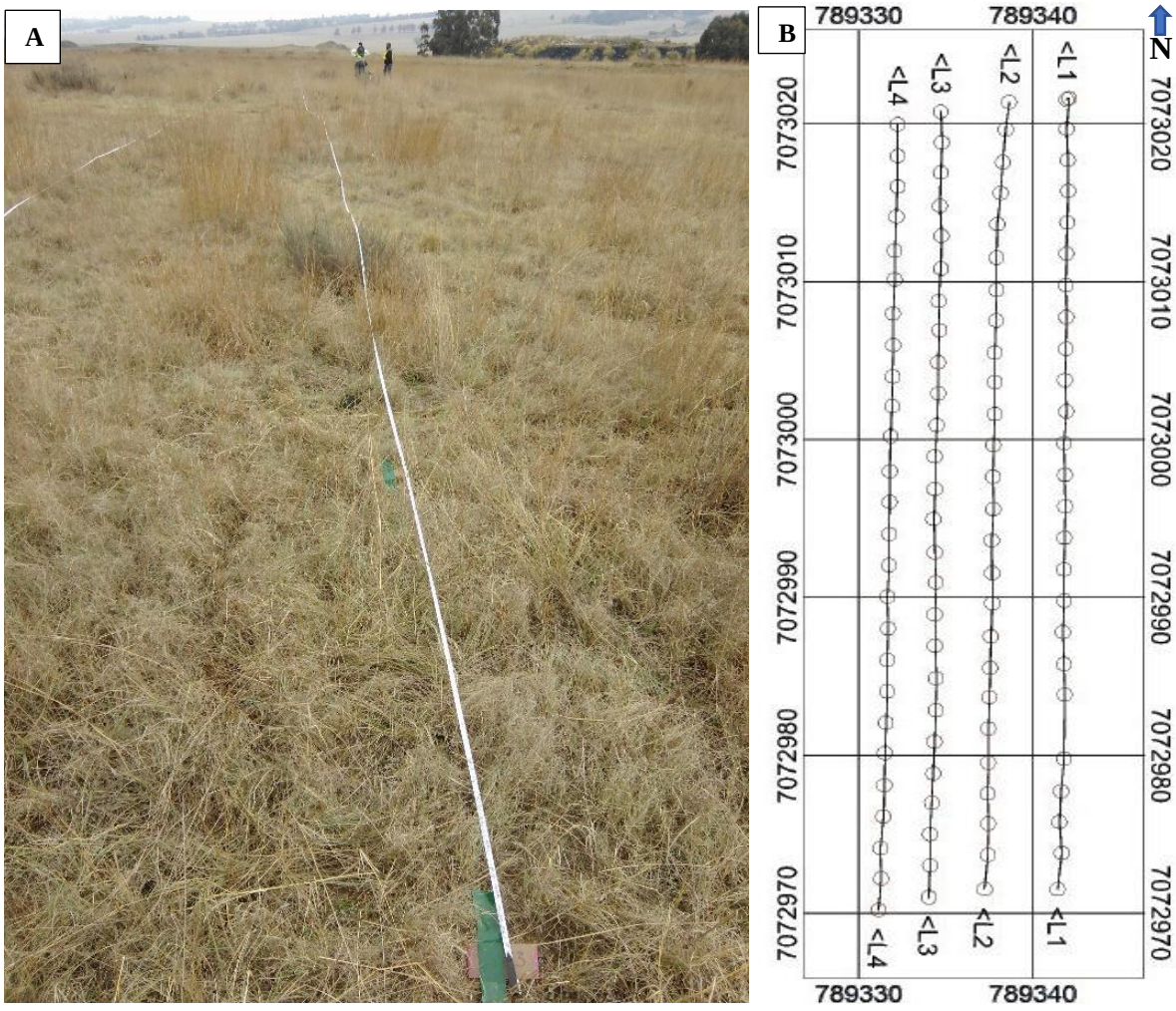



**Figure 2.13.** (A) Field photo and (B) location diagram of the grid pattern layout of the microgravity data collection plotted in Geosoft Oasis Montaj (Educational kit 2018). L1 is the first traverse away from the cliff edge (as seen in Figure 2.9) accessing entrance to the tunnels up to the fourth line (L4) and the circles show measurement points spaced at 2 m apart. The picture on the left shows how the tape was laid out on the ground and where the stations were separated with brown tags adhered to the ground by green duct tape. This picture also shows that the terrain was relatively level and not rugged (see Appendix B for a topographic sheet of the study area).

Figure 2.14 shows a pattern that was followed to acquire the microgravity data including the 14 repeat measurements. Four lines were collected in total as shown in Figure 2.14. The red dots represent the internal repeat measurements, while the yellow dots represent the external repeat measurements. The total repeat measurements collected are shown in Table 2.2

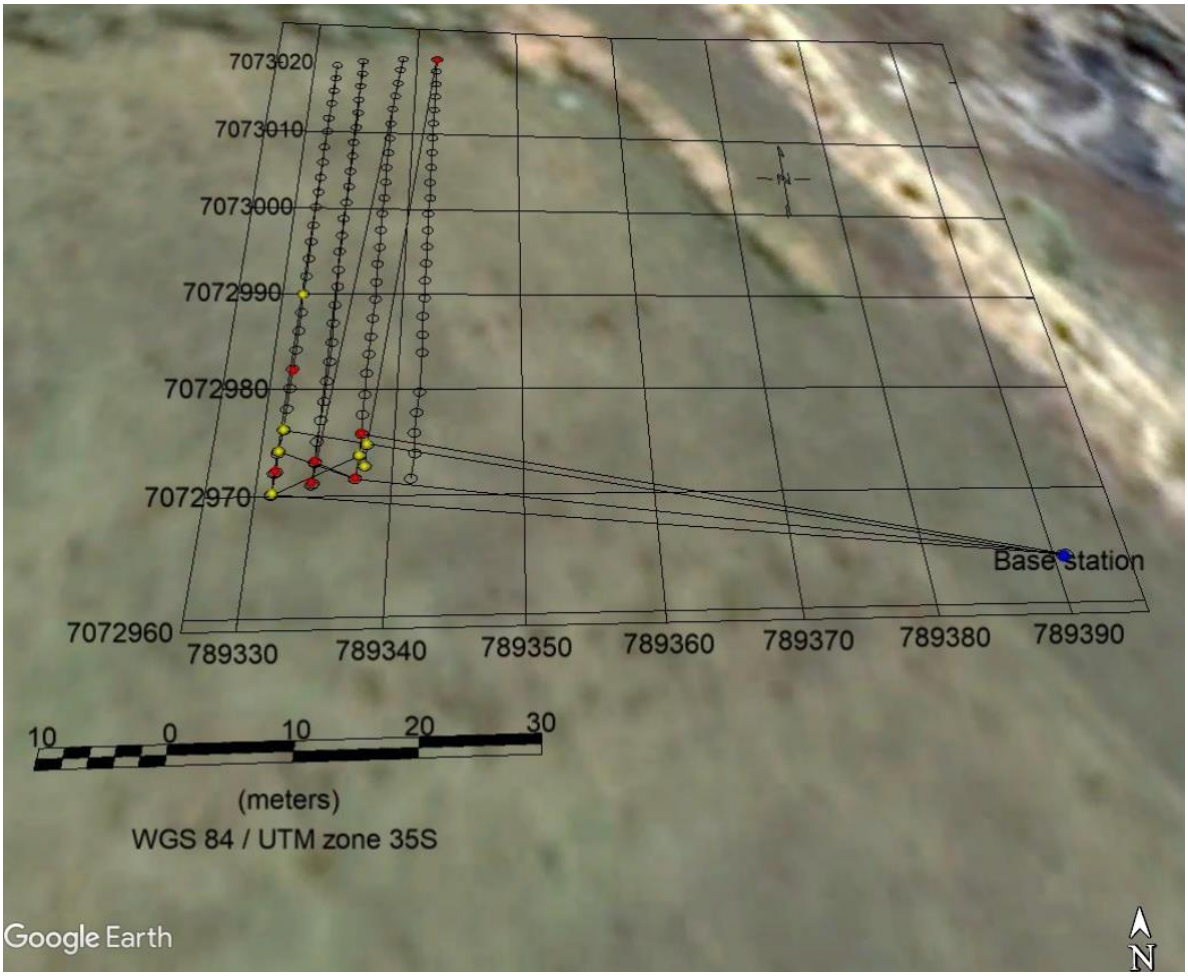



**Figure 2.14.** Google Earth map of the field station, repeat and base station measurements locations showing the pattern followed to acquire the microgravity data. There are a total of 14 repeat measurements from the 4 lines making 3 loops. The red dots represent the internal repeat measurements, while the yellow dots represent the external repeat measurements. The blue dot represents the base station which is about 50 m EES of the survey grid location.

## 2.3.2 Time domain electromagnetic method

Time domain electromagnetic data were collected using a TEM-FAST48 system using a loop size of 25 m. Only one line was acquired for this method and it had a 5 m station spacing with a total of 20 soundings (Figure 2.15). Similar to acquiring the gravity data on a larger grid pattern, this could not be fulfilled due to the time constraints. Figure 2.15 shows a Google Earth map of the location of the all the geophysical datasets (microgravity, time domain electromagnetic, electrical resistivity and magnetic data) collected on the site including the resistivity data location.

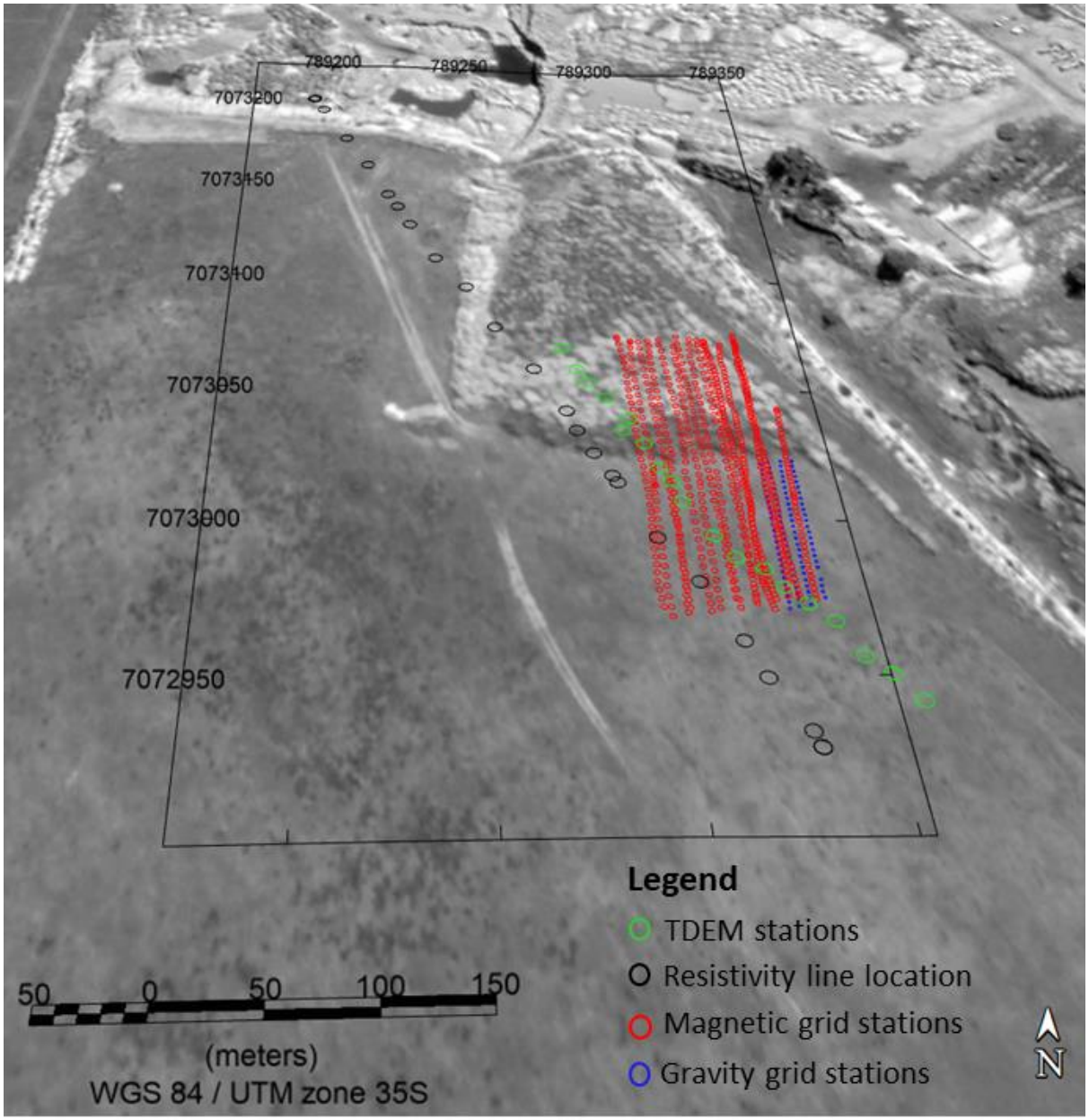



**Figure 2.15.** GPS data plot of the microgravity grid (black), magnetic grid (red) and TDEM line (blue) where the data were collected.

For the three geophysical methods used, the acquisition parameters are summarized in Table 2.3 for clarity.

**Table 2.3.** A summary of the acquisition parameters used for microgravity, TDEM and magnetic datasets.

| Geophysical method | Station spacing (m) | Line separation (m) | Number of lines | Length of a line (m) |
|---|---|---|---|---|
| Microgravity | 2 | 3 | 4 | 50 |
| TDEM | 5 | None | 1 | 150 |
| Magnetics | 2 | 3 | 14 | 100 |

### 2.3.3 Magnetic Method

The magnetic grid (Figure 2.16) was traversed with a walk-mag (G859) and the proton precession magnetometer (G856) was used as the base station to monitor the diurnal variations every 30 seconds during the survey. The base station was situated about 100 m south of the survey grid. A repeat line running E-W was measured at about 200 m away from the grid (outside the range of Figure 2.15) at the beginning and end of the survey to monitor and correct for the instrument drift if there was a need. All these data were collected in one day.

The magnetic data grid had a line separation of 3 m and 0.5 seconds sampling time which made-up approximately a 2 m station spacing at the rate at which the operator was walking. Each line was 100 m in length (except the first line which was 80 m because it was towards the cliff edge) and a total of 14 lines were completed. A hand-held GPS was used to guide the movement of the person carrying the walk-mag and for the stations location, the walk-mag internal GPS was used. The lines are not entirely straight however, despite following the hand-held GPS with pre-programmed coordinates, walking on the area that was clear of bushes and had easy access. This may have been due to a ±4 m inaccuracy associated with a hand-held GPS.

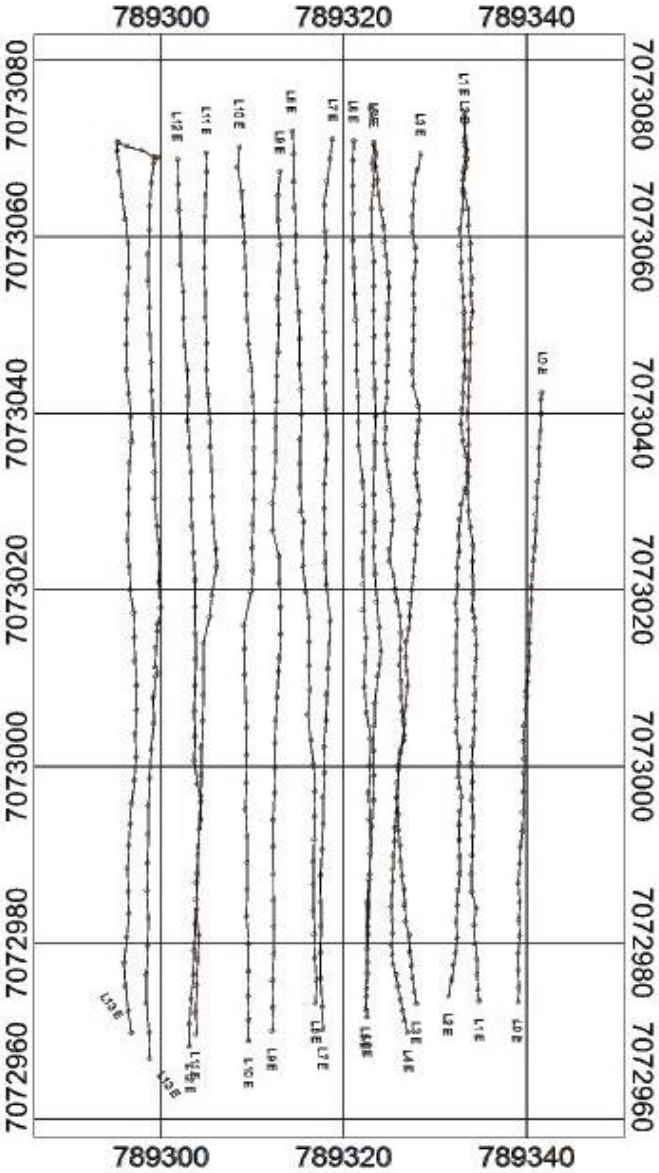



**Figure 2.16.** Grid layout of how the magnetic data were collected showing all the 14 lines plotted in Geosoft Oasis Montaj (Education kit 2018). The lines are labelled L0E which is the first line from the right to the last line L13E. The lines were collected from the south to north (bottom-up direction).

## 2.4 Chapter 2 Summary

This chapter addressed the methods/or techniques used in the study, namely microgravity, magnetic and time-domain electromagnetic (TDEM) methods and the procedures followed to implement the methods. Firstly, a look was taken at the background theory behind each method, because this is vital in understanding why each method was chosen for this study given the objectives of the research. This then aided in the survey design of each method which is the next aspect that was addressed. The survey design was done making use of the knowledge based on the information (reconnaissance resistivity survey and physical measurements and observations) acquired upon a visit to the site prior to the commencement of the study.

Before data acquisition, the success or failure of a project can be assessed through forward modelling that helps in determining the prospect of the method in question to achieve the objectives. Forward modelling of microgravity and magnetic surveys were done using the physical property information from the literature of the lithology which matches that of the study area. Also, the knowledge of the dimensions of the causative bodies under investigation was taken from the measurements that were done with a laser rule when the site was visited prior to the design phase of the project. Forward modelling of magnetic and microgravity data were done using Mag2dc (Cooper, 2013) and Grav2dc (Cooper, 1993) respectively, 2.75D modelling software written by Prof. Gordon Cooper of the University of the Witwatersrand.

Forward modelling of the tunnel TDEM models was not undertaken because of a general lack of access to such forward modelling software which would require 3D modelling using finite element formulation of the problem (Cai et al., 2017). While algorithms to handle 3D conductive plate-like bodies (which are approximated as current carrying ribbons or loops) in a resistive environment are available for the exploration geophysicists, a highly resistive body in a slightly less resistive environment would be extremely difficult to model (Cai et al., 2017) and thus considered beyond the scope of this work. Software for layered earth responses are however available and the general trend in the industry is to interpret each TDEM sounding as a layered earth model and then gridding the layered earth model as ‘known’ at each sounding position in 3D to obtain a resistivity voxel of the subsurface (Mc Neill, 1996). Such software are commercially available, and no student license was obtained. Although this is theoretically not correct it works surprisingly well if there are no large variations in both lateral and vertical

resistivity, for instance highly conductive bodies in the substratum. For these exceptions, conductive plate algorithms are required. Thus a 3-D grid pattern was designed for TDEM surveying with lines 10 m apart and with a station interval of 10 m since the TDEM technique with a minimum loop size of 25 m x 25 m, samples already a large area to determine a bulk resistivity. Unfortunately, this intension to survey had to be abandoned because of time constraints and a single line of TDEM soundings were completed, again at an angle striking NW-SE to the planned gravity and magnetic survey lines to cover a longer distance than the gravity and magnetic survey and shed more light on the position of a suspected fault (to be discussed later through the TDEM data). From Figure 2.9, there is a suspicion of a fault denoted by the layer of a resistivity of about 166 Ωm offset by a layer of lesser resistivity of about 114 Ωm seen on the far right of the section.

Lastly the chapter documented the survey parameters for each survey. For the magnetic method and microgravity technique, a fair amount of data were collected albeit not the area that was initially planned for microgravity in particular. With the TDEM however as explained above, just a single line of data was covered on a last day of the survey when the area had to be vacated. Going forward, in the following chapters, reference to 3-D modelling will only be made to the magnetics and microgravity datasets and not TDEM.

# CHAPTER 3 - GEOPHYSICAL DATA FILTERS

## 3.1 Preamble

This chapter addresses the theory and ways in which the filters are employed in this dissertation to enhance, filter and remove a realistic regional field from the data. These filters are available as standard application procedures in Geosoft (some other filters used in this dissertation stem from these ones addressed and it must be clear that no new filters were designed) but regardless, it is worth knowing the enhancement principles behind these Geosoft filters. These filters were mainly applied to the magnetic dataset and some to the gravity data for regional field removal.

### 3.1.1 Fourier Transform

This filter is addressed because it is employed from Geosoft when microlevelling the magnetic data in Chapter 4. Practically, most signals in their raw format are in the time-domain or distance, i.e. whatever the signal measures it is a function of time (Polikar, 2001), in this case the magnetic data that were collected. However, the important information in a time-based signal can be summarized much more easily in the frequency domain within the frequency spectrum of a signal. It is the frequency spectra which show what frequencies or wavelengths do exist in that signal. Another huge advantage of the frequency domain is that complex mathematical operations in the time domain like convolution, become a simple multiplication in the frequency domain, resulting in a large saving of computer time (Polikar, 2001).

The important question is how to decompose such signals to obtain the frequency content? Polikar (2001) states that the answer is found in the Fourier Transform (FT) developed by Fourier (1822) who showed that some mathematical functions could be re-written as an infinite sum of harmonics consisting of sines and cosines, and its digital formulation called the Fast Fourier Transform (FFT) first developed by Cooley and Tukey (1965). According to Cohen et al. (1993); Fletcher and Sangwine (2017), the Fourier Transform gives information about the frequency content of a signal but offers no information about where in space or time its various frequencies exist.

There are many uses for the FT but the way the FT is applied to filtering is as follows. Using the transform to filter equally spaced digital data involves applying a forward transform of the dataset, transforming it into a new (frequency) domain and then to affect the filtering process whereby the transformed data are modified in a desired way (Dentith and Mudge, 2014) in the new domain. Thereafter, applying the inverse transform takes the modified transformed data series to its original time domain as the filtered data series (Dentith and Mudge, 2014).

Mathematically, the Fourier Transform (FT) decomposes a signal to complex exponential functions of different frequencies and this is defined by the following two equations (Polikar, 2001) of which the second is the reverse transform of the first:

$$X\,(f) = \int_{-\infty}^{\infty} x\,(t).\,e^{-2j\pi ft}dt \tag{3.1}$$

$$x\,(t) = \int_{-\infty}^{\infty} X\,(f).\,e^{2j\pi ft}df \tag{3.2}$$

where *t* is time, *f* is frequency, *j* is a complex number, x denotes the signal at hand, *x* denotes the signal in the time domain and the *X* denotes the signal in the frequency domain. Equations (3.1) and (3.2) are the Fourier and inverse Fourier Transforms of *x (t)* and *X (f)* respectively.

The Fast Fourier Transform (FFT) has millions of applications and in geophysics is extensively used in commercial software such as Geosoft and Intrepid (Geosoft, 2018; Intrepid, 2012). Cooley and Tukey (1965); Rao (2010) state that the FFT is an extremely efficient implementation of the discrete Fourier transform (DFT) which was developed for discreetly and evenly sampled data series (i.e. normal gridded data). A mathematical relationship between the DFT and the sequence *x(n)* mapped onto the frequency domain is thus (Rao, 2010):

$$X^F(k) = \sum_{n=0}^{N-1} x(n)W_N^{kn}\,, k = 0,1,\dots,N-1, N\ DFT\ coefficients \tag{3.3}$$

$$W_N = \exp\left(\frac{-j2\pi}{N}\right)\ ;is\ the\ N^{th}\ root\ of\ unity\ and\ j = \sqrt{-1} \tag{3.4}$$

where *x(n)*, *n* = 0, 1..., N-1 is a strictly uniformly gridded data in the case of this study.

For uniform gridding, the data will be gridded using a minimum curvature gridding algorithm as will be seen in chapter 4. According to Swain (1976), for the given data points, a minimum curvature surface is a smoothest possible surface that will fit them.

### 3.1.2 Butterworth Filter

Upon the levelling of the magnetic data, the Butterworth filter is employed as will be seen in chapter 4. This is the reason why it is addressed in this section. Ideally, filters would have magnitude responses that are rectangular (box shaped) in nature (Rorabaugh, 1993) where the lower and higher frequencies to be retained or removed are clearly cut from the spectrum. In these ideal filters, the required frequencies would be passed unaltered or attenuated while the unwanted frequencies would be blocked. Such filters would ideally be low-pass, high-pass, band-pass and notch filters. However, those are ideal filters and in practice filters can only approximate the ideal filter characteristics. One such filter is the Butterworth filter which optimizes approximation of the alteration, attenuation or blocking of frequencies whether they are required or should be blocked (Rorabaugh, 1993).

The Butterworth filter (diagram shown in Figure 3.1) is very good for applying straightforward high-pass and low-pass filters to data because one can regulate the presence of ringing in the filtered data (Geosoft, 2013). Butterworth low-pass filters (LPF) are designed to have an amplitude response characteristic that is as flat as possible at low frequencies and then decreasing with rising frequency (Rorabaugh, 1993). The filter function is given by (Geosoft, 2013) as:

$$L(k) = \frac{1}{1+ (\frac{k}{k_c})^n} \tag{3.5}$$

where:

- $k_c$ is the central wavenumber of the filter. It can be left fixed when controlling the degree of the filter roll-off.
- $n$ is the degree of the Butterworth filter function. The default roll-of assumption is for a degree of 8.

- 0/1 is residual/regional flag used to specify if either a residual high-pass (HP) or a regional low-pass (LP) is needed. The system however has a default choice of being a regional filter. Thus, if the flag is 1 (L(k) = 1), then a regional LP filter is applied, else if the flag is 0 (L(k) = 0), then a residual HP filter is applied.

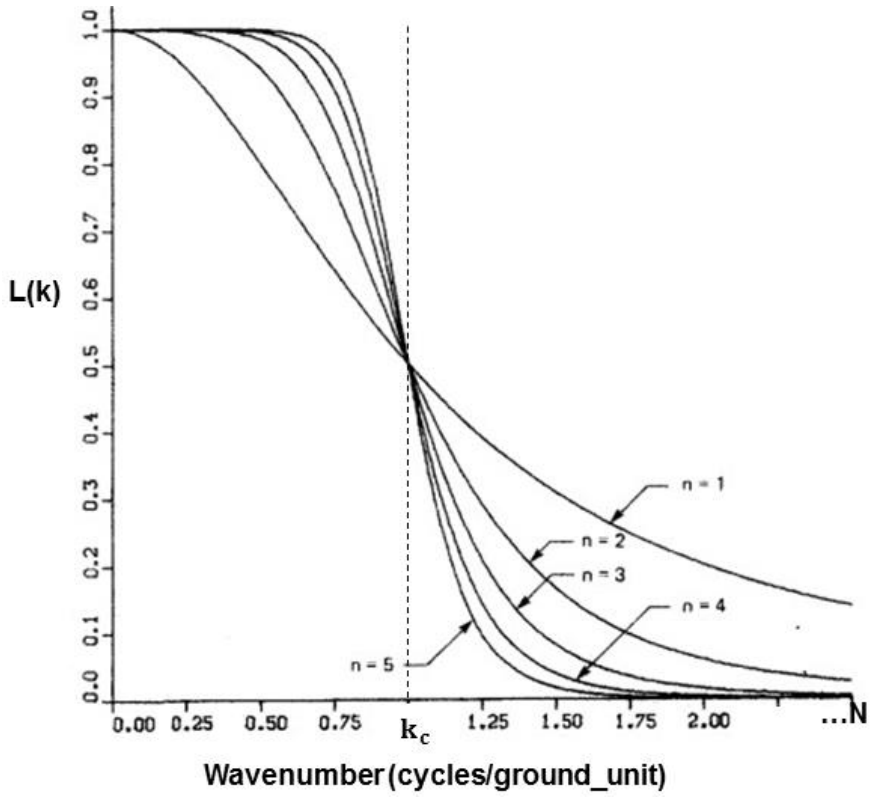



**Figure 3.1.** Shape of the Butterworth filter function for different filter degrees (n), as used in Geosoft Educational Kit (2018). Modified from Pashtoon (1987).

### 3.1.3 Nth-order polynomial (for removing the regional field)

The microgravity and the magnetics datasets needed to be enhanced by removing the regional field. This was done in 2D forward modelling of the data through curve fitting in the process that is explained in this section. Nominally, curve fitting determines the best fitting mathematical function through a collection of data points and most commonly polynomial functions are used although there are many other choices of functions. This choice depends on the nature of the data. A polynomial of N-1 degree will fit a dataset with N data points best (Dierckx, 1993; Walsh et al., 1962). However, using curve fitting in the definition of a

background field in the process of interpreting geophysical measurements is to fit a function *f(x)* to only selected points in a dataset. The interpreter's perception comes into play as to which data points fall outside the anomalous values as measured, and a regional field curve should only be fitted to those data points perceived to not being part of the anomalous part as the purpose is to isolate only the anomalous effect. It is the anomalous part of the data that is used to determine the dimensions of the anomalous geological body amongst a background of other sources.

The choice of a curve is also influenced by how scattered the data are and whether the need is to fit certain points or all of them. A linear function (the simplest polynomial) which is a straight-line, fits only certain points of the data unless all the points are in a straight line and there would be no anomalous component in the data set. The equation for a straight line is:

$$f(x) = ax + b \tag{3.6}$$

where: *a* is the slope of the line and *b* is the y-intercept. The aim is to determine the coefficients of *a* and *b* in a least squares sense (since *a* and *b* are obtained from an over determined solution matrix). But clearly if there are many points not ordered in a straight line, the function of a straight line will not suffice. A higher order polynomial becomes an improved solution, and a third order polynomial will be discussed in this case:

$$f(x) = a_0 + a_1 x + a_2 x^2 + a_3 x^3 \tag{3.7}$$

The best fit to the data is determined by the order or degree of the polynomial function. As already mentioned, the higher the order the better the function can fit the data. However, such a better fit to the data, also can cause wild oscillations between the data points. In gravity and magnetic modelling programs Grav2dc and Mag2dc respectively, a set of functions (known as cubic interpolation) can be fitted to different portions of the 2D data (x, *f(x)*) deemed to be the background portion of the data, in addition to attempting to fit one sloping straight line function to the background data points or through all the data points.

The cubic interpolation in 2D between data points is labelled as an “interactive spline” choice in the software because the user can decide on how the function is to fit the data, hence interactive. It must be noted that the spline goes through all the data points deemed by the interpreter as being part of the regional or background data, ignores the anomalous part(s) of the data set and therefore interpolates smoothly and with minimum curvature between the anomalous and regional parts of the dataset. The regional trend must always be selected as smooth and near to linear as the complete dataset and the interpreter’s knowledge about the geology allows. A proper regional can never contain another anomalous trend that cannot be explained by the known geology (Mickus, 1991).

# CHAPTER 4 - DATA REDUCTION AND PROCESSING

## 4.1 Preamble

According to Hinze et al. (2013), data reduction is a process of mathematically converting the measured raw geophysical data into a form that allows geological interpretation of the data. This is then commonly known as the anomaly. The purpose of data reduction, Hinze et al. (2013) state is to convert the field measurements into a format that can be interpretable. This interpretable format can be further manipulated in different ways such as filtering to enhance images making geophysical models that can give a representation of the underlying geology depending on what the target is.

## 4.2 Microgravity

### 4.2.1 Data Reduction

The CG-5 gravimeter performs some of the gravity data corrections including earth tide variations, micro-seismic noise filtering, instrument tilt, temperature drift, long term linear drift and noisy sample filtering automatically (Murray and Tracey, 2001). Remaining corrections not performed by the gravimeter were done upon reducing the data as detailed in the following sections.

#### 4.2.1.1 Drift correction

Apart from external factors such as earth tides and temperature gravimeters also drift due to mechanical stress and strain in the mechanism as the meter is moved around and is called the meter-related drift component (LaFehr and Nabighian, 2012). It is corrected for by determining the gravimeter constant from time to time and entails comparing the gravimeter's ability to determine the difference in gravitational attraction between two or more known absolute base stations. In general drift is a gradual change in the reference value with respect to which measurements are made. The meter-related drift with time, which is linear in some gravimeters, tends to decrease with increasing age of the meter. The quartz spring mechanism of the CG-5

gravimeter tends to produce a high drift (LaFehr and Nabighian, 2012) and this needs to be checked for data quality control regularly.

To correct for internal and external types of drift, the gravimeter should occupy the same station (base station, or a station with a known value) on a ~hourly basis in what is known as a drift loop and noting the changes in gravity readings at the station, usually at the beginning and end of the loop (Murray and Tracey, 2001). In this study a single gravimeter was used to take readings along the survey line and take base station measurements.

The less time between base readings, the easier the drift as a function of time can be removed as a linear drift is assumed between base readings. As the CG-5 does correct for long term non-linear drift such as tidal drift, preferably a time of less than 6 hours per loop should be allowed (Murray and Tracey, 2001). It must however be noted that the more time it takes to close a loop, the larger the chance that the remaining drift not compensated for by the meter being non-linear.

Gravimeter drift is removed to accurately determine the difference in gravitational attraction between the base (where the gravity is known) and the measurement station. This is achieved by measuring at points of known absolute gravity called base stations (The Council for Geosciences (CGS) has a distribution of known gravity base stations known as the National Network across South Africa and encourages their use) or performing repeated measurements at a convenient arbitrary ‘base station’ to which a relative gravity value is assigned. Surveys based on such relative base stations are known as relative gravity surveys as they are not tied to the National Network. Such a relative base station can be tied into the National Network of Base Stations and would enable the gravity survey to be compatible with other gravity surveys in the vicinity already tied to the National Network. Repeat measurements are also performed routinely on measurement stations by occupying them more than once during different drift loops and should account for about 10% of the measurements taken in a normal gravity survey (Murray and Tracey, 2001). To compute and remove the drift, the remaining time-varying component of the gravity field not corrected for by the CG-5 must be calculated using linear interpolation (LI) between base station measurements and the formula below is used:

$$LI = \frac{B_2 - B_1}{(T_{B_2} - T_{B_1}) * (T_S - T_{B_1})} \quad (4.1)$$

where $B_2$ and $B_1$ are the base station observed gravity readings at time 2 and 1 respectively, $T_{B_1}$ and $T_{B_2}$ are the times in minutes at base station reading at times 1 and 2 respectively and $T_S$ is the time at every gravity station between $B_1$ and $B_2$ . LI is the drift correction/minute to be applied to the CG-5 measurement.

The drift corrected measurement is then calculated by subtracting the interpolated reading from the measured reading. The drift corrected measurement is the gravity (observed) minus the instrument drift (interpolated value). A more complicated process can, where convenient, also be followed where drift loops are not closed on a single base station but between different base stations in a technique called Leap Frogging (Murray and Tracey, 2001). Leap frog method was not used in this study because a single base station location was used.

For this survey, during the measurements along the four lines of data collected, the relative base station was occupied six times throughout the survey. The first line was completed with a time loop on its own (3 total repeat measurements), the next two lines were completed within another loop (8 total repeat measurements) and the last line within a loop of its own (3 total repeat measurements). These will be referred to as loops 1, 2 and 3. The position of the single relative base station was chosen to be adjacent to line 1 (Figure 2.14). The procedure for removing the drift is taken from the Society of Exploration Geophysicists (SEG) gravity notes.

Using the above procedure, the drift was corrected for on these loops and the resulting plots (Figure 4.1, Figure 4.2, Figure 4.3) were made to quantify the amount of drift that was present in the data. This drift is calculated as the difference between the high and minimal value of the y-intercept of the raw data (Gravity reading in mgal – with drift, represented by the blue solid line) taken with respect to the trend line (blue broken line) of the plot of raw gravity data against time. The plot of the drift corrected data (solid orange line) obtained from subtracting the LI values from the gravity readings and its trend line (orange broken line) indicates the drift correction as also seen from the drift corrected curve going back to 0 mgal.

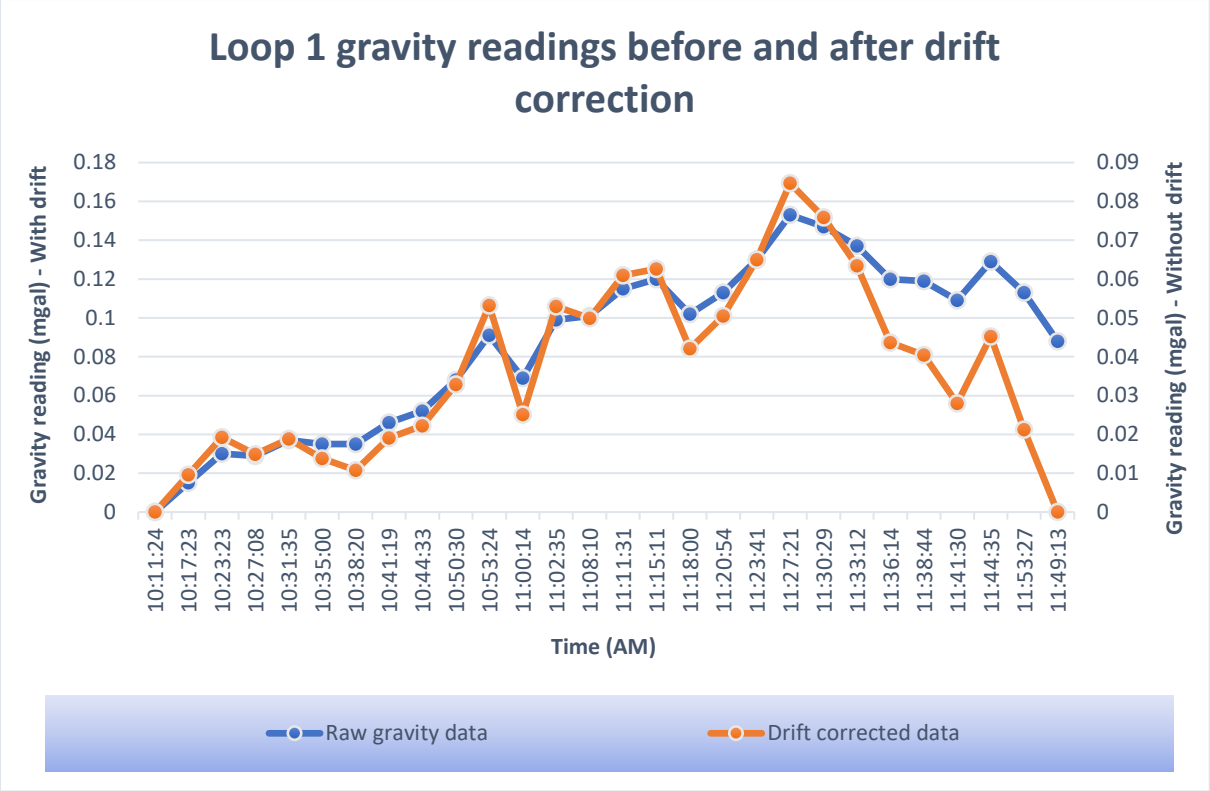



**Figure 4.1.** A plot of gravimeter readings in mgal before (blue solid line) and after (orange solid line) the removal of drift. The drift in this loop is about 0.085 mgal over a period of 1 hour 40 minutes.

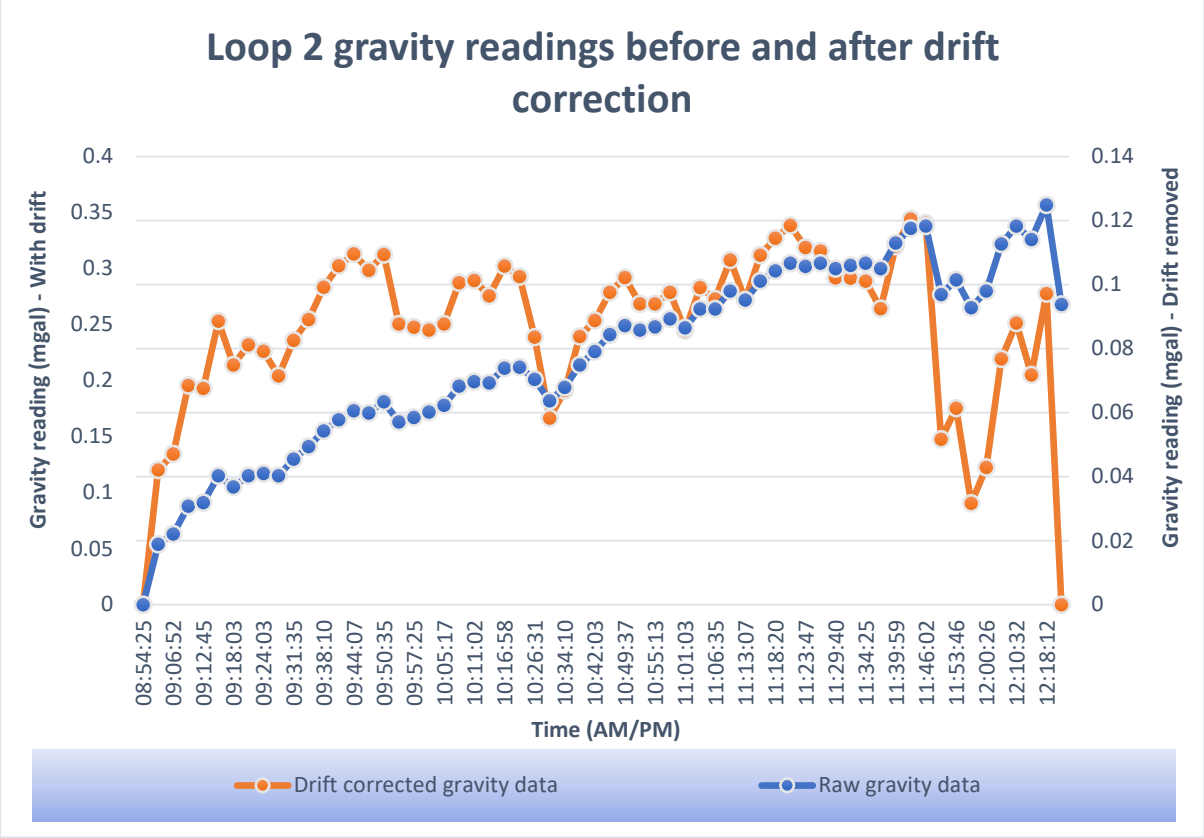



**Figure 4.2.** A plot of gravimeter readings in mgal before (solid blue line) and after (solid orange line) the removal of drift. This is loop 2 which is made of two lines. The drift in this loop over a longer period of 3 hours 20 minutes is about 0.205 mgal. This drift is removed, and this is seen from the fact that the gravity reading at the base station is zero for the drift corrected plot. The meter drifted much, and it is not surprising because of the 3-hour plus loop period.

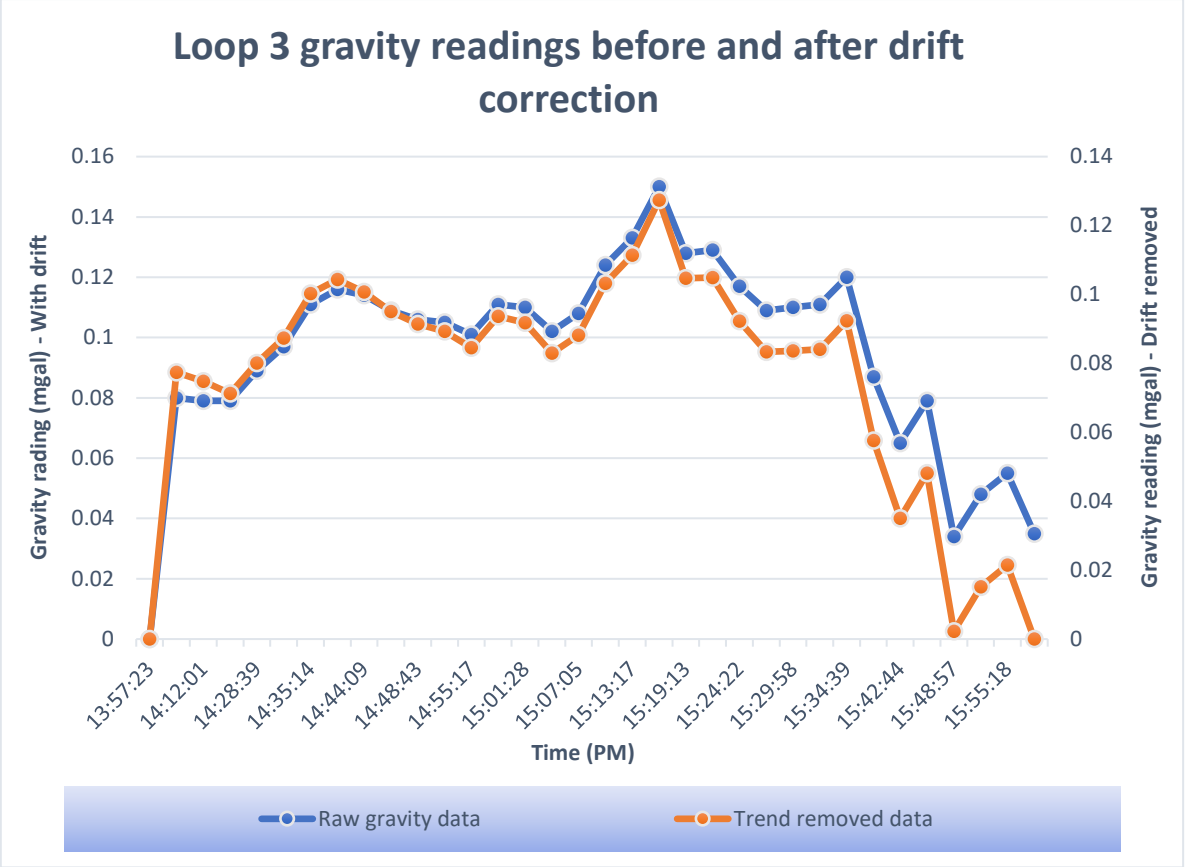



**Figure 4.3.** A plot of gravimeter readings in mgal before (solid blue line) and after (solid orange line) the removal of drift. This is loop 3 which is made-up of one line. The drift in this loop is 0.03 mgal over a period of 2 hours. This is quite interesting compared to the drift of the first loop which is 0.085 mgal over a shorter time of 1 hour 40 minutes as it hints that a loop period of around 2 hours is probably optimum for this gravity meter.

### 4.2.1.2 Latitude correction

There is a need to correct for the gravitational acceleration which is latitude dependent arising from the Earth's elliptical shape and rotation. The gravitational attraction is more at the poles than is at the equator because of their respective distance differences from the centre of the Earth. This is the effect that the shape of the Earth has on the gravity field. This normal gravity field increases by about 5.3 gal from equator to pole, and if not corrected for, it will yield a north-south gradient in measured gravity data (LaFehr and Nabighian, 2012). The latitude correction removes the normal field from the measured gravity to eliminate this gradient (LaFehr and Nabighian, 2012). A mathematical formula is used to subtract these effects and

the resulting gravity is called normal gravity, which is the gravitational acceleration expected for a rotating ellipsoidal Earth without any geologic complications and no surface features. The formula for the latitude corrected value $d_g$ is given below, simplified from the 1980 International Gravity Formula (IGF) for working in a small area (LaFehr and Nabighian, 2012).

$$d_g = 0.812\ (sin2\phi)ds \tag{4.2}$$

where ***ds*** is the horizontal distance north or south of the base station (in km but converted to m for calculations) and $\boldsymbol{\phi}$ is the latitude of the base station. A value of $\boldsymbol{\phi}$ = 26.434 for the base station was used in this study.

The latitude correction is then added to the drift corrected value obtained earlier to obtain the latitude corrected value. The latitude correction is added when moving towards the equator and subtracted when moving towards the poles. So, in this case it is added because we are in the southern hemisphere and the lines were trending from South to North.

### 4.2.1.3 Free-air correction

This correction is needed to ensure that the interpretation is not affected by spatial variations in gravitational acceleration that are related to elevation differences in the observation points as being due to subsurface geology. Put simply, this is for correcting local variations in the vertical gradient of gravity measurements due to local differences in elevation between observation points and are small compared to the radius of the earth (LaFehr, 1991).

The comparison is made between the observation point elevation and the radius of the Earth (LaFehr, 1991). This correction is done by mathematically converting the observed gravity values to simulate as if they were all recorded at the same elevation, thus further isolating the local geological component of the gravitational field. The gravitational acceleration observed on the surface of the Earth varies by about -0.3086 mgal per meter in elevation difference. The

negative sign indicates that as the elevation increases the gravitational acceleration decreases. Thus, the free-air ($F_A$) correction is given by the equation below:

$$F_A = 0.3086\ mgal * \Delta h \tag{4.3}$$

where Δh is station elevation in metres. A precision of 0.01 mgal will be achieved by an elevation difference of 3 cm which is 0.03 m. Even better precision can be obtained with smaller elevation differences per station measured with a differential GPS. From the three loops undertaken for this survey the difference of repeat measurements (internal and external measurements in loops) was calculated and then averaged to obtain a value of 0.013 m = 1.3 cm elevation precision. In this case, the precision of the Free Air correction for this survey is 0.3086 mgal * 0.013 m = 0.004 gu. To obtain the free-air corrected value, the free-air correction is added to the previous latitude corrected value.

### 4.2.1.4 Bouguer correction

This is referred to as the Bouguer slab correction to account for the excess uniform crustal mass beneath observation points located at elevations higher than the chosen elevation datum which can be sea-level but usually referenced to the base station, which was the case in this study. Otherwise, it accounts for a mass deficiency at observation points located below the elevation datum. The slab correction is a good approximation if the terrain is gently undulating and no rugged topography is present such as on Driehoek on the study site. Normally a feature such as the ~6 m high cliff ~200 m east of the survey area would require terrain corrections but due to its very small dimensions with respect to cliff length, the terrain correction would be very similar at each measurement point and its effect would be a long wavelength effect taken out with the regional effect. Thus, no terrain corrections were calculated. The bouguer correction ($\Delta g$) is defined as:

$$\frac{\Delta g}{\Delta h} = 0.04192\rho \ \text{(mgal/m)} \tag{4.4}$$

where $\Delta h$ is the height of the station above or below the base station (datum) and $\rho$ is the density of the subsurface rocks. For this study, a value of $\rho$ = 2.67 g/cm$^3$ which is the average

value of surface continental rocks was used. This value is usually used for regional gravity surveys (Hinze, 2003). The data were reduced using the Bouguer correction after all the other corrections mentioned were applied (now referred to as the relative Bouguer anomaly or BA since it is not tied to an absolute gravity base station) and the composite plots of elevation and Bouguer anomaly against northing were made as a result (Figure 4.4, Figure 4.5, Figure 4.6). It must be noted that the regional trend is present in the plots of elevation and Bouguer anomaly against northing. The regional field was removed using Grav2dc (Cooper, 1993) as will be discussed in the following section (4.2.2 Microgravity).

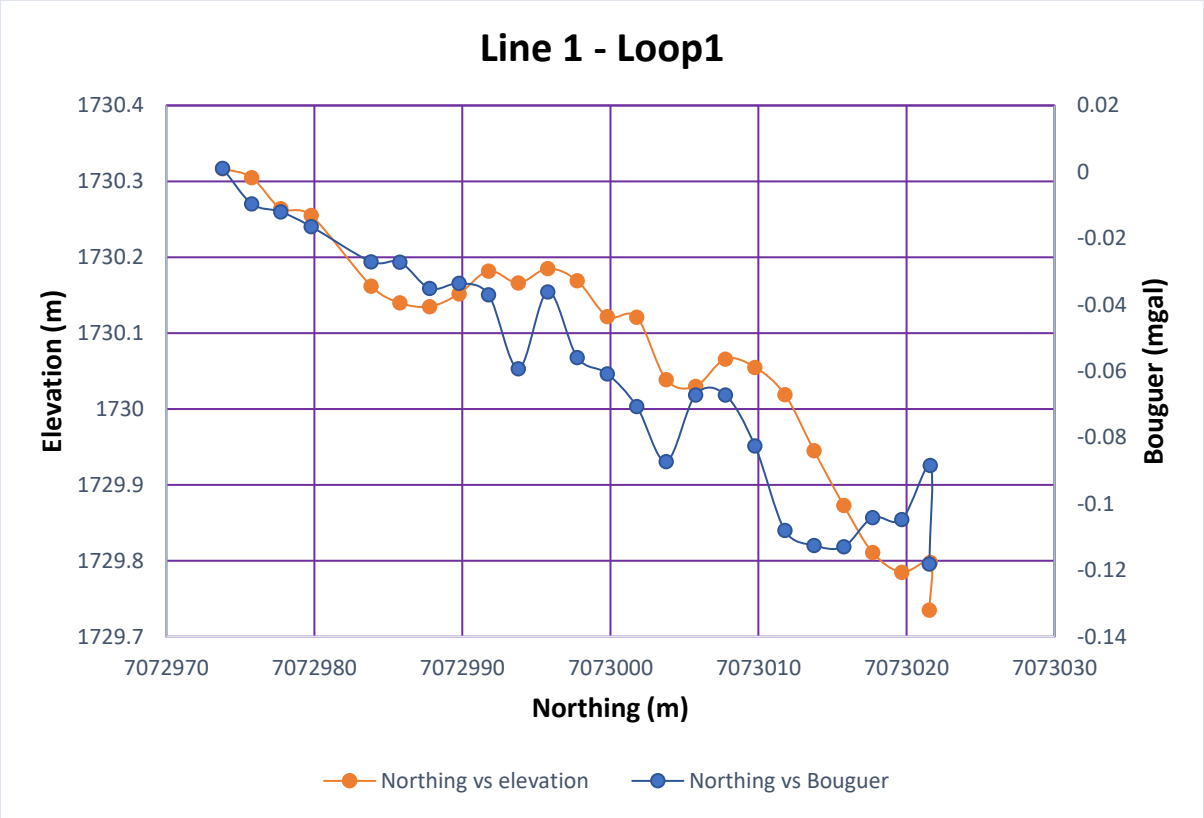



**Figure 4.4.** A plot of line 1 which is the first loop showing plots of elevation (m) and Bouguer anomaly (mgal) against northing. From the figure, the variation of the amplitude in mgal of the anomalies is ±0.03 mgal and no regional trend is removed yet. This loop has 1 internal and 2 external (on loop 2) repeat measurements. Although there is a positive correlation between the elevation data and the BA values, this is considered fortuitous as the variation in BA values is much more than the variation in elevation differences (these have a 0.2 m maximal value).

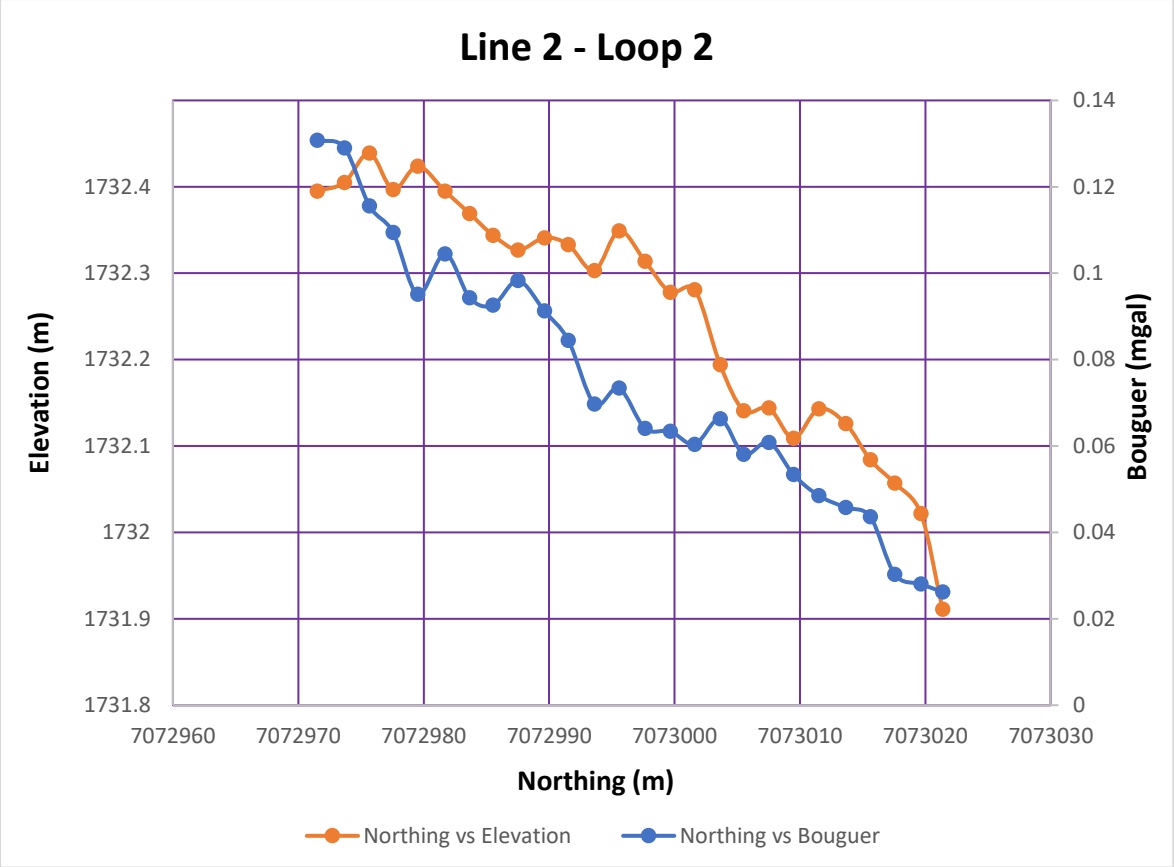






**Figure 4.5.** Plots of lines 2 and 3 of elevation (m) and Bouguer anomaly (mgal) against northing making loop 2. The amplitude variation of the anomaly size is ±0.02 mgal. Again, no regional field is removed yet. This loop has a total of 4 internal and 4 external repeat measurements.

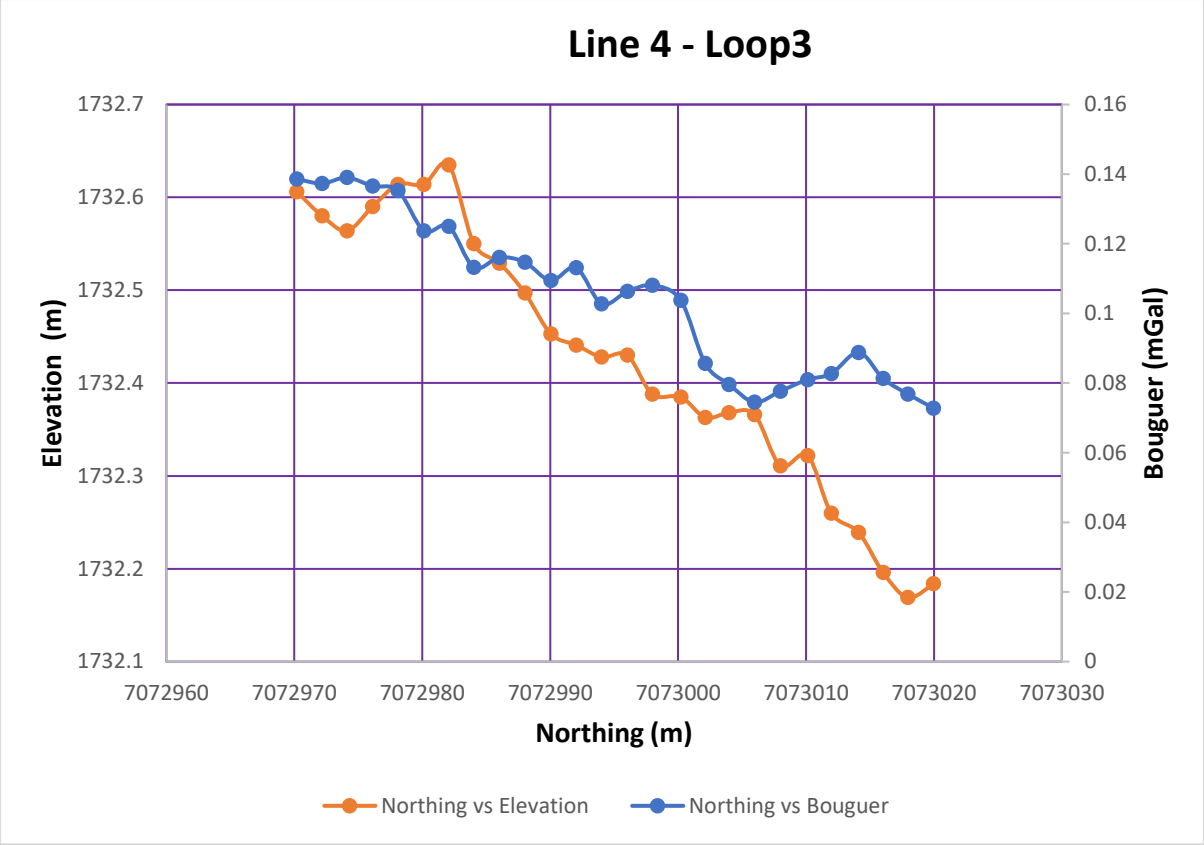



**Figure 4.6.** A plot of line 4 which is the third loop showing elevation (m) and Bouguer anomaly (mgal) against northing. The amplitude of the anomaly is ±0.03 mgal.

## 4.2.2 Data processing and gridding

The relative Bouguer anomaly data from section (4.2.1.4) were imported into Geosoft Oasis Montaj, (2018) as a database (see Appendix C). The processing workflow is summarized in Figure 4.7. The data forming the 4 lines were checked if they were without spikes or outlier points. Had there been spikes in the data, those data would have been removed, but no points were discarded. Upon satisfaction that the data were ready for gridding, a grid of the Bouguer data was produced using a "minimum curvature gridding algorithm". A minimum curvature surface is the smoothest possible surface that will fit the given data values (Swain, 1976). The recommended cell spacing for this gridding algorithm is $\frac{1}{4} * \boldsymbol{line\ separation}$. The line separation in this case was 3 m so the grid cell size was 0.75 m.

The gridded data contained the regional field since it had not yet been removed (Figure 4.8). To remove the regional effects and concentrate on local features, a residual gravity field is calculated by subtracting a smooth regional trend from the relative BA gravity (Bechtel et al., 2014). The regional field is typically a 3D polynomial trend surface fitted to points inside and outside the area of interest where the relative BA values are not influenced by undermining and represent the gravity surface that would have been observed if the target body was not present. The regional gravity data of the survey area is not known upfront; to solve this problem, the gravity values were estimated (from the measured grid values in Geosoft Oasis Montaj) within and outside the area of the BA grid and a regional field grid was produced (Figure 4.9). This grid was then subtracted from the relative BA grid to get the residual gravity grid (Figure 4.10).

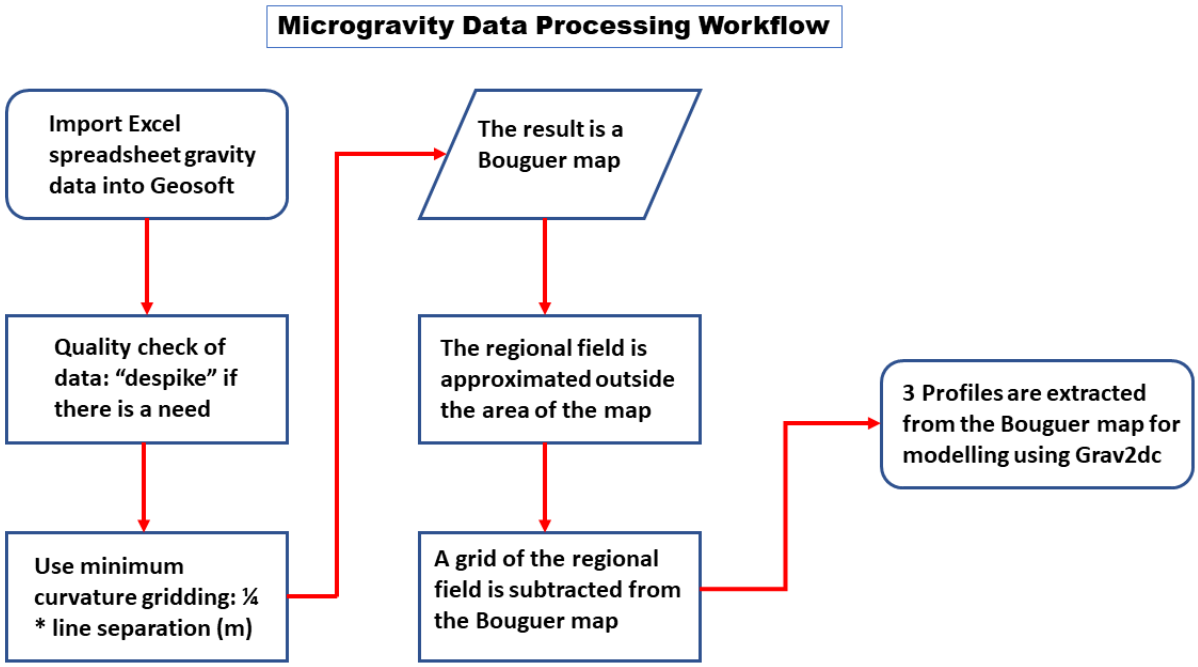



**Figure 4.7.** A workflow of processing and gridding microgravity data in Geosoft Oasis Montaj where the result is three profiles that are modelled in Grav2dc.

The 3D regional field was considered a first order effect and if not totally satisfactory, then the resultant residual map would still show a remnant of the original regional field, that would be further removed in Grav2dc from individual profiles that were to be extracted from the residual gravity map. It should also be remembered that possible density variations in the sandstone (as

seen in section 2.2.2) itself have been ignored as this complicates the modelling process, especially if the variations are gradual and would constitute a regional trend. The residual gravity grid was converted into a map and from the map, three profiles (lines) were extracted in Geosoft. The extracted profile data had headers; **X**, **Y** (both in metres) and **gravity values** (in mgal). The extracted data were then imported into Grav2dc (Cooper, 1993) to be converted into models of the subsurface from the observed data.

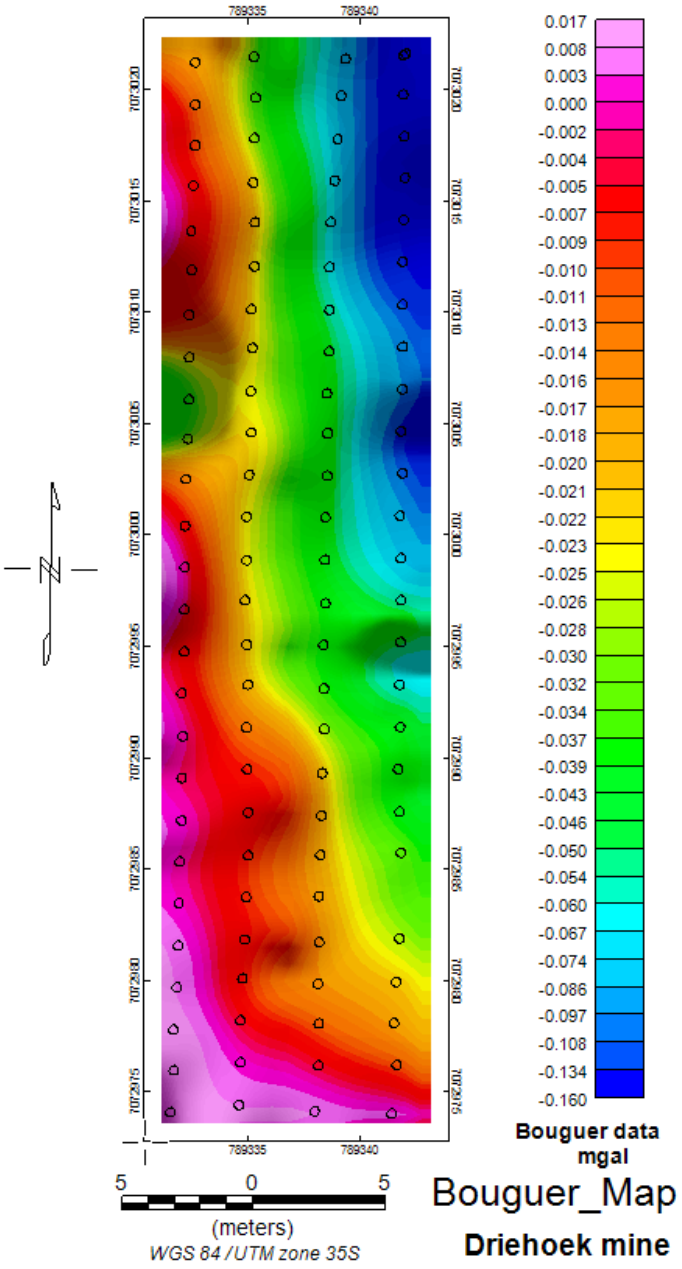



**Figure 4.8.** An artificially sun shaded map of the relative Bouguer anomaly data which includes the regional field to be removed. The colour bar is histogram equalized and the black circles on the map indicate the locations of the data points.

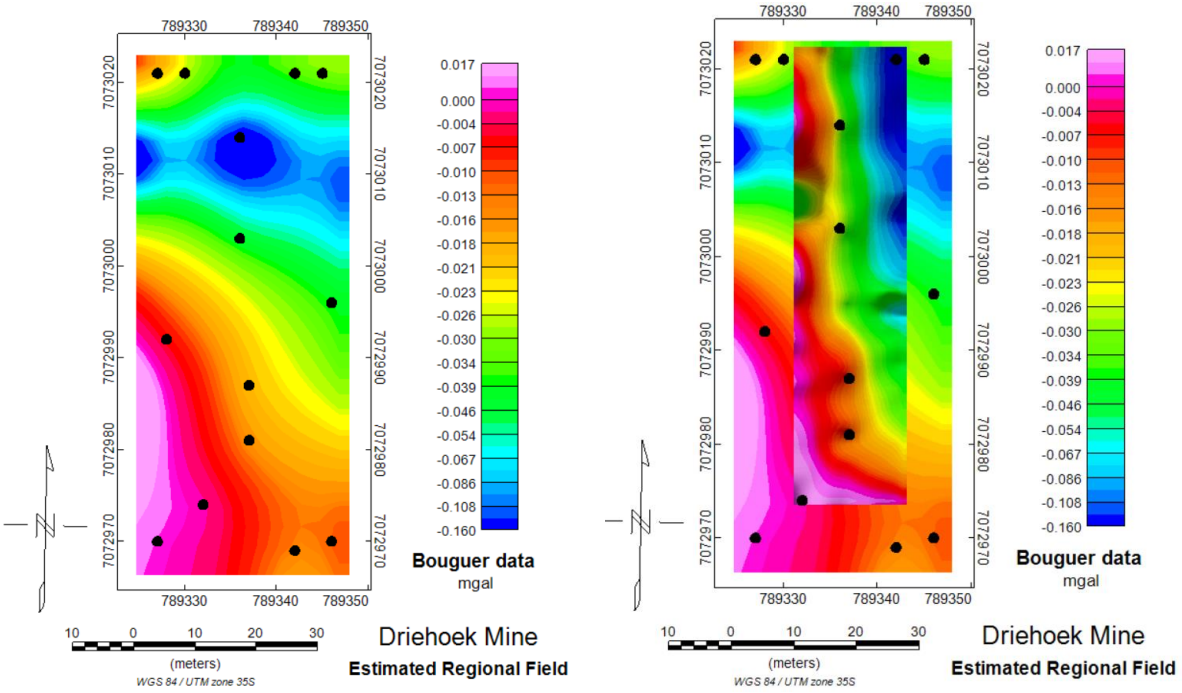



**Figure 4.9.** A grid of the estimated first order regional field within and outside the Bouguer map. The regional field must extend outside the BA map to control the behaviour of the 3D polynomial surface on the boundary of the BA map. The black dots show points where the estimated gravity values were located to which the polynomial surface was fitted, which represented the regional field. The regional field is a third order 3D polynomial surface. The image on the right shows the insert of the artificially sun shaded Bouguer anomaly map overlain onto the larger regional field map.

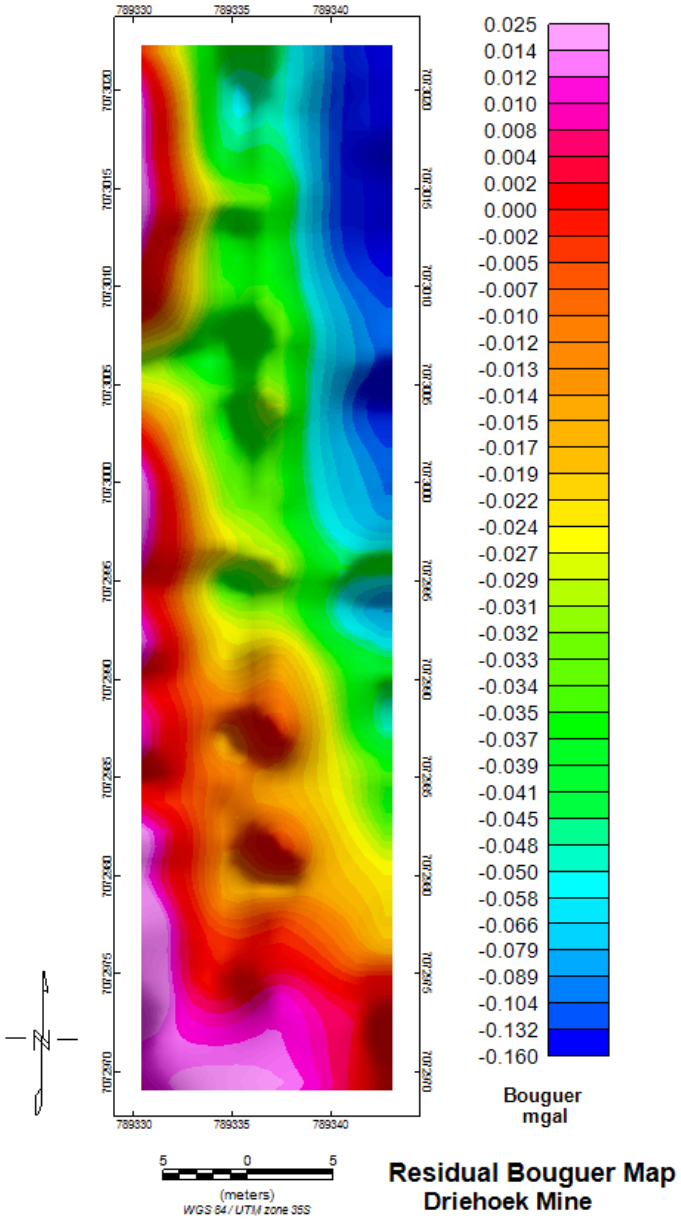



**Figure 4.10.** An artificially sun shaded map of the residual gravity data after the removal of the first order regional gravity field. However, a slight increase in gravity values is still visible going from north to south that will be removed in a second step of regional removal.

The residual gravity field shows a very small increasing trend of approximately 0.02 mgal/m going from north to south. As this would have to be incorporated in the modelling and difficult to do, this effect will be removed during the modelling of the individual traverses on a line basis using Grav2dc with the interactive cubic spline tool as will be shown later. This regional field will be referred to as the second order regional field in Chapter 5.

## 4.3 Magnetic Method

### 4.3.1 Data reduction

For quality control and reduction of magnetic data, two magnetometers that were synchronized in time were used, the G859 caesium vapour ("walk-mag") and the G856 proton precession magnetometer. The walk-mag was used as the rover with a sampling rate of 0.5 seconds (2 Hz) and the proton precession magnetometer was used as the base station with a sampling rate of 30 seconds (0.0334 Hz). Base station readings were smoothed with a running average filter of degree 8 in Magmap2000 (Figure 4.11). As a result, the data experienced a decrease of 0.8 nT in amplitude of the diurnal variation. No cultural noise stemming from powerlines (at least near the site) or metal objects nearby were noted or even vehicles. The only cause of noise on the diurnal plot would possibly be a magnetic storm and not wind buffeting as it was not a windy day when these data were acquired. The night before the survey there were thunder storms and that could result in a magnetic storm (Keary et al., 2002).

After the base station data were smoothed, they were then used to correct for the diurnal (i.e. subtracted) on the rover's data using Magmap2000. With the data having their correct coordinate system projection (WGS84) from the walk mag GPS, the next step was to grid the data using Geosoft, (2018). Besides subtracted diurnal effects, there was no significant need for reductions of the magnetic data. The latitude variation is rarely > 6 nT/km and thus elevation and latitude corrections are not necessary (Telford et. al., 1990). Both the gravity and magnetic data need to be corrected for drift because as mentioned, the gravimeter experiences drift while the magnetometer has no intrinsic drift.

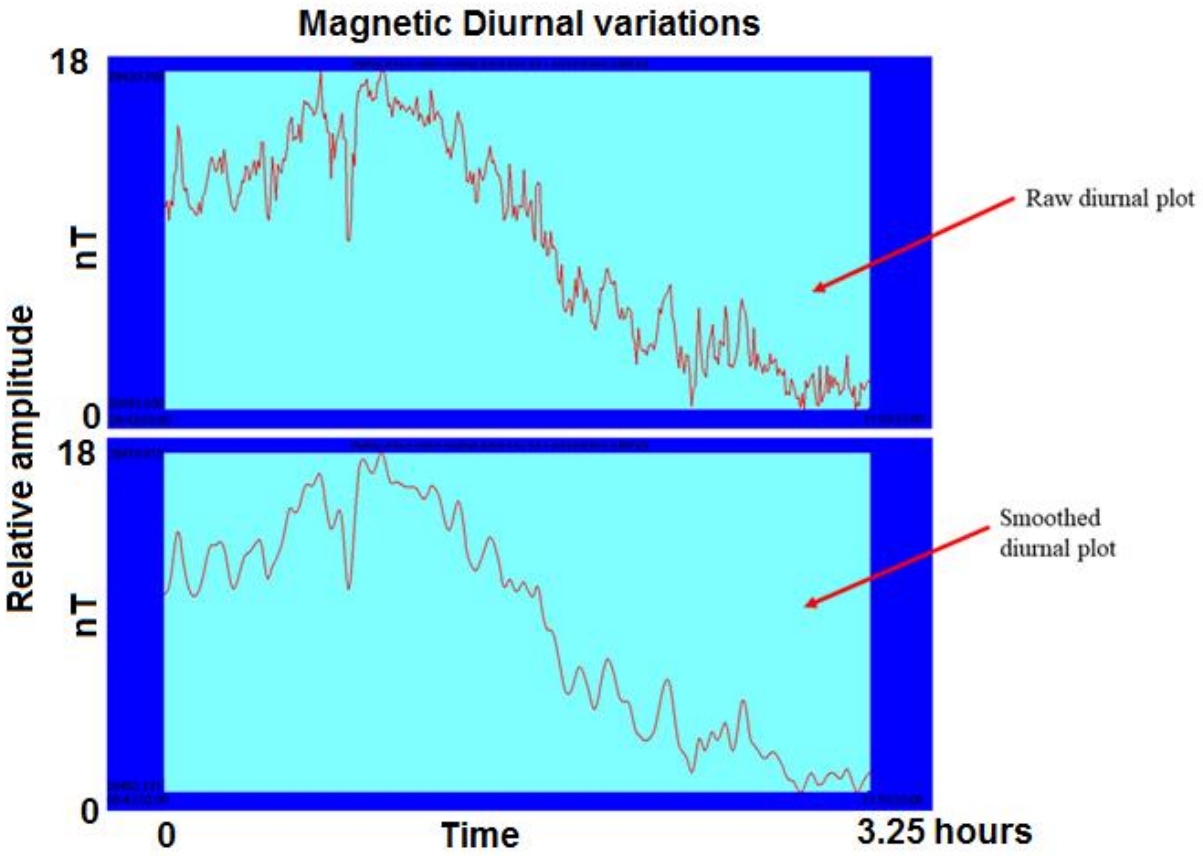



**Figure 4.11.** Base station readings (top figure) showed a diurnal variation of 18.6 nT (28420.0 nT – 28401.6 nT) over a period of about 3 hours and 13 minutes. The diurnal variation of the base station after smoothing became 17.8 nT (28419.915 nT – 28402.121 nT) over the same period as before smoothing. This is a small change in the amplitude of the magnetic field intensity which shows that the base station data were not noisy and this would not have an effect on the field station readings.

### 4.3.2 Data processing and gridding

The diurnally corrected data were imported into Geosoft for gridding. As was the case with gravity data, the data were checked for quality. Few spikes in the individual profiles were removed and a grid of the data was made using the minimum curvature gridding algorithm. Note that the correct field procedure would have been to do measurements also along tie-lines after completion of the survey lines to be able to 'level' the data but due to time constraints and

the small size of the area this was foregone. Therefore, the gridded data show streaky looking lines in the same direction as the survey lines (Figure 4.12) which is accentuated as the map is artificially sun shaded. Those streaky lines are due to non-geologic effects caused by long wavelength noise along survey lines which could be from reversing direction. This kind of noise portrays itself as shifts from one survey line to the next and that may be misinterpreted as information (Geosoft Technical Note, 2018). The procedure of removing such noise is called microlevelling and is outlined below.

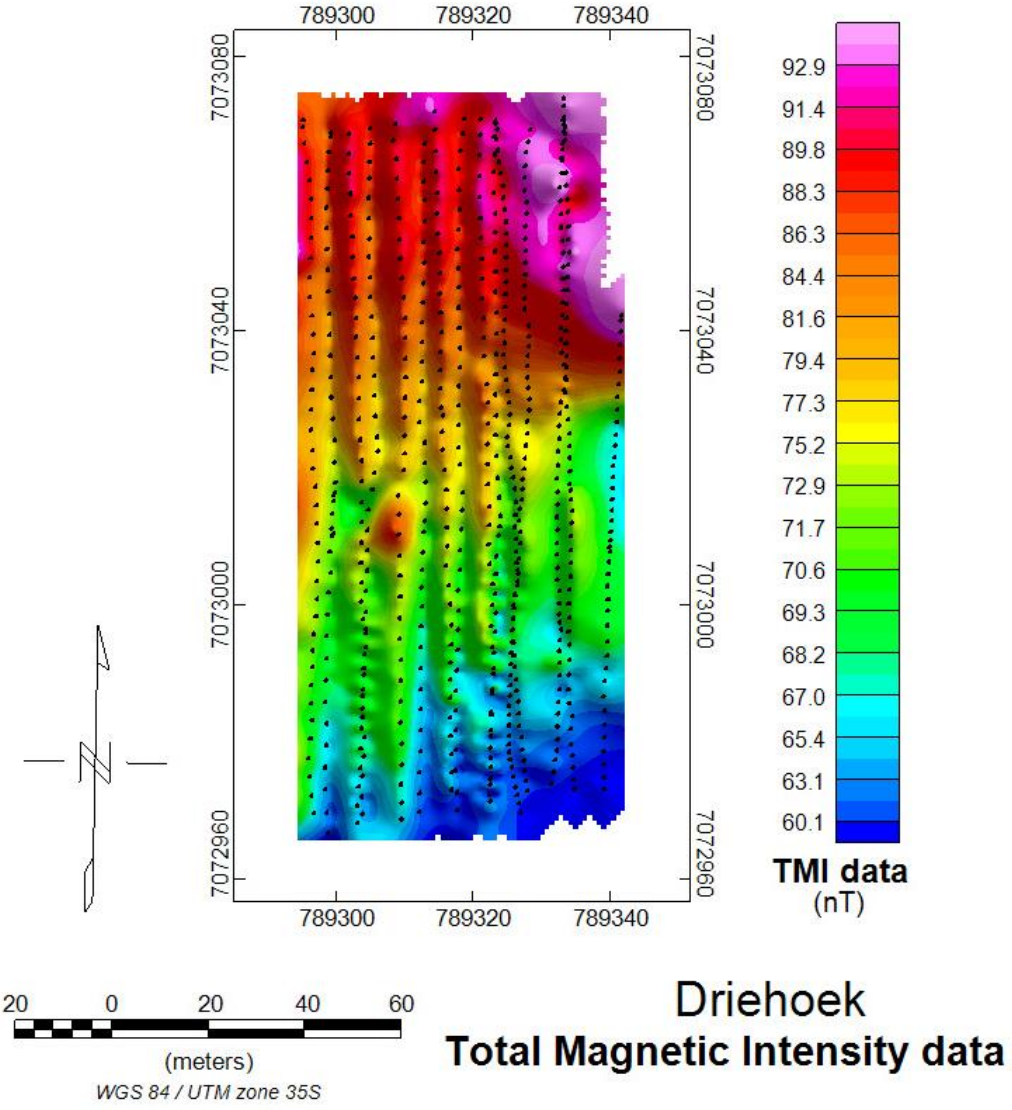



**Figure 4.12.** Sun shaded total magnetic intensity map which has line levelling errors. The noise emphasized by the sun shading is apparent as streaky lines which should not be interpreted as geological information.

To microlevel data in Geosoft, the MAGMAP module is used to apply a decorrugation filter in the frequency domain based on a directional filtering down or across survey lines or

alternatively cosine and Butterworth filters described in Chapter 3. For the directional cosine filter, a degree of 0.5 was used. A cutoff wavelength of 12 m (4 x line spacing (3 m)) and a high pass filter of order 8 were used for the Butterworth filter. These clean up the levelling corrections before applying them to the original data with line levelling errors (Figure 4.12). The decorrugation filter removes the "corrugations". From the Geosoft Technical Note, 2018 the procedure of how the data were levelled to obtain a microlevelled data (Figure 4.13) is outlined below:

- As standard levelling procedures are normally conducted on the line data, this procedure cannot remove all levelling effects and in the resultant grid much smaller embedded levelling errors remain. Here I refer to this grid (Figure 4.12) as the Grid&Error or G1 and it is the result of the original grid having already been treated with tie-line leveling, a Butterworth high-pass filter combined with a directional cosine filter in the frequency domain found in MagMap module in Geosoft (See Chapter 3).

- A low pass filter was applied on the Grid&Error grid along the lines and the data were gridded along this line direction. This creates an initial regional grid at right angles to the Grid&Error grid, a grid called G2. The low pass filter must be long enough to remove all unwanted geological effects that are embedded in the data as line levelling errors. By re-gridding the above grid with the same low pass filters but again in the E-W direction, the levelling errors are removed, and this is called G3. Applying a further low-pass filter results in smoothing of a grid G3 to give a grid G4. A decorrugated grid, G5 = G1 - G2 + G4 is calculated.

- Finally, a levelling error grid G6 can be calculated by G6 = G1 - G5 or G6 = G2 - G4 from which a micro-levelling error channel can be produced and subtracted from the original unlevelled data channel. A total magnetic intensity map, Figure 4.13 from the levelled data was thus produced.

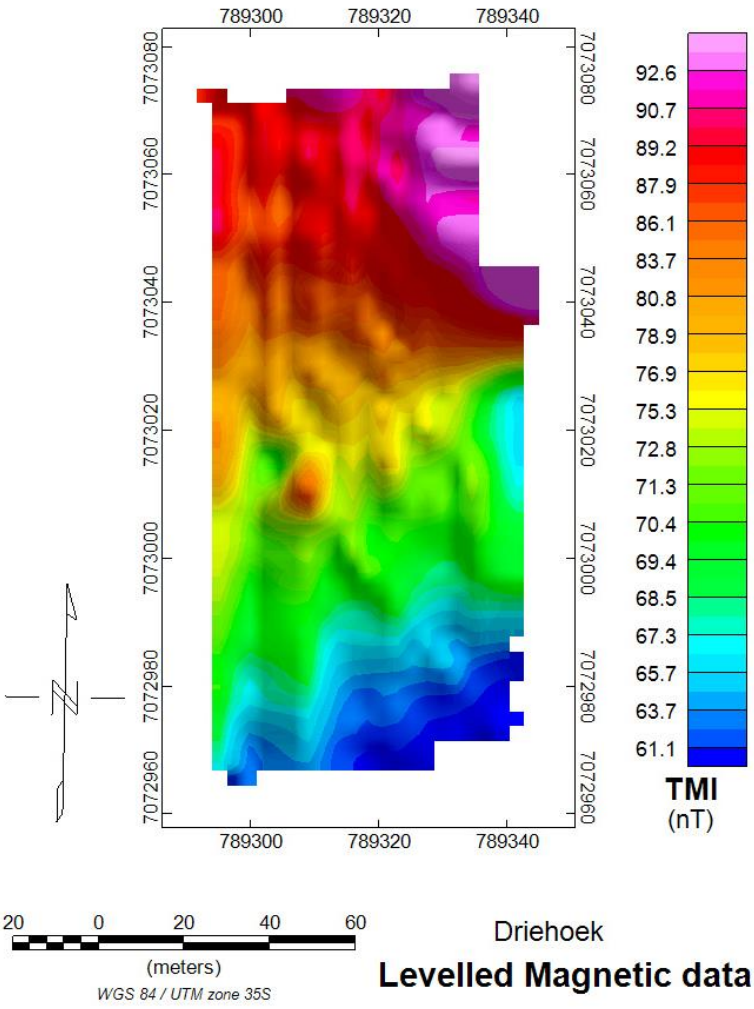



**Figure 4.13.** Levelled sun shaded total magnetic intensity map. The map still has the regional field trend which is removed using Mag2dc especially on the part that is overlain with the microgravity map because that region is the subject of interpretation and target area for correlation of the two datasets.

The levelled grid map was then overlain with the microgravity grid and profiles (lines) were extracted. The data had headers **x**, **y** (in **metres**) and **gravity** (in **mgal**) for microgravity and magnetic intensity (in **nT**) for magnetic data. The purpose of this was to produce subsurface models of both magnetic and microgravity datasets using Mag2dc (Cooper, 2013) and Grav2dc respectively (See Chapter 5).

## 4.4 Time domain electromagnetic method

### 4.4.1 Data reduction and processing

The time-domain electromagnetic data were reduced and processed using a 1-Dimensional commercial processing software, ZONDTEM1D that uses a least squares inversion algorithm (ZondTEM1D, 2017). The software is capable of handling individual TDEM recording station modelling and inversion for a layered earth (1D), as well as inversion of the whole profile (stitched 1D soundings). The free-ware allows 10 soundings at a time, but in this case the data consisted of 20 soundings and the dongle to activate the commercial version of ZONDTEM1D whereby all 20 soundings could be incorporated into a single inversion was kindly made available by David Ngobeni who also gave guidelines on the proper usage of the software for better results.

Figure 4.14 shows the workflow that was followed in processing of the data. The *.TEM (Transient Electromagnetic Data: input data format of ZONDTEM1D) data should have the co-ordinates of each sounding, preferably in UTM (Universal Transverse Mercator) coordinate system. The data were then edited through a "data editor window" and bad data points, those that were evident as vast deviations from the rest of the points were manually removed (Figure 4.15). The data were edited station by station using a station editing window (Figure 4.15, right figure) removing the bad data points on the red apparent resistivity curve and the change is noted on the left figure of the data editing windows. Before making a starting model prior to inversion, the data were smoothed by applying a "denoise" function in ZONDTEM1D that removes individual spikes on sounding curves that may have been missed upon manual removal of spikes. An inversion was run after a geologically realistic *a priori* 'starter' model was created consisting of initially a 3-layer model with a thin, slightly conductive overburden, a more resistive 2$^{nd}$ layer and a highly resistive 3$^{rd}$ layer as dictated by the geological observations (Figure 2.10 and Table 5.1). The initial model is built with the intention of fitting the model curve to the observed apparent resistivity, $\rho_a$ (Figure 4.16). The discrepancy in the fit is taken care of by adjustment of the salient layer resistivity and thickness parameters through the inversion process.

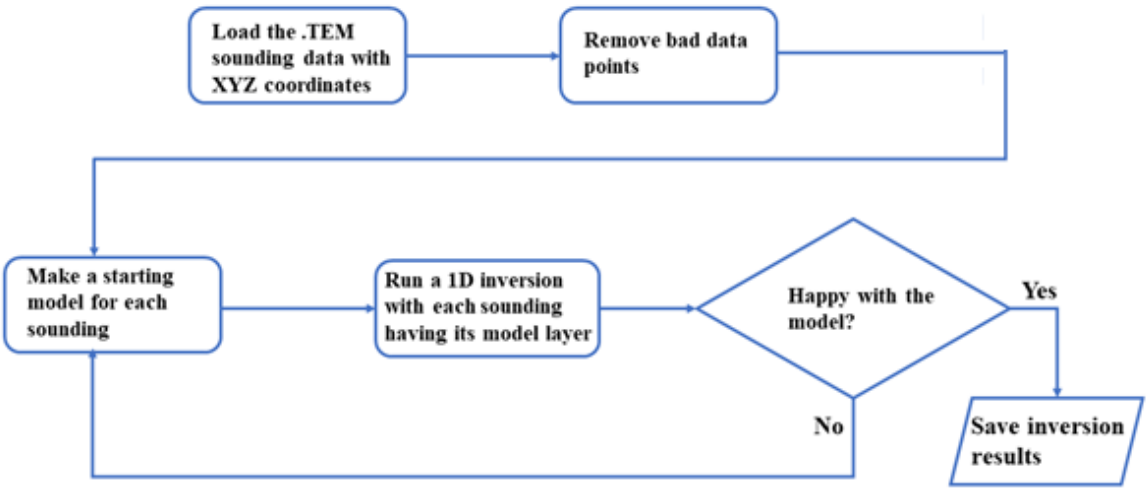



**Figure 4.14.** A flow chart model followed to process the TEM data

What then influences the decision of whether the inversion result should be kept or not? During the inversion, the layer thicknesses and the number of the layers needed to provide the best fit to the data are taken from the parameters table (Figure 4.16, bottom right corner) in which the values were input for the starting model. So, if the output of the parameters table shows a huge deviation from the initial table and does not provide any geological sense in terms of the layer thickness and resistivities of the layers, the inversion must be run several times until a geologically satisfactory model is achieved.

As already discussed in Chapter 2.4, a quasi 2D cross section can be produced from the software (see Chapter 5, Figure 5.26), which is a stitch of several 1D sections produced from the inversion. This is after satisfactory models are produced from the inversion. A cross section helps with the more qualitative interpretation of the data. The next procedure is explained in more detail upon discussing of actual data in the next chapter.

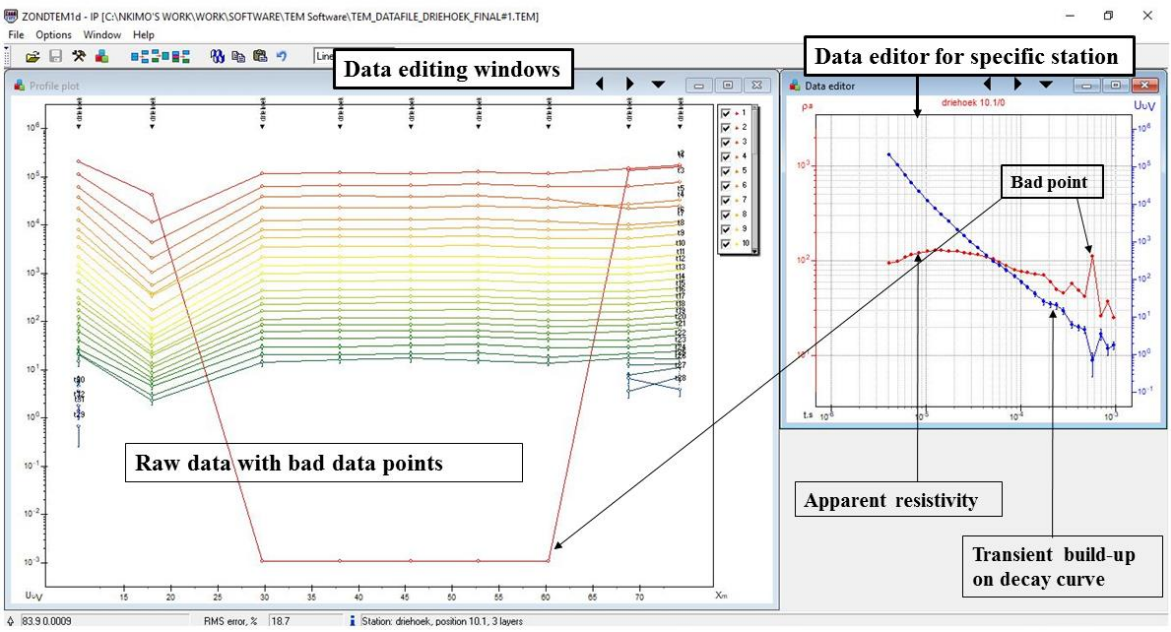



**Figure 4.15.** Data editing windows (ZONDTEM1D) that are used to remove bad data points probably due to superparamagnetic effects. Care must be taken not to erroneously remove points with information, only those believed, to represent noise. The frame on the right-hand side represents apparent resistivity (red axis) against time and transient response (blue axis) against time.

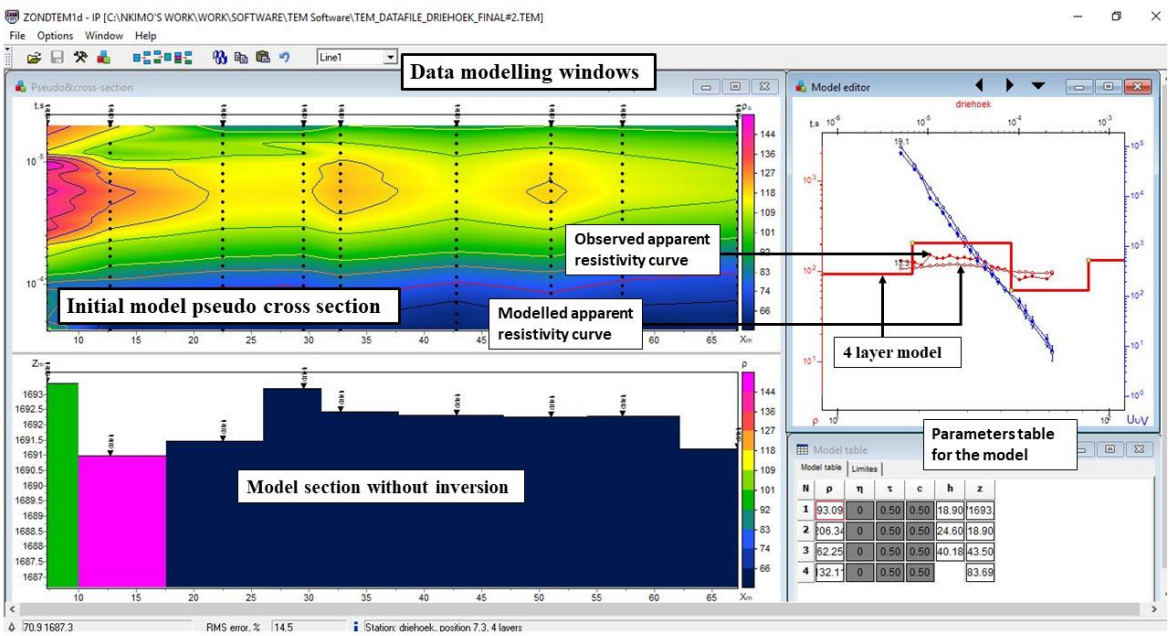



**Figure 4.16.** Windows used for forward modelling of the data. Top left is the pseudo section of the model, top right image is the **interactive** model that can be edited by clipping and moving the blocky red line that shows the layers thickness. Bottom left is the model section which is a response of the layered model as controlled by the top right corner. Bottom right shows the model parameters table whose values can be manually input for the initial model. These values are the number of layers **N**, depth to the layers **h,** the thickness of layers **z,** and 3 parameters not specified here namely the polarizability **η** of a layer**,** decay constant **τ** and conductivity **ς**.

## 4.5 Chapter Summary

This chapter focused on how the acquired geophysical data were reduced and processed. It entails crucial information which is necessary for the generation of the results going forward. Reduction of the geophysical data must be done with care because the rest of the interpretations and further processing will be based on how well or bad the data were reduced. The reduction of the microgravity data is very detailed because gravity data are known to require many associated corrections for quality data. As already mentioned, there are many factors that can affect the quality of the acquired gravity data.

The magnetic data are equally important to reduce like gravity data, but base station readings are not necessary for instrument drift monitoring as modern magnetometers have no intrinsic drift, but such stations are important for correcting diurnal variations (Kearey et al., 2002). Moreover, as a result of the modern magnetometers reading faster and not requiring precise levelling like gravimeters, magnetic surveys are quicker than gravity surveys and less errors are associated with them. Hence no detailed reduction procedures were listed. This is because after the application of the diurnal and geomagnetic corrections, the resultant magnetic field variations are a result of spatial distribution of subsurface magnetic variations and such are called magnetic anomalies (Kearey et al., 2002). The reduction of the TDEM was kept brief and more detail will be addressed when modelling the data in Chapter 5.

# CHAPTER 5 - DATA MODELLING AND RESULTS

## 5.1 Preamble

In this chapter the author discusses the results and how the observed field data were modelled but not making extensive qualitative interpretations as they will be done in Chapter 6. The data were forward modelled using geophysical property parameters such as density, magnetic susceptibility and resistivity to ultimately produce a probable 2D geological model.

A forward model is a theoretical or mathematical simulated response of the geology in terms of physical parameters used to calculate a geophysical response that produces a synthetic response for comparison with the actual geophysical measurements. It is also described as the direct modelling approach (Hinze et al., 2013). An acceptable model of the subsurface is described by how accurate the calculated model matches the observed data in both amplitude and shape.

A model may be deemed acceptable based on how well it reflects a true representation of the subsurface, but it does not necessarily guarantee a unique solution because a model is a mathematical simplification of the subsurface conditions and the model itself and the observed data always contain errors (Hinze et. al., 2013). In this chapter, a direct modelling approach of the field data will be considered for the reasons to be mentioned later. As Hinze et. al. (2013) state this so-called "forward or direct modelling approach" is especially appropriate when dealing with a relatively small dataset and a simple subsurface model where only a few unknown parameters must be evaluated as is the case here since the modelled block is a small volume of 13500 $m^3$ (9 m width, 50 m length and 30 m depth).

In order to produce 2-D models for both the gravity and magnetic data using Grav2dc and Mag2dc software respectively, grids of both residual gravity (obtained from the Bouguer anomaly) and total magnetic intensity datasets were overlain over each other in Geosoft as seen in Figure 5.1). Three lines trending from north to south were then extracted using Geosoft. These 50 m long lines were in a text file format showing both gravity (in mgal) and magnetic (in nT) data with the same X, Y, Z coordinates.

Why were these lines extracted from the overlain grids? Hinze et al. (2013) state that although modelling of individual results can give a best fit to the data, multiple solutions from different methods must be complimentary to each other and be compatible with the multi method of geophysical and geological information available. It must be noted however that there is no joint inversion of the microgravity and magnetic datasets. The advantage of extracting the profiles of both methods on the gridded data is that similar gridding parameters are used and so the coordinates of the extracted profiles will be the same. There is ambiguity potential fields modelling and part of it is that sources with a density contrast may or may not necessarily have direct magnetization or resistivity contrasts as dictated by the geology and as a result there may be magnetic/resistivity anomalies that can be matched. So, this raises here a need for modelling of both gravity and magnetic data to constrain possible geometries and develop an increased confidence in the results obtained from the modelling.

The workflow in Figure 5.2 summarizes the 3D modeling procedures. It must be noted that the 3-D models of both gravity and magnetic datasets have the same dimensions (distance axes, but not the anomaly axes) since they are extracted from the same location and have the same coordinates. This means that the magnetic data that are outside the gravity data region are not used in the interpretation. The Fortran codes (Figure 5.2) for Conreg.for, GmodIntrp.for and MagModIntrp.for were used with permission from the developer Prof. Edgar Stettler (Personal communication).

Six boreholes were drilled by the mine owner prior to the geophysical survey with the intention of intercepting virgin coal or determining if there is still good grade coal to mine at greater depths in the under-mined area. These borehole logs were provided by the coal mine owner but only one hole was near enough, about 70 m from the geophysical study area to provide constraints and a section was produced from the provided logs of borehole nearest to the survey area (BH001) as depicted in Figure 5.3. The rock layering according to the borehole log (Figure 5.3) is sandstones, shaley coal and coal. The log of BH001 does not provide much information about the adits and the coal seam which is observed at a depth of ~4 m in the cliff face (Figure 2.9) but only provides information about the existence of the sandstone in the first 13 m This could be that the old stopes (openings) are not logged, no significant core was recovered, or the seam was down faulted. The log was initially thought to be important to help constrain the depth to layers in the geological models and this is now not considered to be such reliable

information due to the reasons mentioned above. Also, the layers thicknesses from the borehole section are not vital since the section offers no record of depth where the targets reside which is within the first 10 m. The borehole is only useful for the knowledge of the lithologies encountered and that information is used to good effect in the models.

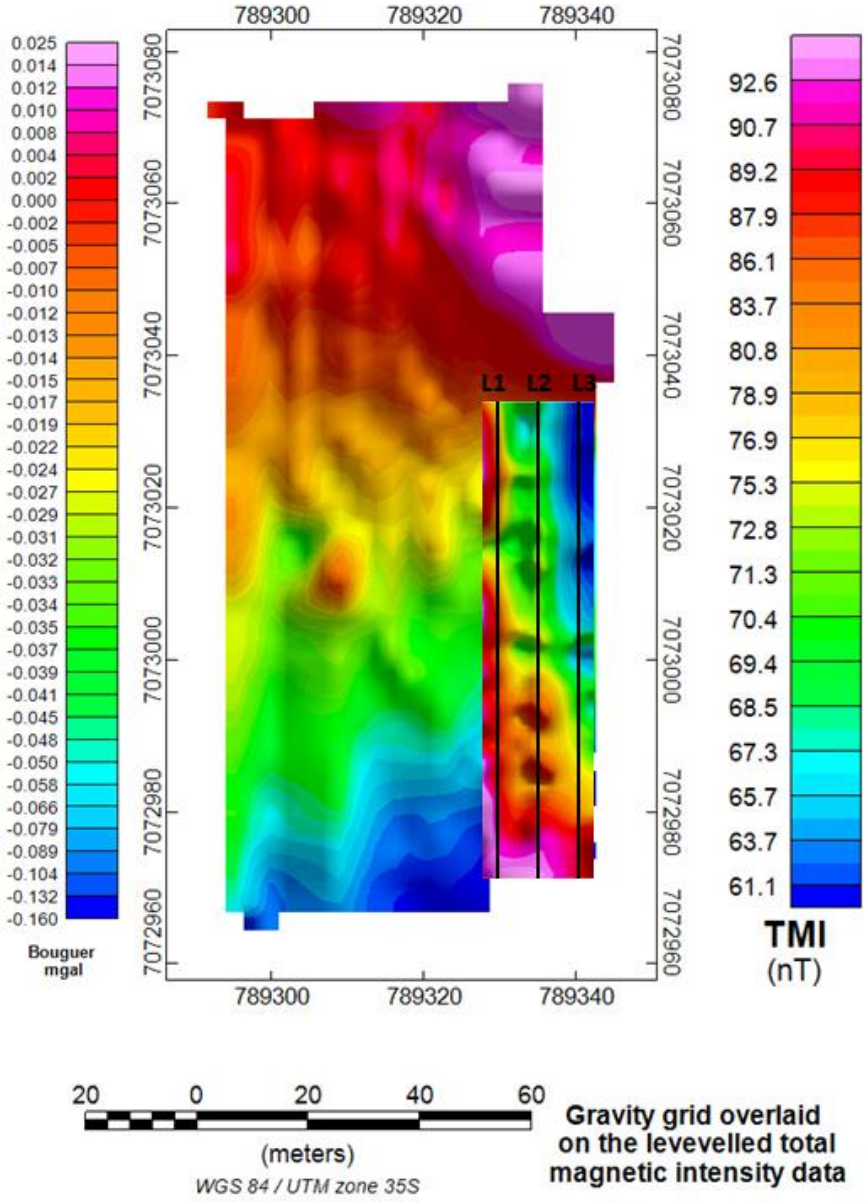



**Figure 5.1.** The sun shaded residual gravity map overlain on the total magnetic intensity map. The total magnetic intensity map's colour bar is on the right and the residual gravity map colour bar is on the left. Black lines L1, L2 and L3 are the lines trending north to south that were extracted from the gridded data and will be modelled with both Grav2dc and Mag2dc.

Due to the very small anomalies being studied, there was a need to remove a more refined regional field in all the gravity and magnetic traverses when modelling with Grav2dc and Mag2dc. The regional field was removed by using either the linear or the interactive cubic spline option that is fitted to the observed data to remove the background field (Section 3.1.3). A regional field has to be smooth with as little curvature as possible as dictated by the data and the geology. The regional field that is removed by the modelling software along different traverses during the modelling process can be reconstituted through the FORTRAN software Conreg (takes input the regional field data from either Grav2dc or Mag2dc), as a text file having X,Y coordinates with the regional field values for both gravity and magnetic data. The regional can then be gridded in Geosoft to depict the field that is removed, again if necessary smoothed and subtracted, and compared with the initial maps (with the regional field) to the residual data maps.

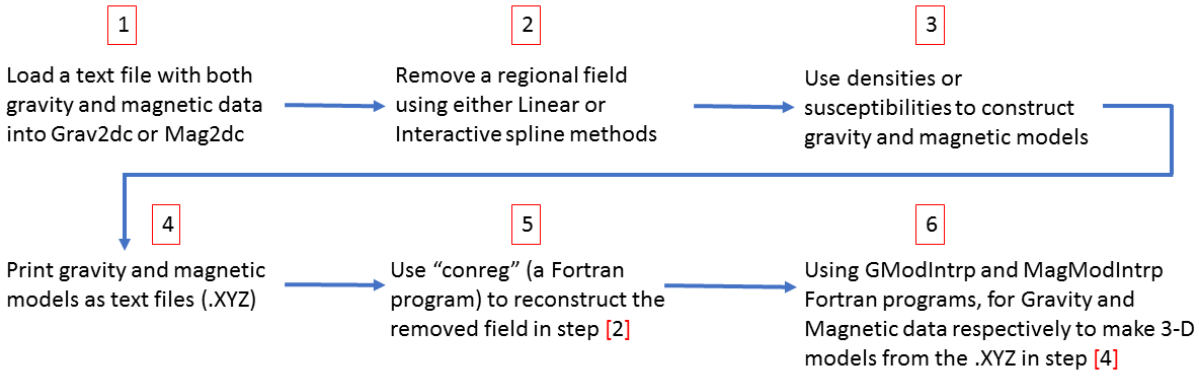



**Figure 5.2.** A workflow used to produce 3-D models of both gravity and magnetic data. The Fortran programs "Conreg", "GmodIntrp" and "MagModIntrp" are code written by Prof. Stettler and are used with permission from the developer.

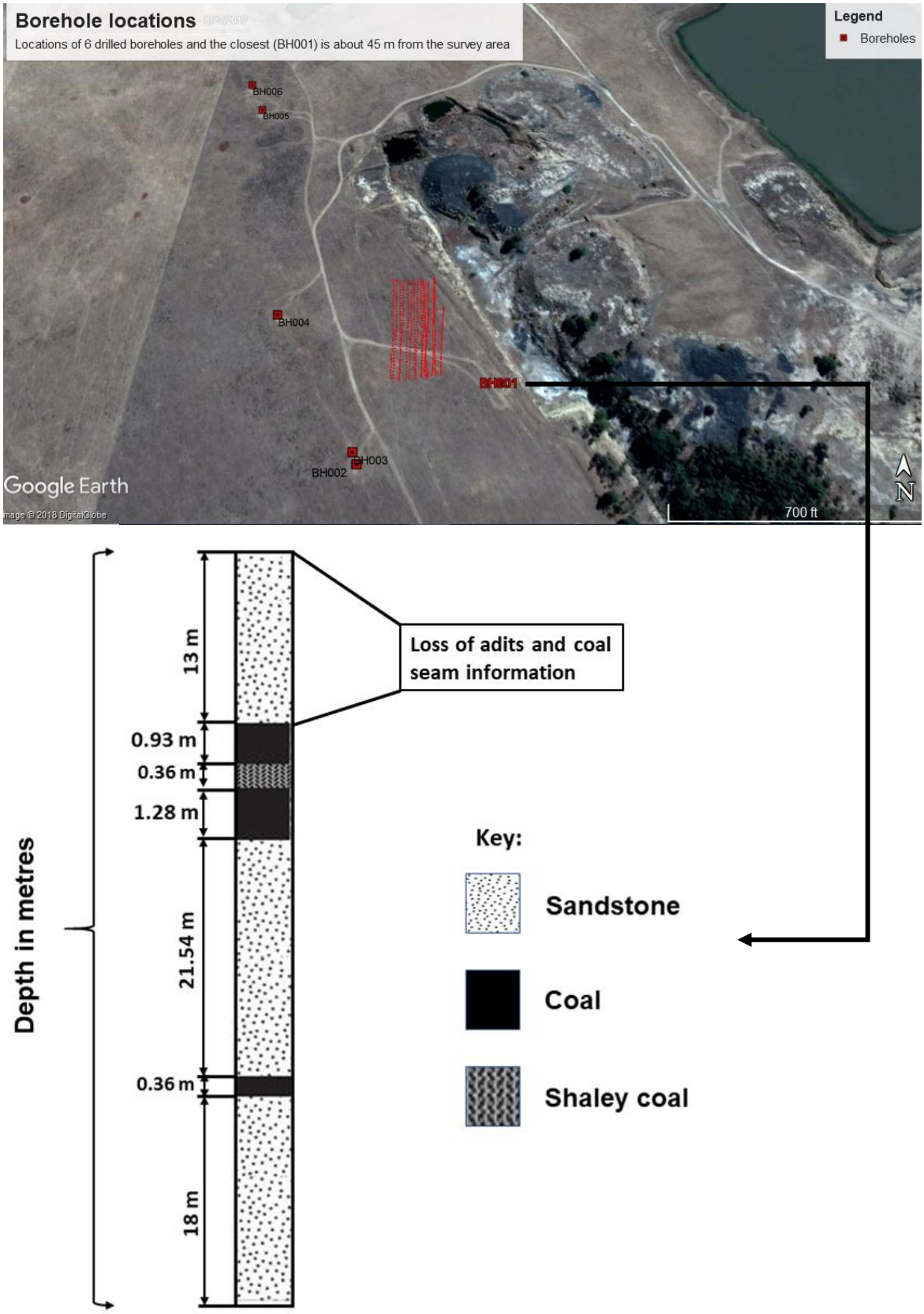



**Figure 5.3.** Borehole locations on the study area plotted on Google Earth marked with red squares. Borehole BH001 is closest to the survey area (red lines) and its log was used to make a vertical borehole section of thickness against lithological layering. The depth from surface of borehole BH001 is 55.47 m and only three lithologies were intercepted.

### 5.1.1 Lithological physical properties

The need to model the microgravity and magnetic datasets with the physical properties of the rocks present on site, physical property measurements were performed on collected samples to ensure the most realistic model of the subsurface and the determined parameters are given in Table 5.1. Although they did not appear to be altered, the samples were somewhat weathered (evident through low density values in Table 5.1) and did not give a true reflection of the physical properties that would be ideal for modelling. These physical properties of the weathered rocks were measured with the help of Dr Leonie Maré from the Physical Parameters Laboratory of the Council for Geosciences (CGS).

The 3 samples of about 4 cm diameter picked from the stopes on the study site, two sandstones and one coal sample were broken up into smaller parts. ESCODB and ESCODE are a shaley coal and the rest are sandstone and coal. From the results (Table 5.1) sandstone densities are evidently very low and do not resemble the known densities of sandstones. Thus, these sandstone data could not be used for modelling the field data. Instead, the data for modelling were acquired from the CGS database that is publicly available (Maré, 1997) using rocks from the database that are within the proximity of the study area and are of the same formation (Table 5.1).

**Table 5.1.** Physical properties of the highly weathered rock samples collected in the study area. Three samples were analysed for density, susceptibility and resistivity. The densities are suspiciously low which would suggest the samples' density data should not be used for modelling. Density is given in $g/cm^3$, susceptibility in SI units and resistivity in Ω.m.

| Sample from study site | Density ($g/cm^3$) | Susceptibility1 (SI) | Susceptibility2 (SI) | Susceptibility3 (SI) | Mean susceptibility (SI) | Resistivity Ω.m |
|---|---|---|---|---|---|---|
| Sandstone | 1.18 | 1.31E-05 | 1.14E-05 | 1.22E-05 | 1.22E-05 | 1.32E-03 |
| ESCODB | 1.89 | 1.05E-05 | 1.10E-05 | 1.08E-05 | 1.07E-05 | 1.43E-03 |
| Coal | 1.14 | 1.64E-06 | 3.84E-06 | 3.23E-06 | 2.91E-06 | 2.55E-03 |
| Coal | 1.66 | 8.24E-06 | 7.89E-06 | 7.88E-06 | 8.01E-06 | 6.11E-03 |
| ESCODE | 1.81 | 4.23E-06 | 4.42E-06 | 4.66E-06 | 4.43-06 | 1.22E-03 |
| Sandstone | 1.57 | 1.26E-05 | 1.23E-05 | 1.25E-05 | 1.25E-05 | 2.35E-03 |
| Sandstone | 1.57 | 1.30E-05 | 1.30E-05 | 1.22E-05 | 1.27E-05 | 2.53E-03 |
| Coal | 1.66 | 8.43E-06 | 8.07E-06 | 8.05E-06 | 8.18E-06 | 2.76E-03 |

The chosen sandstone of the Vryheid formation (Lat = -26.021, Lon = 29.450) from CGS database for modelling had the following physical property values:

- Density = 2.560 $g/cm^3$
- Resistivity = 364 Ω.m
- Susceptibility = $0.227x10^{-3}$ SI

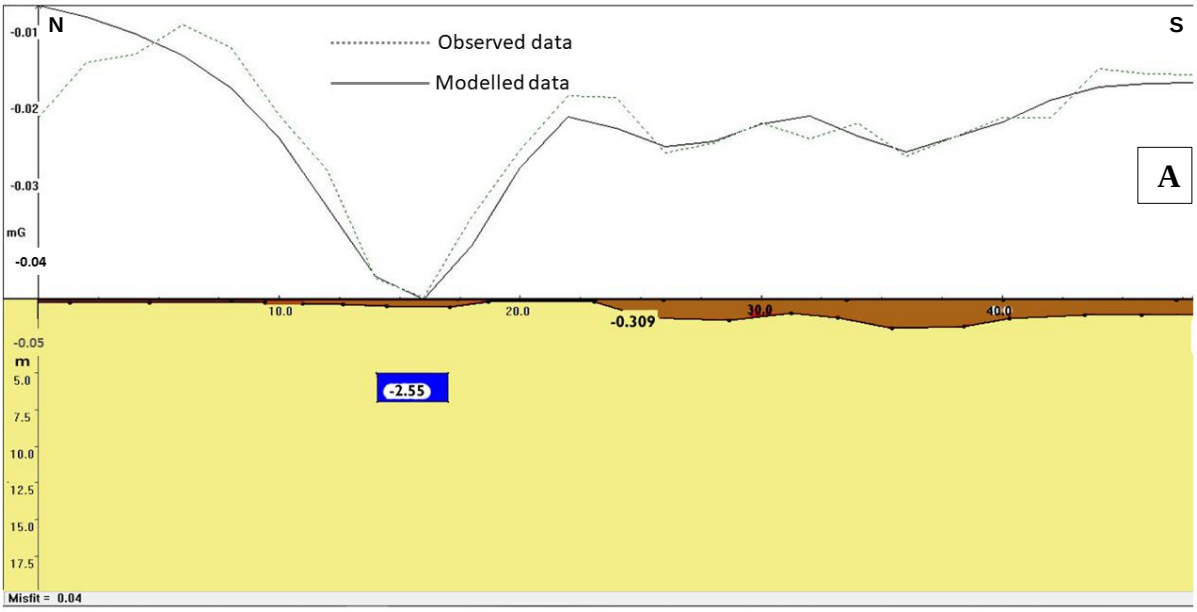
## 5.2 Microgravity

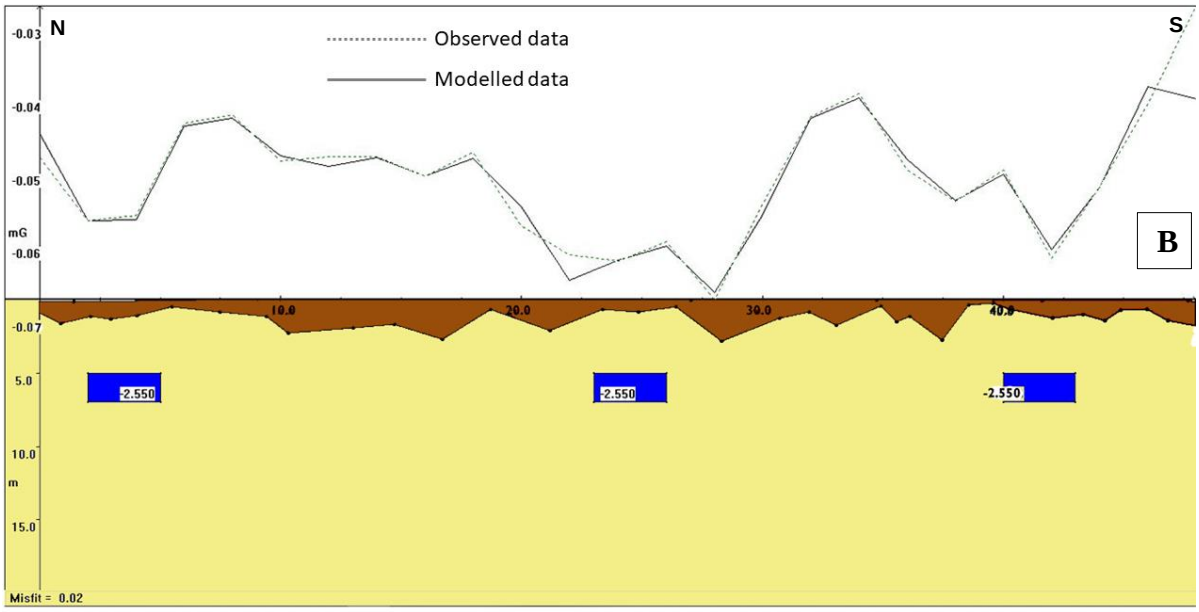
It must be noted that in the density model, the coal is not incorporated under the assumption that the tunnels lie within the coal layer that is almost entirely mined out especially to the roof as seen in Figure 5.4. Only the sandstone, the empty tunnels (filled with air) and the overburden were considered when making the gravity model.



**Figure 5.4.** A stope completely depleted of coal and only the sandstone layer left behind. The poles are used to support the roof. This shows why there was no need to include the coal seam in the models.

The three gravity lines L1, L2 and L3 were modelled using Grav2dc and steps 1 to 3 of Figure 5.2 were followed. The results of the modelled lines are shown in Figure 5.5. The tunnels (in blue) have a density contrast of -2.55 $g/cm^3$ and are within the sandstone layer (beige colour) which is the host rock. Initially, when direct modelling the causative bodies, the overburden (brown) density was taken to be 1.92 $g/cm^3$ (Telford et. al., 1990). But to fit the models, the overburden density varied between 2.24 $g/cm^3$ and 2.36 $g/cm^3$ as shown by overburden density contrast in Figure 5.5A and Figure 5.5C respectively. At first, these density values for the overburden were quite surprising and worrying to see that they are close to the density of the host rock, yet they are supposed to be very much lower (Telford et. al., 1990). However, looking at the geoelectric resistivity section in Figure 2.9, the overburden clearly shows that it is heterogeneous and has aggregations of highly resistive bodies. An increase in resistivity may indicate an increase in density, and conversely an increase in density often implies an increase in the electrical resistivity (Kamenetsky et al., 2010). This is also seen in Figure 2.9; the overburden is very thin and has a high resistivity. Thus, the effect and presence of the overburden in the models can be deemed reliable. The uneven overburden in the models can be attributed to the possible collapse and widening of the tunnels mentioned earlier. The overburden's thickness is taken from the reconnaissance electrical resistivity section shown in Figure 2.9 which importantly can now be used to constrain the gravity forward modelling. The overburden thickness in the resistivity section seems fairly flat and this is due to the spread length of 300 m and the electrode spacing that resolved depth more than the top layers. In all the models, the tunnels are at the same depth from the top of ±5 m as observed in the cliff face. The models cover a depth extent of only 20 m because the target cavities are shallow and do not occur beyond 15 m depth.


N
S
Observed data
Modelled data
A
-0.01
-0.02
-0.03
mG
-0.04
-0.05
m
5.0
7.5
10.0
12.5
15.0
17.5
10.0
20.0
30.0
40.0
-0.309
-2.55
Misfit = 0.04


N
S
Observed data
Modelled data
B
-0.03
-0.04
-0.05
mG
-0.06
-0.07
5.0
10.0
m
15.0
10.0
20.0
30.0
40.0
-2.550
-2.550
-2.550
Misfit = 0.02

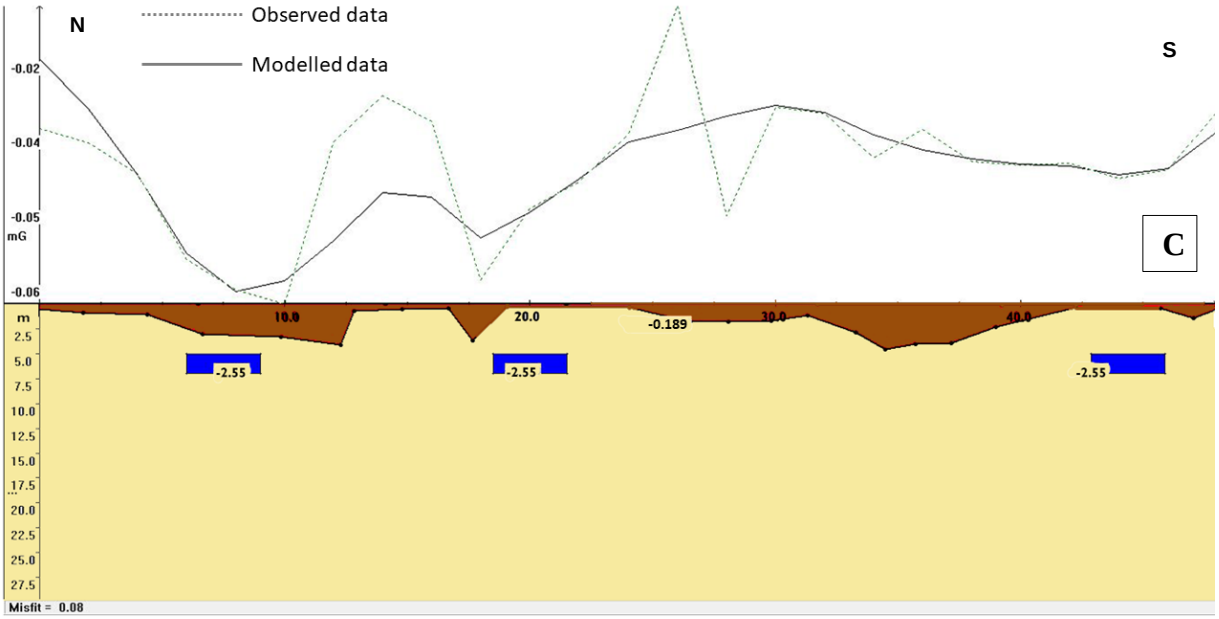



**Figure 5.5.** Gravity models showing a good fit to the data extracted from the grid for a postulated realistic geological scenario and known densities consisting of tunnels (in blue), sandstone (beige) and overburden (brown). (A) Is a model of line1 trending showing a single tunnel/void which gives an anomaly amplitude of about -0.045 mgal. (B) A model of line2 depicting three tunnels/voids giving a good fit to the measured gravity data and with the largest anomaly with an amplitude of about -0.065 mgal. (C) A best attained fit to the measured data with three tunnels/voids and the maximum response from one of the tunnels being about -0.063 mgal. The discrepancy between the observed and modelled gravity data in C is not as small as with both A and B and is ascribed to density variations in the sandstone not considered in the general geological scenario.

The models were then printed from Grav2dc as ASCII text files containing the corner points of all the bodies in the models. These corner points are used to construct first a model in vertical section consisting of a dense pattern of X, Y, Z, density values mimicking the original Grav2dc model. This is done through GModIntrp (personal communication with Edgar) in order to produce the data that would be visualized in 3D. When more than one parallel or semi parallel vertical section is available, they can be converted into a 3-D model by interpolating laterally between the vertical section models.

The second order regional field which is isolated and removed from the three individual modelling traverses is converted into a surface by interpolation. This second order regional field represents a smooth surface (Figure 5.6B). With the 2nd order regional gravity map

subtracted from the 1st order residual Bouguer map (Figure 5.6A), this presents the final residual microgravity map on which interpretations will be made (Figure 5.7).

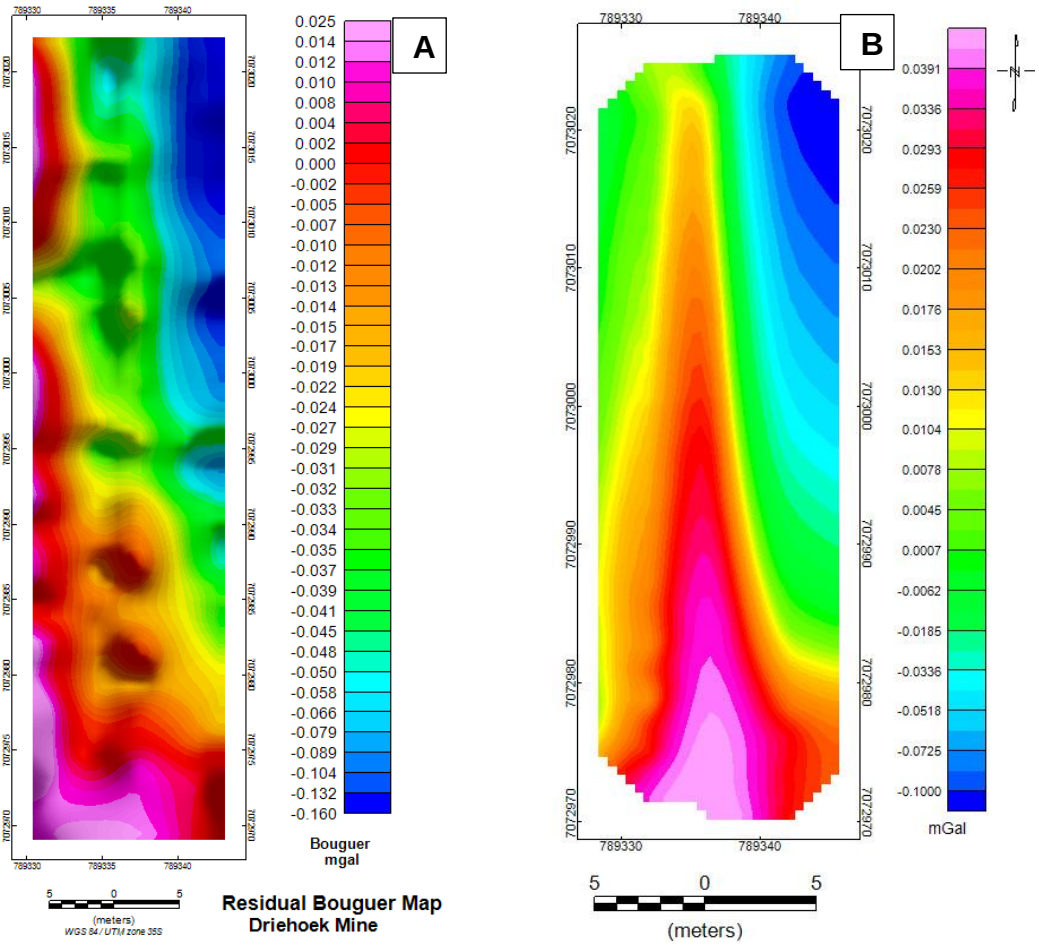



**Figure 5.6.** A) The artificial sun shaded BA map with 1st order regional field removed. B**)** The 2nd order regional field removed during modelling in Grav2dc, reconstructed with Conreg (as explained earlier) is subtracted from the BA map with 1st order regional field removed. The resulting surface of the 2nd order regional field **(B)** is not sun shaded. The resulting residual map is shown in Figure 5.7.

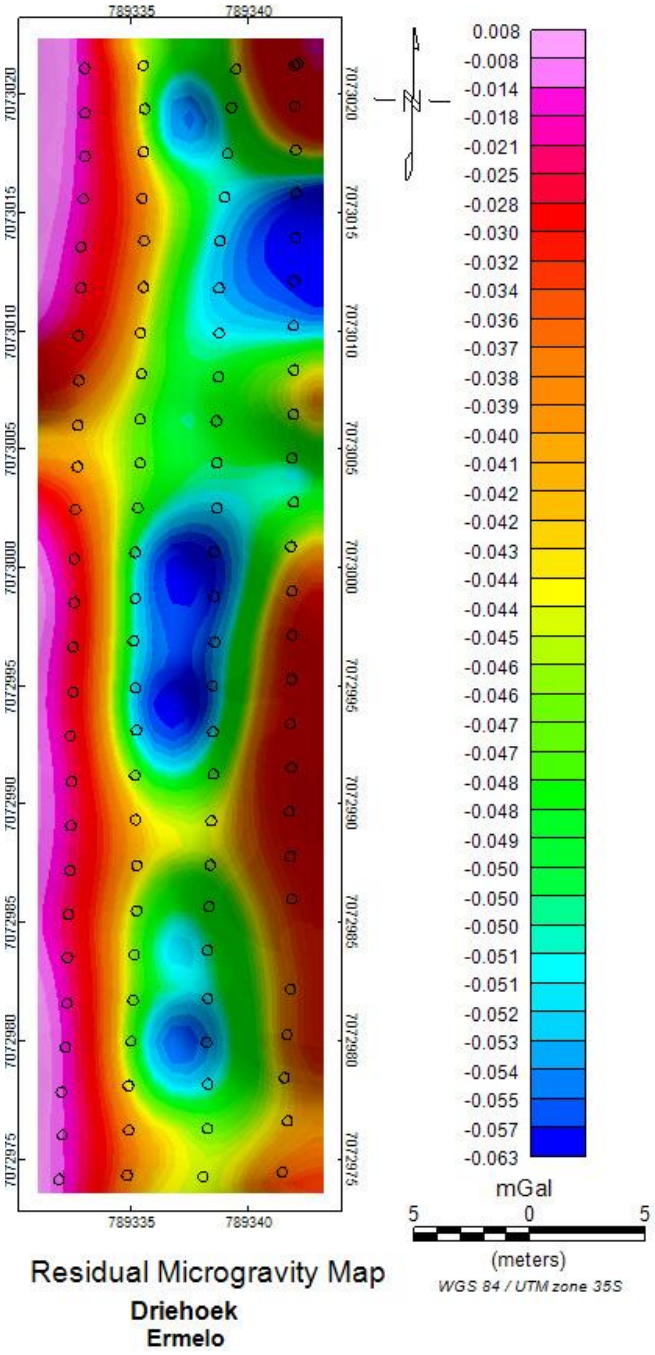



**Figure 5.7.** The sun shaded residual microgravity map devoid of any N-S trends on which interpretations will be made.

### 5.2.1 3D Modelling and visualization

FORTRAN code developed by Stettler, GModIntrp, takes output models from the Cooper developed Mag2dc and Grav2dc programs, discretizes the models to form a collection of much smaller cubes with centres having a unique x, y, z, density value to form a grid that describes each body best and to enable creating an x, y, z version of the bodies in the model. Importing these discretized models into Geosoft and gridding between the three traverses produces a 3D model of the density variations of the subsurface to give a better 3D visualization of the interpreted results and make geological sense of the data.

The x, y, z data sources produced from GModIntrp are layers of voxels gridded in Geosoft to produce a 3D block volume of the subsurface. The voxel model can be used as a 'starter model' for further inversion if so desired but would produce little or no improvement for this study. For this study, direct modelling of the observed field data is enough and 3D inversion of the data is not necessary for the reasons mentioned below:

1. If the inversion were to be done, when making the mesh to invert the microgravity dataset, a cell separation that is as small as possible must be used in order to produce a refined model. Unfortunately for Geosoft's voxi inversion, the minimum XY cell size is 10 m. The targets in this research are about 2 m high and 4 m wide. So, a 10 m minimum cell size will not constrain the inversion and aliase the model.

2. According to LaFehr and Nabighian (2012) the inverse problem does not usually give a unique solution. Thus, the interpreter of the data must decide, guided by certain tolerances which model gives the best representation of the geology being investigated. In this case the tolerances would be almost crippled because the minimum cell separation for the inversion software is bigger than the targets themselves.

To image the subsurface, the 3D voxel (Figure 5.8) was produced using an inverse distance weighting algorithm which is preferred for gridding variable potential field data and enabled in Geosoft (2014). The x, y, z data from GModIntrp were interpolated/gridded in Geosoft to

produce a voxel model. The voxel model was slightly filtered and then re-gridded to achieve a less blocky smoothly varying representation of the subsurface density and to fill minor gaps in the model. During filtering and re-gridding, there was to be no deviation from the initially gridded voxel and the filtered voxel, in terms of the geological representation of the model.

The residual microgravity map from Figure 5.7 is overlain on the 3D model, being topographically clipped since the interpolation technique acts in all directions even beyond the surface. In the 3D model, low density bodies are well preserved in the model. They can be more accentuated if portrayed as iso-surfaces, a tool allowed in Geosoft. These are illustrated in Figure 5.9 and Figure 5.10. The depth scale of the voxel is limited to 20 m as illustrated on the Z axis, as this is the depth interval in which the voids occur.

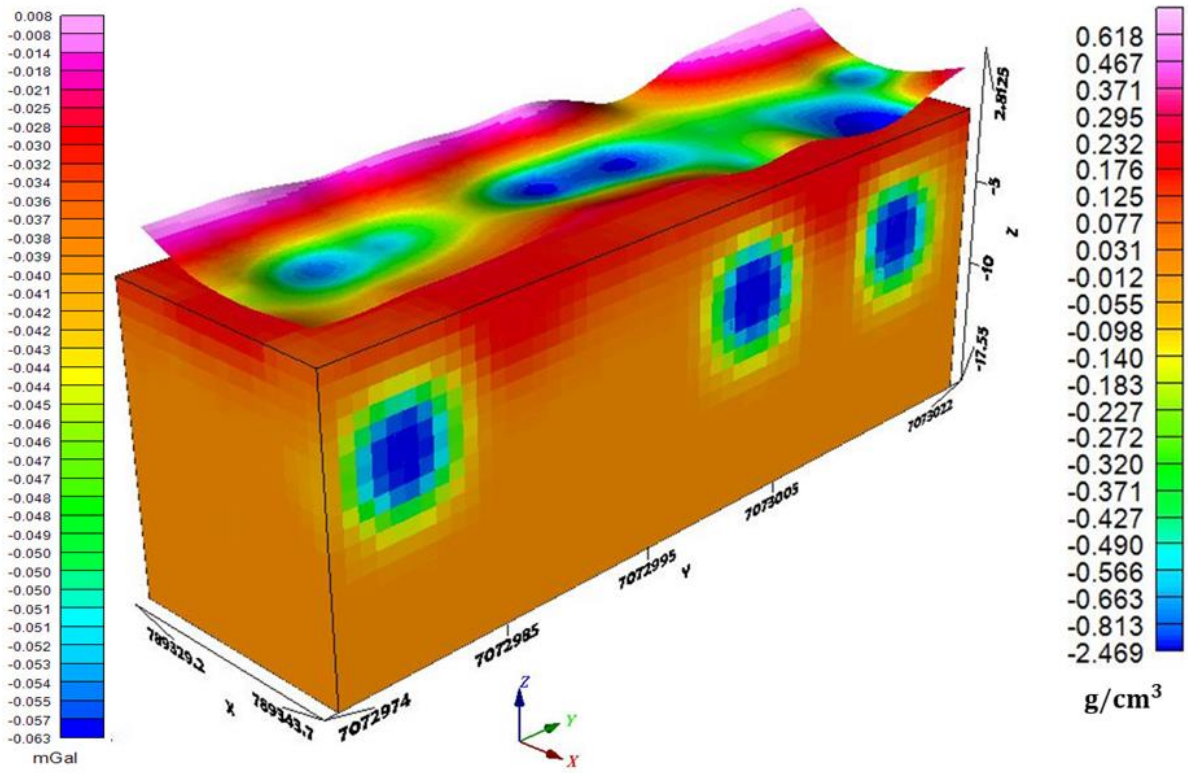



**Figure 5.8.** An inverse distance weighted GModIntrp voxel model imaged in Geosoft. It is a 3D representation of the half-space from the microgravity data models and above it, the residual microgravity map as a digital terrain data is overlain. The colour bar on the left is for the residual microgravity data while the one on the right represents the density contrasts within the model with respect to sandstone. The hot colours represent high density and cold colours represent low density values.

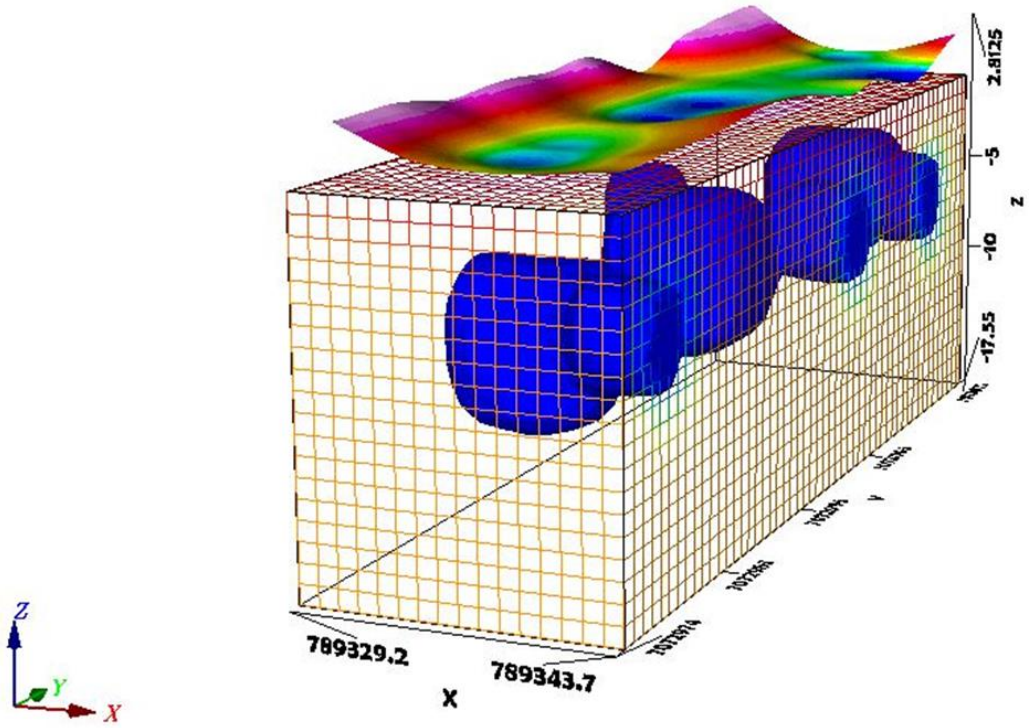



**Figure 5.9.** A 3D model showing the isolated iso-surfaces (blue bodies) that represent volumes of low densities preserved in the inverse distance weighted gridded model as seen in Figure 5.8.

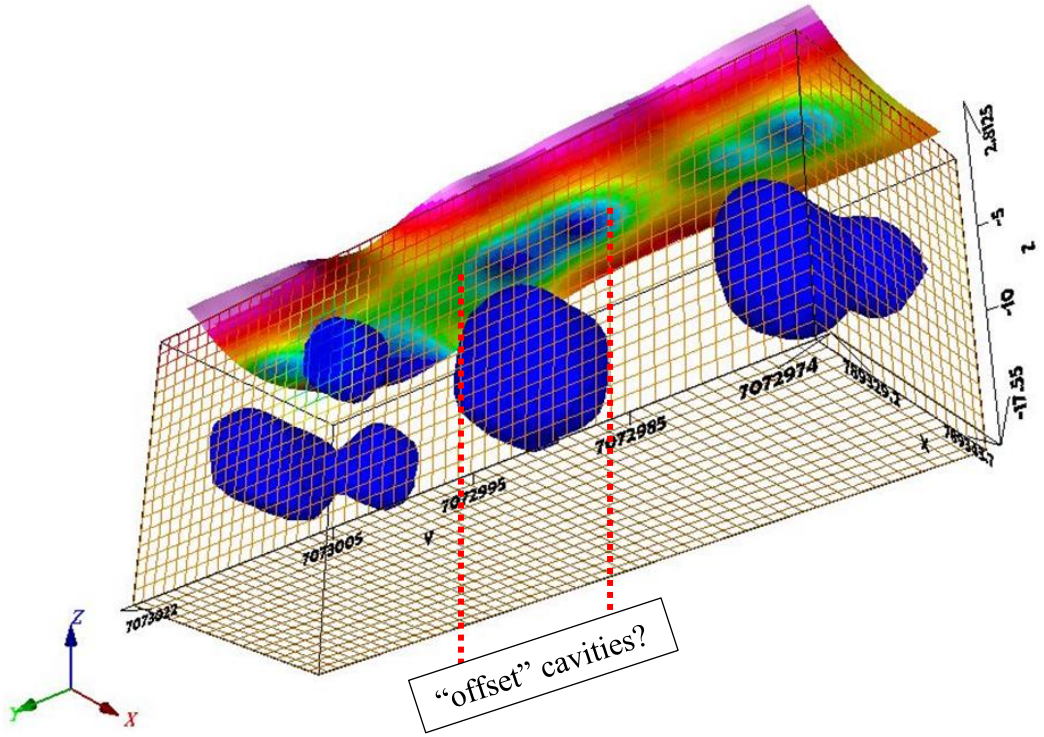



**Figure 5.10.** A 3D rotated model looking underneath shown from below looking upwards and the back showing the iso-surfaces. It is rotated to display the bottom alignment of the map with respect to the iso-surfaces.

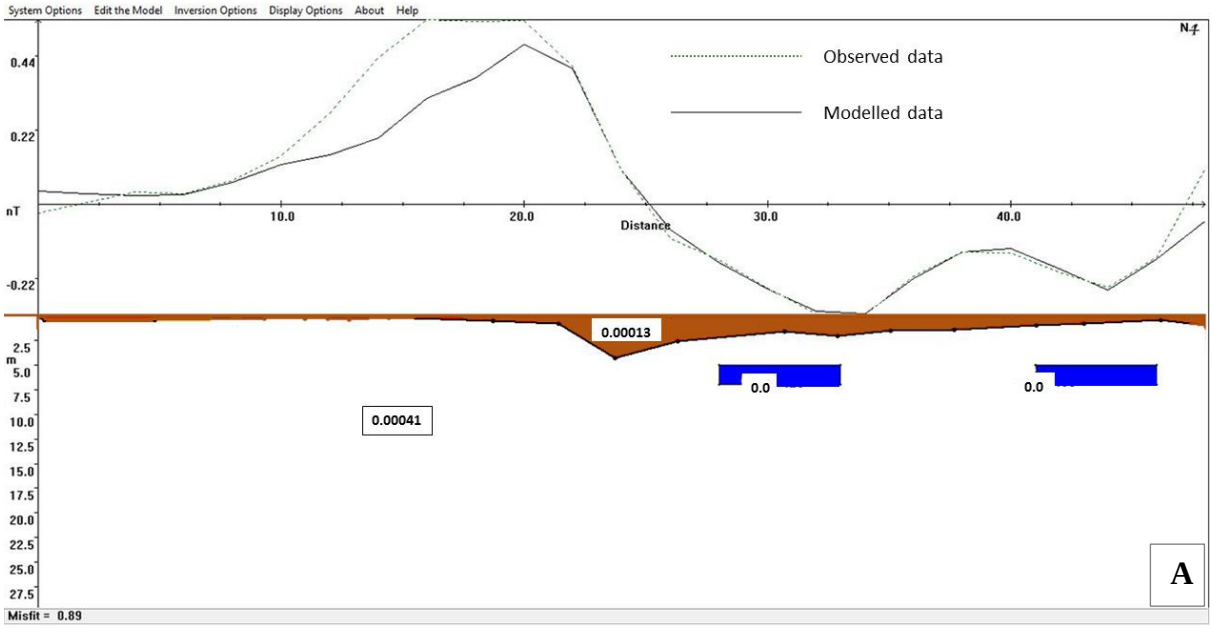
## 5.3 Magnetic Method

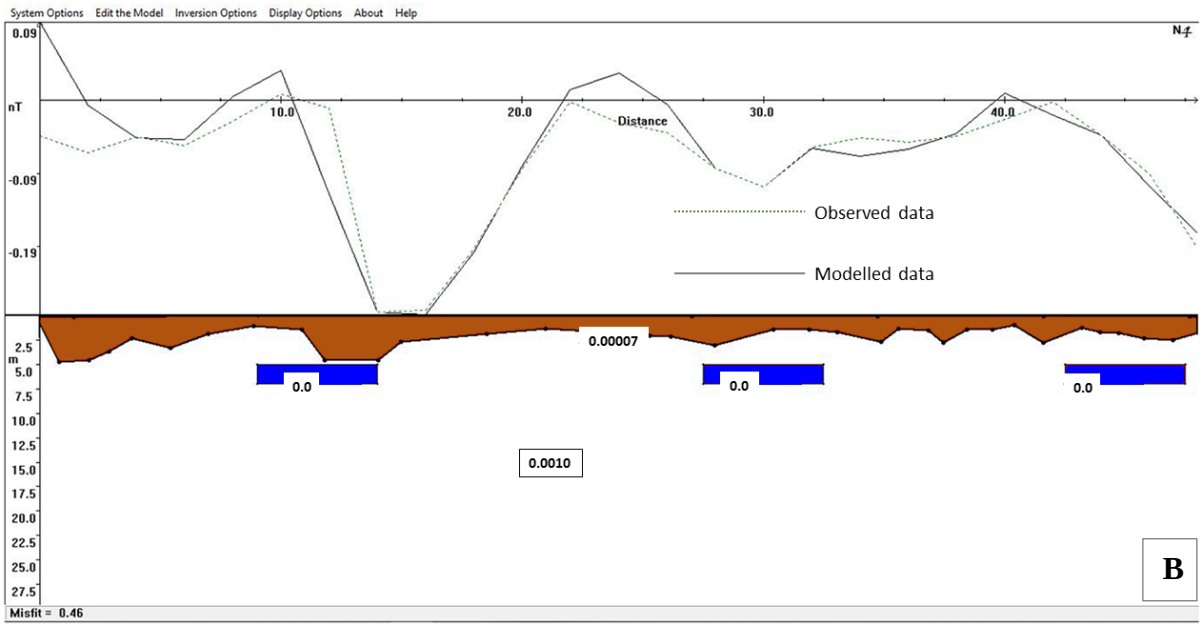
As was the case with the microgravity data, the magnetic line data for modelling with Mag2dc was extracted from total magnetic intensity map (Figure 5.1) along exactly the same lines as the gravity data. An assumption was made on the gravity models that the tunnels/stopes are within the coal seam which is almost entirely removed except where the pillars are still intact. That worked well for the gravity method because theoretically the only response would be due to tunnels (voids) and host rock, the voids manifesting themselves as the larger gravity lows.

With the magnetic method it is a different case. As previously mentioned in Section 2.1.4.2, pyrite and its decomposed minerals would give rise to a slight susceptibility increase providing a discernible magnetic susceptibility contrast (Bell et al., 2001). It would then be reasonable to assume the presence of the coal in the magnetic models especially the pillars. The target is not so much to delineate the pillars but the tunnels with modelling, and so the contrast would have to be between the tunnels (with susceptibility of ~0 SI), the sandstone (with susceptibility of $0.23x10^{-3}$ SI) and the altered coal (of susceptibility $0.01x10^{-3}$ SI) (Table 5.1). From these values, the coal alone does not offer an increase in susceptibility as does the sandstone. It was shown in Chapter 1 that the magnetic susceptibility between the host rock and the void/tunnel is the most important factor in being able to identify a signature possibly due to a void, and the larger the susceptibility of the host rock the more pronounced the signature. It will not be easy to discriminate between the sandstone and the coal since the coal collected in-situ had a susceptibility value that is less than that of the sandstone based on few samples.

The decision that the susceptibility of the sandstone should be used and varied to best fit the model was thus made when making the models (Figure 5.11). The contrast would be between the sandstone's variable susceptibility and the tunnels. Thus, the presence of the tunnels will be denoted by the low magnetic susceptibility on the models (Figure 5.11) and low magnetic intensity of the total magnetic intensity map. The overburden of varying susceptibility as seen in the models, was included and its thickness was also taken from the resistivity section (Figure 2.9). The interactive spline method was used to remove the regional magnetic field on the observed data when modelling. All three the lines L1, L2 and L3 were modelled using Mag2dc and the removed regional field was gridded in Geosoft (Figure 5.13). No comparison is done in this particular instance between the magnetic data and models (Figure 5.11) from their

gravity equivalents (Figure 5.5). Such comparison between the modelled lines will be made in Chapter 6.



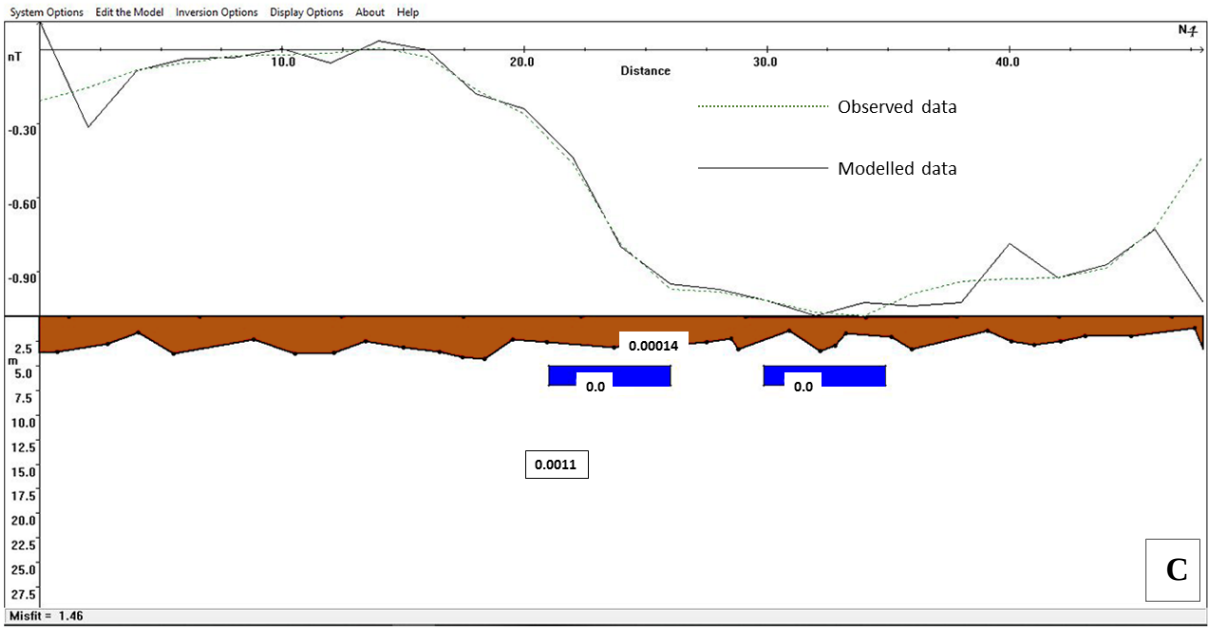



**Figure 5.11.** Model lines L1, L2 and L3 produced from Mag2dc. The tunnels (blue) have a zero magnetic susceptibility and the host rock was assigned a susceptibility that is a compromise between the coal susceptibility and the host rock's own susceptibility which provides a good fit to the measured data. The brown layer is the overburden included in the models with a very small susceptibility and average thickness of about 2 m. A) shows the model with two tunnels fitted and the total amplitude of the anomaly is about 0.66 nT. B) Three tunnels are fitted into the model with the biggest anomaly size of about -0.29 nT. C) Two tunnels are fitted into the model with the anomaly size of about -1.0 nT.

The magnetic method is not as commonly applied as the gravity method to delineate tunnels. In order to prove the validity of the models in Figure 5.11, a simple magnetic forward model was created by modelling a single tunnel within a sandstone host rock. This was to show that a tunnel within the sandstone host rock which is similar to what is evident from the field data, a magnetic anomaly would be produced. The forward model was made with similar properties to that of the observed visual field data. To prove the existence of the anomaly in these conditions, only one tunnel was modelled, and the anomaly size then quantified in nT with respect to the sensitivity of the magnetometer. The forward model in Figure 5.12 shows that the host rock with susceptibility of 0.002 SI, which is slightly higher than the models in Figure 5.11 which produces a slightly larger anomaly. To put all these models (Figure 5.11 and Figure 5.12) into perspective, Table 5.2 presents conclusions that can be made

**Table 5.2.** The magnetic anomaly responses observed from modelled magnetic data as a result of the tunnels' susceptibility contrast.

| | **Susceptibility contrast (SI)** | **Anomaly amplitude (nT)** |
|---|---|---|
| **Tunnel (Figure 5.11A)** | $-4.10 \times 10^{-4}$ | -0.25 |
| **Tunnel (Figure 5.12)** | -0.002 | -1.25 |
| **Tunnel (Figure 5.11C)** | -0.001 | -1.0 |

From the above, it is seen that the higher the susceptibility of the host rock, the larger the anomaly size. The forward model thus supports the confidence in the results of the modelled field data models.

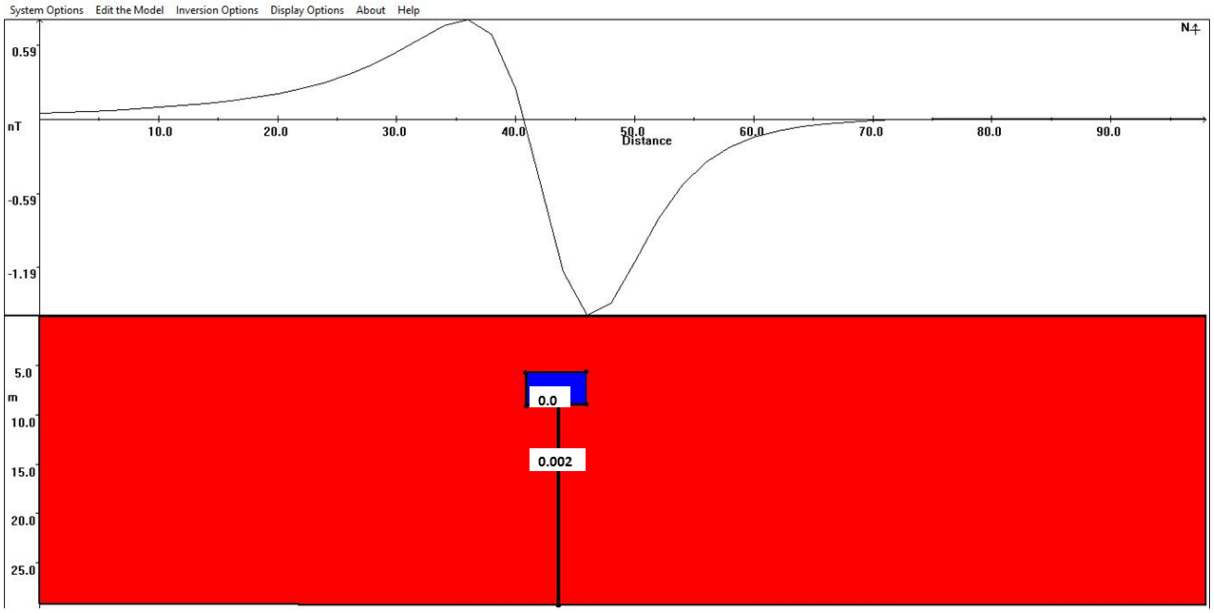



**Figure 5.12.** Forward model with a "hole" in the model aimed at validating the magnetic models based on the observed data. The model has a background rock in red, with a susceptibility of 0.002 SI, a tunnel of 0 susceptibility and an anomaly amplitude of about -1.25 nT.

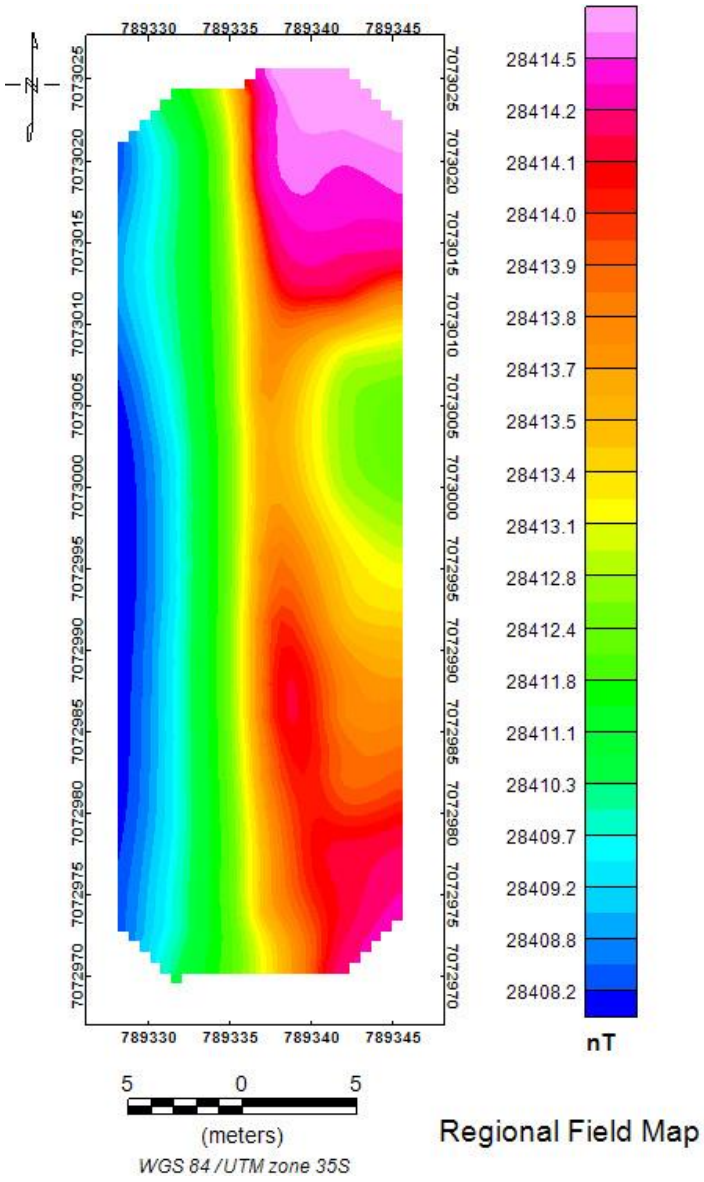



**Figure 5.13.** The regional magnetic field reconstructed from the Mag2dc modelled lines which were each 50 m long. It must be noted that this map covers the same area as the BA gravity map for consistency of interpretation and not the entire total magnetic field map

Figure 5.14 shows the diurnally corrected total magnetic intensity (TMI) map. Figure 5.14A is a diurnally corrected TMI map but has directional noise. Figure 5.14B is a diurnally corrected and levelled (levelling procedure as seen in Chapter 4) map .

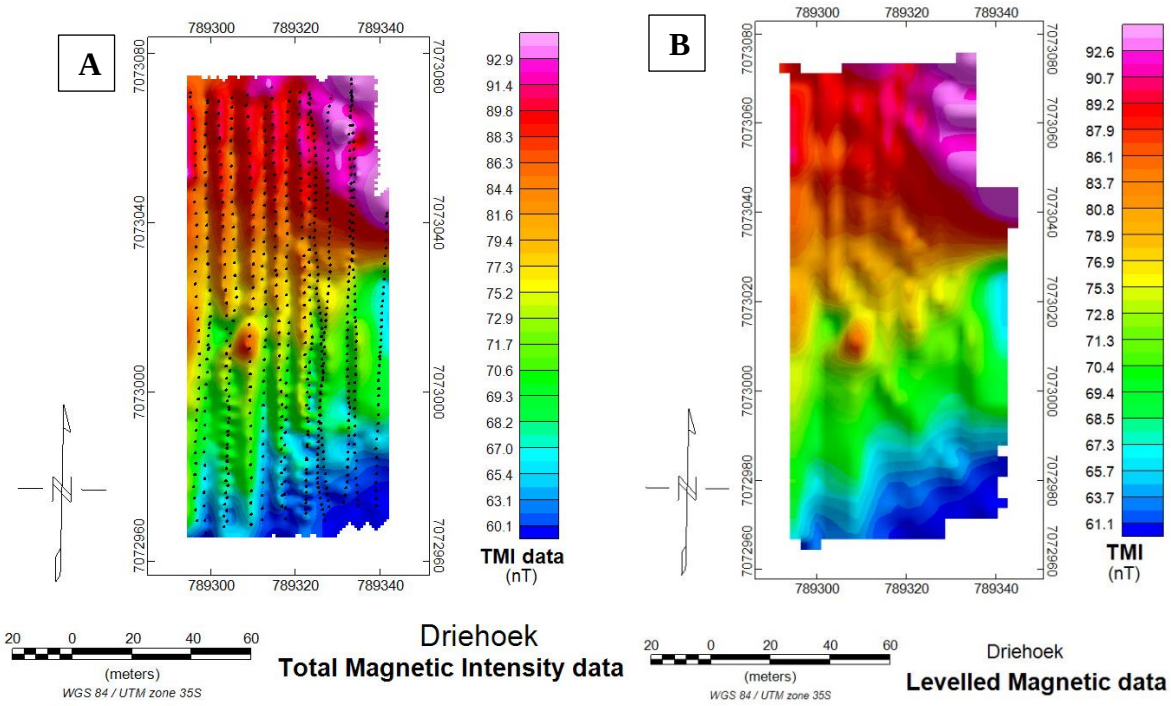



**Figure 5.14.** (A) Diurnally corrected artificially sun shaded total magnetic intensity map that has directional noise along the survey lines that is clearly seen as streaky lines in the data. (B) A levelled total magnetic intensity map exhibiting less or no streaks than seen on the unlevelled map. This micro-levelled map will be used in the interpretation of the data.

### 5.3.1 3D Magnetic Modelling and visualization

MagModIntrp, FORTRAN code written by Prof. Stettler does the same for magnetic data that GmodIntrp does for gravity data, but it uses susceptibility instead of density. The data produced from this program are an x, y, z, susceptibility ASCII text file for each modelled traverse and are an interpolation between the 3 traverses in Geosoft which creates the voxel model (Figure 5.15 and Figure 5.16). It must be noted that this is not an inversion model, but a 3D model produced from MagModIntrp and imaged in Geosoft. The inversion is not done for the same reasons as for microgravity data of minimum XY cell sizes to achieve a good resolution of small targets.

The gridding algorithm used is inverse distance weighting which is used for gridding variable data as found in Geosoft Oasis Montaj (2014). The voxel models are clipped on data to show the low-susceptibility regions (iso-surfaces) within the high susceptibility background (Figure 5.15). Figure 5.16 shows the 3D models which are additionally spatially clipped on the top of the z axis but still identical to the model in Figure 5.15. This was to show the orientation of the iso-surfaces within the high susceptibility background. The model in Figure 5.17 has the iso-surfaces preserved within the wireframe to show how the low susceptibility regions within the vicinity of high susceptibility background.

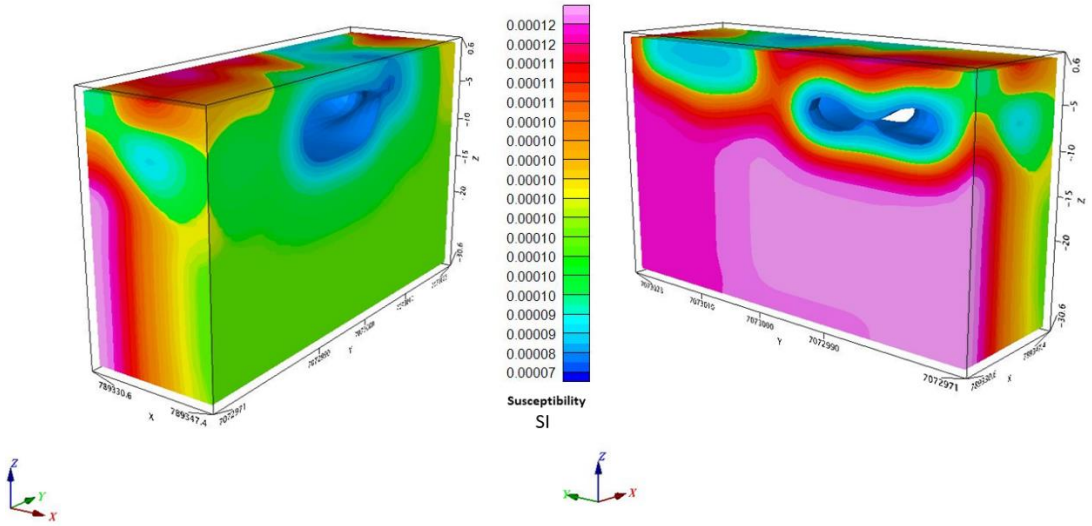



**Figure 5.15.** 3D models of susceptibility of the half-space interpolated between 2D magnetic data models. Both models are similar but rotated. The low susceptibility regions are clipped out of the model to visualize such regions within high susceptibility regions.

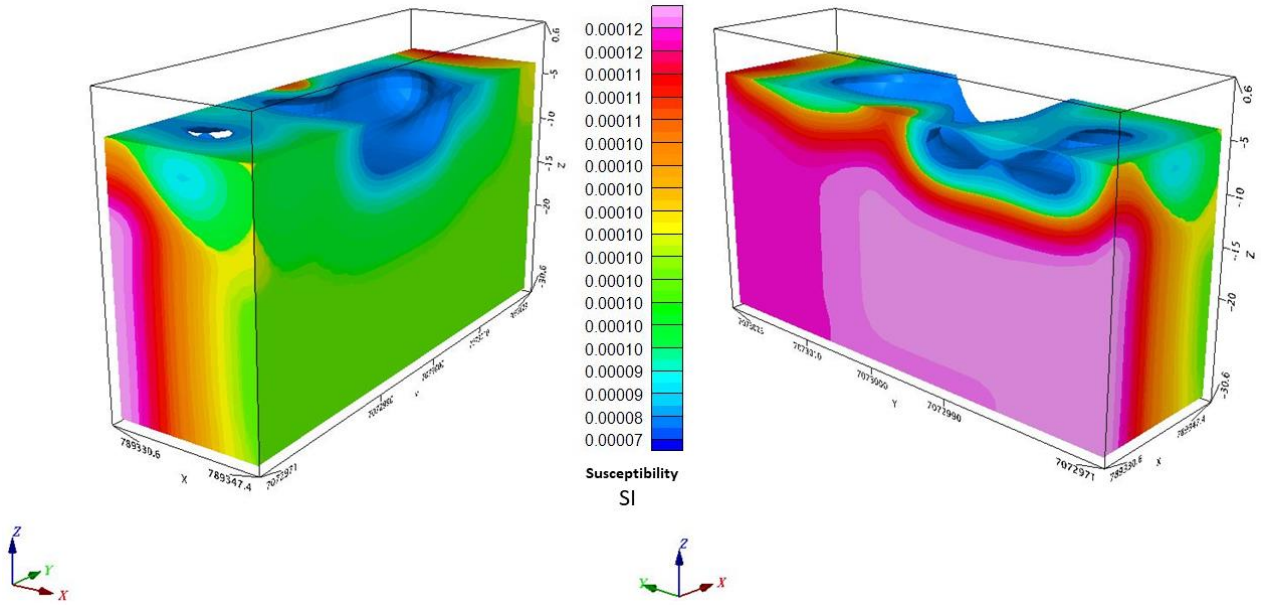



**Figure 5.16.** 3D magnetic susceptibility models spatially clipped at about the top -5 m to show the low susceptibility regions that are inside of the model.

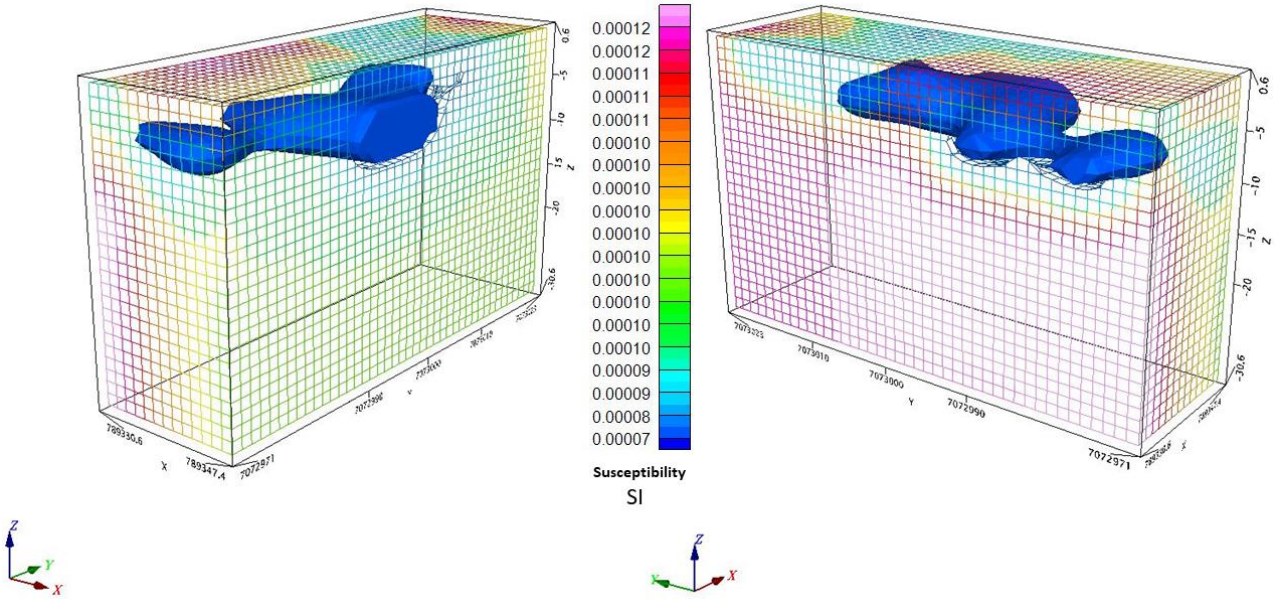



**Figure 5.17.** Models that are not filled but edge plotted and the low susceptibility iso-surfaces (blue bodies) preserved in the models. The iso-surface of ~7.0 x $10^{-5}$ SI starts at a depth of 5 m below the surface.

## 5.4 TDEM Method

### 5.4.1 TDEM modelling and results

Simple plotting of the decay curve of each TDEM sounding can aid in the interpretation and determine if the geology is homogenous or more complex (EM Geosci, 2018). For the time domain electromagnetic data, the voltage (d**B**/d**t**) recorded in the receiver loop always has an exponential fall-off curve that depicts the voltage decay with time (Figure 5.18). A fall-off gradient of 3/2 on log-log scale identifies a true layered earth (layering discretized with various resistivities).

This voltage decay against time relationship shows the response given by a subsurface resistivity distribution that is approximated by horizontal layers of different resistivities and thicknesses because it is mathematically the simplest (Nabighian, 2008). The resistive parts of the subsurface can be identified by giving a more rapid voltage decay with time while the conductors display a slower decay (EM Geosci, 2018). Converting the voltage decay curve against time to apparent resistivity against depth and then a layered earth model is called a 1D solution (Fitterman and Anderson, 1987). However, for a better geological model, many soundings are combined to give a 2-dimensional cross-section of the subsurface or 2D solution, or a 3-dimensional (3D) model for a comprehensive earth model. However, 3D-modelling is extremely computationally intensive and can take hours to create one model and only performed if warranted. Performing many soundings and interpolating between the many 1D solutions mostly also give satisfactory 3D models (Santos and El-Kaliouby, 2011; Cox et al., 2010). The 3D models are considered satisfactory if the inversion outcome gives realistic layer parameters such as resistivity and thickness that were fed into the initial model. These values would also be compared with the lithological physical properties.

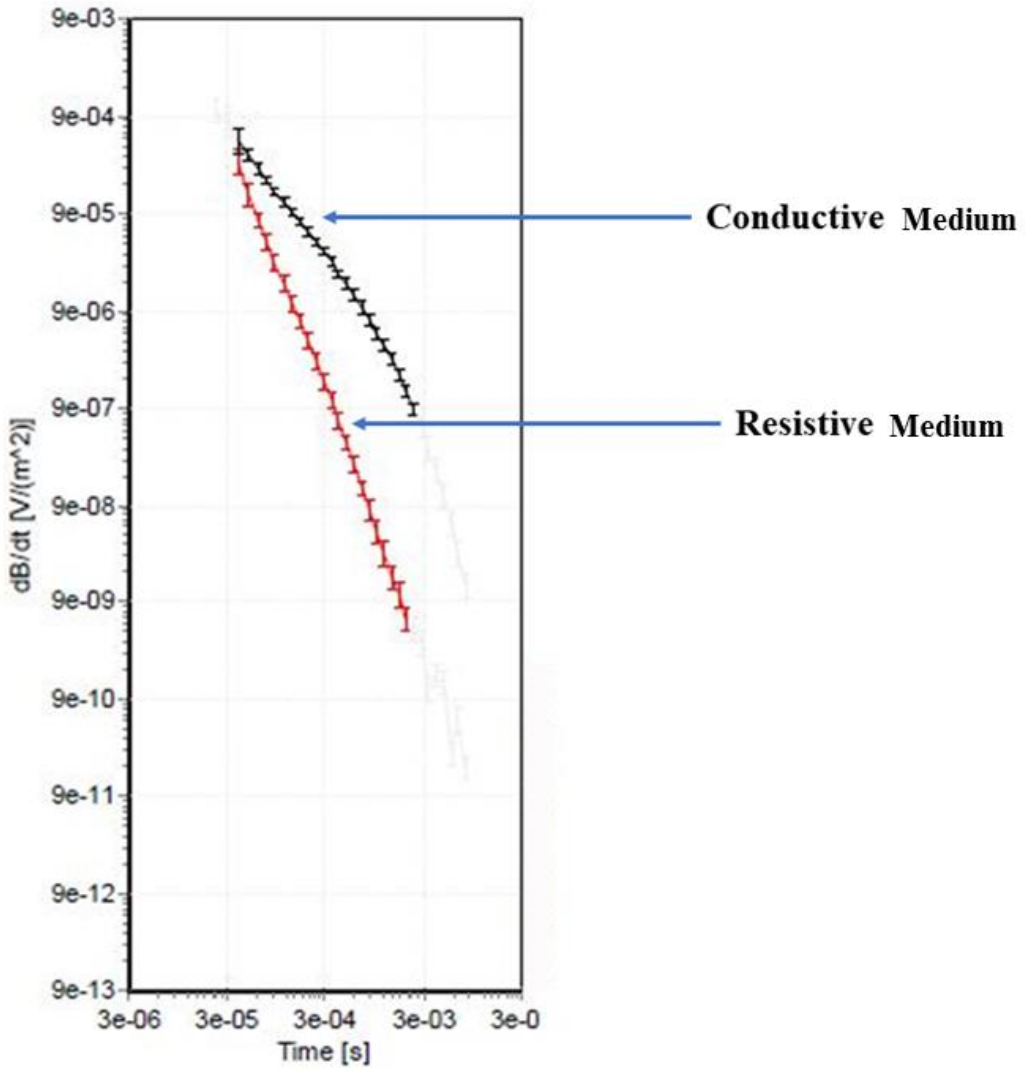



**Figure 5.18.** An example taken and modified from Cooper and Munday (2012) showing the relationship between the voltage decay with time. The decay is rapid/sharp on resistive ground (red curve) and slow/smooth on conductive ground (black curve).

Another first order quantitative approach for interpreting the decay of the voltage with time is called time channel analysis (EM Geosci, 2018). This interpretation helps primarily to discretize the layers even before the inversion of the data is made and is a means of quality control of the data. Using the idea of exponential curves as a function of time (as shown in Figure 5.18) to distinguish the resistors from the conductors, the time channel method shows various layers of different thickness and resistivity with depth (EM Geosci, 2018). For instance, in Figure 5.19, the decay curve of d**B**/d**t** between time channels 0 to 20 and 50 to 60 show strong resistive layers denoted by a steep slope, while time channels 25 to 50 show a more conductive layer denoted by a smooth slope that is concave.

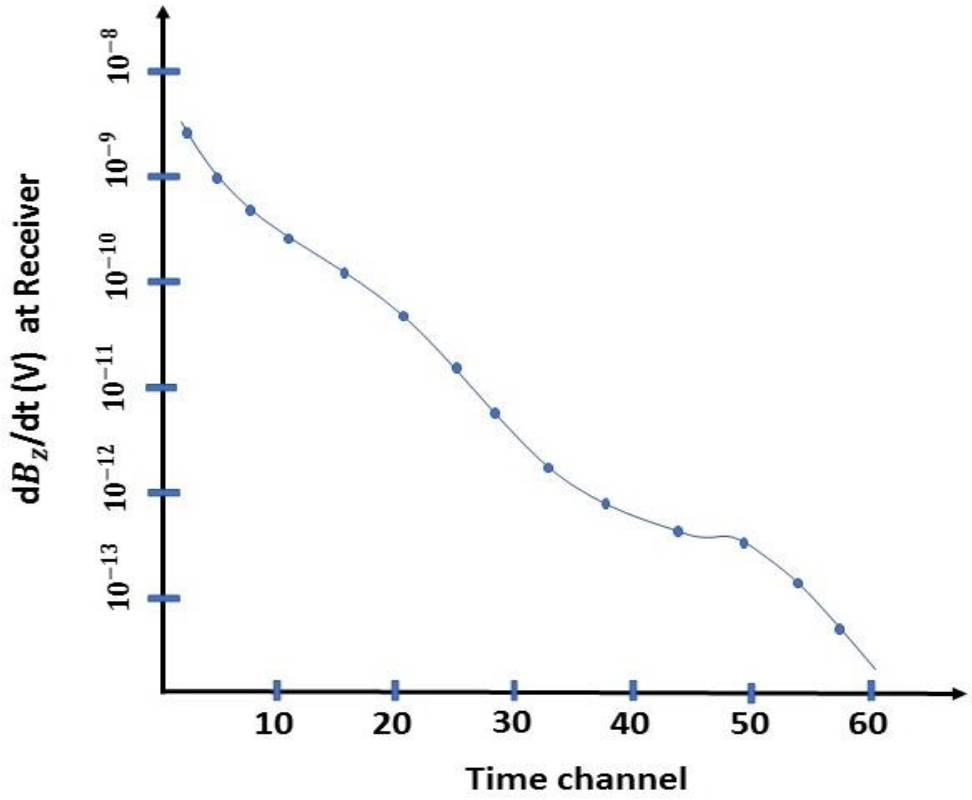



**Figure 5.19.** A representation of "conductivity" equated with the rate of decaying voltage (emf) against "depth" equated with increasing time channels (Modified from EM Geosci, 2018). "Conductivity" (vertical axis) gives an average "conductivity" of the half-space, subsurface and its variation with depth (increasing time channels) of different successive layers and can give a conductivity depth image, or CDI as it is known.

Time channel analysis theory was applied in this study when modelling the data using ZondTEM1D software. In ZondTEM1D, this analysis is made on a window called the Data Editor (Figure 5.20) which depicts observed curves of apparent resistivity in red and measured electromotive force (EMF) or transient response on the decay curve on the blue axis. From this data editor window, the model editor window (Figure 5.20) is used to change the observed apparent resistivity and/or thickness of the layers. Then from it, unlike in the case of using voltage decay as shown in Figure 5.18 to discriminate between the conductive and the resistive layers, apparent resistivity is used to distinguish between the respective layers. An increase in calculated resistivity with depth will denote a resistive layer while a decrease in calculated resistivity with depth will denote a less resistive or conductive layer. This analogy is used in the data interpretation of sounding curves before the interpretation can be made on the total imaged data along a traverse.

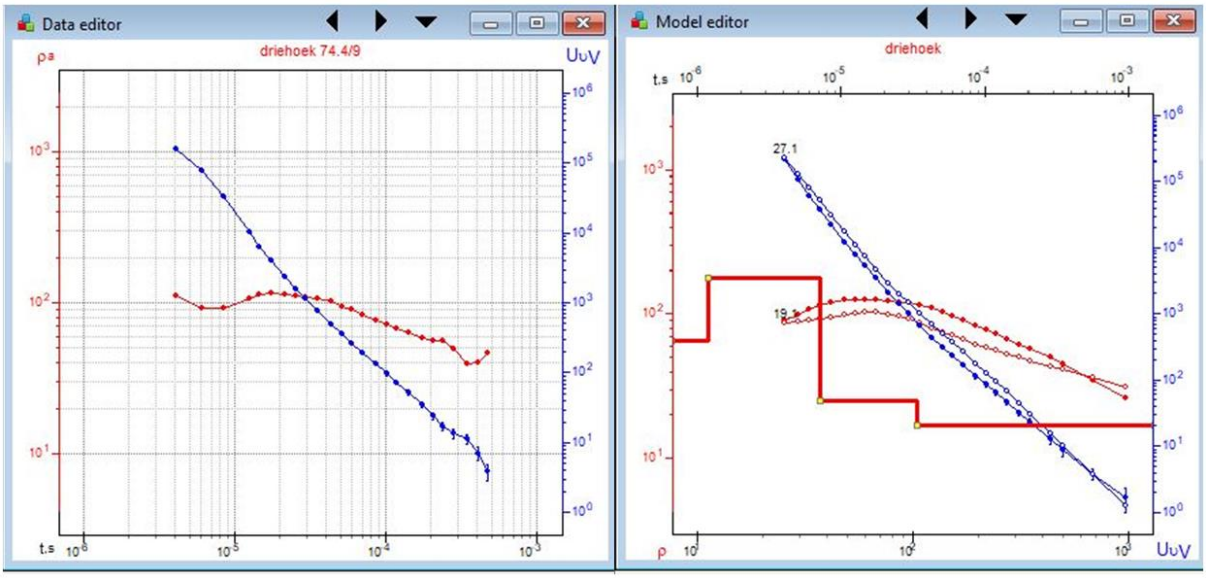



**Figure 5.20. Left**: Data editor window used to clean the observed transient build-up (blue axis) and apparent resistivity curves (red axis). **Right**: Model editor window used to calculate the resistivity and transient behaviour from the observed curves. The bottom axis shows model depth in metres. The blocky red solid line indicates the layered earth model where the vertical sections indicate changes in layer resistivity and the horizontal sections layer thickness (Taken from ZondTEM1D manual, 2017).

A comparison of the measured sounding data and the sounding model master curves within a horizontally layered medium guides the quantitative interpretation of the TEM data through a curve fitting method called inversion (Kamenetsky et al., 2010). The advantage here is that a 'starter model' is created by manipulating the solid red line (Figure 5.20, right figure) and that *a priori* information can be supplied for the starter model. Moreover, there are other qualitative methods of interpretation known as imaging; these are based upon numerous differential transformations of the transient signal (Kamenetsky et al., 2010). Transformation of the time-dependent signal to the apparent conductivity as a function of depth is achievable by placing an imagery current filament in the subsurface and moving it downwards from the surface and through simplified mathematics (Nabighian, 2008). The next step is to calculate the current and resistance necessary in the filament to match the response seen in the time channels at each sounding station and once the current is known, the resistivity can be determined and imaged (Nabighian, 2008).

The data were inverted using apparent resistivity because it aids in choosing the parameters of the layered model. Using the results of the reconnaissance resistivity survey (Chapter 2), the

layer thicknesses and resistivities obtained were used as the starter model parameters in the table using ZondTEM1D as shown by a box on the bottom right corner of Figure 5.21. It should be noted that the electrical resistivity is a variable parameter because the electrical resistivity of the subsurface materials is affected by several factors some of which include but are not limited to porosity, moisture and clay content (Kamenetsky et al., 2010). The variation in resistivity as a result is seen to range from $10^{-8}$ Ω.m to $10^{5}$ Ω.m or even $10^{6}$ Ω.m.

The targets in this study are very shallow and so the late time channels were not considered. Most of the late time channels in the soundings between $10^{-4}$ and $10^{-3}$ ***s*** were noisy anyway as shown in Figure 4.15 on the data editing windows, marked as "bad points". This is the behavior that is normally anticipated in the TEM method for small loops (AEMR, 2002). Late time channels depict the deeper structures but as the EM field weakens, the signal to noise ratio decreases (AEMR, 2002). With small loops TDEM data may also display the effects of superparamagnetic soils or induced polarization (distorted transients) on the signals (Descloitres et al., 2000) but for geological reasons such as clayey lithology and disseminated sulphides this is not expected here. This behavior is consistent for most of the stations and every station's sounding was edited to remove the late time channels.

There are 20 soundings along the traverse. The first sounding was used as the starting point for the complete inversion of the TEM traverse and the process is illustrated by the ZondTEM1D screen dump in Figure 5.21. It is divided into 3 horizontal panels where the upper panel gives the variation in resistivity along the profile (distance) and time down the medium, the middle panel the layered earth representation for each sounding and the lower panel is where three soundings adjacent to one another (for easy comparison) and the parameter matrix is found. The first sounding is represented by the coloured layered section block on the left side of the middle panel of Figure 5.21. The middle panel in this figure shows a model layered section and it has different levels due to small topographic variations denoted by the elevation scale on the left in metres. The left part is coloured because for this first sounding the apparent resistivities and thicknesses of the layers are professed to be known. This first sounding is used as a 'starter model' and fits into the model editor window (the first of the three windows on the bottom left of Figure 5.21), while the rest of the section is not coloured because the sounding parameters are not yet entered into the model editor (the next two windows and many other on the bottom left panel). So, the model was built for this first sounding with the parameters extracted from

the resistivity geoelectric section and entered into model table shown in Figure 5.21. The starter model initially had 4 layers (indicated by a red blocky solid line on the bottom left of Figure 5.21) and a misfit of 32.6% before the inversion. The top panel shows the quasi-2D section of apparent resistivity with respect to time and distance. This panel illustrates the response obtained from assigning resistivity and thickness parameters to the 3-layer model on the left side of the middle panel. Once a reasonable fit between calculated and measured apparent resistivities is obtained the model is inverted (using least squares inversion as found in the ZondTEM1D software) with or without constrains. The final response obtained from the inversion is shown in Figure 5.26. It is the result on which the interpretation will be made. The apparent resistivity is represented by the colour bar on the right of the top panel. The left axis shows time in seconds and the bottom horizontal axis shows the distance in metres.

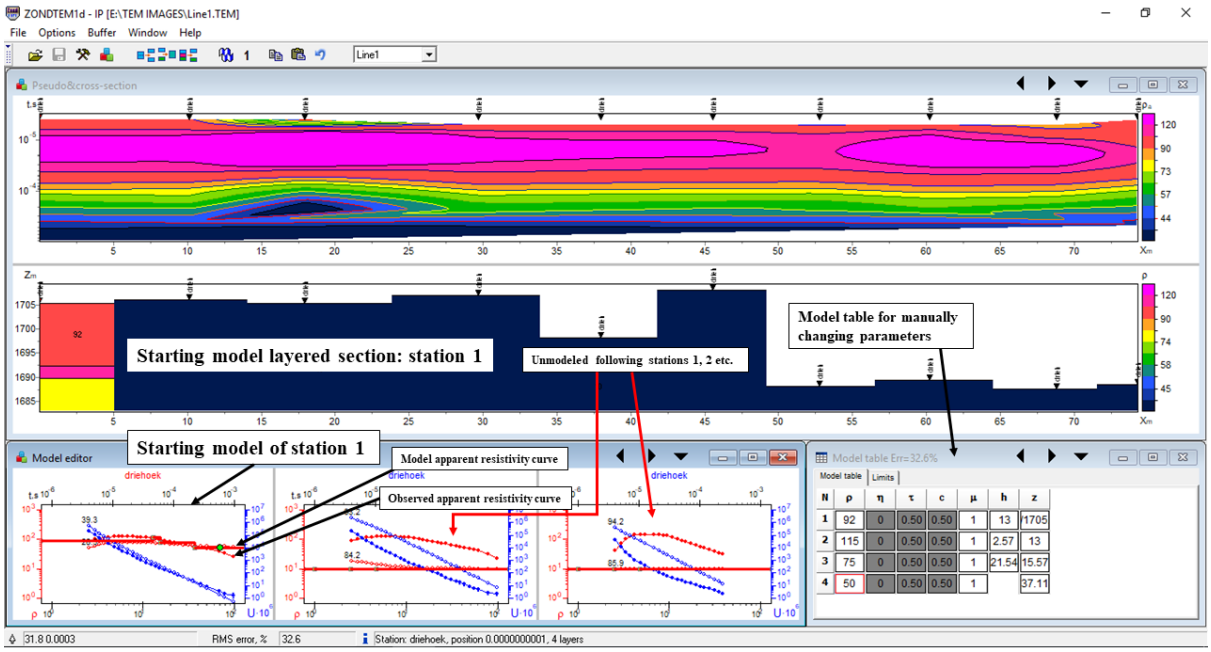



**Figure 5.21.** ZondTEM1D screen dump window used for modelling of the data before carrying out the inversion. The top panel is the model apparent resistivity against time, the middle panel is the starting model layered section which is a response from the individual soundings that are modelled using the model editor windows (bottom panel, left) and the model table window (bottom right). The solid dotted line shows the observed apparent resistivity curve while the open dotted line curve shows the modelled apparent resistivity curve. The misfit between the two curves gives the root mean square error (RMS).

Layered earth modelling was made on individual soundings, before the full modelling was applied to the imaged data set in Figure 5.26. Special attention was paid to sounding numbers: 3, 8, 9, 12, 16 and 18 from a possible 20 soundings as these depicted a change in character from the preceding ones and therefore were chosen for individual layered earth modelling prior to the full inversion of the whole profile. Interpretation is made on the apparent resistivity sounding curves and sections. The shape of such curves change down the traverse due to different layering being present and will assist in the quantitative interpretation of the data and examples of such curves are shown in Figure 5.22 to Figure 5.25 (Screenshots taken from ZondTEM1D software).

The interpretation is made on the apparent resistivity curves (red lines) and not so much on the transient response curves (blue lines). Also, the least resistive layer, $say\ \rho_1$, will be denoted by a low on the apparent resistivity curve and the most resistive layer, $say\ \rho_4$, for a four-layered model, will be denoted by a rise or increase in the apparent resistivity curve. This resembles a direct relationship between the layers' resistivity and the apparent resistivity curves.

The models in Figure 5.22 depict sounding numbers 3 and 8 on the left and right respectively.

**Sounding 3:**

It appears to be a three-layer earth with a top layer that is very thin ($h_1$ = ~1 m) and a low resistivity ($\rho_1$ = ~12 Ω.m). The second layer is quite thick ($h_2$ = ~40 m) with resistivity of ($\rho_2$ = ~750 Ω.m). The third layer is infinitely thick with ($\rho_3$ = ~13 Ω.m). An observation drawn from this behavior is that the second layer, $\rho_2$ is a resistive layer wedged between the top 1m of conductive material and the bottom conductor.

**Sounding 8:**

It also shows a three-layer earth that has a decreasing resistivity with increasing depth. The resistivity layering resembles Sounding 3 except that the overburden layer disappeared. The layering is summarized as follows:

$h_1$ = ~30 m  $\rho_1$ = ~170 Ω.m

$h_2$ = ~30 m  $\rho_2$ = ~ 90 Ω.m

$h_3$ = infinite  $\rho_3$ = ~30 Ω.m

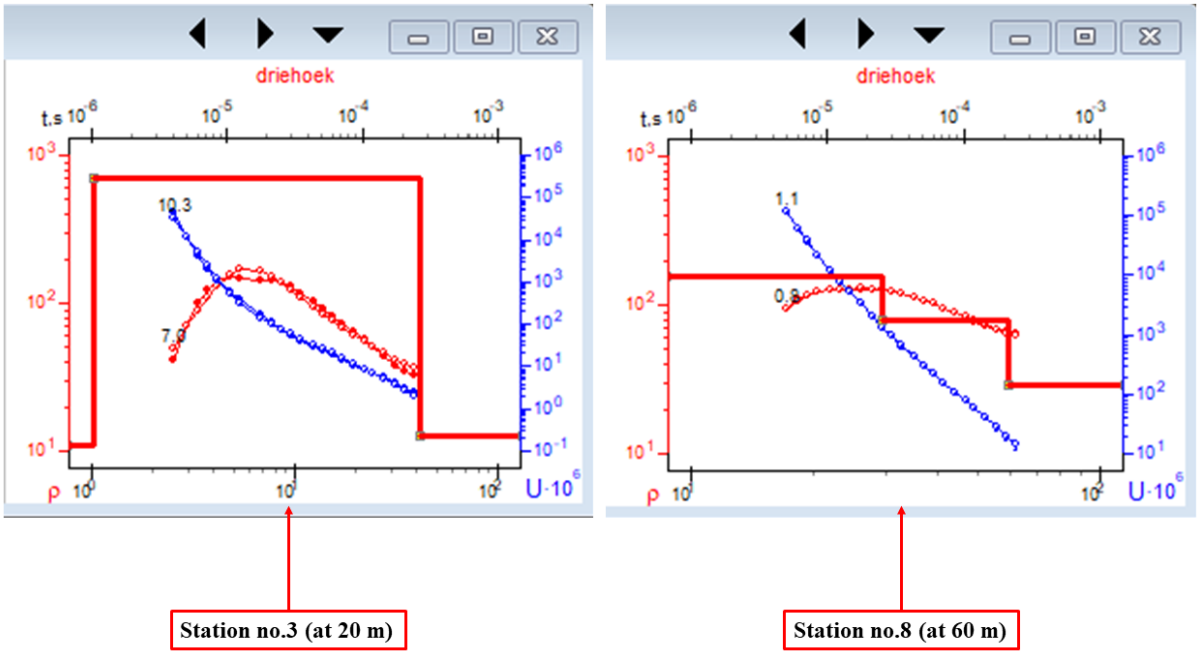



**Figure 5.22.** Inverted models from sounding curves. Lines with solid dots represent measured curves and lines with open circles represent curves fitted by the inversion algorithm to the measured data and produce the best model at the station that best represents the subsurface at that point. The resultant model is given by the solid blocky line which for sounding 3 (on the left) represents: Layer 1 = 1m thick, 12 Ω.m; Layer 2 = 40 m thick,750 Ω.m; Layer 3 = 15 Ω.m and infinitely thick. Sounding 8 (on the right) represents: Layer 1 = 30 m thick, 170 Ω.m; Layer 2 = 30 m thick, 90 Ω.m and Layer 3 = 30 Ω.m

**Sounding 9:**

Figure 5.23 shows a best fitting 4 layer earth model for sounding number 9 with the model parameters calculated by the inversion and as tabled. This model has a less resistive second layer but is otherwise similar to Soundings 3 and 8. The summary is:

$h_1$ = ~13 m  $\rho_1$ = ~487 Ω.m

$h_2$ = ~14 m  $\rho_2$ = ~66 Ω.m

$h_3$ = ~26 m  $\rho_3$ = ~168 Ω.m

$h_4$ = infinite  $\rho_4$ = ~26 Ω.m

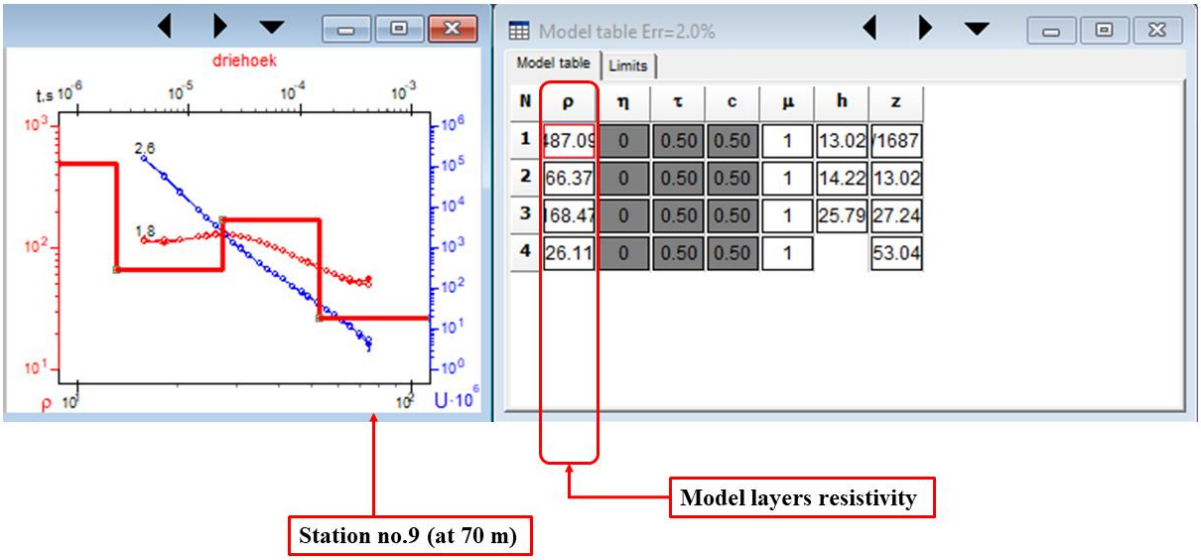



**Figure 5.23.** Inversion models for sounding curve 9. Solid dots represent observed curves and lines with open circles represent curves fitted by the inversion. The image on the right is the model table that shows the layer parameters that were incorporated into the inversion to produce such model: highlighted in red is the resistivity and thickness of the layers. The model converged with an error of 2.0%.

### Soundings 12, 16 and 18:

The inversion models of soundings 12 and 16 (Figure 5.24) are very similar in layer parameters. The resistivity $\rho_1$ is most resistive in both models with a resistivity ranging over $10^2$ Ω.m but less than $10^3$ Ω.m. The layering of sounding 18 also resembles that of 12 and 16 but the best fitting inversion model has a thicker third layer, $\rho_3$. The resistivity of the top layer on Sounding 18 is 144.59 Ω.m as shown in Figure 5.25.

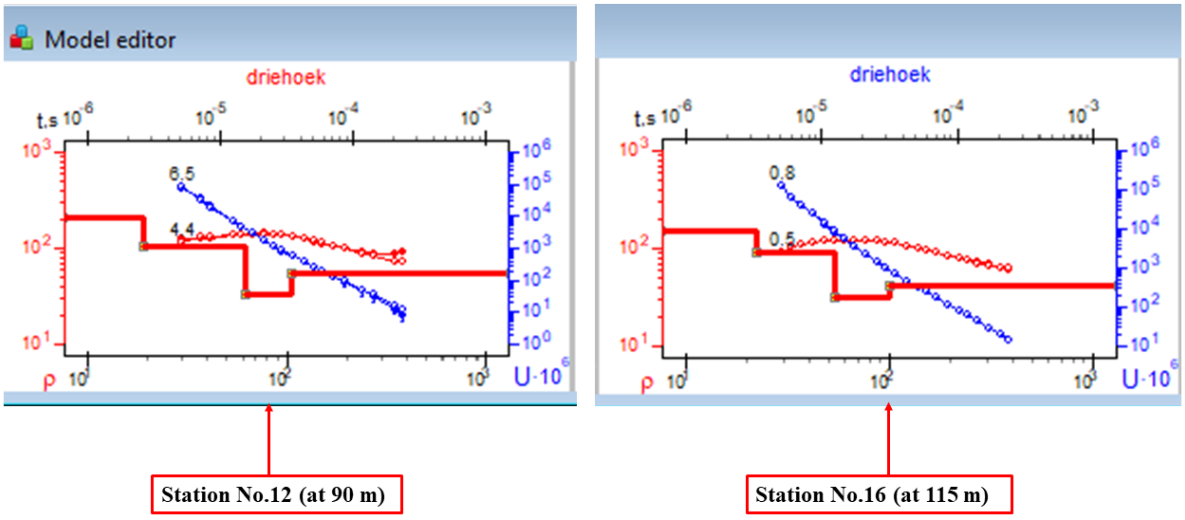



**Figure 5.24.** Soundings 12 and 16 depicting four-layer inversion models. Lines connected by solid dots represent the measured curves and lines connected by open dots represent the curves of the best inversion estimate of the layered earth that fits the sounding data at that point.

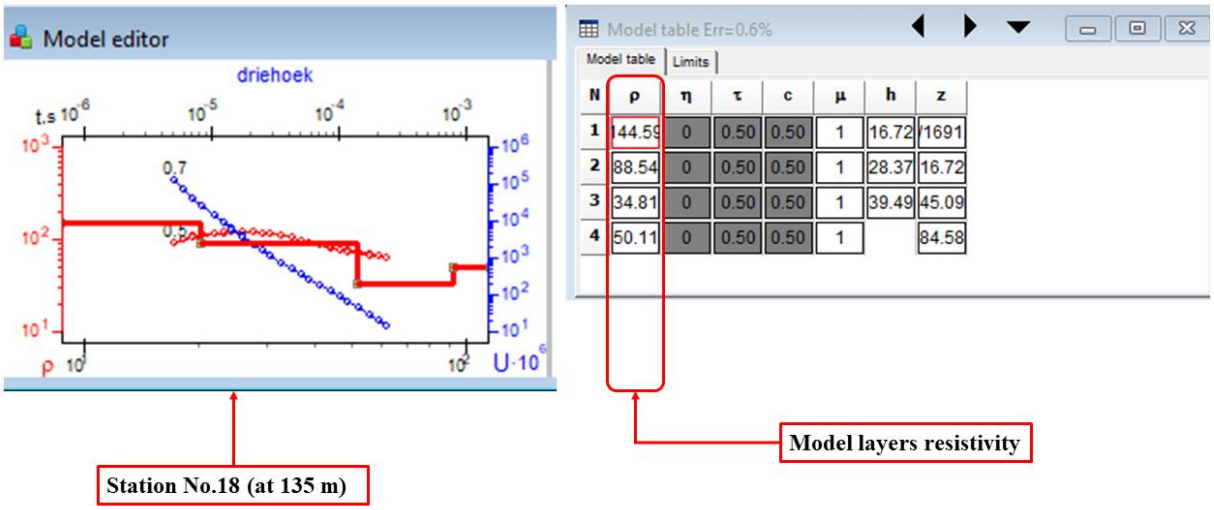



**Figure 5.25.** Four-layer inversion model of Sounding 18 at distance 135 m of a 150 m long line. Lines connected by solid dots represent the measured curves and lines connected by open dots represent the curves of the best inversion estimate of the layered earth that fits the sounding data. The image on the right is the model table that shows the parameters that were obtained from the inversion to produce the model on the left. The model converged with the error of 0.6%.

The initial conclusion drawn from these models is that the resistive layers represent the sandstone (the resistive host rock). This host rock has a resistivity of about $10^2$ Ω.m as seen in all the models with more resistive sections (lenses?) in the sandstone have a resistivity slightly or very much higher than $10^2$ Ω.m but less than $10^3$ Ω.m. This is evident on all the interpreted stations 3, 8, 9, 12, 16 and 18.

A 1D inversion was undertaken at each sounding, progressively going through the whole model. Thereafter a quasi-2D (pseudo-2D) model is produced, that is, the 1D inversions are stitched together by the software to produce a pseudo section shown ultimately in Figure 5.26. In this case, a satisfactory apparent resistivity section with respect to time and the initial inverse model were obtained as shown in Figure 5.26 which will be used for interpretation of the TDEM data. The cold colours show low conductivity while the hot colours show high conductivity.

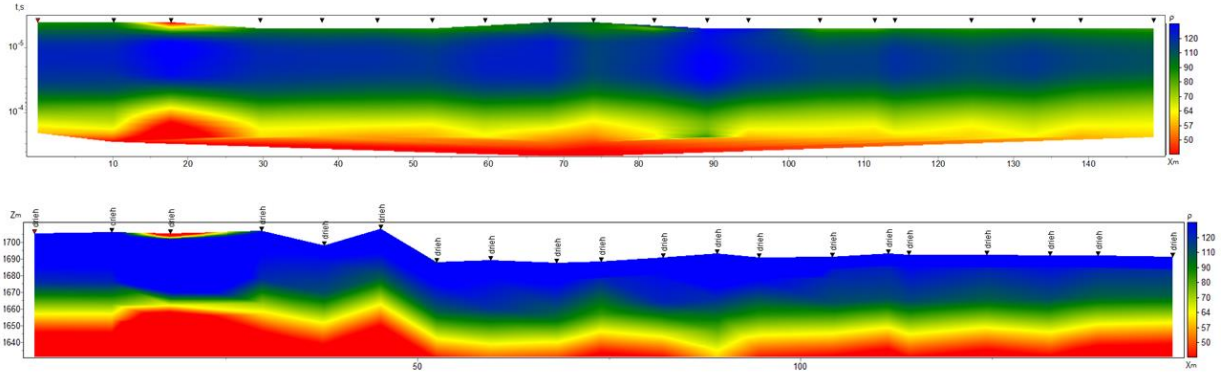


**Figure 5.26.** Inversion results from the sounding data. The top section is the apparent resistivity with respect to time after switch-off and the bottom section is the colour coded first pass apparent resistivity section showing model depth vs distance. The cold colours show low conductivity and the warm colours show high conductivity.

## 5.5 Chapter 5 Summary

In this chapter no attempt was made towards giving a qualitative geological interpretation of the data, but the focus was on quantitative interpretation. In essence, modelling is a quantitative interpretation of the data (see Chapter 6, Section 6.1) since it uses geophysical properties of the data to obtain a close match to the observed anomaly. Whether or not the anomaly is there and what it geophysically means with respect to the geology is referred to as qualitative interpretation and it will be addressed in Chapter 6.

This chapter analysed how the causative bodies in the three datasets of microgravity, magnetic and TDEM were directly modelled using physical properties of the lithology within the study area. The objective of the modelling was to achieve a close match between the observed anomaly from the field data and the calculated modelled data. This information will be carried forward to the next chapter where the geological interpretation will be made. In this chapter both 2D and 3D models of the microgravity and magnetic datasets were produced. In the TDEM data modelling of the individual soundings, several soundings were highlighted because they are the foundation for the interpretation to follow in the next chapter. Only a 2D TDEM model of the subsurface was produced as collected along a single traverse (see Chapter 2, Section 2.4).

# CHAPTER 6 - DATA INTERPRETATION, INTEGRATION AND DISCUSSION

## 6.1 Preamble

Hinze et al. (2013) stated that qualitative data interpretation is entirely based on the presence or absence of an anomaly while quantitative interpretation is based on comprehensive data modelling of physical properties and borehole data to obtain a close match to the anomaly as is seen in Chapter 5. Geophysical data interpretation is based upon inferring the earth model from the geophysical and geological data.

This chapter will focus on the aspect of qualitative data interpretation with the purpose of quantifying the results and eventually integrating all the data. This will be to answer the question of whether these methods can successfully delineate the tunnels/voids and to indicate any drawbacks or difficulties associated with them as based on these results. The chapter will explain how the gravity, magnetic and TDEM models produced in Chapter 5 were deduced from the available data, guided by quantitative interpretation and how they permit generation of a realistic geological model.

## 6.2 Data Interpretation

### 6.2.1 Microgravity

The microgravity forward models made using Grav2dc shown in Figure 2.11 showed that microgravity would be a feasible technique for delineating tunnels in this study given the dimensions, geophysical properties of the tunnels/voids and the geology of the area. The forward model in Figure 2.11 showed that a residual anomaly of size -0.158 mgal is possible for a tunnel/void in this study. Three lines were extracted from the residual Bouguer map, Figure 6.1. This map resulted from removing a 1$^{st}$ order regional field consisting of a 3D polynomial surface, but this surface did not entirely remove all effects not related to the tunnels/voids. Subsequently, a 2$^{nd}$ order regional field was removed during modelling as

previously mentioned in Chapter 4. This 2nd order regional field was reconstructed using Conreg and subtracted to give a final residual Bouguer map (Figure 6.3) that clearly shows the positions of the low gravitational acceleration zones which are inferred and modelled to be bords or voids.

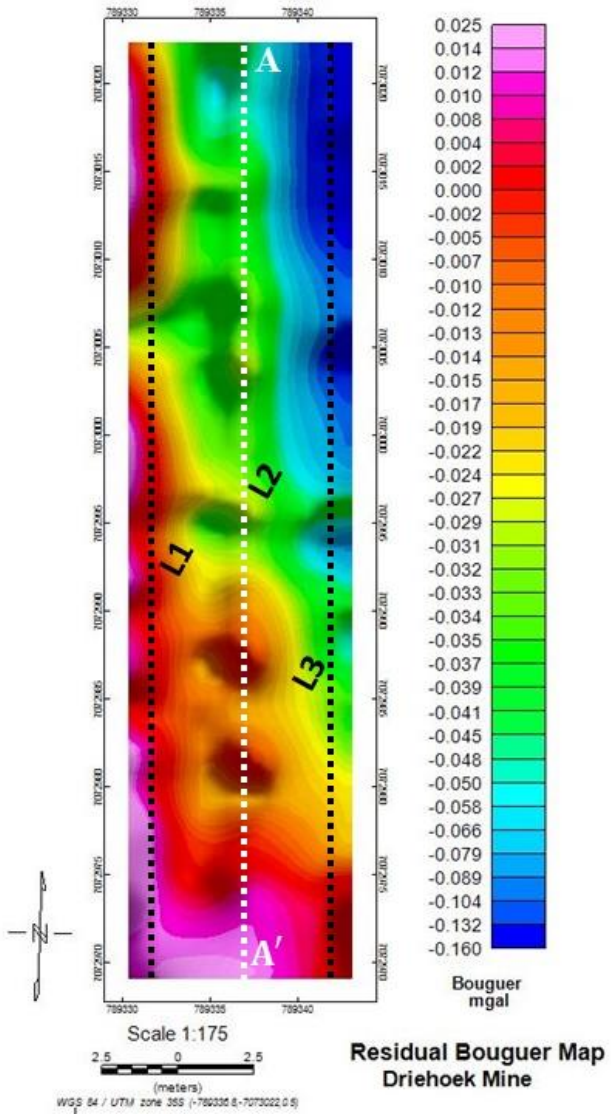



**Figure 6.1.** Bouguer anomaly map from which three lines, L1, L2 and L3 were extracted and modelled in Grav2dc. **A** to **A**' shows the direction of L2 that is modelled to produce a 2D model of the earth.

Three lines L1, L2 and L3 were modelled individually as seen in Figure 5.5 and the sources of the negative anomalies in the models were thought to be tunnels. The interpretation of the results suggests otherwise, however. What are delineated seem more fitting to be interpreted as stopes/bords rather than tunnels because of the orientation of these causative bodies. The

mine owner provided verbal information that the underground mining method at Driehoek farm was bord (meaning room) and pillar mining, hence one of the reasons why these bodies are interpreted as “bords” or “cavities” and not tunnels. From now on, the words bords and cavities will be used interchangeably when referring to these delineated bodies.

Tunnels would be expected to have a long strike and at least be continuous for more than the width and length of the stopes and pillars, which is not the case here. The tunnels’ strike would be longer than 9 m which is the width of the microgravity grid pattern. This grid ran perpendicular to these openings and parallel to the edge of the cliff where these openings were accessed upon a site visit (Figure 2.9). These causative bodies are then interpreted as bords/stopes in the vicinity of protective pillars. The gravitational acceleration due to these bords with special attention on the largest amplitudes on L1, L2 and L3 are -0.045 mgal, -0.065 mgal and -0.063 mgal respectively. These are larger than the sensitivity of CG-5 gravimeter and hence it is safe to assume that indeed the bords are resolved with this gravimeter given that the terrain is not that rugged.

Figure 6.2 is a copy of Figure 5.5B with the addition of the horizontal coal seam that makes no difference to the gravity response of the model. A coal seam layer is included in the model as suggested from the borehole log (deemed not quantitatively useful for cavity/void interception but can be used for layer thickness, see Section 5.1) that shows the occurrence of the coal seam at 13 m and has a thickness of 2.57 m including low-grade coal (shaley coal). The coal seam will not bring about change in the gravitational acceleration because the gravity method measures the vertical component ($\boldsymbol{g_z}$) of gravitational acceleration, $\boldsymbol{g}$ shown in equation (2.3) allowing the coal seam to be easily incorporated into the basic model. Only L2 (**A** to **A**’) of the three model lines L1, L2 and L3 of Figure 5.5 is used; any of the lines however could have been chosen.

From this basic concept, a 2.75-dimensional earth model is inferred and a 3-dimensional model of the subsurface is produced as a result of 3-dimensional interpolation between the 3 survey lines. The 3 survey lines of field data could be adequately explained by three bords with similar dimensions for each bord as shown in Figure 6.2. The bords are each seen to have a width of 3 m and a thickness (stope width) of about 2 m with a density contrast of about -2.55 g/cm$^3$. The

model does not however show the strike of these bords. The 3D model will attempt to assist in answering this question.

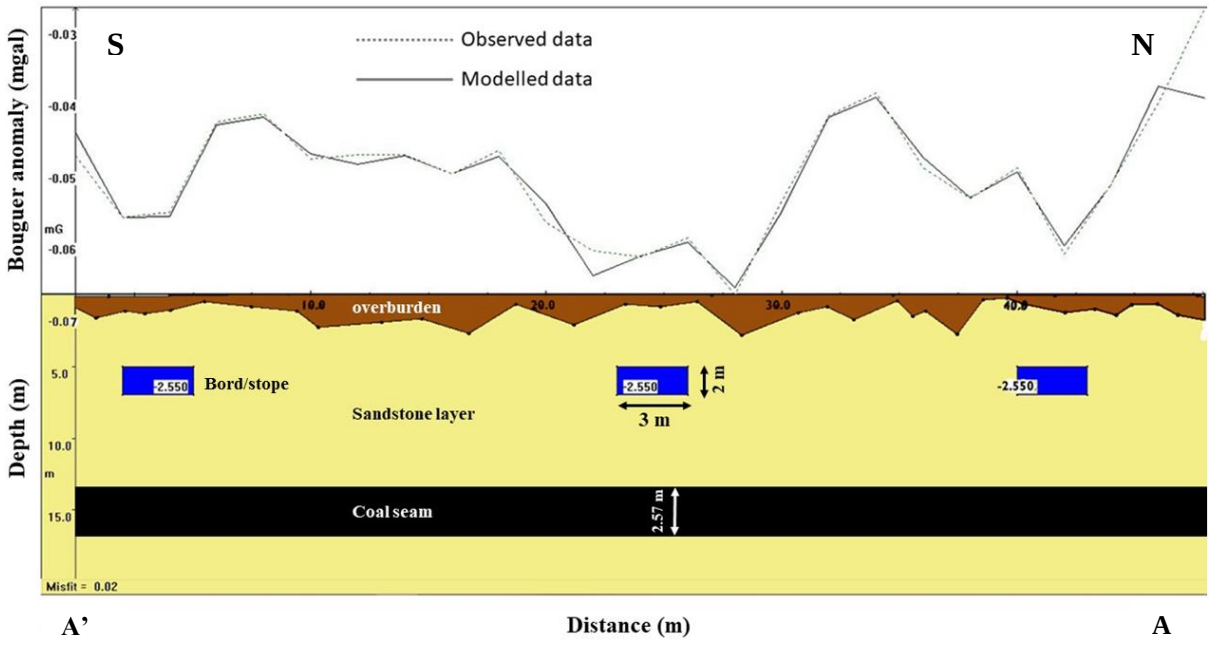



**Figure 6.2.** 2D model of the 50 m long Line2 running from North (**A**) to South (**A**') showing three bords fitted to the observed data and with a misfit of 0.02 mgal between the observed and modelled data. The size of the biggest anomaly is -0.065 mgal and of the smallest anomaly is about -0.058 mgal. This figure is similar to Figure 5.5B but with the addition of the coal seam.

The largest gravitational acceleration caused by these bords as quantified by the size of the anomaly is about -0.065 mgal (Figure 6.2). This is almost equal to the values of the low- density regions (about -0.063 mgal) as seen on the final residual microgravity map (Figure 6.3). Also, the gravitational acceleration of -0.141 mgal (for a best-case scenario of varying overburden) is caused by the targets from the forward model in Chapter 2 (Figure 2.11). This difference in the anomaly size between the forward model and the observed data can be attributed to largely varying overburden thickness if density variations in the sandstone are discounted. The important observation from the two models that increases the confidence in the microgravity technique is that both the forward models and the observed data's anomaly sizes (-0.141 mgal and -0.065 mgal respectively) are larger than the resolution of the instrument used, CG-5 (-0.04 mgal). Figure 6.4 attempts to compare the model of L2 (Figure 6.2) to the residual microgravity map with the intention of comparing the two datasets.

It has been observed that the size of the anomaly on the 2-dimensional gravity model caused by the bords is almost equal to the values of low-density regions on the residual microgravity map. The comparison is a qualitative one to determine if indeed the bords as predicted by the model are aligned with low density regions on the microgravity map (Figure 6.4).-It must be noted however that the final residual microgravity map is rotated by 90 degrees so that the directions of both the map and the model do match in Figure 6.4.

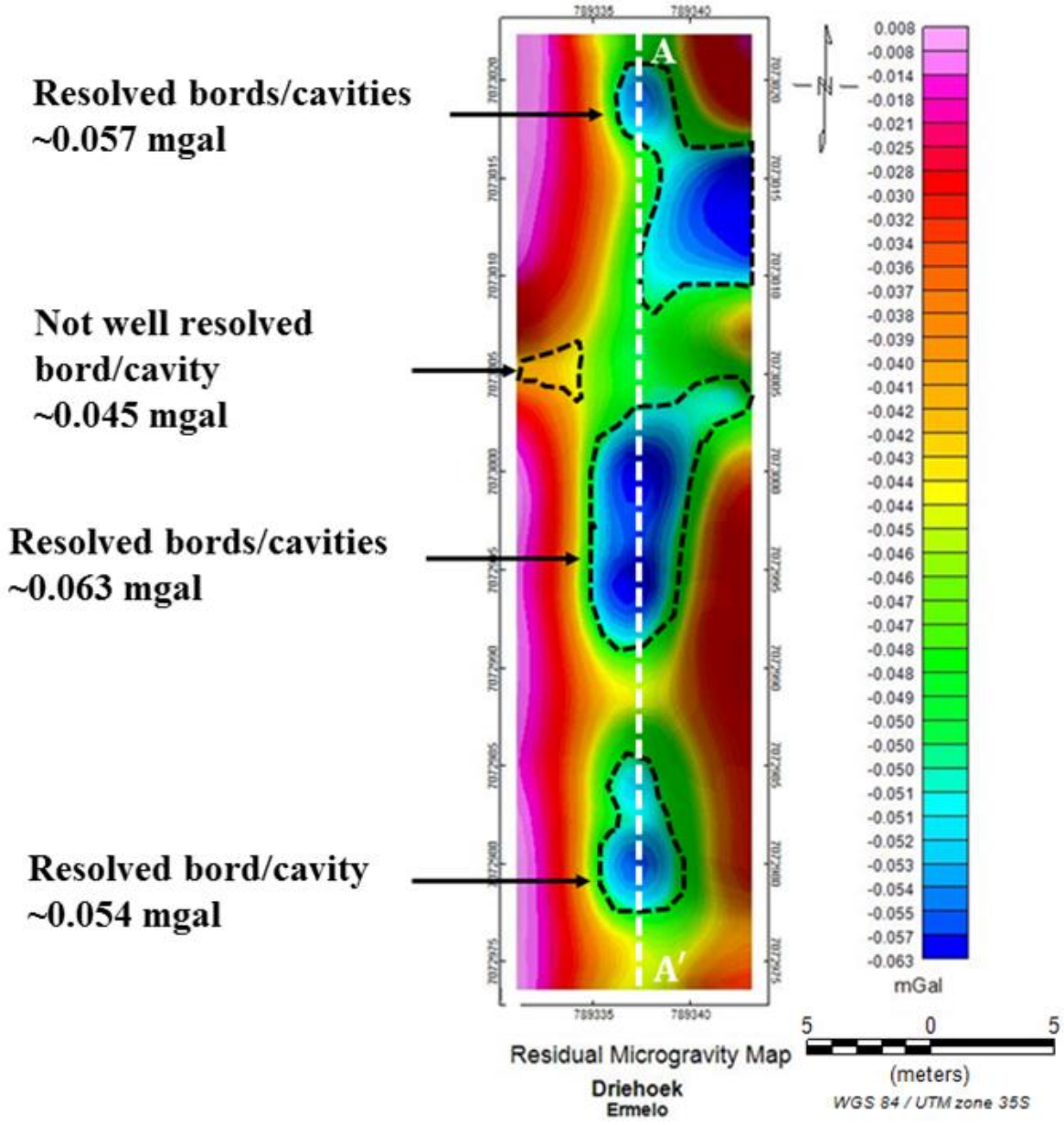



**Figure 6.3.** A residual gravity map showing what are interpreted as bords. Special attention is paid to the bords intercepted by line, L2 shown by the white dotted line **A** to **A'**. Some bords are not clearly resolved on the map.

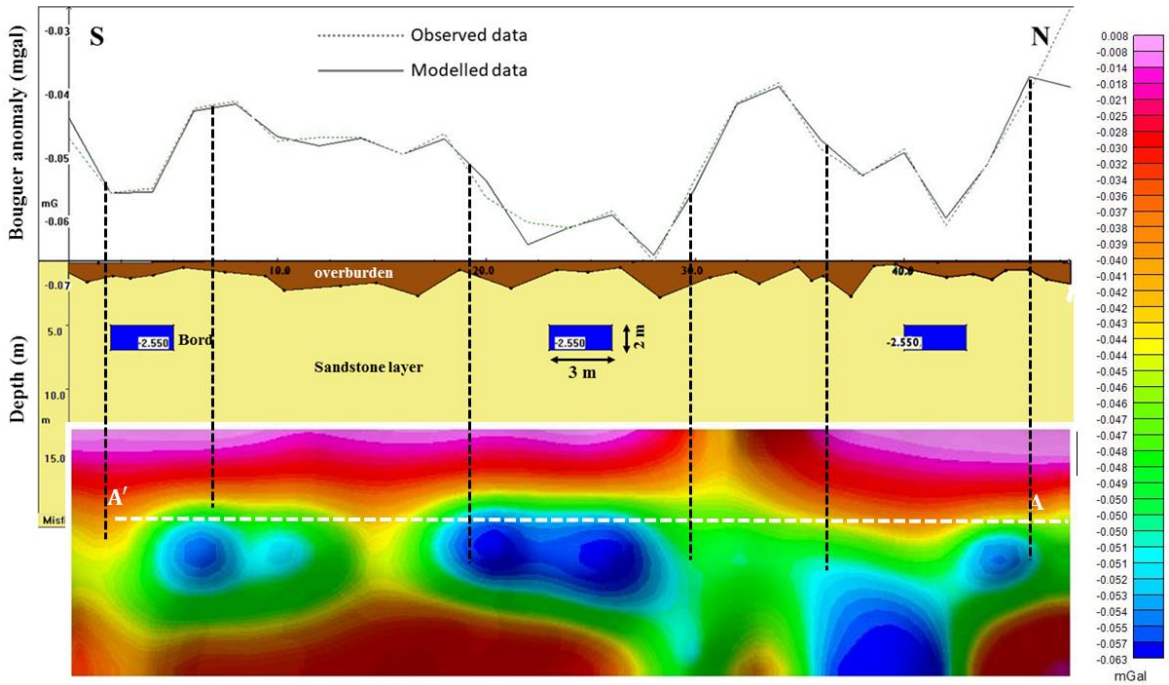



**Figure 6.4.** Gravity data model compared with the final residual microgravity map. The model is made from line **A** to **A'** which is north to south. The residual microgravity map from Figure 6.3 is rotated 90 degrees clockwise so as to align it with the model in correct directions. Note the values of the gravitational acceleration produced by the bords; -0.065 mgal on the model and -0.063 mgal on the map.

The residual microgravity map was overlain on the voxel visualization which is a 3-dimensional representation of the half space (earth model produced from the microgravity data) as is shown in Figure 6.5. The anomalies depicted by the residual microgravity map do not only give information about the location of the bords but also their depth and, orientation. The earth model produced aids in determining the depth of the bords that were located by the microgravity map. To help in quantitatively interpreting the earth model and what the low-density regions (blue iso-surfaces) mean, a reference is made to Styles et al. (2005):

- Air-filled cavities usually produce a density contrast that is in the order of $d\rho =$ -2.5 g/cm$^3$. Where $\rho$ is density.
- For a water filled cavity which is the same size as the air-filled cavity, its anomaly size would be 60% of the air-filled cavity offering a density contrast of approximately, $d\rho =$ -1.5 g/cm$^3$.
- A rubble or mud-filled cavity will produce an anomaly which is about 40% of the air-filled cavity and its density contrast is in the range of about $d\rho =$ -0.4 g/cm$^3$ to $d\rho =$ -1.2 g/cm$^3$.

The low-density zones on the 3-D model interpreted as bords have a density contrast of about -2.47 g/cm$^3$ as shown by the colour bar (Figure 6.5). These structures are interpreted as air-filled cavities/bords and not as tunnels. The tunnels would be geometrically elongated and tubular. Again, this model shows that these structures are not elongated, and their strike is no more than 9 m which is the width of the grid lines that were running along the y-axis and spaced by 3 m along the x-axis with respect to the model shown. The observations made on site when accessing the mined-out openings (the east side of the y-z plane with respect to the model) also showed that they were neither water-filled nor rubble filled. This strengthens the interpretation that the cavities are indeed air-filled.

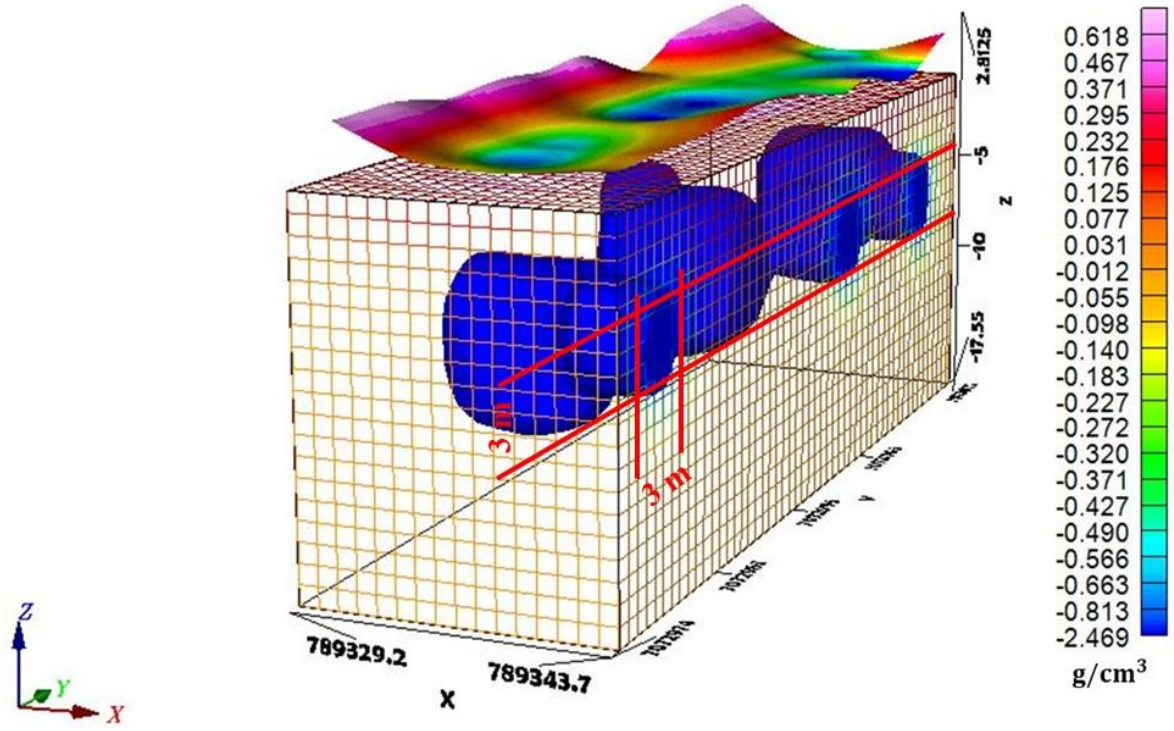



**Figure 6.5.** Iso-surfaces representing the modelled bords are shown in blue and have a density contrast of -2.467 g/cm$^3$ as depicted by the colour bar. The model is a wire-frame so that the bords can be easily shown. This model is a 9 m x 50 m x 20 m (9000 m$^3$) volume. The bords from this model have 3 m width and 3 m thickness (height). The thickness is not 2 m as on the 2D models. This may be due to non-precise clipping (lowest density values were preserved as iso-surfaces) of the low-density regions in the 3D visualization.

It is seen from the 2-dimensional Grav2dc forward modeling of the subsurface that the bords are about 3 m wide, 2 m thick and have a density contrast of about -2.55 g/cm$^3$. The wire-frame model was meant to help in making an inference of the bords' length. The bords do not have a uniform length as shown in Figure 6.5. Some bords are connected while some are disconnected

(not well resolved as shown in Figure 6.3). The disconnection would mean that they are closed to offer pillar support. This was evident from one of the mined-out openings (Figure 6.6) that was accessed upon a visit to the mine. This is shown by the brick wall that is built to offer support to the roof rock and keep illegal miners out.



**Figure 6.6.** A mined-out opening that was accessed and had dimensions of 2 m thickness (stope width) and 4 m wide as was measured with a laser rule when accessed. Of interest is the single line brick wall built to offer roof support and keep illegal miners out.

### 6.2.2 Magnetic Method

Three lines were extracted from the levelled total magnetic intensity (TMI) map as shown in Figure 6.7 and were modelled with Mag2dc as previously seen. Only the model of profile L2, which is the white dotted line will be presented for interpretation. This is chosen because it is the same profile that was chosen for the microgravity data interpretation, so this will help compare or correlate the two methods using data from the same profile. It must be noted that

the profiles are not extracted from the entire map but only in the area that corresponds to the region where the residual microgravity map was overlain.

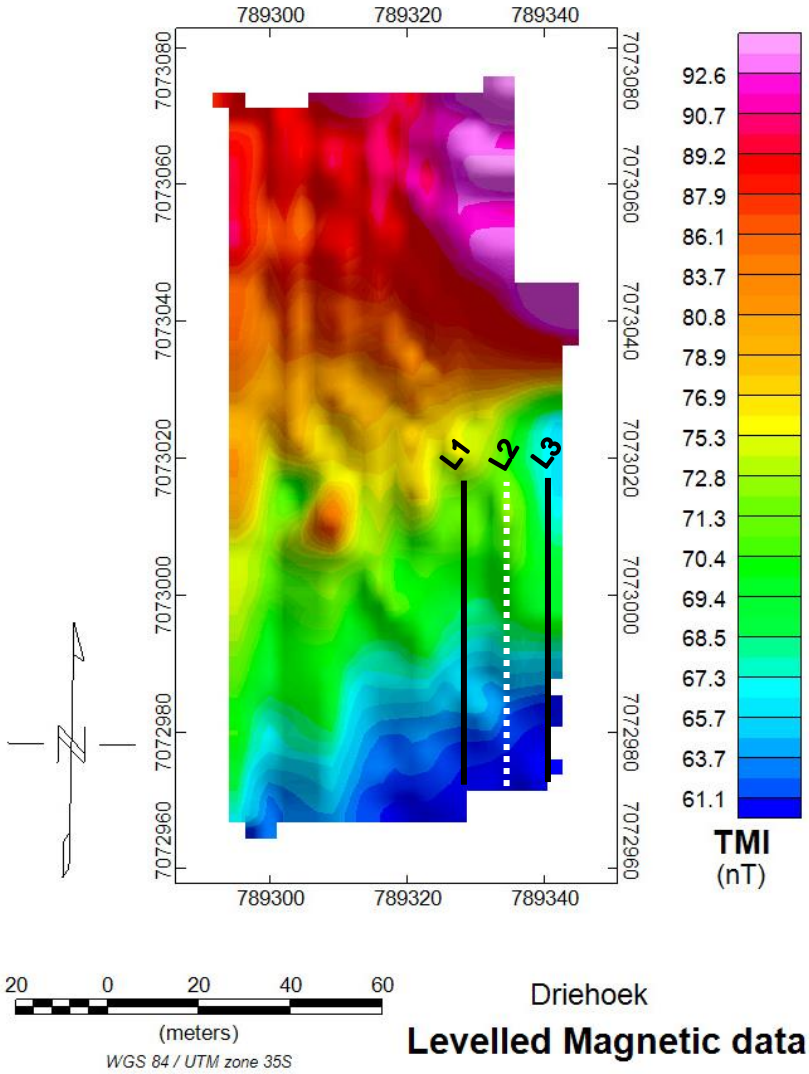



**Figure 6.7.** Levelled Total Magnetic Intensity (TMI) map from whose portion lines of magnetic data were modelled in Mag2dc. Interpreted model is from line, L2 trending North to South.

As mentioned in the magnetic data modelling section, the susceptibility contrast is between the sandstones and the bords (dry air of 0. SI susceptibility) and not between the expectedly altered coal and the bords. For this reason, the presence of the bords will be denoted by low magnetic susceptibility which is the low amplitude anomaly on Mag2dc models and a low magnetic intensity on the TMI map. It will therefore not be easy to discriminate the bord-pillar boundaries using the rise in susceptibility of the coal as the source since the susceptibility of the sandstones alone masks such susceptibility of the coal. Hence the importance of the 2-D models in Mag2dc.

The model in Figure 6.8 made from profile L2 trending from south to north shows three bodies of low susceptibility believed to represent bords (blue). Each bord is 5 m wide, 2 m stope height and 5 m below the surface. The bord of susceptibility contrast of -0.00021 SI provides the anomaly with the largest amplitude of about -0.29 nT. The host rock (in white) is the sandstone and the overburden is the brown top layer and the model extends to the depth of 30 m. The data are fitted to the model with a rms misfit of 0.46 nT.

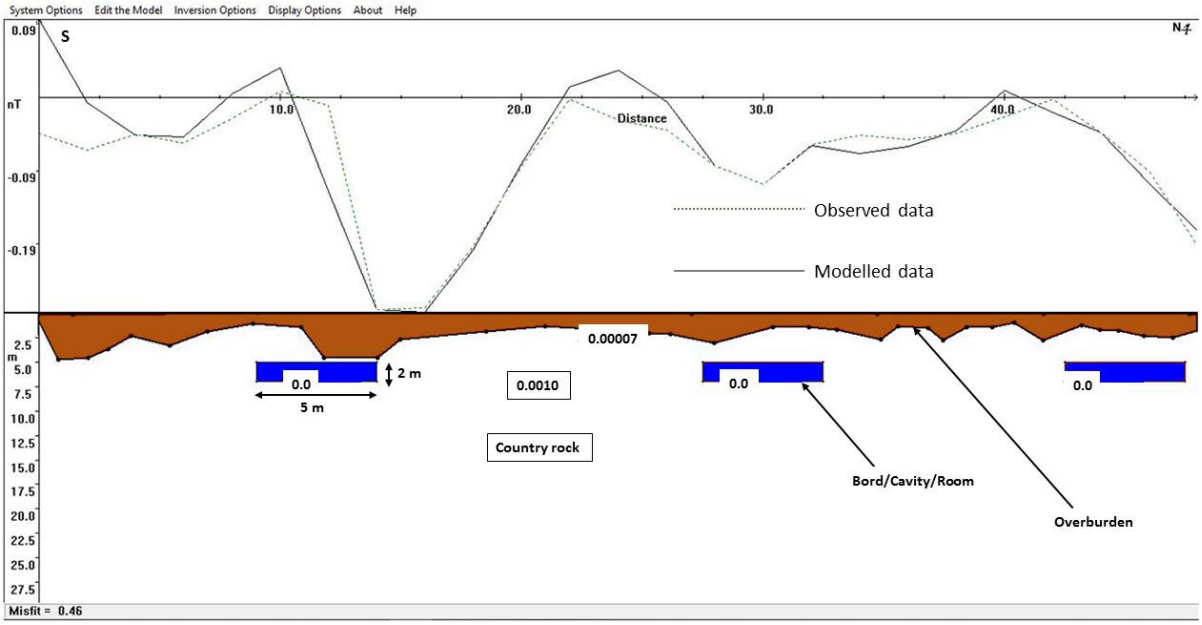



**Figure 6.8.** 2D Mag2dc model of line, L2 trending south to north. Notice how the wording has been changed from tunnels to bords/cavity since the interpretation.

Figure 6.9 is a representation of the earth model produced from the magnetic data. It is guided and constrained by the models of Mag2dc. The models have the position of profile L2 highlighted. It must be reiterated that the models are not the voxels of the whole TMI map but produced from the three profiles L1, L2 and L3 extracted from the TMI map.

From the iso-surface model within the wireframe, the low susceptibility values represented by the blue surfaces are interpreted as the bords/cavities with the susceptibility of $0.07x10^{-3}$ SI or less as shown on the colour bar on the far left (Figure 6.9). These bords/rooms are about 7 m wide and have a stope width of about 5 m. These dimensions are more than what was seen on the 2-dimensional models of Grav2dc. A simple possible reason behind this discrepancy is that the low susceptibility regions may have been clipped too sparingly. The question of the strike of the bords remains unanswered because the bords are not uniform (See also Chapter 1 for

disruptive patterns in the Bord & Pillar Mining); some are continuous from one end of the model to the other and some are not continuous. Again, these models highlight the geometry of these structures that are now called bords/rooms/cavities rather than tunnels.

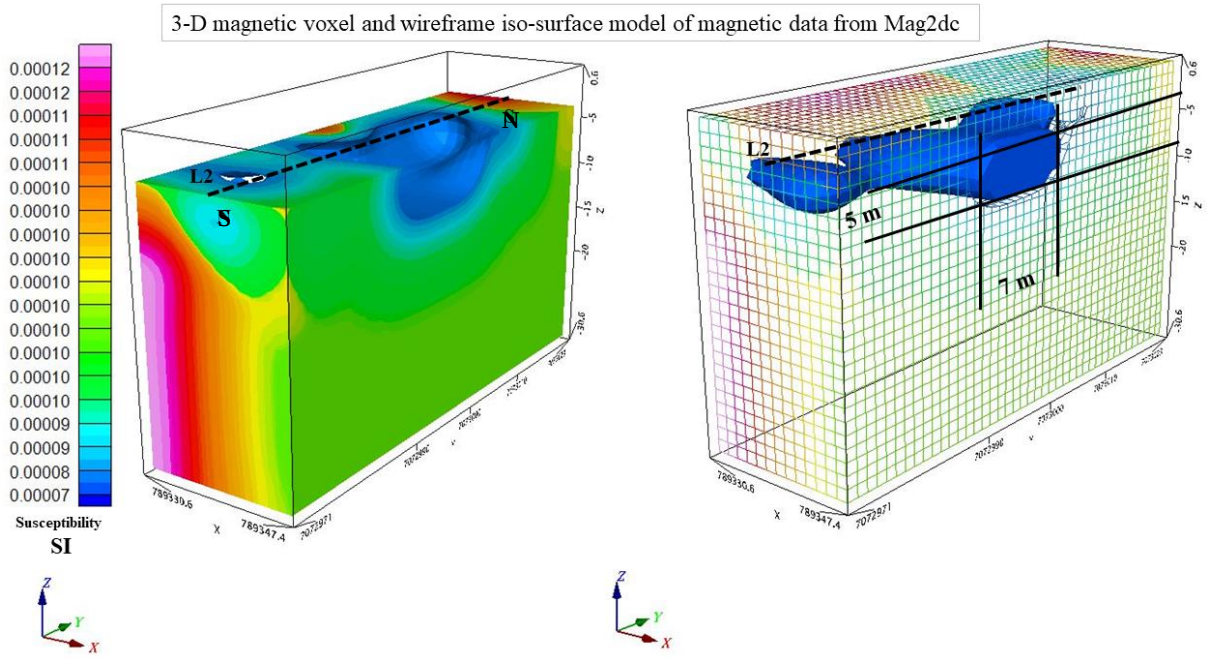



**Figure 6.9.** A 3-D voxel visualization of the earth model. **Left**: solid model with low susceptibility data values clipped. **Right**: wireframe model showing iso-surfaces that represent low susceptibility values as represented by the colour bar on the left.

### 6.2.3 Time Domain Electromagnetic Method

An important parameter that is used in the interpretation of time domain electromagnetic data is the apparent resistivity as a function of time, $\rho_a(t)$. Because of mathematical difficulties (the transient response is usually a complex function of conductivity and time), this apparent resistivity, $\rho_a(t)$ is calculated for late times in the near field of the source and consequently the early times during the transient process may be distorted (Spichak, 2015; AEMR, 2002). To address this distortion of the transients, the reconstruction of the total section from the apparent resistivity is done in such a case, by solving the inverse problem, a common choice

being a least squares inversion for a layered medium (Spichak, 2015). As previously mentioned in Section (5.4.1) of TDEM data modelling, it is of importance that before the inversion is carried out, the initial model must be guided by the geological information available (*a priori* information), but of more importance is that the choice of the initial model be based on the available information about the section.

Figure 6.10 is an apparent resistivity pseudo section along the TDEM profile. The vertical scale (y-axis) of the top image shows time in seconds and the equivalent depth is shown on the layered section beneath it. The bottom horizontal scale (x-axis) shows the profile distance. The sounding stations were made to be 5 m apart during data acquisition making a profile length of 100 m. But the profile is 150 m long instead (Figure 2.15). The reason behind this is that the separation was not uniformly 5 m as shown in Figure 2.15 by the blue dots depicting the locations of TDEM soundings which are clearly not uniformly separated. The pseudo section assists with a more visual or qualitative interpretation of the sounding data that were investigated in Chapter 5 from Figure 5.22 to Figure 5.25. The individually addressed soundings (3, 8, 9, 12, 16, and 18) at the top of Figure 6.10 are highlighted to strengthen the initial conclusion drawn from the sounding curves as a result of the interpretation. From the sounding curves in Section 5.4.1, it was suggested that there reside confined, more resistive bodies in the sandstone believed to be hosting dry air within the resistive sandstone layers. The resistivity of these highly resistive bodies estimated from one of the apparent resistivity curves is about 487.1 Ω.m and 750 Ω.m while the resistivity of the sandstone layer itself is about 168.5 Ω.m. There is a clear contrast between these two layers or bodies which is seen on the section as very light blue portions within the dark blue region. There is a lateral apparent resistivity variation along the pseudosection in Figure 6.10 which highlights the presence of this resistivity contrast of the section as seen on the individual station soundings. The cold colours represent high resistivity (low conductivity) and the hot colours represent low resistivity (high conductivity). The highly resistive bodies within the sandstone layers are believed to represent the cavities/bords that are under investigation in this study as the resistivity of air is considerably higher than the host rock.

While the resistivity of air is much higher, the TDEM performs a bulk resistivity measurement (Goldman and Kafri, 2004) and the addition of a relatively small void in the bulk sample will not have a dramatic increase in the measured resistivity. Nevertheless, it was noticeable (Figure

6.10, labelled stations with very light blue colours on the section). Furthermore, as already mentioned, detecting a resistive body in a resistive environment is more achievable by the DC resistivity technique (Corriols et. al., 2009). This is the reason that compelled the focusing into the top 35 m of the section because the bulk sampling may not clearly discriminate small voids, yet they do exist. The bottom section in Figure 6.10 is a figure of apparent resistivity against distance and depth plotted in Geosoft from the interpreted model results (inversion results) of the first two sections as produced from ZondTEM1D. The cold colours represent low resistivity while the hot colours represent high resistivity as shown by the colour bar on the right.

This Geosoft pseudosection is representative of the middle section (Figure 6.10) but only enlarged to highlight the top 35 m contrary to 65 m of the middle section. Both the middle and bottom sections show topographic variations. The bottom plot clearly highlights an offset on the resistive layer containing very high resistive zones interpreted as cavities. This was not well resolved on the top section of Figure 6.10 because it is showing the complete 65 m deep section. It is important to note that the bottom plot also highlights the high resistivity bodies that occur at the same location as shown on the top pseudosection. The blue layer with low resistivity is attributed to the overburden and the yellow to red layer is interpreted as the sandstones while the green layer beneath the sandstones has the resistivity which matches that of coal ($10^2$ Ω.m).

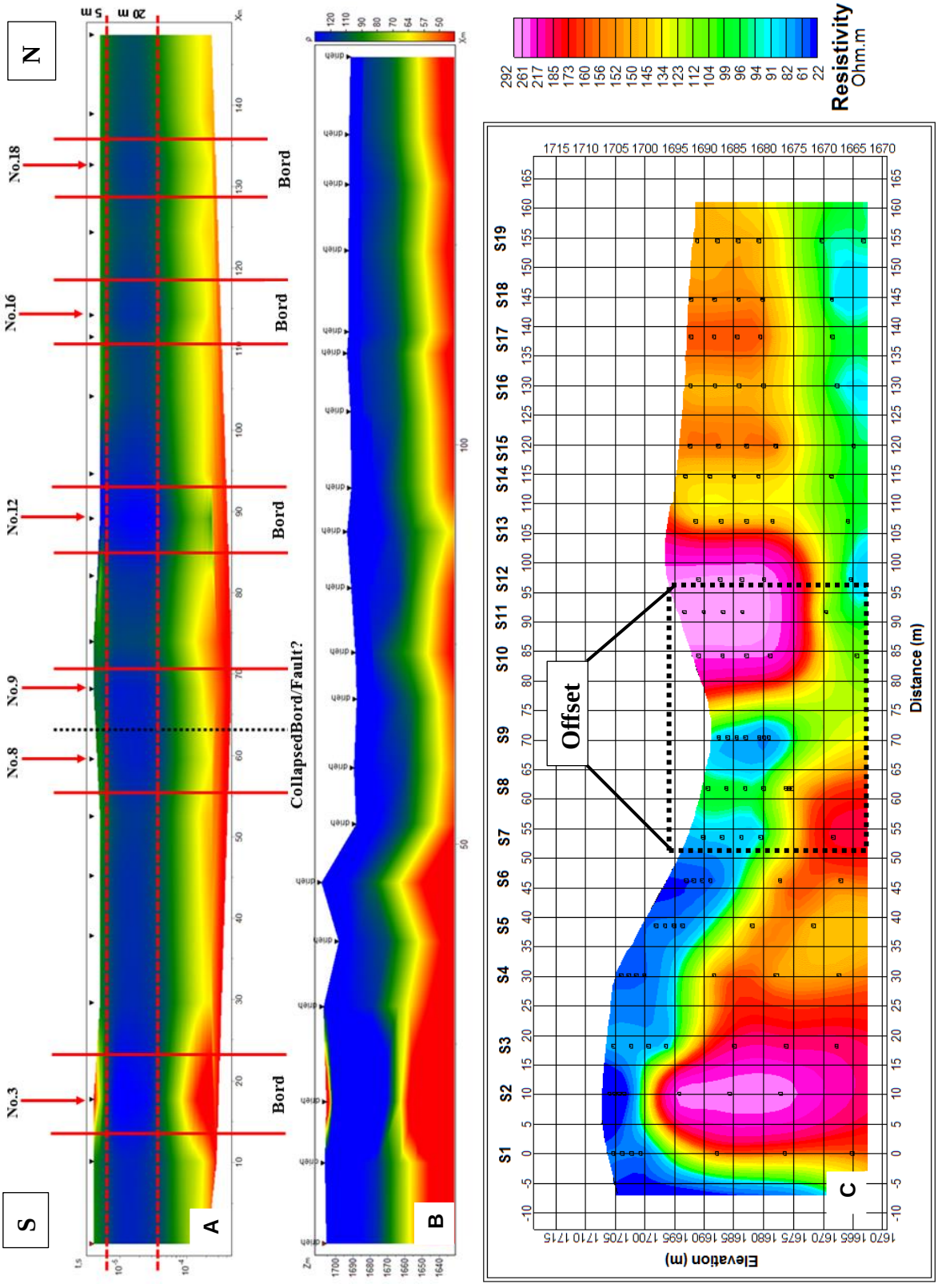



**Figure 6.10.** Apparent resistivity pseudo section (top) and the colour coded model section (middle) from which the pseudo section is calculated through the least squares inversion process. The bottom image (C) is a plot of apparent resistivity against depth and distance of the interpreted data from ZondTEM1D (results of the middle image). This highlights better the first 35 m and depicts an offset on the sandstone layer on the top image. The dots indicate where the sounding measurements are known and were used for the interpolation.

## 6.3 Data Integration and Discussion

This section is aimed at correlating the three datasets; magnetics, microgravity and time-domain electromagnetics. The first approach is to compare the magnetic and microgravity 2.75D models from Mag2dc and Grav2dc. The next step will be to compare the residual microgravity map with the TDEM pseudo section and plot them on Google Earth with precise coordinates of their acquisition locations and then discuss their implications based on the observations. The discussions will then further concentrate on the strengths and weaknesses of each method, how each method can be improved, what were the possible causes of the shortfalls if any, what lessons are learnt from the strengths of the methods and finally whether these methods are a good tool to jointly use for underground openings investigation.

The magnetic intensity variation (Figure 6.11, bottom figure) caused by the cavities is less than 1 nT on the magnetic data model. This variation is very small because 1 nT is usually used to test the magnetometer variation for any source of noise that could emanate from the operator before starting the survey. So, it is evident that a slight variation in the susceptibility of the sandstones and/or the coal may cause similar variations of less than 1 nT and it would be hard to tell what actually caused that variation. This makes it very difficult and uncertain to confidently attribute those variations in the magnetic intensity to the cavities because the country rock had very low susceptibility as seen from Table 5.1. Regardless, these variations are attributed to the cavities because it is seen in Chapter 1, Figure 1.5 that given the favourable geology of well contrasted susceptibility, the bords can be discernible.

Figure 6.11 compares of the models of gravity data (top) and magnetic data (bottom) modelled from the same profile, L2 (Figure 2.15; Figure 5.1). The models are of the same length, 50 m and trending from south to north. Both models have three anomalies that are believed to be bords/cavities albeit at slightly different locations despite being on the same line. From the gravity model, the bords are 3 m wide and have a 2 m stope height, while from the magnetic model, the bords are 5 m wide and have a stope height of 2 m. The similarity notable from the models is the stope height of the bords and depth of 5 m from surface of the bords, and that there are 3 bords in both models. It is seen from the models that:

- From the gravity model, the first bord starts at about 2.5 m while on the magnetic model the first cavity starts at about 8 m. There is an obvious offset of 5.5 m.
- From the gravity model, the second bord starts at about 22.5 m while on the magnetic model the second bord starts at about 27.5 m and there is an apparent difference of 5 m.
- Lastly from the gravity model, the third and last bord starts at about a distance of 40.0 m while from the magnetic model the last bord starts at about 42.5 m and there is a difference of 2.5 m.

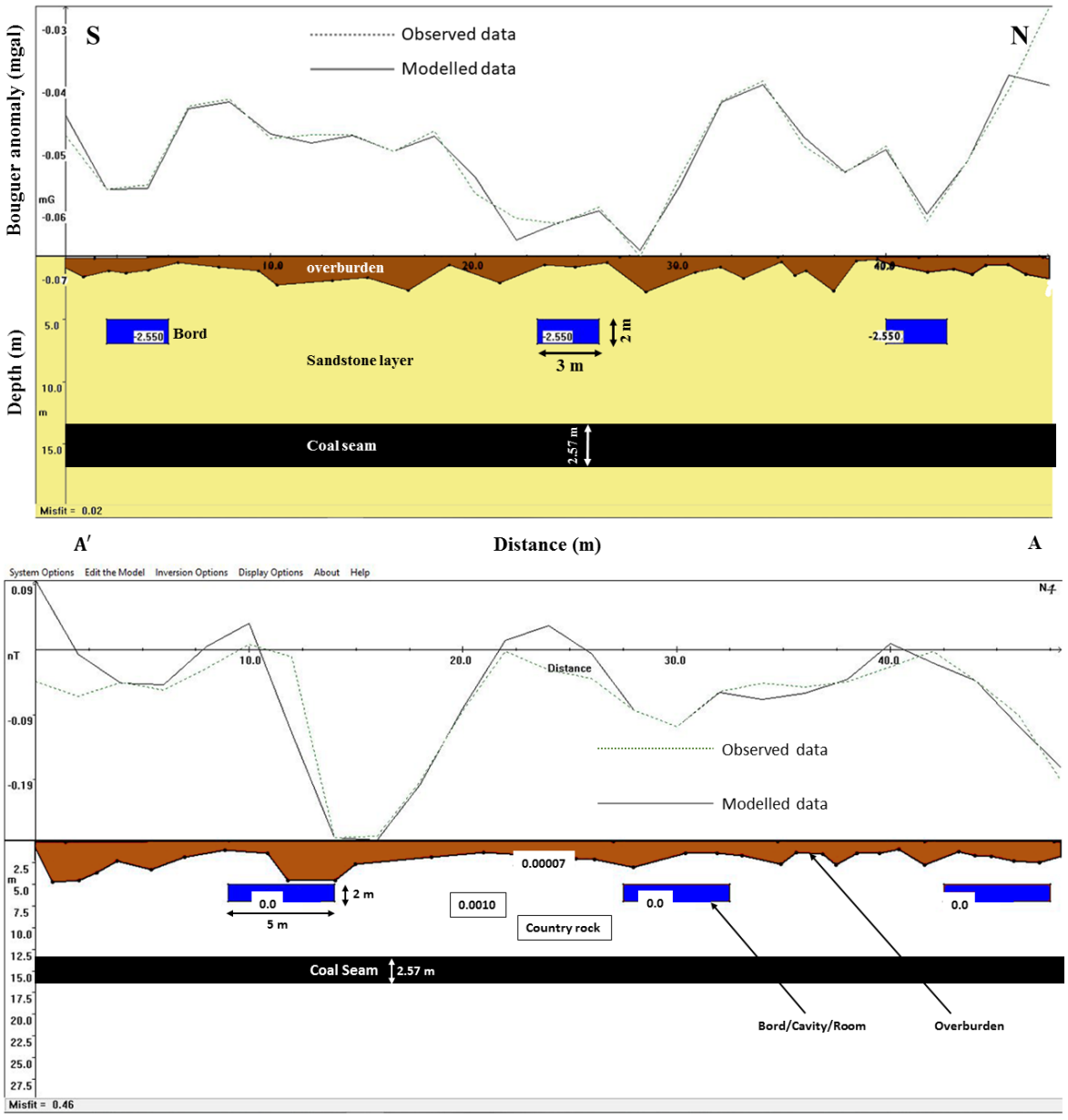



**Figure 6.11.** A comparison of 2.75D models from line 2 of microgravity data from Grav2dc (top) and magnetic data from Mag2dc (bottom). The overburden is thicker on the magnetic model.

Provided the geology offers reasonable susceptibility contrast and any variations can be attributed to the causative bodies with confidence, then microgravity and magnetic methods can jointly be used to investigate the presence of underground bords/cavities. This is because both methods can pick the same number of bords from the same profile. These methods can delineate the bords because both have physical property contrasts that are exploited by each method.

The magnetic method has a contrast between the sandstone susceptibility (0.0002 SI) and air (0 SI) which gives an anomaly amplitude of about 0.29 nT. This results in low susceptibility bodies in the models interpreted as the bords/cavities. The microgravity on the other hand has the density contrast between the sandstones (2.55 g/cm$^3$) and air (0 g/cm$^3$) and this gives an anomaly amplitude of about -0.065 mgal which is detectable by the Scintrex CG-5 gravimeter. From both magnetic and gravity methods, the bords are seen as regions of low magnetic intensity (in nT) and low gravitational acceleration (in mgal).

Another comparison is made between the residual microgravity map and the TDEM pseudo section because part of the TDEM section coincides with the microgravity map. The idea is to determine whether what is interpreted as bords on the TDEM pseudosection does match with what is interpreted as bords in the residual microgravity map. The top image of Figure 6.12, is an image from Google Earth showing the residual microgravity map and the superimposed TDEM pseudosection. To plot the TDEM section on Google Earth, a "Cross Section model generator" from James Madison University is used (Whitmeyer, 2012). The script used is found in Appendix A.

As is seen from Figure 6.12, the TDEM pseudosection running from SSE to NNW traverses the microgravity map across regions of low gravitational acceleration (about -0.063 mgal) interpreted as "offset/faulted cavities" within the sandstone layer (Figure 6.12, bottom). Also, on the TDEM pseudo section at that same point where it traverses the residual microgravity map, the interpretation is two bords/cavities that are suspected to be offset as shown by the Geosoft plot of apparent resistivity against depth and distance (Figure 6.10), possibly because of a collapsed pillar. These "offset cavities" have a resistivity of 487.1 Ω.m as is noted from Sounding 9. These "offset cavities" are also evident on the 3D gravity model in Figure 5.9 and Figure 5.10, with a density contrast of -2.469 g/cm$^3$.

Changes in host rock resistivity are caused by fracturing in the rock and, composition such as shale/siltstone content amongst other factors (Kamenetsky et al., 2010). As the sandstones at the test site looked fairly homogenous, the lower host rock resistivities here are ascribed to sandstone with more fracturing. The only regions with a resistivity higher than that of the solid sandstones would be of dry air. Apart from the presence of a thin overburden layer in the first 13 m depth, the rest of the layers are sandstone with a band of partially mined out coal (~1.6 m thick) at about 5 m depth (Figure 2.9). Within this resistive sandstone reside highly resistive bodies, more resistive than the sandstone and are believed to be hosting dry air. These “air pockets” are thus seen within the sandstone and taken as indication of the existence of air filled spaces as seen on the 1D layered models.

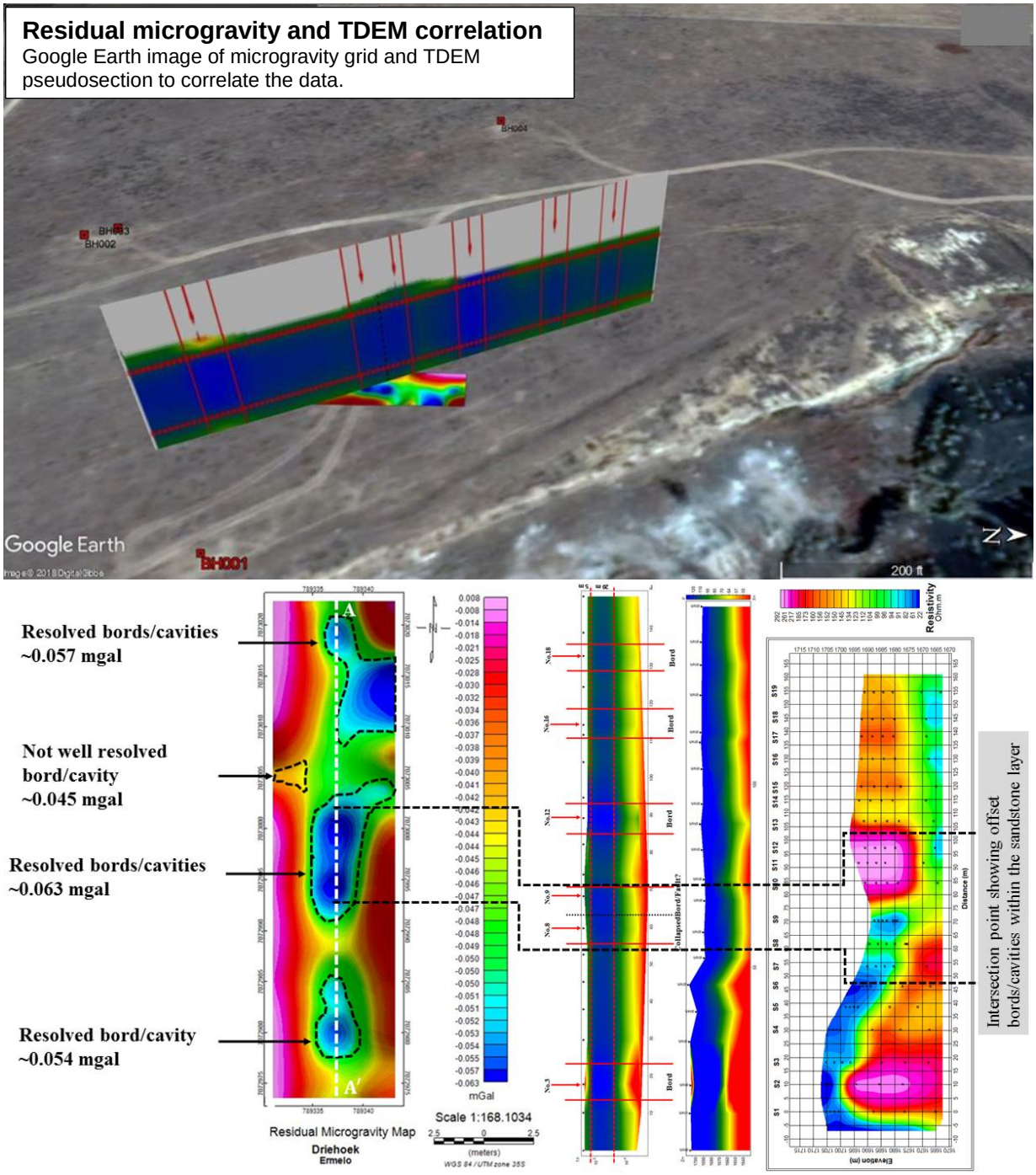



**Figure 6.12. Top**: TDEM pseudosection plotted in relation to the residual microgravity map on Google Earth. North is to the right. **Bottom**: Interpreted residual microgravity map (left) compared with the interpreted TDEM section (right). Both images show offset cavities at the point where they intersect. This is better shown by the image on the bottom right corner. This image shows an offset on the highly resistive layer shown in pink.

The geology cross section of Figure 2.10 was idealized from the mine visit without geophysical data acquisition except the reconnaissance resistivity survey. That geology cross section was used to visually aid the forward modelling of the data. Having interpreted the data, a new geology cross section is drawn in Figure 6.13 This cross section is derived from the information of Figure 6.12, lithological layers from the borehole cross section and the stope width is taken from the 3D density model visualized in Geosoft. A 3-D geology model emanating from the geophysical data would have been possible if all the datasets produced were 3D, particularly the TDEM data because it correlates well with the microgravity grid and 3-D density model data. The two offset bords delineated by the TDEM section that correlates with the microgravity grid (Figure 6.12) are labelled as 3 and 4 in Figure 6.13. The layers in the cross section are fairly flat because only one borehole log is used since it is closest to the survey site while other boreholes are quite far (beyond 100 m from the site). If the survey site were larger than 100 m, it would be reasonable to have used the other boreholes so as to get the dip of the strata. Moreover, the rest of the boreholes like the one used (BH001, Figure 5.3) do not have information in the first 13 m. So, one borehole suffices for this model because it is a model of a small surveyed area (9 m x 50 m) and not the regional study.

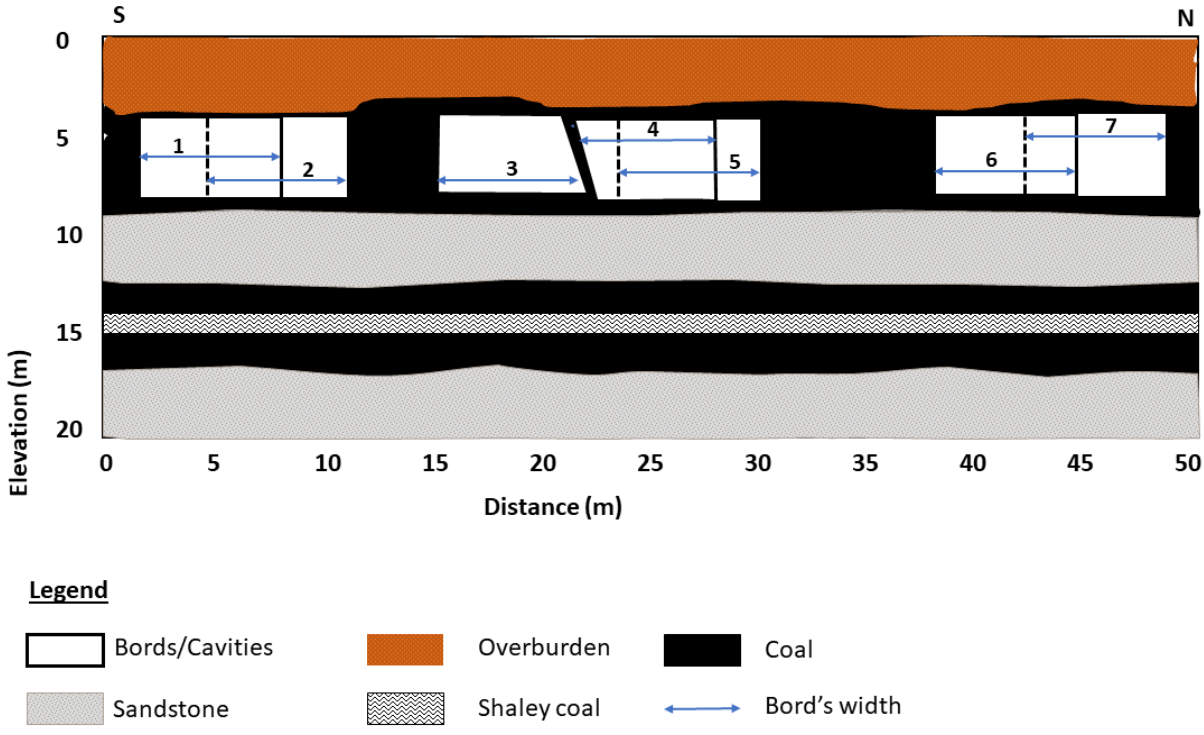



**Figure 6.13.** Interpreted geology cross section derived from 3D density models (visualized as Geosoft's voxel model), microgravity residual grid, TDEM cross section and borehole geophysical data

The first implication drawn from the correlation of these datasets is that for this kind of study, only two geophysical methods are not enough to confidently say that the bords/cavities are delineated, let alone using one geophysical method. The microgravity offers the best choice for the delineation of underground bords/cavities because it uses the largest property contrast (density of air and host rock) especially if the tunnel is not filled with rubble or collapsed roof rock. This is made obvious by the fact that microgravity was able to be correlated with the TDEM data with more confidence. The same cannot be said about the magnetic data's correlation with microgravity. This is no surprise because microgravity is known for its robustness in cavity, tunnel, karst systems and sinkhole delineation (Van Schoor and Fourie, 2015; Orfanos and Apostolopoulos, 2012; Butler, 2008; Johnson and Snow, 2002).

The discernible success of microgravity in delineating the bords/cavities as seen, does not nullify the strengths of the magnetic and TDEM methods. Taking cognizance of the strong possibility of naturally occurring lateral or vertical resistivity variations in the sandstone layering, the TDEM method has undoubtedly detected five bords/cavities along the 150 m long traverse. As seen in Figure 6.12, the offset cavities from the TDEM section correspond to those on the microgravity map. This gives confidence that the other four high resistivity sections are bords because from the 1D soundings, they showed the same behavior of increase in apparent resistivity with depth along the host rock hosting air as did the soundings that coincide with the microgravity map. But one clear aspect is that each possible cavity identified on the TDEM section can be correlated to a possible cavity identified on the microgravity data. Furthermore, the exact location of a cavity cannot be obtained with a layered earth interpretation of the soundings without doing multi-lines and then stitching together the data. Then, there is also the aspect discussed earlier where TDEM is much better at identifying better conductors in a conductive environment than strong resistors in a resistive environment which is the realm of DC resistivity. But as explained, there are ubiquitous examples of resistivity detecting voids but very little on TDEM techniques.

Despite the confidence expressed above and in Chapter 5 in the interpretation of the TDEM data, it would have been very interesting to have acquired multiple lines of TDEM data that perfectly overlay the microgravity. This would have helped improve the confidence in the qualitative data interpretation and could have even produced a pseudo 3D model which would be a representation of the half space and compared it to the 3D model of the microgravity data

and the resistivity data. This was not possible given that the data acquisition was hurried due to the blasting that was about to commence at the study area. The TDEM method like the microgravity method is a robust applicable technique only if the environment does not have a conductive overburden with a strongly varying depth profile that may mask the presence of a void. TDEM is recommended to have a complimentary role in cavity detection except if the cavities are in a conductive environment.

The magnetic method is complimentary to the microgravity method but as shown in Chapter 1 can be used as a quick exploration tool just to determine whether a coal bearing area is underlain by underground workings. The initial expectation that the magnetic method could be the primary choice for detecting stopes in old underground collieries, as the contacts between the tunnels and the pillars would offer a rise in susceptibility because of the presence of burnt coal (Bell et al., 2001), was not fulfilled in this study but could well work at other premises (See Figure 1.5). On Driehoek, this was not seen to be the case as the sandstones had a larger susceptibility than the coal. Fortunately, there was still a contrast between the sandstone and the air, and this helped in the modelling. The magnetic method could be improved by doing extensive susceptibility measurements on the core samples and not just the susceptibilities of the rocks collected from the study area. This is because the rocks may be weathered as was the case with the sandstones and the coal in this study area. The susceptibility measurements on fresh core should result in a more informed modelling of the data. A lack of this exercise led to little confidence on the magnetic models to affirm that the magnetic intensity variation is indeed influenced by the cavities and not any other factors. No comparison is made between the datasets of magnetic and TDEM because as mentioned, the magnetic variations could have been due to other factors such as variations in the properties of geological formations and not only the cavities. On a larger scale, it would have been very interesting to compare the results of the electrical resistivity and TDEM had the TDEM profile not been so far separated from the reconnaissance resistivity line due to time constraints.

# CHAPTER 7 - CONCLUSIONS AND FUTURE RECOMMENDATIONS

The research was carried out with the microgravity, TDEM and magnetic techniques to investigate the strengths of the three methods in delineating underground tunnels at a coal mine. It must be emphasized that tunnel detection has never proven to be an easy task and numerous articles in the literature reiterate that. The study was intended to answer the question of whether these three geophysical methods can, in addition to DC resistivity and GPR, also be used to delineate tunnels successfully when buried just a few metres below surface, tell whether the tunnels were water-filled or dry, delineate the strike of the tunnels and produce a comprehensive earth model.

On the question of successfully delineating tunnels, all three methods produced a signal well above the noise level and a different result was found instead of the expected tunnels. Bords/cavities/rooms were delineated instead of tunnels. There are two possible reasons why the bords were detected and not tunnels. The first possibility is that the grid patterns were laid above the bords/rooms and not at the tunnels' location. This discrimination between tunnels and bords would not have been known prior to the study because, upon the site visit, the openings that were accessed were closed with brick walls after the first 5 m from the entrance as mentioned before (Figure 6.6). Moreover, the reconnaissance resistivity profile that was used to guide the location of the survey grid was a 2D cross section that would not tell the geometry of the targets beforehand. Also, no geophysics was done at this site before, so the data in this study were expected to reveal a lot of unknown information. The second possible reason for delineating bords and not tunnels is that the survey grid (50 m x 9 m) was small and would not sample the full geometry (extending more than 9 m) of the tunnels. Not much was done in this regard because this focused research was a proof of concept to test the ability of integrating three methods to delineate underground openings. The reconnaissance resistivity survey, and the three geophysical methods/technique used later showed that the bords are buried at ±5 m from surface. This was evident from the 2D gravity and magnetic forward models using Cooper's Grav2dc and Mag2dc software respectively, 3D voxel visualization of microgravity and magnetic data and the TDEM pseudo section of apparent resistivity against time.

The borehole log did not show the location of any cavities at depth, nor the coal layer at a depth of 5 m as seen in the cliff face, but one 55 mm diameter HQ size core can only give a general inference of the rock types (at least this is the thought because only the log was provided by the geologist). The understanding is that the bords must occur within the coal seam as that is the target seam. The borehole deemed to have loss of information indicated the first coal seam to be at a depth of 13 m. The reason for this discrepancy between the drill log, visual observations at the cliff edge and the four geophysical datasets that correlate in terms of bord depth from surface may have a number of reasons. It may be because this drill log was only intended to log the coal seam of high calorific value (C lower seam and below, and not the upper C seam coal that had lost value resulting in the underground mine being closed before) and the other layers may not have been logged, an unknown fault exists (as can be interpreted from the TDEM traverse), or no significant core was recovered, resulting in core loss. This illustrates that to rely solely on core is also not the answer.

The study was able to characterize the bords as dry and not water filled. The answer to this is offered by the microgravity and TDEM methods. The microgravity 3D model could be best modelled with a density contrast of -2.469 g/cm$^3$ for the bords, using the measured dimensions of the bords as a constraint and as portrayed by the iso-surfaces. Styles et al. (2005) state that air-filled cavities typically have a density contrast in the order of -2.5 g/cm$^3$ while water-filled cavities have a density contrast of the order of about -1.5 g/cm$^3$. From the TDEM data, if the cavities were water filled, the resistivity of the cavities would possibly be lower than that of the surrounding rock, but in this case the resistivity of the bords (487.1 Ω.m and 750 Ω.m) is higher than that of the host rock (168.5 Ω.m) which leaves the author to conclude that the bords are dry and not water-filled.

Whether or not the methods could delineate the strike of the tunnels is a question that remains unanswered. Despite a finding that the targets are actually bords, from magnetic and microgravity 3D models, these bords appear to be connected and a strike could possibly be approximately inferred as WNW but due to the small width surveyed no single value can fairly quantify the strike of these bords. What could help answer this question would perhaps be an old mine map as shown in Chapter 1 at Vlakhoogte colliery. Such a map would be overlaid on the survey area and then a script that makes a mathematical approximation of the widths and lengths of the areas marked as mined-out areas as mapped from surface would have to be

written. Such a mine plan map would not only help to delineate the strike of these bords but to also bolster beyond doubt their locations as mapped by the three methods particularly the magnetic method which is not known to delineate tunnels. As a future recommendation, this and other studies could be much improved by acquiring such maps if available and overlaying them on the surveyed area. For this research, such maps were not available although they should be part of DMR (Department of Mineral Resources) records and the current owner had unfortunately no proper records. Therefore, the study was done in the first place.

A comprehensive 3D geological model that is a representation of the half space was not accomplished by this study. This would have been achieved if the TDEM data were collected on a larger grid pattern and a 3D model was produced. Thus, the earth model was built from density, magnetic susceptibility and resistivity datasets. Now only two 3D models that are a representation of the subsurface were produced, namely magnetic data and microgravity data voxels built from MagmodIntrp and GmodIntrp programs respectively. Despite the lack of the comprehensive earth model, it can be reported that the microgravity delineated bords/cavities ~5 m deep from surface, 2 m stope width, ~3 m width, density contrast of -2.47 g/cm$^3$ and gravitational acceleration of about -0.065 mgal. The magnetic method recorded bords/cavities of ~5 m depth from surface, 2 m stope width, ~5 width, susceptibility contrast of about -0.0002 SI and magnetic intensity of about 0.29 nT as seen on a 2D magnetic model from Cooper's Mag2dc.

Other future recommendations besides using mine plans, if available are to record all the datasets at similar locations (and where acquisition parameters do not conflict use similar parameters such as station spacing and line separation) to help build a comprehensive model that will be a more reliable representation of the subsurface under investigation. Coupled to this should be detailed physical property measurements of the drill core samples and not only samples collected in-situ because these may be weathered as witnessed in the physical property measurements recorded in Table 5.1. It is imperative that the person doing the study verifies the drill core logs themselves and not only accept the logs from the mine geologist so as to identify discrepancies that may exist. This is an important lesson learnt from this study with regards to the magnetic models in particular.

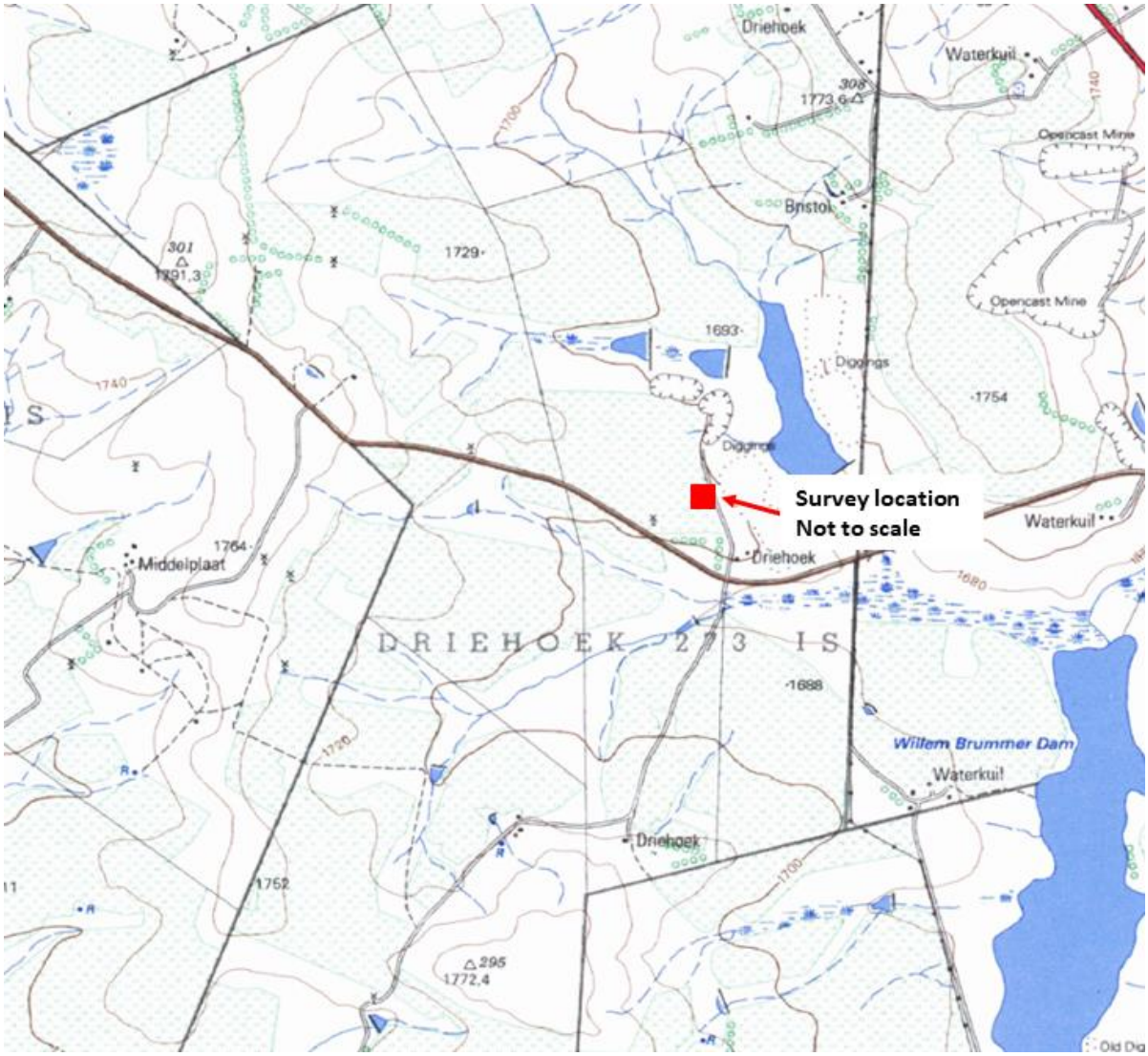
# Appendix A

The code below was used to generate and position a vertical cross section of the TDEM data on Google Earth (Whitmeyer, 2012) as seen in Figure 6.12.

```
<?xml version="1.0" encoding="UTF-8"?>
<kmlxmlns=http://www.opengis.net/kml/2.2xmlns:gx="http://www.google.com/kml/ext/2.2"
xmlns:kml="http://www.opengis.net/kml/2.2" xmlns:atom="http://www.w3.org/2005/Atom">
<Document>
	<name>Cross section</name>
	<open>1</open>
	<LookAt>
		<longitude>30.051357999999997</longitude>
		<latitude>-26.474421</latitude>
		<altitude>0</altitude>
		<range>30000</range>
		<tilt>70</tilt>
		<heading>-80</heading>
		<altitudeMode>relativeToGround</altitudeMode>
	</LookAt>
	<Placemark id="Model">
		<name>Cross section</name>
		<Model id="XSmodel">
			<altitudeMode>relativeToGround</altitudeMode>
			<Location>
				<longitude>29.901358</longitude>
				<latitude>-26.434421</latitude>
				<altitude>-10</altitude>
			</Location>
			<Orientation>
				<heading>-80</heading>
				<tilt>0</tilt>
				<roll>0</roll>
			</Orientation>
			<Scale>
				<x>0.015</x>
				<y>1</y>
				<z>0.08</z>
			</Scale>
			<Link>
				<href>Xsection.dae</href>
			</Link>
			<ResourceMap>
				<Alias>
					<targetHref>TEMCROSSSECTION.png</targetHref>
					<sourceHref>reyemtihw.png</sourceHref>
				</Alias>
			</ResourceMap>
		</Model>
	</Placemark>
</Document>
</kml>
```

# Appendix B

This shows a topographic map, sheet WGS2629BD of the study area. The map is cropped to focus on the elevations of the study area smoothly seated at 1700 m. The area is quite small, but this map is to give an idea that the topography was not that rugged. The map is used with permission from Professor Paul Nex of the University of the Witwatersrand.



# Appendix C

The figure shows the Geosoft database of microgravity data after the Bouguer correction. Four lines are shown with 26 stations per line. The data also show the elevation data as measured with the differential GPS. The digital form of the data may not be distributed without the consent of the mine owner Simon Netshiozwi of Kimopax Ltd.

| L1:0 | Stations | X | Y | GPS_Height | Time | Bouguer |
|---|---|---|---|---|---|---|
| 0.0 | 1.0000 | 789341.4040 | 7072971.5040 | 1730.2700 | 0010/03/11 | 0.1172 |
| 1.0 | 2.0000 | 789341.6400 | 7072973.8000 | 1730.3170 | 0010/04/16 | 0.1138 |
| 2.0 | 3.0000 | 789341.5120 | 7072975.7650 | 1730.3050 | 0010/05/23 | 0.0985 |
| 3.0 | 4.0000 | 789341.6010 | 7072977.7210 | 1730.2640 | 0010/06/15 | 0.0933 |
| 4.0 | 5.0000 | 789341.7640 | 7072979.7740 | 1730.2550 | 0010/07/12 | 0.0855 |
| 5.0 | 6.0000 | 789341.8120 | 7072983.8320 | 1730.1620 | 0010/08/01 | 0.0723 |
| 6.0 | 7.0000 | 789341.7670 | 7072985.7680 | 1730.1400 | 0010/08/22 | 0.0697 |
| 7.0 | 8.0000 | 789341.7050 | 7072987.7890 | 1730.1350 | 0010/09/09 | 0.0594 |
| 8.0 | 9.0000 | 789341.7890 | 7072989.7840 | 1730.1520 | 0010/09/29 | 0.0585 |
| 9.0 | 10.0000 | 789341.7700 | 7072991.7720 | 1730.1820 | 0010/11/04 | 0.0506 |
| 10.0 | 11.0000 | 789341.8060 | 7072993.7810 | 1730.1660 | 0010/11/21 | 0.0261 |
| 11.0 | 12.0000 | 789341.8390 | 7072995.7670 | 1730.1850 | 0011/01/02 | 0.0541 |
| 12.0 | 13.0000 | 789341.8250 | 7072997.7580 | 1730.1690 | 0011/01/16 | 0.0226 |
| 13.0 | 14.0000 | 789341.7820 | 7072999.7810 | 1730.1220 | 0011/02/19 | 0.0134 |
| 14.0 | 15.0000 | 789341.9060 | 7073001.7790 | 1730.1210 | 0011/03/12 | 0.0010 |
| 15.0 | 16.0000 | 789341.8290 | 7073003.7630 | 1730.0390 | 0011/04/03 | -0.0183 |
| 16.0 | 17.0000 | 789341.8910 | 7073005.7470 | 1730.0300 | 0011/04/20 | -0.0004 |
| 17.0 | 18.0000 | 789341.9110 | 7073007.7580 | 1730.0660 | 0011/05/08 | -0.0026 |
| 18.0 | 19.0000 | 789341.8900 | 7073009.7620 | 1730.0550 | 0011/05/25 | -0.0201 |
| 19.0 | 20.0000 | 789341.9180 | 7073011.7840 | 1730.0190 | 0011/06/16 | -0.0483 |
| 20.0 | 21.0000 | 789341.9570 | 7073013.7540 | 1729.9450 | 0011/07/05 | -0.0552 |
| 21.0 | 22.0000 | 789342.0050 | 7073015.7550 | 1729.8730 | 0011/07/21 | -0.0576 |
| 22.0 | 23.0000 | 789341.9840 | 7073017.7020 | 1729.8110 | 0011/08/09 | -0.0511 |
| 23.0 | 24.0000 | 789341.9290 | 7073019.6850 | 1729.7850 | 0011/08/24 | -0.0536 |
| 24.0 | 25.0000 | 789342.0610 | 7073021.6140 | 1729.7980 | 0011/09/10 | -0.0394 |
| 25.0 | 26.0000 | 789341.9300 | 7073021.5390 | 1729.7350 | 0011/09/29 | -0.0714 |
| L2:0 | Stations | X | Y | GPS_Height | Time | Bouguer |
| 26.0 | 1.0000 | 789337.2270 | 7072971.5110 | 1732.3950 | 0009/01/24 | 0.1308 |
| 27.0 | 2.0000 | 789337.4050 | 7072973.6740 | 1732.4050 | 0009/02/11 | 0.1291 |
| 28.0 | 3.0000 | 789337.4280 | 7072975.6710 | 1732.4390 | 0009/03/01 | 0.1157 |
| 29.0 | 4.0000 | 789337.3790 | 7072977.5550 | 1732.3970 | 0009/03/19 | 0.1096 |
| 30.0 | 5.0000 | 789337.4330 | 7072979.5240 | 1732.4240 | 0009/04/03 | 0.0953 |
| 31.0 | 6.0000 | 789337.4270 | 7072981.6970 | 1732.3950 | 0009/04/20 | 0.1047 |
| 32.0 | 7.0000 | 789337.4880 | 7072983.6690 | 1732.3690 | 0009/05/08 | 0.0945 |
| 33.0 | 8.0000 | 789337.5340 | 7072985.5290 | 1732.3440 | 0009/05/27 | 0.0928 |
| 34.0 | 9.0000 | 789337.5760 | 7072987.5270 | 1732.3270 | 0009/06/23 | 0.0985 |
| 35.0 | 10.0000 | 789337.6650 | 7072989.6270 | 1732.3410 | 0009/07/12 | 0.0915 |
| 36.0 | 11.0000 | 789337.6510 | 7072991.5290 | 1732.3330 | 0009/08/02 | 0.0848 |
| 37.0 | 12.0000 | 789337.6250 | 7072993.6130 | 1732.3030 | 0009/08/21 | 0.0701 |
| 38.0 | 13.0000 | 789337.7140 | 7072995.5810 | 1732.3490 | 0009/09/06 | 0.0737 |
| 39.0 | 14.0000 | 789337.6960 | 7072997.6390 | 1732.3140 | 0009/09/26 | 0.0644 |
| 40.0 | 15.0000 | 789337.7130 | 7072999.6550 | 1732.2780 | 0009/10/11 | 0.0638 |
| 41.0 | 16.0000 | 789337.7940 | 7073001.6190 | 1732.2810 | 0009/11/04 | 0.0608 |
| 42.0 | 17.0000 | 789337.8140 | 7073003.6410 | 1732.1940 | 0009/11/22 | 0.0667 |
| 43.0 | 18.0000 | 789337.7880 | 7073005.5220 | 1732.1410 | 0009/12/16 | 0.0585 |
| 44.0 | 19.0000 | 789337.8800 | 7073007.5290 | 1732.1440 | 0010/01/13 | 0.0613 |
| 45.0 | 20.0000 | 789337.9060 | 7073009.4860 | 1732.1090 | 0010/02/02 | 0.0539 |
| 46.0 | 21.0000 | 789337.9020 | 7073011.5120 | 1732.1430 | 0010/02/21 | 0.0490 |
| 47.0 | 22.0000 | 789337.9540 | 7073013.6520 | 1732.1260 | 0010/03/09 | 0.0463 |
| 48.0 | 23.0000 | 789338.1350 | 7073015.6130 | 1732.0840 | 0010/03/27 | 0.0442 |
| 49.0 | 24.0000 | 789338.2690 | 7073017.5640 | 1732.0570 | 0010/04/14 | 0.0309 |
| 50.0 | 25.0000 | 789338.4300 | 7073019.6420 | 1732.0220 | 0010/05/04 | 0.0286 |
| 51.0 | 26.0000 | 789338.6270 | 7073021.3770 | 1731.9110 | 0010/06/11 | 0.0268 |

| L3:0 | Stations | X | Y | GPS_Height | Time | Bouguer |
|---|---|---|---|---|---|---|
| 52.0 | 1.0000 | 789334.0200 | 7072970.9930 | 1732.5010 | 0010/07/11 | 0.1351 |
| 53.0 | 2.0000 | 789334.0860 | 7072973.0160 | 1732.5050 | 0010/07/27 | 0.1286 |
| 54.0 | 3.0000 | 789334.0730 | 7072975.0000 | 1732.5140 | 0010/08/11 | 0.1148 |
| 55.0 | 4.0000 | 789334.1860 | 7072976.9900 | 1732.5270 | 0010/09/13 | 0.1136 |
| 56.0 | 5.0000 | 789334.2750 | 7072978.8390 | 1732.5040 | 0010/10/13 | 0.1016 |
| 57.0 | 6.0000 | 789334.3320 | 7072980.8680 | 1732.5150 | 0010/10/29 | 0.1005 |
| 58.0 | 7.0000 | 789334.4190 | 7072982.8430 | 1732.4610 | 0010/11/18 | 0.0993 |
| 59.0 | 8.0000 | 789334.4260 | 7072984.8750 | 1732.4640 | 0010/12/02 | 0.1012 |
| 60.0 | 9.0000 | 789334.3680 | 7072986.9320 | 1732.4350 | 0010/12/19 | 0.0933 |
| 61.0 | 10.0000 | 789334.3520 | 7072988.9180 | 1732.3870 | 0011/01/07 | 0.0971 |
| 62.0 | 11.0000 | 789334.4150 | 7072990.9440 | 1732.3890 | 0011/01/24 | 0.0854 |
| 63.0 | 12.0000 | 789334.3590 | 7072992.8440 | 1732.3470 | 0011/02/10 | 0.0819 |
| 64.0 | 13.0000 | 789334.2870 | 7072994.9600 | 1732.3450 | 0011/02/28 | 0.0707 |
| 65.0 | 14.0000 | 789334.3560 | 7072996.8550 | 1732.3390 | 0011/03/21 | 0.0833 |
| 66.0 | 15.0000 | 789334.3550 | 7072998.9200 | 1732.3450 | 0011/04/05 | 0.0719 |
| 67.0 | 16.0000 | 789334.4730 | 7073000.9120 | 1732.3440 | 0011/04/22 | 0.0676 |
| 68.0 | 17.0000 | 789334.5660 | 7073002.9220 | 1732.3300 | 0011/05/06 | 0.0622 |
| 69.0 | 18.0000 | 789334.5520 | 7073004.8890 | 1732.2950 | 0011/05/25 | 0.0635 |
| 70.0 | 19.0000 | 789334.6190 | 7073006.9290 | 1732.2420 | 0011/06/14 | 0.0555 |
| 71.0 | 20.0000 | 789334.5810 | 7073008.7740 | 1732.2170 | 0011/06/30 | 0.0602 |
| 72.0 | 21.0000 | 789334.7160 | 7073010.8170 | 1732.1960 | 0011/07/15 | 0.0575 |
| 73.0 | 22.0000 | 789334.7330 | 7073012.8990 | 1732.1660 | 0011/07/29 | 0.0539 |
| 74.0 | 23.0000 | 789334.6600 | 7073014.7980 | 1732.1550 | 0011/08/15 | 0.0616 |
| 75.0 | 24.0000 | 789334.7010 | 7073016.9010 | 1732.1540 | 0011/09/01 | 0.0433 |
| 76.0 | 25.0000 | 789334.7580 | 7073018.8140 | 1732.1630 | 0011/09/22 | 0.0378 |
| 77.0 | 26.0000 | 789334.6970 | 7073020.7660 | 1732.1490 | 0011/10/08 | 0.0376 |
| L4:0 | Stations | X | Y | GPS_Height | Time | Bouguer |
| 78.0 | 1.0000 | 789331.1330 | 7072970.1980 | 1732.6060 | 0014/02/09 | 0.1386 |
| 79.0 | 2.0000 | 789331.2780 | 7072972.1810 | 1732.5800 | 0014/03/15 | 0.1374 |
| 80.0 | 3.0000 | 789331.2470 | 7072974.1150 | 1732.5640 | 0014/05/31 | 0.1391 |
| 81.0 | 4.0000 | 789331.4090 | 7072976.1160 | 1732.5900 | 0014/06/24 | 0.1367 |
| 82.0 | 5.0000 | 789331.4680 | 7072978.1030 | 1732.6140 | 0014/07/10 | 0.1355 |
| 83.0 | 6.0000 | 789331.5010 | 7072980.1260 | 1732.6140 | 0014/08/03 | 0.1239 |
| 84.0 | 7.0000 | 789331.5510 | 7072982.0690 | 1732.6350 | 0014/08/21 | 0.1252 |
| 85.0 | 8.0000 | 789331.6190 | 7072984.0320 | 1732.5500 | 0014/09/26 | 0.1134 |
| 86.0 | 9.0000 | 789331.6380 | 7072986.0440 | 1732.5290 | 0014/10/11 | 0.1163 |
| 87.0 | 10.0000 | 789331.6760 | 7072988.0260 | 1732.4970 | 0014/10/24 | 0.1149 |
| 88.0 | 11.0000 | 789331.6280 | 7072990.0520 | 1732.4530 | 0014/11/16 | 0.1097 |
| 89.0 | 12.0000 | 789331.7370 | 7072992.0290 | 1732.4410 | 0014/12/03 | 0.1134 |
| 90.0 | 13.0000 | 789331.7480 | 7072994.0230 | 1732.4280 | 0014/12/22 | 0.1031 |
| 91.0 | 14.0000 | 789331.7750 | 7072996.0300 | 1732.4300 | 0015/01/09 | 0.1066 |
| 92.0 | 15.0000 | 789331.7870 | 7072997.9900 | 1732.3880 | 0015/01/25 | 0.1084 |
| 93.0 | 16.0000 | 789331.8300 | 7073000.2070 | 1732.3850 | 0015/02/13 | 0.1041 |
| 94.0 | 17.0000 | 789331.9090 | 7073002.1180 | 1732.3630 | 0015/03/05 | 0.0860 |
| 95.0 | 18.0000 | 789331.9460 | 7073003.9810 | 1732.3680 | 0015/03/22 | 0.0800 |
| 96.0 | 19.0000 | 789331.9760 | 7073005.9750 | 1732.3660 | 0015/04/12 | 0.0649 |
| 97.0 | 20.0000 | 789331.9610 | 7073007.9930 | 1732.3110 | 0015/04/27 | 0.0781 |
| 98.0 | 21.0000 | 789332.0700 | 7073010.1210 | 1732.3220 | 0015/05/14 | 0.0815 |
| 99.0 | 22.0000 | 789332.0570 | 7073011.9740 | 1732.2600 | 0015/05/29 | 0.0832 |
| 100.0 | 23.0000 | 789332.1580 | 7073014.1150 | 1732.2390 | 0015/06/16 | 0.0893 |
| 101.0 | 24.0000 | 789332.2360 | 7073016.0230 | 1732.1960 | 0015/07/02 | 0.0819 |
| 102.0 | 25.0000 | 789332.2340 | 7073017.9560 | 1732.1690 | 0015/07/15 | 0.0774 |
| 103.0 | 26.0000 | 789332.2280 | 7073019.9660 | 1732.1840 | 0015/07/30 | 0.0734 |

## REFERENCES


AEMR. (2002) TEM-RESEARCHER, Version 6, Manual Applied Electromagnetic Research AEMR.

Barrocu, G. and Ranieri, G. (2000) TDEM: A useful tool for identifying and monitoring the fresh-saltwater interface. Faculty of Engineering-University of Cagliari, Italy.

Bechtel, T.D. Bosch, F.P & Gurk, M. (2014) Methods in Karst Hydrogeology: Geophysical Methods.

Bell, F.G. Bullock, S.E.T. Hälbich, T.F.G. Lindsay, P. (2001) Environmental impacts associated with an abandoned mine in the Witbank Coalfield, South Africa, International Journal of Coal Geology, vol. 45, pp. 195-216.

Bishop, I. Styles P. Ensley, S.J. and Ferguson, N.S. (1997) The detection of cavities using the microgravity technique: case histories from mining and karstic environments. Modern Geophysics in Engineering Geology. Geological Special Publication. No.12, pp. 153-166.

Buselli, G. (1981) The effect of near-surface superparamagnetic material on electromagnetic measurements. Geophys, vol. 47, pp. 1315-1324.

Butler, K.D. (2008) Detection and characterization of subsurface cavities, tunnels and abandoned mines. Near-Surface Geophysics and Human Activity, pp. 578-584.

Cai, H. Hu, X. Xiong, B. Auken, E. Han, M. and Li, J. (2017) Finite element time domain modeling of controlled-source electromagnetic data with a hybrid boundary condition, Journal of Applied Geophysics, vol. 145, pp. 133-143.

CGS. (2012) Coalfields of the republic of South Africa. (Accessed April 2017). http://www.geoscience.org.za/index.php?Option=com_content&view=article&id=19&Itemid=565

Cohen, A. Daubechies, I. and Vial, P. (1993) Wavelets bases on the interval and fast algorithms, J. of Appl. And Comput. Harmonic Analysis, no.1, pp. 54-81.

Cooley, J.W. and Tukey, J.W. (1965) An algorithm for the machine calculation of complex Fourier series. Mathe. Comput., vol. 19, pp. 297-301.

Cooper, G.R.J. (1993) Grav2dc; 2.5D Gravity Modelling and Inversion for Microsoft Windows, School of Geosciences University of the Witwatersrand, Johannesburg 2050 South Africa. Available at https://www.researchgate.net/publication/264711117_Grav2dc_25D_Gravity_Modelling_and_Inversion_for_MS_Windows (Accessed March 2017).

Cooper, G.R.J. (2013) Mag2dc. An interactive 2.5D magnetic modeling and inversion software for Microsoft Windows, School of Geosciences University of the Witwatersrand, Johannesburg 2050 South Africa. Available at https://www.researchgate.net/publication/255696606_Mag2dc_Software_for_MS_Windows (Accessed April 2017).

Cooper, Y.L. and Munday, T. (2012) Electromagnetic methods used for the characterization of aquifers in Timor-Leste, ASEG Extended Abstracts, 2012:1, 1-4, DOI:10.1071/ASEG2012ab409

Corriols, M. Nielsen, M.R. Dahlin, T. and Christensen, N.B. (2009) Aquifer investigations in the Leon-Chinandega plains, Nicaragua, using electromagnetic and electrical methods, Near surface Geophysics, vol. 7, Issue 5-6, pp. 413-426.

Cox, L.H. Wilson, G.A. and Zhdanov, M.S. (2010) 3D inversion of airborne electromagnetic data using a moving footprint, Exploration Geophysics, vol. 41, pp. 250-259.

Daniels, J. (1988) Locating caves, tunnels and mines, The Leading Edge, vol. 7, no. 3, pp.1-64.

Dentith, M. and Mudge, S.T. (2014) Geophysics for the Mineral Exploration Geoscientist. Cambridge University Press, New York. DOI: 10.1017/cbo9781139024358.007

Descloitres, M. Guerin, R. Albouy,Y. Tabbagh, A. and Ritz, M. (2000) Improvement in TDEM sounding interpretation in presence of induced polarization. A case study in resistive rocks of the Fogo volcano, Cape Verde Islands. Journal of Applied Geophysics, vol. 45, pp. 1-18.

Dierckx, P. (1993) Curve and surface fitting with splines. Monographs on numerical analysis. Oxford University Press.

Dobrin, M.B. (1976) Introduction to Geophysical Prospecting. 3rd Edition, New York, McGraw Hill.

Dohr, G. (1975). Applied Geophysics, Pitman, London.

EM Geosci. (2018) Retrieved from https://em.geosci.xyz/content/geophysical_surveys/airborne_tdem/interpretation.html

Everett, M.E. (2013) Near-Surface Applied Geophysics. Cambridge University Press, New York.

Fantaye, T. (2010) Magnetotelluric and Transient electromagnetic methods in geothermal exploration with examples from the Krysuvik area, SW-Iceland, Report, no. 12, pp. 151-182. Figure accessed February 2018, at https://orkustofnun.is/gogn/unu-gtp-report/UNU-GTP-2010-12.pdf

Fitterman, D.V. and Anderson, W.L. (1987) Effect of transmitter turn-off time on transient soundings, Geoexploration, vol. 24, Issue 2, pp. 131-146.
Fletcher, P. and Sangwine, S.J. (2017) The development of the quaternion wavelet transform, Signal Processing vol. 136, pp. 2-15.
Fourier, J.B.J. (1822) Theorie analytique de la chaleur, Didot, Paris, pp. 499-508.
Geosoft Oasis Montaj. (2018) Available at www.geosoft.com (Educational kit version 9.4).
Geosoft Technical Note. (2018) Microlevelling Using FFT Decorrugation.
Geosoft. (2014). Montaj Geophysics How-To Guide. www.geosoft.com.
Geosoft. (2013). Montaj Geophysics How-To Guide. www.geosoft.com.
Goldman, M. and Kafri, U. (2004) The use of the time domain electromagnetic (TDEM) method to evaluate porosity of saline water saturated aquifers, 18 SWIM, Cartagena Spain, pp. 327-340.
Golturenko, I. (2018) The application of the LOZA-N GPR system (Ground penetrating Radar) to demonstrate the technology for imaging the subsurface at Vlakhoogte colliery, Report translated from Russian by Hallbauer, V.Z. and Stettler, E. pp. 21.
Hallbauer, V.Z. and Nyabeze, P.K. (2013) Time Domain Electromagnetic sounding in Southern Africa: Recent case studies, 13th SAGA Biennial Conference and Exhibition.
Hai, L. Xue, G. Zhou, N.N. and Chen, W. (2015) Appraisal of an array TEM Method in detecting a mined-out area beneath a conductive layer, Pure and Applied Geophysics, vol. 172, pp. 2917-2929.
Hancox, P.J. and Götz, A.E. (2014). South Africa's coalfields - A 2014 perspective: International Journal of Coal Geology, vol. 132, pp. 170-254, DOI: 10.1016/j.coal.2014.06.019 (Figure retrieved and modified on September, 2019).
Hatherly, P. (2013) Overview on the application of geophysics in coal mining, International Journal of Coal Geology, vol. 114, pp. 74-84.
Heath, P. Gouthas, G. Irvine, J. Krapf, C. and Dutch, R. (2017) Microgravity surveys to identify potential hidden cavities on the Nullarbor, Report Book 2017/00021, Department of the Premier and Cabinet, South Australia, Adelaide.
Hinze, W.J. (2003) Bouguer reduction density, why 2.67? Short Note. Geophysics, vol. 68, no.5, pp.1559-1560. DOI: 10.1190/1.1620629
Hinze, W.J. Von Frese, R.R.B. and Saad, A.H. (2013) Gravity and Magnetic Exploration. Cambridge University Press, New York.
Intrepid User manual. (2012). Spectral domain (FFT) grid filters (G16). Available at

https://www.intrepid-geophysics.com/ig/uploads/manuals/documentation_pdf_intrepid/gtspecfl.pdf (Accessed on September 2019).
Jacobs, J.A. (1967) The Earth's Core and Geomagnetism. Permagon Press.
Johnson, W.J and Snow, R.E. (2002) Surface geophysical methods for detection of underground Mine workings. Symposium on Geophysical Methods for Mine Mapping Verifications, pp. 1-18.
Kamenetsky, F.M., Stettler, E.H. and Trigubovich, G.M. (2010) Transient Geo-Electromagnetics. Ludwig-Maximilian-Universtity of Munich, Dept. of the Earth and Environmental Sciences, Section Geophysics.
Kaufman, A.A and Hoekstra, P. (2001) Electromagnetic soundings, Methods in Geochemistry and Geophysics, vol. 34, pp. 1-526.
Kearey, P. Brooks, M. and Hill, I. (2002) An Introduction to Geophysical Exloration. Third Edition. Blackwell Publishing.
Kleywegt, R.J. Mäkinen, J. Merry, C.L. and Wonnacott, R.T. (1996) Absolute gravity measurements in South Africa, Bulletin d'Information of the Bureau Gravimétrique International, pp. 40-46.
LaFehr, T.R. and Nabighian, M.N. (2012) Fundamentals of Gravity Exploration. Geophysical monograph series. Number 17.
LaFehr, T.R. (1991) Standardization in gravity reduction. Geophysics. vol. 56, no.8, pp .1170-1178.
Loke, H.M. (1999) Electrical imaging surveys for environmental and engineering studies; a practical guide to 2-D and 3-D surveys.
Long, L.T. and Kaufmann, R.D. (2013) Acquisition and Analysis of Terrestrial Gravity Data. Cambrige University Press, New York.
Martinez-Pagán, P. Gómez-Ortiz, D. Martin-Crespo, T. Manteca, J.I. Rosique, M. (2013) The electrical resistivity tomography method in the detection of shallow mining cavities. A case study on the Victoria Cave, Cartagena (SE Spain), Engineering Geology, vol. 156, pp. 1-10.
Maré, L.P. (1997). Council for Geoscience Petrophysical Properties Atlas.
McCann, D.M. Jackson, P.D. and Culshaw, M.G. (1987) The use of geophysical surveying methods in the detection of natural cavities and mineshafts: Quarterly Journal of Engineering Geology, London. vol. 20, pp. 59-73.
Mc Neill, J.D. (1996) Geonics Limited, Principles and applications of time domain electromagnetic techniques for resistivity sounding. Technical note TN-27.

Mickus, K.L. Aiken, C.L.V. and Kennedy, W.D. (1991). Regional-residual gravity anomaly separation using the minimum-curvature technique. Geophysics, vol. 56, no. 2, pp. 279-283.
Mohalik, N. K. Lester, E. & Lowndes, I. S. (2016) Review of experimental methods to determine spontaneous combustion susceptibility of coal – Indian context, International Journal of Mining, Reclamation and Environment, vol. 31, Issue 5, pp. 301-332. DOI: 10.1080/17480930.2016.1232334
Munk, J and Sheets, R.A. (1997) Detection of Underground Voids in Ohio by use of Geophysical Methods. U.S. Geological Survey: Water-Resources Investigations Report, pp. 97-4221.
Murray, A.S. and Tracey, R.M. (2001) Best Practice in Gravity Surveying. Geoscience Australia, Unpublished.
Nabighian, M.N. (2008) Electromagnetic methods in applied Geophysics. Investigations in Geophysics, vol. 2, no.3, Application, Parts A and B.
Nayak, R.C. and Dalai, S.K. (2010). Evaluation of Bord and Pillar Mining System in MCL coal Mines. BTech thesis.
Orfanos, C and Apostolopoulos, G. (2012) Analysis of different geophysical methods in the detection of an underground opening at a controlled test site, Journal of the Balkan Geophysical society, vol. 15, no. 1, pp.7-18.
Pashtoon, N.A. and Elliot, D. (1987) Handbook of Digital Signal Processing. Chapter 4 – IIR Digital Filters, pp. 289-357. DOI: 10.1016/B978-0-08-050780-4.50009-6
Peters, L. JR. Daniels J.J. and Young, J.D. (1994) Ground Penetrating Radar as a Subsurface Environmental Sensing Tool. Proceedings of the IEEE, vol. 82, no. 12, December 1994.
Polikar, R. (2001) The engineer's ultimate guide to wavelet analysis, The wavelet tutorial.
Rao, K.R. Kim, D.M. and Hwang, J.J. (2010) Fast Fourier Transform: Algorithms and Applications. Springer Science & Business Media, pp. 5-235.
Rorabaugh, C.B. (1993) Digital filter designer's handbook. Featuring C Routines. Division of McGraw-Hill, Inc, pp.
Reeves, C. (2005) Aeromagnetic Surveys. Principles, Practice & Interpretation, Published by Geosoft, pp. 19.
Reid, A.B. (1980) Aeromagnetic survey design. Geophysics, vol. 45, no.5, pp. 973-976.
Santos, F.A.M and El-Kaliouby, H.M. (2011). Quasi-2D inversion of DCR and TDEM data for shallow investigations, Geophysics, vol. 76, no. 4, pp. 239-250.
Scintrex Limited. (2017) Operating Manual for the CG5 Gravity Meter (electronic resource), https://www.scintrexltd.com, accessed April 2017.

Sloan, S. (2015). A current look at geophysical detection of illicit tunnels. The leading Edge: Near surface geophysics. vol. 34, no. 2, pp. 154.
South African Committee for Stratigraphy (S.A.C.S), (1980). Handbook Geological Survey of South Africa, vol. 8, pp. 690.
Spichak, V.V., (2015). Electromagnetic Sounding of the Earth's Interior: Theory, Modeling, Practice, Second Edition, pp. 51-52.
Styles, P. McGrath, R. Thomas, E. and Cassidy, N.J. (2005) The use of microgravity for cavity characterization in Karstic terrains, Quarterly Journal of Engineering and Hydrogeology, vol. 38, no. 2, pp.155-169.
Swain, C. J. (1976) A Fortran IV program for interpolating irregularly spaced data using the difference equations for minimum curvature, Computers & Geosciences, vol. 1, pp. 231-240.
Telford, W. M. Geldart, L. P. and Sheriff, R. E. (1990) Applied Geophysics, 2nd ed., Cambridge University Press, 1990.
Van Schoor, M and Fourie, C.J.S. (2015) A guide for applying geophysics to coal mining problems in South Africa, Coaltech.
Van Schoor, M and Fourie, C.J.S. (2014) The application of geophysics in South Africa coal Mining and exploration. The Journal of The South African Institute of Mining and Metallurgy. vol. 144, pp. 875-879.
Van Schoor, M. (2002) Detection of sinkholes using 2-D electrical resistivity imaging: Journal of applied Geophysics vol. 50, pp. 393-399.
Walsh, J.L. Ahlberg, J.H. and Nilson, N.E. (1962) Best Approximation Properties of the Spline Fit. Journal of Mathematics and Mechanics. vol.11, no.2, pp. 225-234.
Whitmeyer, (2012) The code used to plot vertical cross sections on Google Earth http://csmgeo.csm.jmu.edu/geollab/Whitmeyer/web/visuals/GoogleEarth/tools/XS.html (Accessed December 2018).
Yohe, G.R. (1958) Oxidation of coal. Report of investigations 207. Illinois state geological survey.
ZondTEM1D. (2017) Zond: User manual. Program for one-dimensional data interpretation of transient electromagnetic method using arbitrary source-receiver configuration. Retrieved from https://geo-device.com/upload/iblock/f5c/zondtem1d_eng.pdf